



Universiteit  
Leiden

The Netherlands

## **From atoms to the cosmos: exploring the cosmic web beyond collisional ionisation equilibrium**

Stofanová, L.

### **Citation**

*From atoms to the cosmos: exploring the cosmic web beyond collisional ionisation equilibrium.* (2024, November 13). *From atoms to the cosmos: exploring the cosmic web beyond collisional ionisation equilibrium.* Retrieved from <https://hdl.handle.net/1887/4109044>

Version: Publisher's Version

License: [Licence agreement concerning inclusion of doctoral thesis in the Institutional Repository of the University of Leiden](#)

Downloaded from: <https://hdl.handle.net/1887/4109044>

**Note:** To cite this publication please use the final published version (if applicable).

# From Atoms to the Cosmos

- Exploring the Cosmic Web Beyond Collisional Ionisation Equilibrium -

## Proefschrift

ter verkrijging van  
de graad van doctor aan de Universiteit Leiden,  
op gezag van rector magnificus prof.dr.ir. H. Bijl,  
volgens besluit van het college voor promoties  
te verdedigen op woensdag 13 november 2024  
klokke 11:30 uur  
door

Lýdia Štofánová

geboren te Banská Bystrica, Slowakije  
in 1995

**Promotores:**

Prof.dr. J.S. Kaastra (SRON)  
Prof.dr. J. Schaye

**Co-Promotor:**

Dr. A. Simionescu (SRON)

**Promotiecommissie:**

Prof.dr. I.A.G. Snellen  
Prof.dr. K.H. Kuijken  
Prof.dr. H. Hoekstra  
Dr. R.J. van Weeren  
Dr. E. Costantini (University of Amsterdam, SRON)  
Prof.dr. E. Behar (Technion)

Copyright © 2024 Lýdia Štofánová

ISBN: 978-94-6496-245-1

Cover design by M.P. Tychoniec ♥.  
This thesis was typeset using  $\LaTeX$ .

*To my beloved parents and grandparents.  
Pre mojich milovaných rodičov a starých rodičov.*

In loving memory of my father Jaroslav Štofan,  
1961 – 2021  
and my grandmother Viera Mydlová.  
1932 – 2022





*Great are the works of the Lord,  
studied by all who have pleasure in them.  
The fear of the Lord is the beginning of wisdom;  
a good understanding have all those who practice it.*

---

*Psalms 111:2,10 (RSVCE)*



# Table of contents

---

<b>1</b>	<b>Introduction</b>	<b>1</b>
1.1	Large scale structure of the Universe . . . . .	1
1.2	Galaxy clusters . . . . .	2
1.2.1	Characteristic radii . . . . .	2
1.2.2	Thermodynamic profiles . . . . .	4
1.2.3	Abundance profiles . . . . .	5
1.3	Cosmic web filaments . . . . .	7
1.3.1	X-ray emission studies of WHIM . . . . .	8
1.3.2	X-ray absorption studies of WHIM . . . . .	9
1.4	Cosmological hydrodynamical simulations . . . . .	10
1.5	Overview of X-ray plasma physics . . . . .	11
1.5.1	Atomic processes: overview . . . . .	13
1.5.2	Atomic processes: continuum . . . . .	15
1.5.3	Atomic processes: spectral lines . . . . .	16
1.5.4	Collisional ionisation equilibrium (CIE) . . . . .	17
1.5.5	Photoionisation equilibrium (PIE) . . . . .	17
1.5.6	Important differences between CIE and PIE plasmas . . . . .	18
1.5.7	Different definitions of temperature of ionised plasmas . . . . .	21
1.5.8	What can be derived from X-ray spectra? . . . . .	21
1.5.9	Galaxy clusters through X-ray spectroscopy . . . . .	23
1.5.10	X-ray plasma codes and databases . . . . .	25
1.6	X-ray detectors . . . . .	28
1.6.1	Wave-particle duality . . . . .	28
1.6.2	High-resolution X-ray detectors . . . . .	28
1.7	This thesis . . . . .	29
<b>2</b>	<b>Prospects for detecting the circum- and intergalactic medium in X-ray absorption using the extended intracluster medium as a backlight</b>	<b>33</b>
2.1	Introduction . . . . .	34
2.1.1	Research set-up . . . . .	35
2.2	Cosmological simulations . . . . .	36
2.2.1	Methods . . . . .	36
2.2.2	Results: properties of Hydrangea absorbers . . . . .	37
2.3	Observational predictions . . . . .	42
2.3.1	Methods . . . . .	42
2.3.2	Results: Simulations with the Athena X-IFU . . . . .	47
2.4	Discussion . . . . .	51

---

2.4.1	The optimal size of the spectral extraction region . . . . .	51
2.4.2	Impact of weighting by different surface brightness profiles . . . . .	52
2.4.3	Prospects for detectors with a different spectral resolution and effective area . . . . .	53
2.4.4	Impact of potential sources of O VII emission . . . . .	54
2.5	Conclusions . . . . .	56
	Appendices . . . . .	58
2.A	Total column density maps . . . . .	58
<b>3</b>	<b>Galaxy cluster photons alter the ionisation state of the nearby warm-hot intergalactic medium</b>	<b>61</b>
3.1	Introduction . . . . .	62
3.2	Methods . . . . .	63
3.2.1	Galaxy cluster selection . . . . .	63
3.2.2	Density and temperature profiles . . . . .	63
3.2.3	SPEX . . . . .	64
3.2.4	Total photon flux seen by an absorbing particle . . . . .	64
3.2.5	Photoionisation model . . . . .	66
3.3	Results . . . . .	66
3.3.1	A2029 . . . . .	66
3.3.2	Comparison to A262 & A1795 . . . . .	71
3.4	Discussion . . . . .	75
3.4.1	Impact on the predicted column densities . . . . .	75
3.4.2	Suppression of cooling rates . . . . .	78
3.5	Conclusions . . . . .	79
<b>4</b>	<b>The <i>clus</i> model in SPEX: projection and resonant scattering effects on the iron abundance and temperature profiles of galaxy clusters</b>	<b>81</b>
4.1	Introduction . . . . .	82
4.2	Methods . . . . .	83
4.2.1	SPEX . . . . .	83
4.2.2	The <i>clus</i> model . . . . .	83
4.2.3	Sample selection and <i>clus</i> model simulations . . . . .	87
4.2.4	Fitting procedure . . . . .	89
4.3	Results . . . . .	92
4.3.1	Simulations with the Chandra ACIS-S CCD . . . . .	92
4.3.2	Simulations with the XRISM Resolve micro-calorimeter . . . . .	96
4.4	Discussion . . . . .	102
4.4.1	Multi-temperature and multi-metallicity structure of the ICM . . . . .	102
4.4.2	Measured Fe abundance drop in the cores . . . . .	102
4.5	Conclusions . . . . .	104
	Appendices . . . . .	105
4.A	Chandra results for other clusters . . . . .	105
<b>5</b>	<b>New radiative loss curve from updates to collisional excitation in the low-density, optically thin plasmas in SPEX</b>	<b>109</b>
5.1	Introduction . . . . .	110
5.2	Methods . . . . .	111
5.2.1	Radiative loss due to collisional excitation in low-density plasmas . . . . .	111

5.2.2	Radiative loss curves in SPEX, MEKAL and CHIANTI . . . . .	111
5.3	Results . . . . .	112
5.3.1	Effect of the maximum principal quantum number . . . . .	112
5.3.2	Contribution of resonant excitation . . . . .	115
5.3.3	Comparison of radiative loss function for SPEX and MEKAL . . . . .	115
5.3.4	Comparison with the CHIANTI and ADAS databases . . . . .	117
5.3.5	Updated dielectronic recombination and its contribution to overall cooling . . . . .	120
5.3.6	Implementation of updates to PIE model in SPEX . . . . .	120
5.3.7	Contribution from metastable levels . . . . .	120
5.3.8	Calculation of the total cooling curve in SPEX and the comparison to MEKAL, Cloudy, and APEC . . . . .	122
5.4	Application: Stability curve for photoionised plasmas . . . . .	126
5.4.1	Thermal stability curve . . . . .	127
5.4.2	Obtaining the S-curve in SPEX . . . . .	128
5.4.3	A new stable branch . . . . .	128
5.4.4	Ionic column densities . . . . .	128
5.5	Discussion . . . . .	129
5.5.1	Theoretical calculations . . . . .	129
5.5.2	Comparison of SPEX to other plasma codes . . . . .	133
5.5.3	Metastable levels . . . . .	133
5.5.4	Update of the pion model in SPEX . . . . .	134
5.6	Conclusions . . . . .	135
<b>Bibliography</b>		<b>149</b>
<b>Nederlandse samenvatting</b>		<b>151</b>
<b>English summary</b>		<b>155</b>
<b>Zhrnutie v slovenčine</b>		<b>159</b>
<b>List of publications</b>		<b>163</b>
<b>Curriculum Vitae</b>		<b>165</b>



# 1

## Introduction

---

### 1.1 Large scale structure of the Universe

The large scale structure (LSS) of the observable Universe – also called the “**Cosmic Web**” (Bond et al. 1996) – describes the Universe on megaparsecs scales. According to the hierarchical structure growth scenario, the Universe evolved from small perturbations present in the primordial density field, which over time, as the Universe was expanding, anisotropically collapsed into more massive objects due to the gravitational force (Zel’dovich 1970).

The cosmic web can be classified into *voids*, *sheets*, *filaments* and *nodes*, depending on the amount of axes in which the density field collapses/expands locally (Fisher et al. 2016). If the gravitational collapse happens along all three principal axes, cosmic web nodes/clusters are formed. If the collapse happens along two axes, while in the third axis the density field keeps expanding, the cosmic web filaments are formed. Cosmic web sheets/walls form during the collapse along just one axis, while voids expand along all three axes. In general, there is a variety of classification methods for different parts of the cosmic web, however, as Libeskind et al. (2018) points out, most of them reach a similar conclusion: cosmic web nodes can be found in the higher density regions in comparison with filaments, while the voids exhibit the lowest densities.

It has been more than three decades that scientists have been looking for the “**missing baryons**” in the Universe (Persic & Salucci 1992; Fukugita et al. 1998; Cen & Ostriker 1999; Shull et al. 2012). At redshift  $z > 2$ , these baryons reside in cool gas and can be predominantly detected in the Lyman  $\alpha$  forest (e.g. Lynds 1971; Sargent et al. 1980; Cen et al. 1994; Zhang et al. 1995; Weinberg et al. 1997; Schaye 2001). At current epoch at  $z = 0$ , the cosmological hydrodynamical simulations predict that baryons are heated to higher temperatures mainly via shock-heating due to the gravitational collapse and the hierarchical growth of structures in the Universe (Bristow & Philipps 1994; Cen & Ostriker 1999). Additionally, the heating can happen also due to supernova feedback, active galactic nuclei feedback or photoionisation by cosmic UV and X-ray background (Tepper-García et al. 2012). Vast majority of diffuse baryons at  $z = 0$  have not yet been converted into stars and are expected to reside in groups of galaxies – the so-called intra-group medium (IGrM), in the haloes of galaxy clusters – the intra-cluster medium (ICM), or in the space between galaxies – the intergalactic medium (IGM). A subset of the IGM is the warm-hot intergalactic medium (WHIM) permeating large-scale structure filaments, while another component of the IGM is comprised of the gas found in the haloes of galaxies – the so-called circum-galactic medium (CGM).



The 2007 discovery of fast radio bursts (FRB, Lorimer et al. 2007) provided a new technique which in 2020 led to a solution to the “missing baryons” problem (Macquart et al. 2020). Since the signal from these radio sources travels from very far away, the matter between these sources and Earth causes a dispersion to the FRB light. The so-called Macquart relation shows that the average dispersion measure (ADM) of the IGM increases with increasing redshift of the FRB host. This means that the further the FRB source is, the more of the total free electron “content” (the diffuse IGM) between the observer and the FRB source it reveals. The detection of FRB signal in combination with identification of its host galaxy, which is used for determining its distance from Earth, finally solved the tension between different values of the baryon density  $\Omega_b$ . Macquart et al. (2020) reported the cosmic baryon density  $\Omega_b = 0.051^{+0.021}_{-0.025} h_{70}^{-1}$  with 95% confidence, where  $h_{70}$  is the dimensionless Hubble constant. Even though the “missing baryons” problem was solved, the ADM can not distinguish between WHIM, cool or photoionised gas, and a large fraction of these baryons is still yet to be detected at  $z = 0$  (see more details in section 1.3).

## 1.2 Galaxy clusters

Galaxy clusters, which consist of tens or hundreds of individual galaxies (see the left panel of Fig. 1.1 which shows an image of Abell 383 galaxy cluster as observed in the optical waveband), are the most massive gravitationally bound systems in our Universe. The underlying dark matter (DM) halo is often described with the halo density profile of Navarro, Frenk, & White (NFW, Navarro et al. 1995, 1996, 1997) obtained from the cold-DM cosmological simulations. These simulations additionally showed that the self-similarity of clusters, predicted by Kaiser (1986), also holds true for their hot X-ray component. However, galaxy clusters are more complicated than just their DM halo, and the non-gravitational processes such as the active galactic nucleus (AGN) feedback, the supernova (SN) feedback or major mergers strongly affect their properties. In the sections below we summarize some of these properties with focus on X-rays, thermodynamic and abundance profiles. For a more comprehensive overview we refer the reader to reviews by Boehringer & Werner (2009); Allen et al. (2011); Werner & Mernier (2020); Kay & Pratt (2022); Sanders (2023).

The X-ray images of galaxy clusters show a presence of a very extensive (1-2 megaparsecs in radius) and diffuse source of light (Kellogg et al. 1972; Forman et al. 1972). The rarefied and hot plasma, which fills in the potential wells of these massive objects (see the right panel of Fig. 1.1) is known as the **intra-cluster medium** (ICM), and forms the majority of baryonic mass in these objects. The ICM has typically temperatures between  $10^7$ – $10^8$  K, densities between  $10^{-4}$ – $10^{-2}$  cm $^{-3}$ , and an average abundance of  $0.3Z_{\odot}$ .

### 1.2.1 Characteristic radii

When talking about galaxy clusters, it is very convenient to define a few characteristic radii to describe their properties. The very first of such radii is the **virial radius**, derived from the Virial theorem, which describes the relaxed galaxy clusters that are not disturbed by a recent merger activity. Since the force which holds galaxies in the galaxy cluster is gravity, we can express the Virial theorem as

$$E_{\text{kinetic}} = -\frac{1}{2} E_{\text{potential}} , \quad (1.1)$$

where  $E_{\text{kinetic}}$  is the average kinetic energy of the system, which can be expressed as

$$E_{\text{kinetic}} = \frac{1}{2} \sum_i m_i v_i^2, \quad (1.2)$$

where  $m_i$  and  $v_i$  are the mass and velocity of test particles (e.g. galaxies, or thermal motions of the ICM particles) in the cluster, and  $v_i$  is measured with respect to the centre of mass of the cluster.  $E_{\text{potential}}$  is the average gravitational potential energy, which is equal to

$$E_{\text{potential}} = -\frac{GM}{R}, \quad (1.3)$$

where  $G$  is the gravitational constant,  $M$  is the total mass, and  $R$  represents the radius of a cluster. By putting together these equations and assumptions, we can derive the virial mass of the cluster  $M_{\text{virial}}$

$$M_{\text{virial}} = \frac{R_{\text{virial}} v_{\text{average}}^2}{G}, \quad (1.4)$$

where  $R_{\text{virial}} = R$ , and  $v_{\text{average}}^2 = \frac{\sum_i m_i v_i^2}{\sum_i m_i}$ . In the spherical top-hat collapse model (see more details in e.g. Kay & Pratt 2022), the density contrast of this virialised halo is

$$\Delta c \approx 178. \quad (1.5)$$

A good proxy to the virial radius, which is often used in the literature, is  $r_{\Delta c=200}$  – the radius of a sphere within which the mean overdensity is 200 times the critical density  $\rho_{\text{crit}}(z)$  of the Universe at redshift  $z$ , which can be expressed as

$$\rho_{\text{crit}}(z) = \frac{3H^2(z)}{8\pi G}, \quad (1.6)$$

where  $H(z)$  is the Hubble parameter at redshift  $z$ . The critical density is derived from the Friedmann equations assuming  $\Lambda = 0$  and that the curvature parameter  $k = 0$ . Under the assumption of spherical symmetry one can derive the mass of a sphere which is enclosed within radius  $r_{200}$  as

$$M_{200} = 200 \frac{4}{3} \pi \rho_{\text{crit}}(z) r_{200}^3. \quad (1.7)$$

In the same manner one can define radius  $r_{500}$  of a sphere within which the mean overdensity is 500 times the critical density of the Universe. An approximate relation between  $r_{200}$  and  $r_{500}$  is

$$r_{200} \approx \frac{3}{2} r_{500}. \quad (1.8)$$

The **accretion shock radius** is the outermost boundary of ICM, and it marks the distance at which the gas from cosmic web voids gets accreted onto the cosmic web filaments or the galaxy clusters, where it becomes a part of the ICM. This radius is located at approximately  $4 - 5 r_{200}$  (Ryu et al. 2003; Molnar et al. 2009; Lau et al. 2015), and it has been found that it closely tracks the **splashback radius**, which represents an outer boundary of the underlying dark matter halo (Diemer & Kravtsov 2014; Diemer et al. 2017; Adhikari et al. 2014). Another characteristic radius is the radius where the **virial shock** is located, which is expected to be at the distance slightly higher than the virial radius, at approximately  $1 - 2 r_{200}$ . At this radius, the gas which has already been shock heated when penetrating to the cosmic web filaments, gets accreted onto the galaxy cluster. Due to the limitations of current X-ray missions, these radii have only been predicted from simulations, however, they have not yet been observationally confirmed.

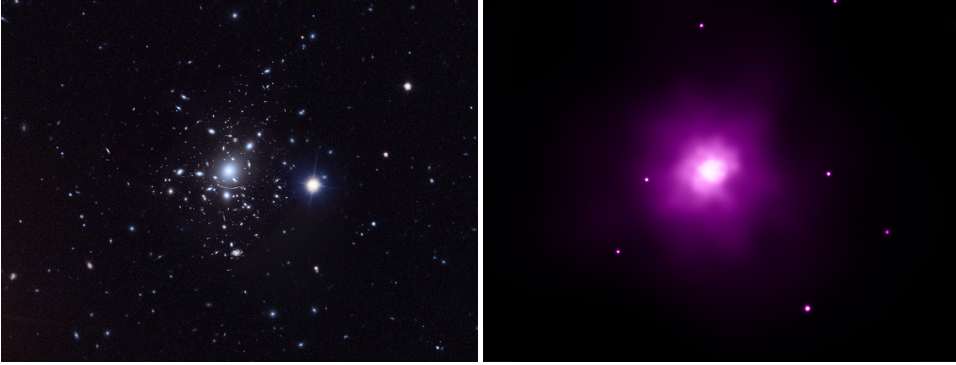


**Figure 1.1:** Galaxy cluster Abell 383 observed in the optical waveband with the Hubble Space Telescope, the Very Large Telescope, and the Sloan Digital Sky Survey (left panel), and in the X-ray waveband with the Chandra X-ray observatory (right panel). In optical wavelengths we can see the individual cluster members, while in X-rays the intra-cluster medium is revealed. Both pictures are  $7.26'$  across. Credit: NASA/STScI, ESO/VLT, SDSS (optical), and NASA/CXC (X-ray).

### 1.2.2 Thermodynamic profiles

Galaxy clusters have a wide range of thermodynamic profiles. For example, measuring these profiles with high spatial resolution is important for determining whether galaxy clusters scale self-similarly.

As Fig. 1.2 (adapted from Kay & Pratt 2022) shows, **density profiles** are either flattened towards the cluster cores, which is the case of morphologically disturbed clusters (by e.g. mergers), or they rise towards the core and show a prominent cusp - the so called *cool-core* clusters (CC). CC clusters are known for their peaky surface brightness profiles, contrary to the flat surface brightness profiles of *non-cool-clusters* (NCC). The CCs and NCCs can be clearly distinguished by the difference in their thermodynamic profiles, as well as the fact that the cooling time of CCs is much shorter than the Hubble time. However, their origin and evolution are not yet completely understood.

The simplest parametrisation of density profiles of galaxy clusters is the *isothermal  $\beta$ -model* suggested by Cavaliere & Fusco-Femiano (1976). This model was later expanded by Mohr et al. (1999) to the *double  $\beta$ -model* using ROSAT archival data of 45 clusters. Some of these clusters showed an emission excess in their cores, and Mohr et al. (1999) concluded that the double  $\beta$ -model provides a significantly better description of these clusters in comparison with the single  $\beta$ -model. Nowadays, the most commonly used models for CC clusters are the modified double  $\beta$ -models, as e.g. described in Vikhlinin et al. (2006), which we used in chapters 2, 3, and 4.

The shape of the **temperature profiles** of galaxy clusters reflects their underlying density profiles: CCs with dense ICM cores exhibit temperatures which are decreasing towards the cluster cores, while NCCs with central densities below  $10^{-2} \text{ cm}^{-3}$  exhibit rather flat (or sometimes also moderately increasing) profiles towards their centres (Vikhlinin et al. 2006; Pratt et al. 2007; Leccardi & Molendi 2008). In the outskirts, the temperature profiles steadily decrease (Ghirardini et al. 2019).

**Entropy profiles** of galaxy clusters are crucial for studying the thermal history of ICM plasma, and for distinguishing between heating of the ICM by either purely gravitational or

non-gravitational processes (e.g. shocks, radiative cooling). By knowing the electron density  $n_e$  and the electron temperature  $T_e$ , and assuming that the studied gas is ideal and monatomic, we can obtain the equation of state for the **electron pressure**  $P_e$  as

$$P_e = n_e k_B T_e, \quad (1.9)$$

as well as the **entropy**  $K$

$$K = \frac{k_B T_e}{n_e^{2/3}}, \quad (1.10)$$

where  $k_B$  is the Boltzmann constant. If the ICM is heated only by the gravitational collapse, the entropy  $K$  scales with radius as

$$K(r) \propto r^{1.1}. \quad (1.11)$$

However, it has been shown that galaxy clusters exhibit much higher entropies in their cores than what the heating by gravitational processes predicts (Ponman et al. 1999). Additionally, Ponman et al. (1999) showed that galaxy groups, which exhibit shallower potential wells, have flatter entropy profiles in their cores in comparison with clusters. The entropy profiles also differ for CCs and NCCs: CCs have rather low entropy in their cores, while NCCs (and mergers/disturbed systems) show a high central entropy.

More recent studies suggest that the entropy is higher than from the gravitational collapse predictions (Nagai et al. 2007; Sun et al. 2009) up to  $r_{2500}$ , and that it can be parametrised as a power law, or a constant plus power law (Donahue et al. 2005; Pratt et al. 2010). E.g. Cavagnolo et al. (2009) studied entropy profiles of 239 clusters and showed that in their centres, the clusters show a bimodal distribution of entropies, with two distinct peaks at  $K_0 \sim 15 \text{ keV cm}^2$  and  $K_0 \sim 150 \text{ keV cm}^2$ , where  $K_0$  is the constant in the parametrized function. In the outskirts (beyond  $r_{500}$ ), the entropy profiles mostly converge to the predictions from gravitational collapse (Ghirardini et al. 2019). Around the accretion shock radius, the entropy is expected to reach its peak and start decreasing towards higher radii. These predictions from cosmological simulations will, however, be only tested with missions planned beyond ESA's Athena (see section 1.6.2).

The **pressure profiles** are often described by the '*universal*' *pressure profile* as proposed by Nagai et al. (2007) for a sample of cool-core and hot ( $kT > 5 \text{ keV}$ ) clusters observed with Chandra. Arnaud et al. (2010) extended this analysis to 33 local ( $z < 0.2$ ) galaxy clusters using the REXCESS XMM-Newton survey (Böhringer et al. 2007). On average, the pressure profiles steadily decrease from the core towards the outskirts, and at  $r_{200}$  the logarithmic slope of this steepening is  $-3.0$  according to Ghirardini et al. (2019), where the authors also concluded that beyond  $0.3 r_{200}$ , CCs and NCCs have very similar profiles. However, in the cluster centres, their pressure profiles differ from each other, and CCs have more peaky profiles in comparison with NCCs (similar to the shape of their density profiles).

### 1.2.3 Abundance profiles

Galaxy clusters show flattened, or peaky abundance profiles towards their cores, while in their outskirts the abundance profiles flatten towards a constant value between  $0.2 - 0.4 Z_\odot$  (the specific value depends on the object, as well as on the set of abundances used during the data analysis). Fig. 1.3 (adapted from Mernier et al. 2017), shows a comparison between averaged iron abundance profiles of galaxy clusters and groups.

The abundance profiles of galaxy clusters also revealed a mystery of **lack of metals in their cores**. Later, it was discovered that some galaxy groups, as well as giant elliptical galaxies have the same mysterious abundance profile. X-ray observations of some of

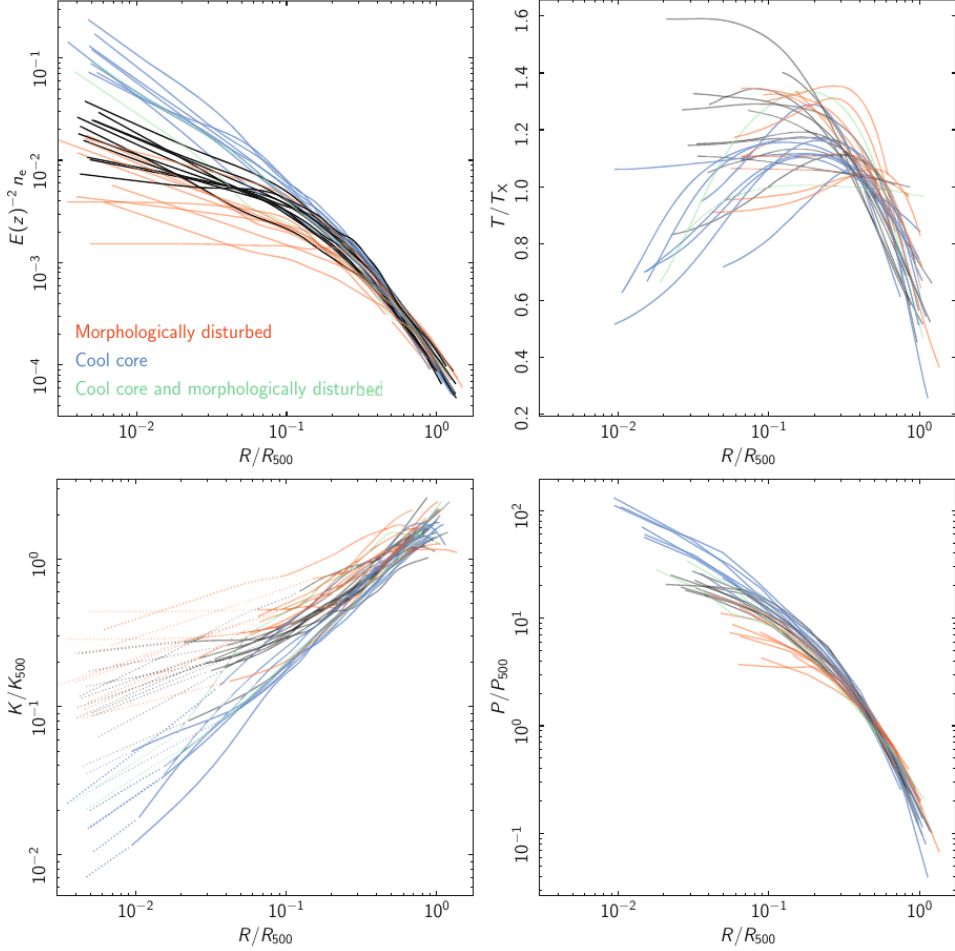


**Figure 1.2:** Thermodynamic profiles of 33 galaxy clusters from the XMM-Newton cluster survey REXCESS (Böhringer et al. 2007). These profiles show the electron density  $n_e$  (scaled by redshift  $z$  through  $E(z)^{-2}$ ), temperature  $T$  (scaled by the spectroscopic temperature  $T_X$ ), entropy  $K$  (scaled by  $K_{500}$ ), and pressure  $P$  (scaled by  $P_{500}$ ). Different colours represent different morphological stages of these clusters. For more details see Kay & Pratt (2022).

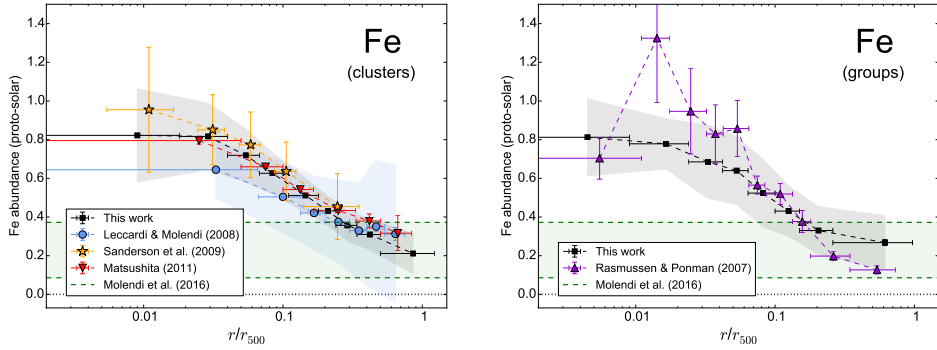


**Figure 1.3:** Averaged iron abundance profiles of galaxy clusters (left) and galaxy groups (right). Different colours represent measurements from different observations, and the black points show measurements by Mernier et al. (2017), from which the plot was adapted.

these objects revealed a steep decrease in abundances (mainly iron) in the few innermost kpc (Johnstone et al. 2002; Churazov et al. 2003; Sanders & Fabian 2007; Million et al. 2010; Rafferty et al. 2013; Mernier et al. 2017), where some of these abundances dropped by 50% of their global maximum. The origin of this abundance drop has not yet been established, however, in chapter 4 we offer a potentially promising explanation for the mystery of lack of metals in the massive elliptical galaxies.

### 1.3 Cosmic web filaments

The observational evidence for LSS can be seen from the spatial distribution of galaxies, as shown in the left panel of Fig. 1.4, which was obtained with the Sloan Digital Sky Survey (SDSS, York et al. 2000). As we mentioned previously, this thesis focuses on the cosmic web filaments and their future observations with high-resolution X-ray spectrometers. Therefore, in the following sections we describe only currently existing measurements of WHIM in X-rays, and the literature studies that have claimed its observation with telescopes such as Rosat, XMM-Newton, Chandra, or eROSITA.

WHIM is expected to contain around 30% up to 60% of all baryons of the Universe (e.g. Fukugita et al. 1998; Davé et al. 2001; Tepper-García et al. 2012; Shull et al. 2012; Martizzi et al. 2019; Tuominen et al. 2021). These baryons reside predominantly in the filamentary structures of the cosmic web (e.g. Martizzi et al. 2019; Tuominen et al. 2021) and can be detected mostly in the ultraviolet (UV, see e.g. Nicastro et al. 2003) and X-ray wavebands/energies (e.g. Hellsten et al. 1998; Fang et al. 2002a; Wijers et al. 2019; Wijers & Schaye 2022) because of their relatively high temperatures ( $10^5 - 10^7$  K). Due to WHIM's high temperature, low electron density ( $10^{-6} - 10^{-4} \text{ cm}^{-3}$ ), and high ionisation state, the observations of this very diffuse and tenuous gas are extremely challenging with currently available X-ray telescopes. There have been many attempts to observe WHIM, either in emission or in absorption. Since the X-ray emissivity decreases as density squared while absorption decreases linearly with density, extreme ultraviolet (EUV) and X-ray emission only probes the densest and hottest parts of the WHIM. Another challenge for observing emission and absorption from WHIM is caused by the interstellar medium (ISM) of our Galaxy, especially the neutral hydrogen of the ISM which absorbs most of the EUV and the softest X-ray band. Many of the local ISM

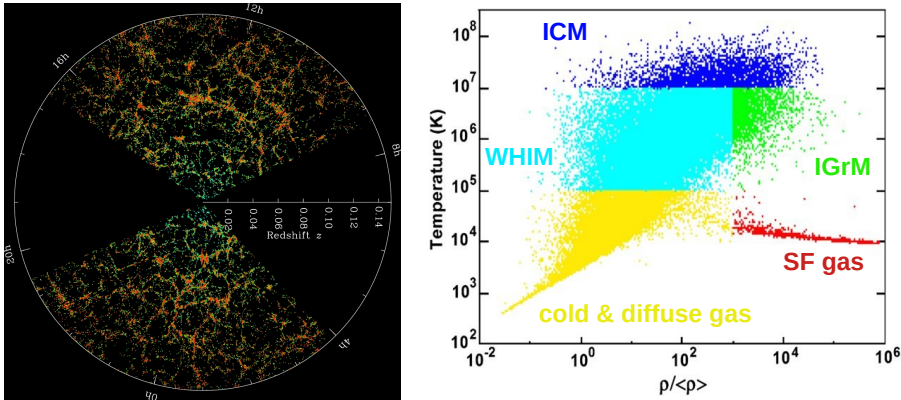


**Figure 1.4:** *Left:* Spatial distribution of galaxies as measured by SDSS. Every dot represents a galaxy, while the colour-coding shows the age of stars in individual galaxies (red points represent older stars). The observer on Earth is placed in the centre, and the outer ring is at a distance of 613.2 Mpc. *Right:* The phase diagram of gas from simulations described in more details in Ursino et al. (2010). Based on the overdensity and temperature threshold, the gas is divided into five groups: star forming gas ( $T < 10^5$  K,  $\rho/\langle\rho\rangle > 1000$ , red), cold diffuse gas in the cosmic web voids ( $T < 10^5$  K,  $\rho/\langle\rho\rangle < 1000$ , yellow), WHIM ( $10^5 < T < 10^7$  K,  $\rho/\langle\rho\rangle < 1000$ , sky blue), IGrM in galaxy groups ( $10^5 < T < 10^7$  K,  $\rho/\langle\rho\rangle > 1000$ , green), and the ICM in the galaxy clusters ( $T > 10^7$  K, blue).

lines unfortunately have energies where a lot of WHIM lines could be found, and therefore knowing the composition of the gas in our Milky Way is extremely important.

### 1.3.1 X-ray emission studies of WHIM

Despite the previously mentioned challenges, there have been multiple papers which reported the detection of WHIM in X-ray emission. Wang & McCray (1993) detected an X-ray radiation component in the Lockman Hole region (Hasinger et al. 1993), which was needed to explain the observed intensity in the 0.5 – 0.9 keV energy band. Authors associated this component to diffuse thermal radiation and gave multiple scenarios for its origin, claiming that it could also be a relic of the large scale structure formation of the early Universe. Briel & Henry (1995) found a  $1 - 2\sigma$  detection of the X-ray emission that was believed to be associated to the filaments detected by the Rosat All-Sky survey. This analysis was based on stacking the emission from 40 galaxy cluster pairs. Authors claimed that a larger sample of such cluster pairs was needed for a higher sigma detection, in order to confirm that the emission comes from the hot cosmic web filaments. Kull & Böhringer (1999) reported an elongated X-ray emission between clusters in the Shapley Supercluster which was detected in the Rosat All-Sky Survey. Another Rosat X-ray detection, which was claimed to be originating from filaments, was presented in Scharf et al. (2000). Tittley & Henriksen (2001) discovered emission claimed to be from the filament between the A3391 and A3395 galaxy clusters. The X-ray emission from filaments was also discovered in later papers, as for example Zappacosta et al. (2002); Finoguenov et al. (2003); Kaastra et al. (2003). Werner et al. (2008) detected the X-ray emission from the filament with  $5\sigma$  significance from deep XMM-Newton observations (144 ks) between clusters of galaxies A222 and A223. The detection was possible thanks to the favourable geometry of this filament which was oriented

almost along the line of sight. This detection was also supported by the weak lensing data of Dietrich et al. (2005). Eckert et al. (2015) found 4 structures connected to the galaxy cluster A2744 in the XMM-Newton data, which were associated with the WHIM and its accretion flow towards the cluster. Some of the newest emission studies of WHIM were done by e.g. Akamatsu et al. (2017); Hattori et al. (2017); Connor et al. (2018); Parekh et al. (2020); Reiprich et al. (2021); Ghirardini et al. (2021); Tanimura et al. (2022); Parimbelli et al. (2022); Churazov et al. (2023a). The most recent detections which were made with eROSITA are described in Veronica et al. (2022, 2024), and Dietl et al. (2024).

### 1.3.2 X-ray absorption studies of WHIM

It is more feasible to observe WHIM in absorption against very bright, point like sources e.g. quasars or blazars. The first detection of WHIM in O VII, O VIII, and Ne IX absorption toward PKS 2155-304 was reported by Nicastro et al. (2002) with the Chandra X-ray observatory. Fang et al. (2003) detected the resonance O VII He $\alpha$  line in the sight line toward 3C 273 also with Chandra. The authors explored two scenarios for the origin of this gas: (a) the Milky Way halo and its ISM, and (b) the IGrM in the Local Group. The second scenario, if true, showed properties comparable to the properties of WHIM predicted with simulations. However, due to the limitations of the instruments back then, authors could not distinguish between these two scenarios. Additionally, they concluded that the collisional ionization is the dominant ionization source in these detections. Another detection, believed to originate from the IGrM of the Local group (based on the constraints on the electron density, scale length, and mass) was reported by Rasmussen et al. (2003) in the sight lines toward three quasars (PKS 2155-304, Mrk 421, and 3C 273) with the XMM-Newton Observatory. The absorption features yielded the column densities of  $N_{\text{O VII}} \sim 10^{16} \text{ cm}^{-2}$ . Fujimoto et al. (2004) reported a detection in O VIII associated with the large scale structure around the Virgo cluster with the column density of  $N_{\text{O VIII}} > 7 \times 10^{16} \text{ cm}^{-2}$ . The first detection of two filaments toward the sight line of the blazar Mrk 421 with Chandra was documented in Nicastro et al. (2005b), however, Kaastra et al. (2006) reanalysed the same dataset and claimed the observations of Nicastro et al. (2005b) to be statistically not significant, which was also supported with higher signal-to-noise ratio in the RGS data of XMM-Newton. Takei et al. (2007) claimed a detection from Ne IX and O VIII with a combined significance of  $3\sigma$  associated with the Coma cluster. The reported temperature  $\sim 4 \times 10^6 \text{ K}$  and density  $\sim 6 \times 10^{-6} \text{ cm}^{-3}$  are in agreement with the predicted WHIM properties from cosmological simulations. A few of the most recent absorption studies (including the simulations of future absorption studies) were reported by e.g. Nicastro et al. (2018); Ahoranta et al. (2021); Spence et al. (2023); Butler Contreras et al. (2023). A detailed review of the WHIM absorption studies can be found in the review by Nicastro et al. (2022).

A complimentary method for an observation of the gas in filaments in absorption is to use the galaxy clusters as the background candles. This method was for the first time suggested by Markevitch (1999); Markevitch et al. (2009), when looking far to the future of the X-ray observations of faint, diffuse and extended sources. Since the galaxy clusters sit at the cross roads of the cosmic web filaments, the sight lines pointed towards the cluster cores are very likely to probe the densest parts of the filaments, and therefore provide the highest column densities and the deepest absorption profiles. Simionescu et al. (2021) extended on this idea by providing simple estimates of such absorption. The WHIM was estimated as a single absorber cloud with temperature  $kT = 0.2 \text{ keV}$ , metallicity  $Z = 0.3 Z_{\odot}$ , and hydrogen column density of  $N_{\text{H}} = 10^{19} \text{ cm}^{-2}$ . Abell 1795 was taken as a background galaxy cluster, assuming



–1500 km/s velocity difference between the cluster core and WHIM. The model for Galactic ISM was simplified to include only a single component (neutral gas) with  $N_{\text{H}} = 10^{24} \text{ cm}^{-2}$ . These predictions were made for the ‘Cosmic Web Explorer’ as a part of the Voyage 2050 call by the European Space Agency (ESA). In chapter 2 of this thesis, we explored this idea, and used the cosmological hydrodynamical simulations to predict whether the cosmic web filaments can be observed in O VII and in O VIII against cool-core galaxy clusters with the micro-calorimeter on board of future ESA’s mission called Athena X-ray observatory. Additionally, we also provided the specific sightlines which will be the most promising for this type of observation.

## 1.4 Cosmological hydrodynamical simulations

Cosmological hydrodynamical simulations became a vital tool for studying LSS, in particular, the low density and low surface brightness regions like outskirts of galaxy clusters, and the cosmic web filaments. With nowadays X-ray instruments, it is extremely difficult to observe this rarefied gas, and therefore the cosmological hydrodynamical simulations help us study its properties, as well as its spatial distribution in more details. This knowledge helps us to prepare for the upcoming X-ray spectroscopic missions, planned to be launched in late 2030s.

Cosmological hydrodynamical simulations study the evolution of the Universe from redshift  $z \sim 100$  up to the present time ( $z = 0$ ). In a chosen volume (large volume or zoom-in simulations) and cosmological framework, which includes the cosmological model and the set of initial conditions (density and velocity field perturbations), they follow the evolution, formation, and structure growth in the simulated Universe. They either include only dark matter and dark energy, or additionally, they take into account baryons and radiation. These different components evolve under the influence of gravity while simultaneously following the hydrodynamical equations. As Fig. 1.5 shows, the LSS can look very differently depending on the presence or absence of baryons. Figure 1.6, adapted from Vogelsberger et al. (2020), shows an overview of different types of simulations.

The dark matter is assumed to be non-interactive, and therefore it is described by the collisionless Boltzmann equation, while the gravity is described by the Poisson equation. Both of these equations are solved for an expanding Universe, whose description follows the Friedmann equations. Since the computational methods do not allow us to simulate an infinite volume of the Universe, the volume of each simulation is restricted to a box with pre-defined dimensions. With the option of periodic boundary conditions this is, however, not a limitation.

Since the main point of simulations is to predict the observational quantities of visible matter, most of the simulations include the baryonic component, as well as the radiation. These components are described as fluids and therefore the hydrodynamical equations can be used. The cosmological hydrodynamical simulations typically use two main methods of describing the hydrodynamics of gas: (a) Eulerian, when gas/fluid parcel is observed in a fixed resolution element as it flows through this element with time, or (b) Lagrangian, when individual gas resolution elements are followed in space and time. The codes implementing the Eulerian hydrodynamics solver usually use the **adaptive mesh refinement (AMR)** technique, while the solvers which use the Lagrangian methods use **smoothed particle hydrodynamics (SPH)** or **moving mesh** methods.

Due to the limited numerical resolution of these simulations, as well as their computational expenses, a lot of baryonic physics is included in the simulations via the so called **sub-**

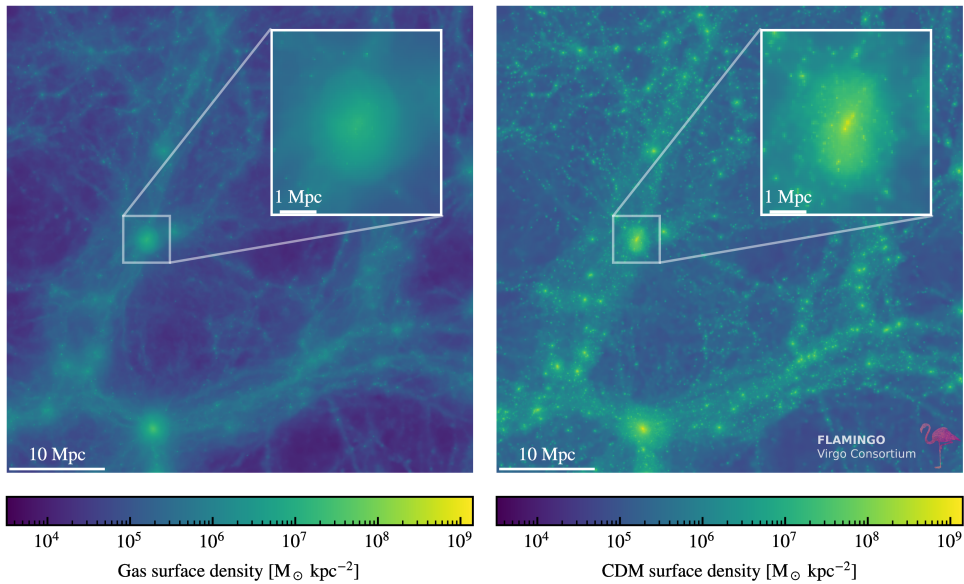


**Figure 1.5:** Gas (left) and cold DM (right) surface density from a  $50 \times 50 \times 20$  Mpc slice of Flamingo simulations (Fig. 8 in Schaye et al. 2023). The zoom in panels show a halo with the mass of  $M_{200c} = 1.26 \times 10^{14} M_{\odot}$ .

**resolution/sub-grid models.** Depending on the type of simulations, the sub-grid models usually include the radiative cooling, photo-cooling and photo-heating rates, the star formation rates, the physics of the interstellar medium, seeding of the supermassive black holes, the stellar feedback, the supernova feedback, and the energy feedback from supermassive black holes (AGN feedback). They can potentially also include the dust physics, neutrino physics, or magnetic fields.

A few examples of cosmological hydrodynamical simulations are: the OWLS simulations (Schaye et al. 2010), EAGLE (Schaye et al. 2015), Hydrangea (Bahé et al. 2017), Illustris (Vogelsberger et al. 2014), Illustris TNG (Springel et al. 2018; Pillepich et al. 2018), FIRE (Hopkins et al. 2014), Magneticum (Hirschmann et al. 2014; Dolag 2015), Simba (Davé et al. 2019), HorizonAGN (Dubois et al. 2014), CAMELS (Villaescusa-Navarro et al. 2021), TNG-Cluster (Nelson et al. 2023a), and FLAMINGO (Schaye et al. 2023).

## 1.5 Overview of X-ray plasma physics

Plasma is the most common state of gas in the Universe. As Fig. 1.7 shows, its temperature and density spans many orders of magnitude, and therefore it can be found in a variety of different astrophysical objects. Objects such as galaxy clusters provide a unique environment (due to their large volume), in which we can study X-ray plasmas with extremely low densities that can not be reproduced in the laboratories on Earth. This makes galaxy clusters one of a kind objects, which help us understand plasmas in such extreme conditions.

As it was mentioned in the previous sections, the cluster environment can be very hot and full of heavy metals. Many ions are fully ionised, however, depending on the density,

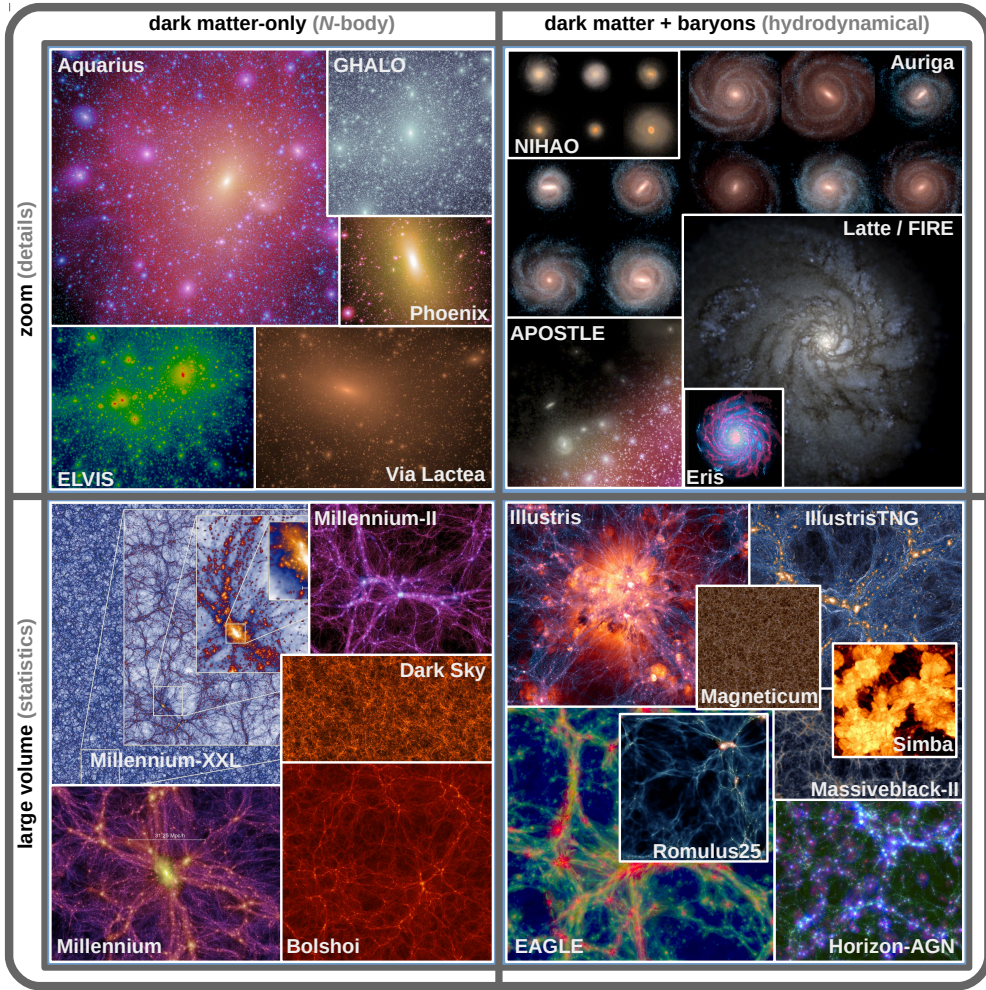


**Figure 1.6:** Overview of different types of simulations as shown in Vogelsberger et al. (2020).

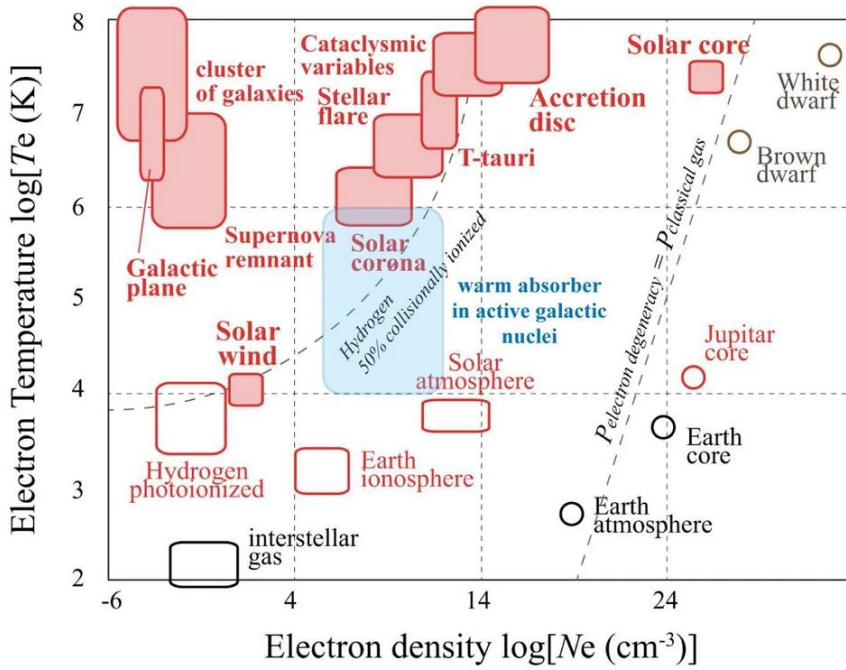


**Figure 1.7:** Phase diagram for different astrophysical plasmas adapted from Ezoe et al. (2021).

temperature, and the metallicity of the gas, some metals are “only” highly ionised. Such ions have more than one bound electron, and many free energy levels, which can serve as possible channels for (de-)excitation, recombination, electron capture, and many other atomic processes which are present in X-ray plasmas. In the subsections below we provide a brief summary of these atomic processes.

### 1.5.1 Atomic processes: overview

In this section we summarize all atomic processes that can happen in X-ray plasmas and that influence the ion concentrations, as well as the shape of the final observed spectrum. More details about individual processes as well as ionisation balance can be found in e.g. Kaastra et al. (2008).

1. *Radiative transitions* (or radiative decay, or radiative cascade) is a process of filling in the “hole” created by any process which kicks out the bound electron from an ion, or excites the electron to a higher energy level. The excited/ionised atom or ion will always have the tendency to fall back to its ground state (if permitted by laws of the quantum physics).
2. *Fluorescence* occurs when a vacancy in an orbital of an ionised atom, which lost a bound electron through the collision with photon, is filled by an electron from one of the upper shells. In simple terms, fluorescence happens if a photoionisation is followed by a radiative decay. The emitted photon has an energy equal to the difference between an energy of the initial state and an energy of the final state.

3. *Auger process (autoionisation)* is an ionisation process which happens through freeing a bound electron while at the same time another electron decays to a lower orbit, resulting in a radiation-less transition.

#### 4. Excitation processes

- The *collisional (radiative) excitation* is a process when a free electron (photon) collides with a bound electron in an ion, and this bound electron is excited to a higher orbit.
- The *collisional de-excitation* is the same process as collisional excitation but the bound electron is brought into a lower orbit. The ion needs to already be in an excited state, and therefore this process is more significant in high density plasmas or for the metastable levels.

#### 5. Ionisation processes

- The *collisional ionisation* is similar to the collisional excitation, however, the free electron now has enough energy to ionise the atom and kick out the bound electron from this system. In this case, the kinetic energy of a free electron needs to be larger in comparison with the binding energy of the atomic shell to which the bound electron belongs. The ionisation happens mostly through the outer-shell electrons.
- The *photoionisation* works on the same principle as collisional ionisation but instead of a free electron, a photon interacts with the bound electron of an atom/ion and ionises it. This results in a different profile of the photoionisation cross section of ions as a function of energy (or temperature). Contrary to the collisional ionisation, the ionisation happens mostly through the inner-shell electrons, which have the largest cross sections.
- Even if a free electron does not have sufficient energy to cause a direct ionisation, the ionisation can happen due to the excitation followed by the Auger process - so called *excitation-autoionisation* process. This affects mostly the Li-like and Na-like ions.
- The Compton scattering is defined as an inelastic scattering of radiation off of free, charged particles (e.g. electrons). The *Compton ionisation* occurs when the radiation undergoes Compton scattering on the bound electrons in an atom/ion.
- *Charge transfer/charge exchange (CX)* happens when two ions collide and one of the ions loses an electron (*CX ionisation*), and this electron is captured by the other ion (*CX recombination*). This process mostly happens at low temperatures (below  $10^5$  Kelvin) between hydrogen or helium and heavier nucleus ions. For example, the interactions of H I and He I with heavier ions lead to the recombination of this heavier ion, while the interactions with H II and He II lead to the ionisation of the heavier elements. For CX the cold and hot phase need to interact without an intermediate temperature phase in-between them. Therefore, if CX is measured, it is an indication that the hot and cold phases are not mixed well.
- The *inner-shell ionisation* happens if a photon, or an electron collides with an ion and removes an electron from any of its inner shells. In more complicated cases this can be followed by another Auger process (the so called *inner-shell ionization-autoionization* process).

## 6. Recombination processes

- *Radiative recombination* happens when a free electron is captured by an ion and simultaneously a photon is emitted. This process can be seen as an inverse process to photoionisation, and it creates continuum emission (see Section 1.5.2).
- In the process of *dielectronic recombination (DR)* a free electron is captured by an ion, and at the same time an electron is excited to a higher energy level. This creates a doubly excited state, which is quite unstable, and often followed by the autoionisation (the so called *DR-Auger effect*). But this doubly excited state can also be followed by a radiative decay to the ground level, when a stable, but excited state of the ion is created. One DR process often leads to multiple emission lines, as well as satellite lines.

### 1.5.2 Atomic processes: continuum

There are three main processes that produce continuum emission in X-rays:

1. **Free-free emission (thermal bremsstrahlung)** is radiated when a free electron is deflected in the electric field of an ion. The electron loses its kinetic energy while the X-ray radiation is emitted. The emissivity of free-free radiation  $\epsilon_{ff}$ , expressed in units of photons  $\text{m}^{-3} \text{s}^{-1} \text{J}^{-1}$ , is proportional to

$$\epsilon_{ff} \propto n_e n_{\text{ion}} \frac{1}{\sqrt{T_e}} \exp\left(-\frac{E_\gamma}{k_B T_e}\right), \quad (1.12)$$

where  $k_B$  is the Boltzmann constant,  $T_e$  is the electron temperature,  $E_\gamma$  is the energy of emitted photon, and  $n_e$  and  $n_{\text{ion}}$  are the electron and ion density, respectively.

2. **Free-bound emission** is produced by radiative recombination. Its emissivity  $\epsilon_{fb}$  can be expressed as

$$\epsilon_{fb} = \sum_i n_e n_{\text{ion}} R_n, \quad (1.13)$$

where  $R_n$  is the recombination rate to an energy level with the principal quantum number  $n$ .

3. **Two photon emission** happens when an excited bound electron from  $2s$  shell decays to  $1s$  shell while emitting two photons. This process is mainly important for H-like and He-like ions, especially in low density plasmas with  $n_e \ll n_{e,\text{crit}}$ , where  $n_{e,\text{crit}}$  scales with the atomic number  $Z$ , and for H-like ions is (see equations 36 and 37 in Kaastra et al. (2008))

$$n_{e,\text{crit}} (\text{H-like}) = 7 \times 10^9 \times Z^{9.5} \text{ m}^{-3}, \quad (1.14)$$

and for He-like ions is

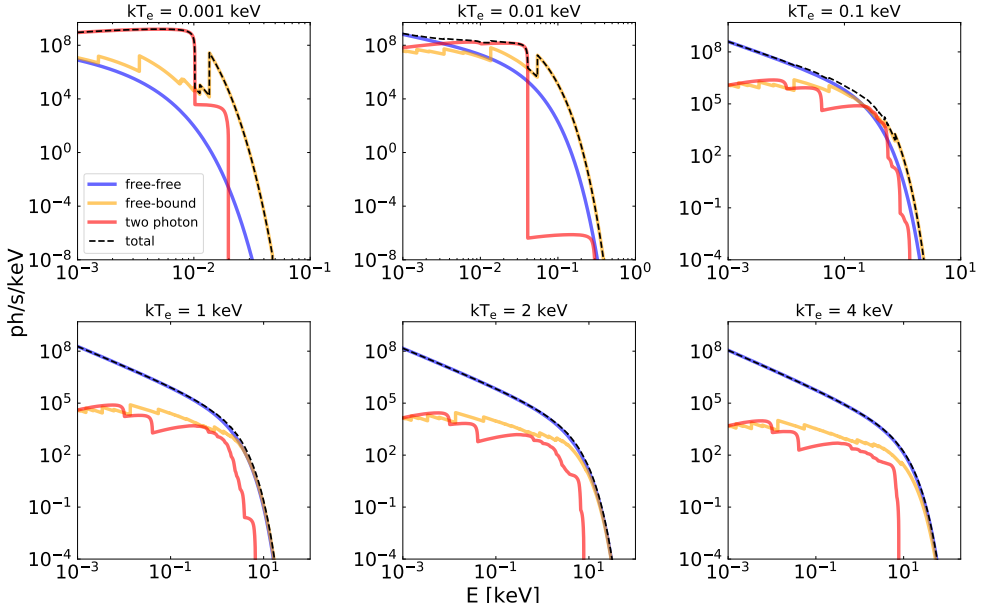
$$n_{e,\text{crit}} (\text{He-like}) = 2 \times 10^{11} \times (Z - 1)^{9.5} \text{ m}^{-3}. \quad (1.15)$$

Fig.1.8 shows a comparison of these continuum processes and how their contribution to the overall continuum spectrum changes with different temperature. From Fig.1.8 we see that above  $k_B T_e = 1 \text{ keV}$ , the spectrum is mostly dominated by thermal bremsstrahlung.

On the other hand, the opacity of the continuum absorption  $\tau_{\text{continuum}}$  is only dependent on the column density  $N_i$  of an ion  $i$  and the photoionisation cross section  $\sigma_i(E)$  at energy  $E$ , and can be expressed as

$$\tau_{\text{continuum}} = \sum_i N_i \sigma_i(E). \quad (1.16)$$





**Figure 1.8:** Contribution of different continuum emission processes to the overall spectrum (black dashed line) as calculated with SPEX (version 3.08) using the *cie* model. The normalisation was assumed to be  $10^5 \times 10^{64} \text{ m}^{-3}$  and the temperature  $k_B T_e$  of every simulation is indicated in the title of each sub-plot.

### 1.5.3 Atomic processes: spectral lines

Besides the continuum emission/absorption, X-ray spectra can have a strong presence of many spectral lines, which in the era of micro-calorimeters can now be resolved in unprecedented detail. Following e.g. Lodders et al. (2009) (see more in Section 1.5.8), the ten most abundant elements (in descending order) are: H, He, O, C, Ne, N, Mg, Si, Fe, and S. In X-rays, the strength of the absorption lines is mainly determined by the abundance, and therefore the strongest X-ray absorption lines are from oxygen, which is the most abundant metal in the Universe (H and He are fully ionised). However, the X-ray emissivity increases as  $\sim Z^4$ , where  $Z$  is the charge of the nucleus. Therefore, the iron emission lines are either stronger or comparable to the oxygen emission lines, even though iron is less abundant than oxygen.

The **emission lines** are essentially produced in two main steps: first, the electron is excited (or the ion is ionised), and secondly, this excitation/ionisation is followed by a spontaneous emission. The excited/ionised ion will always have a tendency to decay back to the ground state or any other level/state which is possible (either because of the selection rules, or just because of the free “space” in an orbital). The excitation processes which create the emission lines are the collisional excitation, radiative recombination, inner-shell ionisation, and dielectronic recombination. The width of these lines can be influenced by the broadening which has different origins (e.g. the thermal Doppler broadening or turbulent velocity, see section 1.5.8 for more details). Additionally, the strength of these emission lines can also be influenced by the **resonant scattering** process. If a photon is resonantly scattered, it gets absorbed and almost immediately re-emitted in a different direction. For example, in the case of galaxy clusters, this causes the flux in the resonant line to drop in their cores, however, in

the outskirts this causes an enhancement in the flux of the same resonant line. We describe this process in more details in chapter 4.

The transmission in an **absorption line** with wavelength  $\lambda$  can be essentially expressed as a function of the ionic column density  $N_{\text{ion}}$ , the velocity dispersion  $\sigma_v$ , and the line profile  $\phi(\lambda)$  as

$$T(\lambda) \propto \exp(-\tau_0 \phi(\lambda)) \propto \exp\left(-\frac{N_{\text{ion}}}{\sigma_v} \phi(\lambda)\right), \quad (1.17)$$

where we approximated the opacity at the line centre  $\tau_0 \propto \frac{N_{\text{ion}}}{\sigma_v}$ . Some examples involve the outer-shell absorption (mostly from resonant lines), inner-shell absorption (caused by Auger processes), or the unresolved transition arrays (inner-shell absorption of heavier elements in the high-density regime).

### 1.5.4 Collisional ionisation equilibrium (CIE)

The simplest case of the ionisation balance which determines how many ions are at which ionisation state in astrophysical plasmas is **collisional ionisation equilibrium** (CIE). It is commonly found in objects such as the solar corona, coronae of stars, the hot intra-cluster medium, or the hot component of the interstellar medium of our Galaxy. This plasma is optically thin for its own radiation, the excitations or ionisations happen mainly due to collisions with electrons, and every ionisation leads to one extra free electron which is kicked out of the atom or ion, and becomes a part of the free electron population in the plasma. The radiation that is produced by filling in the void in this ionised/excited atom then leaves the system, and does not interact with the ions in the plasma, and therefore it does not cause any additional photo-ionisation (Kaastra et al. 2016, 2017). The collisions in this plasma happen only with electrons and not with photons, and therefore processes such as photo-ionisation and Compton ionisations can be neglected. Effectively, all ions present in the plasma have their electrons in the ground state, and the populations of non-ground levels can be neglected with an exception for hydrogen and helium (Kallman & McCray 1982; Dopita & Sutherland 2003)).

In order to obtain the ion concentrations, and therefore the X-ray emission and absorption from this plasma under specific physical conditions, one needs to solve the equations of the ionisation balance. What makes the case of the CIE plasmas “easy” is the fact that there is essentially just one equation that needs to be solved:

$$\text{number of ionisations} = \text{number of recombinations} . \quad (1.18)$$

The dominant atomic processes that contribute to the ionisations are the electron impact collisional ionisations (collisional ionisation and excitation-autoionisation). The dominant recombination atomic processes are the radiative and dielectronic recombination. At low temperatures the important processes that also need to be taken into account are charge transfer ionisation and recombination. The ionization state of CIE plasma is essentially determined just by the temperature of gas. It is important to realize that the ionisation balance established in CIE is different from the balance achieved under the thermodynamic equilibrium, when the level populations obey the Saha-Boltzmann equation.

### 1.5.5 Photoionisation equilibrium (PIE)

If an external source of radiation is the dominant process of the ionisations and excitations in plasma, the most simple case of the equilibrium state is the **photoionisation equilib-**



**rium** (PIE), when the electron temperature  $T_e$  is much lower than the ionisation temperature  $T_{\text{ionisation}}$ . In addition to solving the Eq. (1.18), which is now more complicated due to multiple ionisations caused by Auger cascades, one needs to also solve the energy balance equations for electrons:

$$\text{total heating} = \text{total cooling} , \quad (1.19)$$

and take into account all different processes that can cause the heating and the cooling of the plasma. Additionally to the processes mentioned in the CIE case, the photoionisation and Compton ionisation need to be considered. The details of these equations can be found in e.g. Osterbrock (1974); Halpern & Grindlay (1980); Kallman & McCray (1982). The atomic processes that contribute to the **total cooling** are: inverse Compton scattering, electron ionisation, radiative recombination, free-free emission, collisional excitation, dielectronic recombination, and adiabatic expansion. The atomic processes that contribute to the **total heating** are: free-free absorption, photo-electrons, Compton ionisation, Auger electrons, collisional de-excitation, and external sources of ionisation.

In the optically thin case, it is common to define the ionisation parameter  $\xi$  (Tarter et al. 1969; Krolik et al. 1981) as

$$\xi \equiv \frac{L_{1-1000 \text{ Ry}}}{n_{\text{H}} R_{\text{abs}}^2} , \quad (1.20)$$

where the ionising source is described by the luminosity  $L_{1-1000 \text{ Ry}}$  over the energy band 1–1000 Rydbergs ( $\approx 1.36 \times 10^{-2} - 13.6 \text{ keV}$ ),  $n_{\text{H}}$  is the hydrogen number density of a photoionised plasma, and  $R_{\text{abs}}$  is the distance of the photoionised plasma to the source of ionisation. If the gas is isobaric, it is convenient to define the ionisation parameter in its dimensionless pressure form  $\Xi$ , which is proportional to the ratio ionizing flux/gas pressure, and can be expressed as

$$\Xi \equiv \frac{1}{4\pi c k_{\text{B}}} \frac{\xi}{T_e} , \quad (1.21)$$

where  $c$  is the speed of light,  $k_{\text{B}}$  is the Boltzmann constant, and  $T_e$  is the electron temperature. The famously known stability curve (or S-curve), which is often used when studying photoionised plasmas in e.g. AGN, is obtained if plasma temperature is plotted as a function of  $\Xi$ . On the S-curve, the total cooling rate is equal to the total heating rate. Based on the slope of the S-curve (positive or negative), one can tell whether the plasma is thermally stable ( $dT_e/d\Xi > 0$ ) or thermally unstable ( $dT_e/d\Xi < 0$ ).

Typical examples of the plasma in PIE are e.g. the broad line region of AGN, gas accreting onto compact objects like black holes or X-ray binaries, or cataclysmic variables.

### 1.5.6 Important differences between CIE and PIE plasmas

In this section we mention a few of the most important differences between two equilibrium states of plasma which we described earlier: CIE and PIE. In the case of PIE plasma, we discuss the photoionisation by the cosmic UV and X-ray background, since it is described in more details in chapter 3. In Fig. 1.9 we show a comparison of different models for the cosmic UV and X-ray background at  $z = 0$  and at  $z = 1$  as described in Faucher-Giguère (2020).

In CIE, the equilibrium ion fractions are only a function of temperature, and are independent of the plasma density, while for the PIE case, the equilibrium ion fractions are simultaneously a function of temperature and density. In Fig. 1.10 (left panel) we show a phase diagram for gas at  $z = 0.1$  using cosmological hydrodynamic simulation EAGLE (Schaye et al. 2015). The figure (adapted from Wijers (2022)) is colour-coded by the gas fraction in the resonant line of O VII at 0.5685 keV, and it shows at which hydrogen densities and temperatures

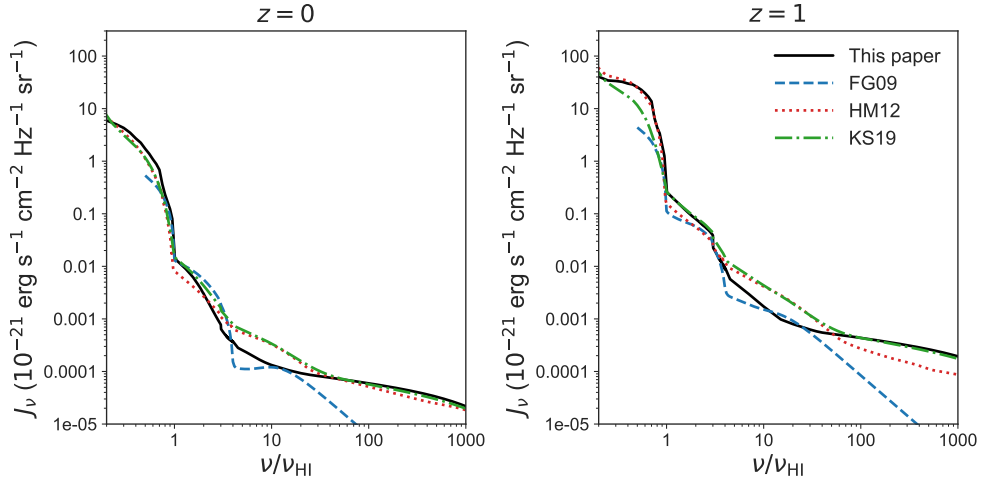


**Figure 1.9:** Comparison of different models for the cosmic UV and X-ray background for two redshifts:  $z = 0$  (left) and  $z = 1$  (right). The figure was adapted from Faucher-Giguère (2020) (black solid line), which we also used as a photoionisation UV/X-ray background in chapter 3.

the gas is predominantly in CIE or PIE equilibrium. The source of photoionisation is the cosmic UV/X-ray background as calculated by Haardt & Madau (2001).

Additionally, as we have shown in chapter 3 for cosmic web filaments and galaxy clusters, there are cases of PIE plasmas when the equilibrium ion fractions can not be tabulated as a function of the ionisation parameter  $\xi$  (defined in equation (1.20)) and temperature, but in order to capture the full complicated ionisation balance, one needs to tabulate the ion fractions as a function of density, temperature of the photoionised gas, as well as the distance between the ionising source and the photoionised gas. To demonstrate how ion fractions change between CIE and PIE, we plot them for O VI, O VII, and O VIII ions in Fig. 1.10 (right panel). As it can be seen from this figure, the oxygen ion fractions rise significantly towards the lower temperatures, if the photoionisation source (in this case modelled by Faucher-Giguère (2020)) is added to the balance equations. This means that the range of temperatures, for which the ionisation happens, is significantly larger in comparison with the CIE case, and at the same time the peak temperature, at which the ion fractions reach their maximum, also changes in the PIE case. From this figure it is clearly shown that the ion fractions are density dependent.

Another difference between CIE and PIE can be seen for the cooling curves. In Fig. 1.11, adapted from Lykins et al. (2013), we show cooling curves for CIE and PIE cases calculated using CLOUDY (Ferland et al. 1998). The cooling rate is defined as the rate, at which collisions convert kinetic energy into light. In the photoionisation case, the cooling is not a unique function of kinetic temperature, and it depends on the underlying photoionisation source, which was assumed to be an AGN for which the spectral energy distribution is described in more details in Mathews & Ferland (1987). Fig. 1.11 demonstrates that the total cooling rate in PIE is lower for all temperatures in comparison with the total cooling rate in CIE. This stems from the fact that the ionization balance in PIE is determined by the interplay between the photoionisation and recombination rates, and this balance is rather weakly dependent on temperature.

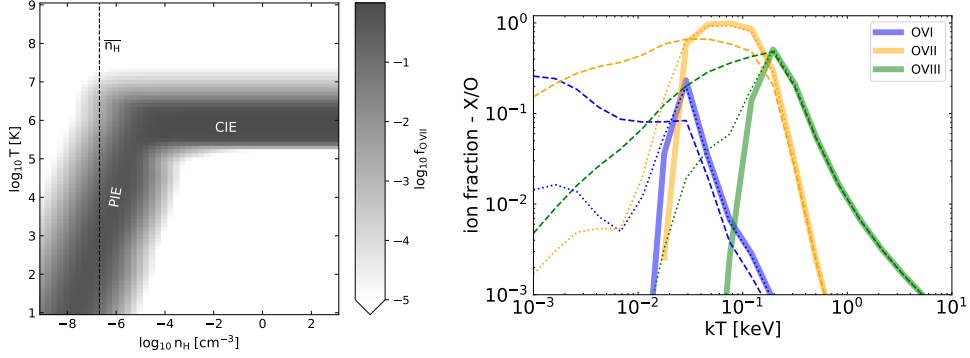


**Figure 1.10:** *Left:* phase diagram of the O VII (resonance line at 0.5685 keV) gas fraction calculated from EAGLE cosmological hydrodynamic simulations at redshift  $z = 0.1$  (adapted from Wijers 2022). The photoionisation source in this case was modelled by Haardt & Madau (2001). *Right:* ion fractions of O VI (blue), O VII (orange), and O VIII (green) as a function of temperature. The solid lines show the ion fractions assuming CIE, while the dashed and dotted lines show PIE ion fractions. The photoionisation source was assumed to be Faucher-Giguère (2020) (see chapter 3 for more details). Different line styles show different hydrogen number densities:  $10^{-5} \text{ cm}^{-3}$  (dashed) and  $10^{-4} \text{ cm}^{-3}$  (dotted). These ion fractions were calculated using SPEX (version 3.08).

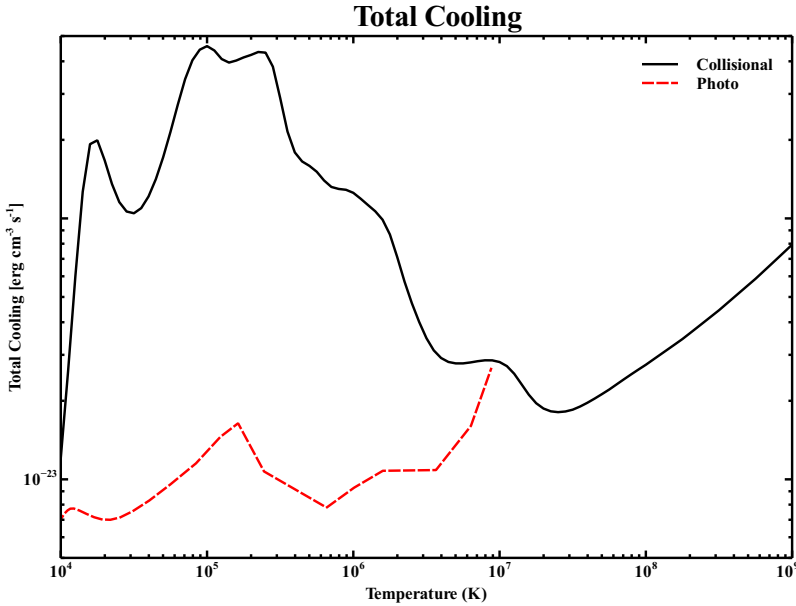


**Figure 1.11:** Cooling curves for CIE (black) and PIE (red) plasmas as calculated by Lykins et al. (2013) (Fig.11). The spectral energy distribution for the PIE case is an AGN described in more details in Mathews & Ferland (1987).

### 1.5.7 Different definitions of temperature of ionised plasmas

It is important to realize that there is no such thing as one temperature of the ionised plasma, unless the plasma is in CIE. In fact, when talking about X-ray plasmas, there are several different definitions of a temperature, and it is crucial to recognize how different plasma temperatures can be obtained from the observed spectra, especially nowadays in the era of high-resolution X-ray spectroscopy with micro-calorimeters (see more details in Section 1.6.2). To determine the ionisation level of plasma, there are four temperatures which can be derived from spectra:

1. the electron temperature  $T_e$ ,
2. the ion temperature  $T_{\text{ion}}$ ,
3. the excitation temperature  $T_{\text{ex}}$ , and
4. the ionisation temperature  $T_{\text{ionisation}}$ .

In CIE, all these temperatures are the same, and  $T_e = T_{\text{ion}} = T_{\text{ex}} = T_{\text{ionisation}}$ . In PIE,  $T_e \ll T_{\text{ionisation}}$  since the collisions with photons dominate over the collisions with electrons. For more details about temperatures in non-equilibrium states, when  $T_e \neq T_{\text{ion}} \neq T_{\text{ionisation}}$ , see Ezoe et al. (2021). In the following Section 1.5.8 we describe how to obtain these temperatures of ionised plasmas from observed spectra.

### 1.5.8 What can be derived from X-ray spectra?

An X-ray spectrum is a powerful tool, from which many physical properties of the observed object can be derived. In the list below we summarize how different physical properties can be derived from an X-ray spectrum:

- The **electron temperature**  $T_e$  averaged along the line of sight can be derived from the shape of the continuum. However, objects like e.g. galaxy clusters have a distribution of temperatures and densities which are represented by the 3D profiles, therefore, already when deriving  $T_e$ , we make assumptions about the geometry of the object, or e.g. about the distribution of the emission measure (see the bullet point below, or for more complicated cases see chapter 4).
- The **electron density**  $n_e$  can be derived from the normalization of the continuum, which is proportional to the emission measure EM. EM is defined as a product of  $n_e n_H dV$ , where  $n_e$  is the electron density,  $n_H$  is the hydrogen density, and  $dV$  is the volume filled by the emitting gas. Therefore, if we assume the geometry of the emitting source, and we know the hydrogen density  $n_H$  (see for more details below), we can calculate the electron density  $n_e$  from the emission measure.
- From knowing the electron density and the electron temperature, we can obtain the **electron pressure**  $P_e$  and **entropy**  $K$  following equations (1.9) and (1.10), respectively (see section 1.2.2). Additionally, the **sound speed**  $c_s$  can be obtained as

$$c_s = \sqrt{\frac{5}{3} \frac{k_B T_e}{\mu m_p}} \quad (1.22)$$

where  $\mu$  is the mean particle mass,  $m_p$  is the proton mass, and  $T_e = T_i$  if gas is in CIE.

- Measuring the equivalent width of a line, which is defined as the total area of the spectral line below or above the continuum level, allows us to obtain the **abundance**. Any time the abundance is measured from spectra, it is crucial to specify which set of tables for (proto-) solar abundances was used (e.g. commonly used abundance tables are Allen 1973; Ross & Aller 1976; Anders & Grevesse 1989; Grevesse et al. 1992; Grevesse & Sauval 1998; Lodders 2003; Lodders et al. 2009; Asplund et al. 2009).
- The **ion temperature**  $T_{\text{ion}}$  is determined from the thermal Doppler broadening of the line, which is a Gaussian function with the width  $\sigma_{\text{Doppler}}$  given by

$$\sigma_{\text{Doppler}} = E_0 \sqrt{\frac{2k_B T_{\text{ion}}}{m_i c^2}}, \quad (1.23)$$

where  $E_0$  is the centroid energy of the line,  $T_{\text{ion}}$  is the ion temperature,  $m_i$  is the ion mass, and  $c$  is the speed of light. If the resolution of an instrument allows it, it is the best to compare the widths of spectral lines originating from different ions.

- The **ionisation temperature**  $T_{\text{ionisation}}$  can be determined from the emission lines of different ions of the same element, and from the recombination edges.
- The **excitation temperature**  $T_{\text{ex}}$  can be obtained from the ratio of different lines of the same ion.
- If the resonance ( $w$  or  $r$ ), forbidden ( $f$  or  $z$ ), and inter-combination lines ( $x$  and  $y$ ) of the same ion can be resolved in a spectrum (e.g. the famously known Fe xxv lines in the Perseus cluster), the ratio  $R$  of line intensities defined as

$$R = \frac{f}{x + y}, \quad (1.24)$$

is a proxy of the electron density, while the ratio

$$G = \frac{x + y + f}{r}, \quad (1.25)$$

is an indicator of the electron temperature. The comparison of the intensity of the resonance line relative to the forbidden line is also a good indicator of how optically thick or thin the plasma is, since the resonant line can be heavily suppressed by the effect called resonant scattering (see chapter 4 for more details), while the intensity of the forbidden line stays unchanged even in the optically thick scenario.

- Since the **turbulence** as well as the ion temperature both cause a broadening of the line, it is crucial to distinguish between them in spectra. This is only possible with high-resolution spectroscopy and micro-calorimeters. The Doppler broadening varies depending on the species of ions, since it is dependent on their mass, however, the broadening due to turbulent velocities is the same for all different ions and species. Therefore, measuring the level of turbulence can not be determined just from one spectral line, but one needs to fit simultaneously multiple spectral lines of different species (e.g. iron, silicon, and sulphur). Similar to the Doppler broadening, the turbulence also has a Gaussian shape, and the width of the line due to turbulence  $\sigma_{\text{turbulence}}$  gives the turbulent velocity  $v_{\text{turbulence}}$  following equation

$$\sigma_{\text{turbulence}} = v_{\text{turbulence}} \frac{E_0}{c}. \quad (1.26)$$

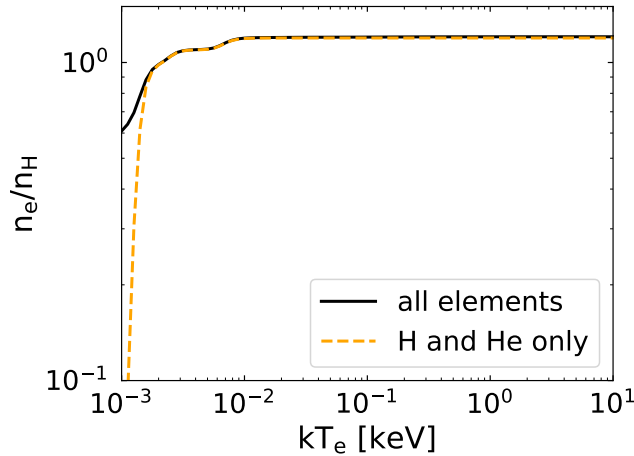


**Figure 1.12:** Electron over hydrogen number density as a function of electron temperature for CIE. The black solid line shows the ratio when all elements available in SPEX are taken into account (H-Zn), while the orange dashed line is calculated for hydrogen and helium only. Above temperature of  $\sim 10^{-2}$  keV, the function reached the constant value of  $\sim 1.2$ . The calculations are made with SPEX (version 3.08).

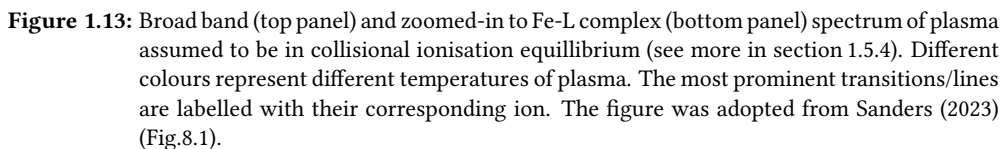
For galaxy clusters and cosmic web filaments, whose densities are not as high as for e.g. compact objects, it is usually safe to assume that

$$n_e \sim 1.2 n_H, \quad (1.27)$$

however, it is important to realize that this is an approximation, and that the ratio of  $n_e/n_H$  is a function of temperature. To demonstrate this, we plot the ratio of  $n_e/n_H$  as a function of temperature in Fig. 1.12 while assuming the plasma is in CIE. We assumed the abundances from Lodders et al. (2009) and the ionisation balance described in Urdampilleta et al. (2017).

### 1.5.9 Galaxy clusters through X-ray spectroscopy

Due to relatively high temperature of galaxy clusters (of the order of a few keV), and high nuclear charge of iron, iron is the dominant element which produces lines in spectra of these objects. In the hot clusters, with temperatures above  $\sim 3-4$  keV, the dominant emission lines come from Fe-K shell transitions (with principal quantum number  $n = 1$ ). At lower temperatures, the spectrum starts to be more complicated due to presence of hundreds of spectral lines, mostly originating from the Fe-L complex. Fe-L shell lines, which originate from the energy levels with principal quantum number  $n = 2$ , become dominant at energies around 1 keV. This makes them a powerful diagnostics tool for lower mass objects such as galaxy groups and massive elliptical galaxies. The Fe-L complex is very complicated to calculate, however, in the recent years, many lab measurements and theoretical calculations have been made to improve our understanding of the Fe-L complex, which was driven by the unprecedented resolution of micro-calorimeters (Gu et al. 2019, 2020, 2022; Kühn et al. 2022). In Fig. 1.13 which was adapted from Sanders (2023), the richness of X-ray spectra is shown for collisionally-ionised plasmas with different temperatures.



### 1.5.10 X-ray plasma codes and databases

In order to properly interpret X-ray spectra, we need models which describe not only the geometry of the observed object, but also all possible atomic physics processes which contribute to the observed spectrum. Without having models which are fit to spectra, one can not derive the physical properties of the object as it was described in Section 1.5.8.

Additionally, ions in an X-ray plasma are more complex than the hydrogen atom, which is the only atom whose Schrödinger equation has an analytical solution. Therefore, in order to solve a more complex multi-electron Schrödinger equation and obtain its numerical solution, many approximations are needed. A few examples of these approximations are e.g. the variational principle (which leads to Hartree–Fock equations), the independent particle model, the many-body perturbation theory, the configuration interaction approximation, the multi-configuration approximation, and more (see review by Kallman & Palmeri 2007). Two widely used approximations are the distorted wave calculations, or the R-matrix calculations (Burke 1993; Burke & Berrington 1993a), where the later uses the many-body perturbation theory.

The distorted wave (DW) calculations use a set of approximations to simplify the wave function of the continuum electrons (see e.g. the HULLAC code Bar-Shalom et al. 2001). They neglect the coupling between different energy channels or the interaction between continuum states, and the resonant enhancement of rate coefficients is usually not taken into account. DW calculations are more suitable for systems when the energy of the projectile electron (or free electron) is much greater than the binding energy of the target electrons (or bound electrons). These calculations are known to be less accurate (in comparison with R-matrix calculations), however, they can handle more levels.

The R-matrix calculations are more suitable for low energies of free electrons, and for low ionization charges, mainly because of the strong coupling between the energy channels. Additionally, they are often used for highly-charged ions when determining the resonance contribution. The R-matrix calculations are more accurate in comparison with DW calculations, but they can handle less levels due to their computational demands.

Historically, the plasma codes developed in two regimes:

1. **collisional**, when  $k_B T_e \sim$  to the ionisation energy of plasma ions. Such codes usually treat plasma as optically thin ( $\tau \ll 1$ ), so the equations of radiative transfer do not have to be solved. Typical examples of codes that developed from this regime are: MEKAL (Mewe et al. 1995), SPEX (Kaastra et al. 1996; Kaastra et al. 2018, 2020), Chianti (Dere et al. 1997; Del Zanna et al. 2021), or APEC (Smith et al. 2001).
2. **photoionised**, for which  $k_B T_e \ll$  to the ionisation energy of plasma ions. These codes were designed for plasmas with moderate optical depth (of the order of unity) and solve the equations of radiative transfer. A few of such codes are Cloudy (Ferland et al. 1998, 2017), XSTAR (Kallman & McCray 1982; Kallman & Bautista 2001), Titan (Dumont et al. 2000), and Mocassin (Ercolano et al. 2003).

Over the years the development of all of these codes started to make the two regimes less prominent when distinguishing between different codes (e.g. SPEX developed its own photoionisation model *pion*). Most importantly, this enabled more direct comparisons between the plasma codes and the atomic databases, which also showed many discrepancies between them. These discrepancies can have different origins, for example they can stem from the incompleteness of the atomic line databases, different approaches to solving the Schrödinger equation, or different approaches in calculating line fluxes. One of such examples, which



shows a discrepancy in effective collision strengths of He-like Fe-K line from the ground state to  $1s.2s$  ( $^3S_1$ ) state is shown in Fig. 4 of Hitomi Collaboration et al. (2018c).

Another example is one of our findings in chapter 5, where we also report on updates of the atomic data of neutral hydrogen in SPEX. Fig. 1.14 serves as an educational example which shows the differences between different codes. Before the updates detailed in paper Štofánová et al. (2021), SPEX used R-matrix calculations for the  $Y(T)$  values of H I, more specifically, the data was based on the extrapolations of R-matrix calculations of C VI, Ne X, Si XIV and Ca XX with the assumption that the Gaunt factor does not depend on the atomic number  $Z$  and that it is close to a constant along the iso-electronic sequence. This assumption, however, influences also the effective collision strengths  $\Omega_{ij}$  (and therefore the cooling rates) between energy levels  $i$  and  $j$  since

$$\Omega_{ij} = \frac{8\pi}{\sqrt{3}} g E_{\text{ryd}} \frac{w_i f_{ij}}{E_{ij}}, \quad (1.28)$$

where  $w_i$  is the statistical weight,  $f_{ij}$  is the oscillator strength,  $g$  is the gaunt factor, and  $E_{ij}$  is the excitation energy between levels  $i$  and  $j$ . Such an assumption is acceptable for all elements from C to Fe, for which the gaunt factor at  $kT_e = 0.25 * E_{ij}$  does not differ by more than 5%, however, it can not be used for the neutral atoms as van Regemorter (1962) shows. In this paper we also reported on other sources of possible discrepancies between different plasma codes. E.g. Aggarwal & Kingston (1991b) shows that the collision strengths calculations using R-matrix method can be influenced if the higher excited states or pseudo-states are included in the wave function of the studied system. Based on the number of states (either real states or pseudo-states) included in the expression of the wave function, the collision strengths are systematically lower by at most 20% if such states are taken into account (Morgan 1980). This is also supported by later work of Ballance et al. (2003) which shows that the low-charge ions up to carbon require R-matrix calculations with pseudo-states and that the Maxwell averaged collision strengths beyond  $C^{5+}$  are affected only minimally if the pseudo-states are taken into account. Even though the pseudo-states are discussed in Aggarwal & Kingston (1991b), it is concluded that due to computational limitations at that time, the collision strengths are computed without taking pseudo-states or higher excited states into account implying the collision strengths might be in the end overestimated. On the other hand, the work of Callaway (1994) clearly states that the effective collision strengths were computed while including the pseudo-states in the calculations. Fig. 1.14 also shows the discrepancies between different codes for high energies. For an electron colliding with the neutral atom at high temperatures, it is established that the so called Born limit shall be used. It considers the plane waves to describe the continuum orbitals (Kallman & Palmeri 2007). As we can see from Fig. 1.14, the plasma codes are not in agreement at high energies for this transition.

In all chapters in this thesis we mostly worked with the SPEX software package which has its own atomic database SPEXACT (The SPEX Atomic Code & Tables). SPEXACT includes around  $4.2 \times 10^6$  lines from 30 different chemical elements (H to Zn). Since the first version of SPEX, many updates have been made, from which the most recent ones are the updated radiative recombination rates (Mao & Kaastra 2016; Mao et al. 2017a), the updated collisional ionisation rates (Urdampilleta et al. 2017), a model for the charge exchange transfer (Gu et al. 2016), updates of the collisional excitation rates (Kaastra et al. 2017), the updated data for the Fe-L complex by Gu et al. (2019, 2020, 2022), the updated radiative loss function due to collisional excitation in the photoionisation model (Štofánová et al. 2021), the updated interstellar dust absorption model *amol* (Zeegers et al. 2017; Rogantini et al. 2018; Costantini et al. 2019; Zeegers et al. 2019; Rogantini et al. 2019; Psaradaki et al. 2020), the time-dependent

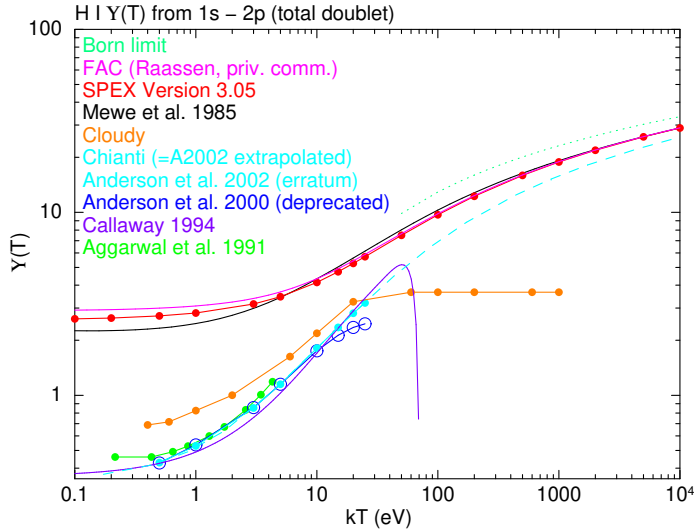


**Figure 1.14:** Temperature-averaged collision rates  $Y(T)$  for the total Lyman  $\alpha$  doublet of neutral hydrogen H I. The black solid line represents the gaunt factor approximation based on Mewe et al. (1985) which was implemented in the MEKAL code. The red solid line, which was used for SPEX version 3.05 and lower and which assumes that the gaunt factor does not depend on the atomic number  $Z$ , is based on the extrapolations of R-matrix calculations of C VI (Aggarwal & Kingston 1991a), Ne x (Aggarwal & Kingston 1991b), Si xiv (Aggarwal & Kingston 1992b), and Ca xx (Aggarwal & Kingston 1992a). The pink curve was calculated by Ton Raassen using FAC code (Gu 2008, private communication). The blue curve represents R-matrix calculations by Anderson et al. (2000) which has an error in extrapolation towards high temperatures and has been corrected by Anderson et al. (2002) (cyan solid curve). The cyan dashed curve represents CHIANTI which also uses Anderson et al. (2002) but the data is extrapolated to the Born limit. The orange line represents Cloudy calculations (version 17.00) in the coronal limit which is based on Callaway (1994), which we independently plot by the purple line. The bright green line represents R-matrix calculations by Aggarwal et al. (1991).

photoionisation model *tpho* (Rogantini et al. 2022), and the new *clus* model that is described in more details in chapter 4.

Additionally, updates of plasma codes are also important for cosmological hydrodynamical simulations. Due to their limited numerical resolution and large simulated volumes, atomic physics processes are usually tabulated and implemented to these simulations through the so called “sub-grid” physics models. For a review about these simulations we refer to Vogelsberger et al. (2020).

In conclusion, there are many differences between different plasma codes and atomic database. Therefore, in the era of high-resolution X-ray spectroscopy with micro-calorimeters it is crucial to analyse data using more than one plasma code to make sure the reported properties of X-ray plasmas are influenced the least by the fitting software and its atomic database.

## 1.6 X-ray detectors

### 1.6.1 Wave-particle duality

For many decades it has been known from quantum mechanics that any quantum (e.g. light or electrons) has wave-like and particle-like properties at the same time. Depending on the design of the experiment, the observed quantum behaves as a wave or as a particle. The cross-over between the wave and a particle happens to be in the soft X-ray band (approximately around 1 keV or  $\sim 12 \text{ \AA}$ ), and therefore the X-ray spectrometers designed until now can be divided into two main groups:

1. **Dispersive spectrometers**, which treat the incoming radiation as a wave, and compare the signal to a unit of length (i.e. grating period or crystal lattice spacing) in order to measure the wavelength  $\lambda$ . This means that if the energy of an incoming radiation is below 1 keV (or  $\sim 12 \text{ \AA}$ ), and one wants a reasonable resolution ( $\Delta\lambda \sim \text{a constant}$ ,  $\Delta\lambda \sim \text{a few m\AA}$ ), then it is more convenient to treat this radiation as a wave.
2. **Non-dispersive spectrometers** treat the incoming radiation as particles, and compare the signal to a unit of energy (e.g. band gap in charge-coupled device CCD or heat capacity) when measuring its energy  $E$ . In order to get a reasonable resolution ( $\Delta E \sim \text{a constant}$ ,  $\Delta E \sim \text{a few eV}$ ) for an incoming radiation with energy higher than  $\sim 1 \text{ keV}$ , it is more convenient to treat this radiation as particles.

In Fig. 1.15 we show the resolving power of different detectors (see more in section 1.6.2) as a function of energy of an incoming photon. This graph demonstrates how resolving power changes for different energies depending on whether the detector is dispersive or non-dispersive.

### 1.6.2 High-resolution X-ray detectors

High-resolution X-ray spectroscopy made a major leap in 1999 with the launch of the **Chandra** and **XMM-Newton** observatories that carried grating spectrometers on their board. Both missions operate roughly in the energy band of 0.1–12 keV with a spectral resolution of 60 mÅ (XMM-RGS), 40 mÅ (Chandra-LETG), 20 mÅ (Chandra-HETG medium-energy gratings) or 10 mÅ (Chandra-HETG high-energy gratings) and till this day help us understand many phenomena across the Universe. Such spectral resolution revealed the absence of cool gas in centres of galaxy clusters. This resulted in a suggestion that the central AGN heats the gas in cool-core clusters - the so called AGN feedback (see e.g. Tamura et al. 2001; Peterson et al. 2001; Kaastra et al. 2001; Peterson et al. 2003). However, many questions still remained unanswered: how exactly the central galaxy interact with its surrounding gas? how the gas moves within its intracluster medium? what are the turbulent and bulk velocities? what is the interplay between radiative cooling and AGN heating? are our plasma models accurate? For finding answers to these questions and many more a new mission with better spectral resolution was necessary.

The next major leap of high-resolution spectroscopy in X-rays came with the **Hitomi** satellite that was launched in 2016. As Hitomi operated only for few weeks, many questions that it was supposed to answer remained open. However, the improvement offered by the instruments and the mission itself showed the importance of constantly updating the atomic data as well as the plasma codes used for modelling and therefore understanding the observed X-ray spectra (Hitomi Collaboration et al. 2018c). The calorimeter detector offered a high

spectral resolution of  $\lesssim 5$  eV throughout the whole energy band 1.7–12 keV and for the first time, it resolved the resonant ( $w$ ), intercombination ( $x, y$ ) and forbidden ( $z$ ) lines of Fe xxv in the Perseus galaxy cluster. Such measurements enabled us to look closely at the dynamics of hot gas in the cluster centre and calculate with high precision the turbulent broadening of the lines and the velocity associated with it (Hitomi Collaboration et al. 2016). This led to more precise estimation of the total galaxy cluster mass, which in wider context helps us to understand the evolution and formation of large scale structures and the cosmic web. With the new generation of X-ray satellites as XRISM (launched in September 2023) and Athena (launch expected in 2037 with even higher effective area), the precise atomic data and models will be much more crucial for the analysis of the plasma properties and therefore for finding answers to yet not answered questions.

For example, the high-resolution X-ray spectroscopy with micro-calorimeters unlocked the possibility to measure the velocities in the ICM with an unprecedented accuracy of  $\sim 10$  km/s. Through the observations of the motions of the ICM with the *Hitomi satellite* in the Perseus cluster it was revealed that the AGN feedback in this massive galaxy cluster is surprisingly very gentle and that the turbulent velocities reach values of only 164 km/s (Hitomi Collaboration et al. 2016). Constraining these velocities for more clusters is crucial for understanding the details of the AGN feedback, and how it displaces the metals in the ICM of objects of various masses and evolution stages.

**XRISM**, the re-flight mission of Hitomi, which was launched to its orbit in September 2023, will not only make measurements that will enable constraining the details of the AGN feedback, but it will also provide details of the SN, and stellar feedback, which are the main producers of metals in the ICM, IGrM, and ISM, and enrich the clusters, groups and elliptical galaxies over their entire volume. Such enrichment happens mostly through either core-collapse SN or Type Ia SN, however, the precise details about supernova progenitor models are still unclear (Simionescu et al. 2019). The measurements of abundances of metals of different origins with *XRISM* will also provide constraints on the supernova yield models (for recent reviews see e.g. Mernier et al. (2018); Biffi et al. (2018)).

The **Athena** X-ray observatory (Advanced Telescope for High Energy Astrophysics) is an L(large)-class mission selected by the European Space Agency (ESA) which plans to study the hot and energetic parts of the Universe. On board it will carry the Wide Field Imager (WFI, Meidinger et al. 2014, 2018) and the X-ray Integral Field Unit (X-IFU, Barret et al. 2018), which is a micro-calorimeter based on a large format array of super-conducting molybdenum-gold Transition Edge Sensors (TESs). The X-IFU will operate in the energy band 0.2–12 keV and it is expected to have an unprecedented combination of a high effective area, together with spectral and spatial resolution with a much larger number of TES pixels than XRISM.

The future of high-resolution X-ray spectroscopy is bright, which is shown by the future planned missions that are not yet adopted. Some of these missions are **Lynx** (Vikhlinin 2018) or **LEM** (Kraft et al. 2022), which promise to solve many mysteries surrounding WHIM, or even CGM of individual galaxies.

## 1.7 This thesis

In this Ph.D. thesis I focused on the spectroscopy of the cosmic web (filaments and galaxy clusters) and a view of this cosmic web beyond the collisional ionization equilibrium with future X-ray telescopes. I showed that future X-ray micro-calorimeter missions will be sensitive to effects that have not yet been detected when studying the cosmic web under simplified assumptions often made in the analysis of its observations. For example, gas in the cosmic

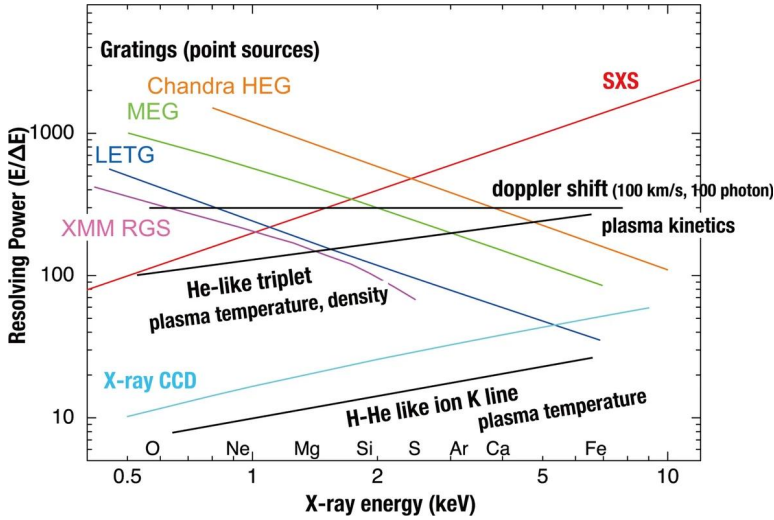


**Figure 1.15:** Resolving power as a function of energy for different types of detectors (dispersive, non-dispersive). Orange, green and blue colours show the Chandra High Energy Transmission Grating (HEG), Medium Energy Grating (MEG), Low Energy Transmission Grating (LETG), respectively. XMM-Newton Reflection Grating Spectrometer (RGS) is shown in pink, and Soft X-Ray Spectrometer (SXS) of Hitomi is shown in red. This graph was adapted from Mitsuda et al. (2010).

web filaments is often assumed to be in collisional ionisation equilibrium (CIE), and the X-ray emitting gas that fills in the halos of galaxy clusters is often assumed to have a single temperature. These assumptions might have been enough in the era of energy resolution with CCD and grating spectrometers, however, that might not be sufficient anymore in the era of micro-calorimeters.

This thesis consists of four main chapters where I studied the cosmic web filaments and galaxy clusters beyond collisional ionisation equilibrium. These chapters can be summarized as follows:

- **Chapter 2** serves as a demonstration of the power of the micro-calorimeters planned to be on board of future missions, such as the Athena X-IFU or the proposed Line Emission Mapper X-ray probe. Using the Hydrangea cosmological hydrodynamical simulations, I predicted the expected properties of intergalactic gas in and around massive galaxy clusters. In this chapter, I showed that the detection of cosmic web filaments in O VII and O VIII absorption against the bright cores of nearby, massive, relaxed galaxy clusters will be feasible in foreseeable future.
- In **Chapter 3** I demonstrated that considering the photoionisation by just the cosmic ultraviolet and X-ray background might not be sufficient to estimate the column densities of the gas in cosmic web filaments. In this publication, I showed that galaxy cluster photons, originating from the ICM, alter the ionization state of the nearby WHIM, which is in conflict with a “typical” view, in which it is assumed that the cosmic web gas can be fully described by just CIE. We show that the ion fractions need to be parametrized with density and temperature of the photoionised gas, as well as the distance between the

ionising source and the photoionised gas. Using a toy model of a cosmic web filament I predicted how the cluster illumination changes the column densities of e.g. O VI, O VII, C V, or Ne VIII.

- In **Chapter 4** I described a model which has been newly implemented in the SPEX software package called the *clus* model. It calculates the spectrum and radial profile for a spherically symmetric approximation of a cluster or a group of galaxies, or even a massive elliptical galaxy. This model includes a self-consistent treatment of the projection effects, multi-temperature, multi-metallicity, and multi-velocity structure of the ICM plasma, as well as the implementation of the resonant scattering. We investigated the magnitude of systematic effects, like projection or resonant scattering, on the inferred temperatures and iron abundances of nearby cool-core galaxy clusters, and the massive elliptical galaxy NGC 4636. In this study, we showed that the input emission measure distribution could not be recovered by using models like single-temperature, double-temperature, or gaussian differential emission measure. Additionally, we showed that for some cool-core clusters, the projection effects significantly affect the projected temperatures. For galaxy clusters such as Perseus, the effect of RS can influence the inferred abundance profile in its centre by maximally 10 – 15%, however, for the massive elliptical galaxy NGC 4636, taking into account the RS effect in its centre can explain the central abundance drop measured with XMM-Newton and Chandra.
- **Chapter 5** focused on the updates of the cooling curve in the photoionization model *pion* of the plasma code SPEX. More specifically, I updated the cooling curve by calculating the radiative loss from collisional excitation in the limit of optically thin and low-density plasmas. I also updated the atomic data for neutral hydrogen and I included the contribution of the dielectronic recombination to the cooling curve in this photoionization model. I showed the comparison to other plasma codes (MEKAL, APEC, Cloudy) and atomic databases (CHIANTI, ADAS). This research resulted in finding new stable branches in the stability curve simulated for the active galactic nucleus NGC 5548.



# 2

## Prospects for detecting the circum- and intergalactic medium in X-ray absorption using the extended intracluster medium as a backlight

---

Lýdia Štofanová, Aurora Simionescu, Nastasha A. Wijers, Joop Schaye, Jelle S. Kaastra, Yannick M. Bahé, and Andrés Arámburo-García

*Published in Monthly Notices of the Royal Astronomical Society, 2024, Volume 527, Issue 3, pp.5776-5791.*

### ABSTRACT

---

The warm-hot plasma in cosmic web filaments is thought to comprise a large fraction of the gas in the local Universe. So far, the search for this gas has focused on mapping its emission, or detecting its absorption signatures against bright, point-like sources. Future, non-dispersive, high spectral resolution X-ray detectors will, for the first time, enable absorption studies against extended objects. Here, we use the Hydrangea cosmological hydrodynamical simulations to predict the expected properties of intergalactic gas in and around massive galaxy clusters, and investigate the prospects of detecting it in absorption against the bright cores of nearby, massive, relaxed galaxy clusters. We probe a total of 138 projections from the simulation volumes, finding 16 directions with a total column density  $N_{\text{O VII}} > 10^{14.5} \text{ cm}^{-2}$ . The strongest absorbers are typically shifted by  $\pm 1000 \text{ km/s}$  with respect to the rest frame of the cluster they are nearest to. Realistic mock observations with future micro-calorimeters, such as the Athena X-ray Integral Field Unit or the proposed Line Emission Mapper (LEM) X-ray probe, show that the detection of cosmic web filaments in O VII and O VIII absorption against galaxy cluster cores will be feasible. An O VII detection with a  $5\sigma$  significance can be achieved in  $10 - 250 \text{ ks}$  with Athena for most of the galaxy clusters considered. The O VIII detection becomes feasible only with a spectral resolution of around  $1 \text{ eV}$ , comparable to that envisioned for LEM.

---



## 2.1 Introduction

The matter distribution in the Universe, as we know and understand it today, is believed to have a filamentary structure on its largest scales – famously known as the cosmic web (de Lapparent et al. 1986; Bond et al. 1996). The cosmic web formed when the initial small density field fluctuations collapsed under the influence of gravity, which resulted in structures such as cosmic sheets, voids, nodes and filaments. In this paper we focus on filaments, which are the bridges between the cosmic nodes. In the nodes, which are the places with the highest concentration of dark matter, galaxy clusters form through hierarchical structure growth.

Cosmological simulations predict that at  $z \approx 0$ , most of the gas resides in the warm-hot intergalactic medium (WHIM), which contains around 30%, and possibly up to 60% of all the baryons in the Universe (e.g. Cen & Ostriker 1999; Davé et al. 2001; Tepper-García et al. 2012; Martizzi et al. 2019; Tuominen et al. 2021). According to the simulations, this diffuse WHIM has been shock-heated to temperatures of  $10^5 - 10^7$  K. It has low electron densities,  $n_e \sim 10^{-6} - 10^{-4} \text{ cm}^{-3}$  (only  $10 - 10^3$  times the mean baryon density of the Universe), which makes it extremely difficult to observe in emission due to its low surface brightness. The high temperatures make O VI ( $10^{5.3} < T < 10^{5.8}$  K, in collisional ionisation equilibrium - CIE) together with O VII ( $10^{5.4} < T < 10^{6.5}$  K, in CIE) and O VIII ( $10^{6.1} < T < 10^{6.8}$  K, in CIE) good tracers of the WHIM.

Multiple papers have reported detections of the WHIM in X-ray emission (e.g. Kull & Böhringer 1999; Finoguenov et al. 2003; Kaastra et al. 2003; Werner et al. 2008; Eckert et al. 2015; Akamatsu et al. 2017; Connor et al. 2018; Reiprich et al. 2021). However, since the X-ray emissivity increases as the density squared, extreme ultraviolet (EUV) and X-ray emission tends to probe the densest and hottest parts of the WHIM (e.g. Bertone et al. 2008, 2010a,b; van de Voort & Schaye 2013; Wijers & Schaye 2022; Churazov et al. 2023b).

Because absorption scales linearly with the density, it is less biased to higher density gas than emission, making absorption more suitable for detecting the bulk of the WHIM (see e.g. Wijers et al. 2019, 2020). A detection of the WHIM in O VII, O VIII, and Ne IX absorption toward quasar PKS 2155-304 was reported by Nicastro et al. (2002). Later detections were reported by Fang et al. (2003) and Rasmussen et al. (2003) in O VII, and Fujimoto et al. (2004) in O VIII. A detection of two filaments towards the sightline of the blazar Mrk 421 with Chandra was documented in Nicastro et al. (2005b), however, later Kaastra et al. (2006) re-analysed the same dataset and found the observations of Nicastro et al. (2005b) were statistically insignificant. Takei et al. (2007) claimed a detection of WHIM in Ne IX and O VIII. Considering more recent works, Nicastro et al. (2018) found two absorbers toward blazar 1ES 1553+113 with reported O VII column densities of a few times  $10^{15} \text{ cm}^{-2}$ . The same sightline was also explored by Spence et al. (2023) who reported a  $\sim 3\sigma$  detection in O VII. Ahoranta et al. (2021) detected O VI and O VII absorptions toward the galaxy Ton S 180 with a significance higher than  $5\sigma$  and reported column densities of few times  $10^{14} \text{ cm}^{-2}$  and  $10^{16} \text{ cm}^{-2}$  for O VI and O VII, respectively, while the O VIII detection was not significant. We emphasize, however, that most of the absorption studies performed with current missions are of a low statistical significance and often challenging in terms of the systematic uncertainties, and therefore the robustness of these detections often remains debated in the literature. Nicastro et al. (2022) summarizes the history of WHIM absorption studies towards bright point-like sources, and discusses the prospects of future WHIM detections.

A complementary method to observe gas in filaments in absorption is to use galaxy clusters as background candles (Markevitch 1999; Markevitch et al. 2009). Since galaxy clusters are located at the intersection of cosmic web filaments, sightlines pointed towards cluster

cores are likely to probe the densest parts of the surrounding filaments, and therefore provide the highest column densities and hence the strongest absorption profiles. Simionescu et al. (2021) extended this idea by providing estimates of the absorption from a simplified WHIM component, approximated as a single temperature, single density, and single metallicity gas. Here we explore this idea further, and provide predictions for multiple cosmic web filaments taken from cosmological hydrodynamical simulations. We simulate observations of these filaments with the future mission Athena (Barret et al. 2018) and the proposed X-ray probe Line Emission Mapper (LEM, Kraft et al. 2022), while taking into account a more complex (three component) model of the Galactic interstellar medium (ISM).

Since we are interested in large-scale structure filaments connecting to galaxy clusters, we need to use cosmological simulations covering a large volume, in order to contain enough massive haloes for our study. On the other hand, the properties of the WHIM depend sensitively on the physics of galaxy evolution, including processes like feedback and star formation, for which it is important to resolve small spatial scales. Cosmological zoom-in simulations are therefore well suited for this study. Specifically, we focus on the Hydrangea simulation suite (Bahé et al. 2017), containing a sample of 24 galaxy clusters identified from dark matter only simulations, and then re-simulated in a volume up to  $10 \times r_{200c}^1$  including baryons and using the same resolution and galaxy formation model as the EAGLE simulations ('Evolution and Assembly of GaLaxies and their Environments', Schaye et al. 2015; Crain et al. 2015). Additional details about these simulations can be found in Sec. 2.2.1.1. Hydrangea is specifically tailored towards describing massive galaxy clusters,  $M_{200,c} \in (10^{14} - 10^{15.4}) M_{\odot}$ , which may make the cosmic web filaments connected to these clusters denser and therefore easier to detect.

### 2.1.1 Research set-up

The main goal of this paper is to determine whether extended sources of light, in particular galaxy clusters, can serve as background sources for detection of the cosmic web filaments in O VII or O VIII absorption. We use the cosmic web filaments from the Hydrangea cosmological hydrodynamical simulations and calculate their properties by probing the gas with many lines of sight (LoS). We create column density maps and average optical depth profiles for O VII and O VIII.

As background sources we select observed bright, relaxed cool-core galaxy clusters, which span a range of redshifts, masses, and temperatures. Although our method can in principle be used with any extended source, these galaxy clusters should be among the most promising background sources for our study. We calculate the spectral energy distributions (SEDs) and the surface brightness profiles (SB) of these galaxy clusters. The SB profiles are used to weight the spatially dependent optical depth profiles from the simulations, while the SEDs are used as the backlight sources.

To realistically simulate the detectability of the absorption from the cosmic web filaments, we use a three-component model of the Milky Way absorption. We simulate the resulting model spectra using response files for realistic X-ray detectors and we determine the significance of the O VII and O VIII detection from the cosmic web filaments for various exposure times.

This paper is organised as follows. In Sec. 2.2 we summarize our methodology (Sec. 2.2.1) and results (Sec. 2.2.2) for the Hydrangea cosmological simulations. In Sec. 2.3 we summa-

---

<sup>1</sup> $r_{200c}$  denotes the radius of the sphere within which the mean overdensity is 200 times the critical density of the Universe.

size our methodology (Sec. 2.3.1) and results (Sec. 2.3.2) for the observational predictions. In Sec. 2.4 we discuss the effects of choosing a different size of the radius for which we extracted the absorption profiles from the simulations, the impact of different SB weighting in the absorption profiles, and how different detectors or an additional radiative cooling in cluster cores might affect our results. And lastly, we provide our main conclusions in Sec. 2.5.

## 2.2 Cosmological simulations

### 2.2.1 Methods

#### 2.2.1.1 Hydrangea simulations

In this section we summarize the main properties of the Hydrangea simulations. For a more detailed description we refer to Bahé et al. (2017) and Schaye et al. (2015). Hydrangea is also part of the Cluster-EAGLE (C-EAGLE, CE) project described in Barnes et al. (2017).

The Hydrangea simulations are cosmological hydrodynamical zoom-in simulations that use the EAGLE galaxy formation model (Schaye et al. 2015; Crain et al. 2015). They use a modified version of the GADGET3 smoothed particle hydrodynamics (SPH) code last described by Springel (2005). The set of modifications to the hydrodynamics and the time-stepping scheme of GADGET3, known as ‘Anarchy’, consists of removing the unphysical surface tension at contact discontinuities by using the discrete particle Lagrangian SPH formulation from Hopkins (2013); the artificial viscosity switch from Cullen & Dehnen (2010); a switch for artificial thermal conductivity (Price 2008); the  $C^2$  Wendland kernel (Wendland 1995); and the energy conserving time-step limiters from Durier & Dalla Vecchia (2012). These modifications are described in more detail in appendix A of Schaye et al. (2015), and in Schaller et al. (2015). The cosmological parameters were adopted from Planck Collaboration et al. (2014).

Hydrangea implements a number of astrophysical processes through sub-resolution (sub-grid) models. The radiative cooling and photoheating rates are based on Wiersma et al. (2009a) which assumes a Haardt & Madau (2001) ionizing UV and X-ray background. The star formation rate of gas particles follows the pressure law given by Schaye & Dalla Vecchia (2008). The mass and metal enrichment of gas due to stellar mass loss is described in Wiersma et al. (2009b) and Schaye et al. (2015). The star formation energy feedback happens in a single thermal mode, with a small number of gas particles heated by a large temperature difference (Dalla Vecchia & Schaye 2012). The energy feedback from supermassive black holes (‘AGN feedback’) is implemented in a similar fashion (Booth & Schaye 2009).

The high-resolution zoom-in regions of Hydrangea have the same baryonic mass resolution,  $m_{\text{baryon}} = 1.81 \times 10^6 M_{\odot}$ , as the largest EAGLE volume and the gravitational softening length is  $\epsilon = 0.7$  pkpc (physical kpc) at redshift ( $z < 2.8$ ). The zoom-in regions were created by running dark matter only simulations with the GADGET code but for a much larger volume ( $3200$  co-moving Mpc)<sup>3</sup>. The cluster candidates were selected from the parent simulation at redshift  $z = 0$  based on three criteria:

- $M_{200c} \geq 10^{14} M_{\odot}$ .
- There is no other massive halo located within 30 pMpc or within  $20 \times r_{200c}$  (the larger of these two was applied).
- No galaxy cluster candidate for re-simulation is located closer than 200 pMpc from any of the periodic simulation box edges.

Application of these three criteria resulted in 30 galaxy cluster candidates that were re-simulated in a high-resolution zoom-in box while including baryons. Outside of the zoom-in region, the box is filled with low-resolution particles that interact only gravitationally. We used 23 clusters at redshift  $z = 0$ , for which the zoom-in region was  $10 \times r_{200c}$ , which is big enough to simulate the intra-cluster medium and the filamentary structures in the vicinity of the galaxy clusters. Six clusters were excluded because they were simulated only to  $5 \times r_{200c}$ , and CE-10 was excluded because it had unphysically powerful AGN explosions due to a bug in the code, and therefore the gas properties were not considered reliable.

### 2.2.1.2 Specwizard

In order to calculate O VII and O VIII column densities in a LoS through the Hydrangea zoom-in volumes, we use the software *Specwizard*, which creates the synthetic spectra from the smoothed particle hydrodynamics simulations. In order to create these synthetic spectra, *Specwizard* uses the physical properties of the simulated gas particles (e.g. density, temperature, metal abundances), and accounts for photoionization from the UV and X-ray background. As shown in Štofanová et al. (2022), in certain cases, photoionization from galaxy cluster photons can also play a role. However, for the case of large-scale filaments aligned predominantly along the line of sight, this effect was found to be negligible; therefore, we do not include it in the present work.

*Specwizard* was developed by Joop Schaye, Craig M. Booth and Tom Theuns (see Sec. 3.1 of Tepper-García et al. 2011). In our study we used its python version, which is described in more detail in Arámburo-García+2023 (in prep).

## 2.2.2 Results: properties of Hydrangea absorbers

To get an initial estimate of the absorber statistics, we first examine 23 clusters in the Hydrangea simulations in 6 different directions along the  $\pm x$ ,  $\pm y$  and  $\pm z$  axes of the simulation volumes. The length of each LoS in every direction is the whole zoom-in region of  $10 \times r_{200,c}$  (which also includes half of the galaxy cluster). In Fig. 2.1 we show the results of this initial inspection, where we draw only one LoS per every direction pointed at the cluster centre, and plot a histogram of the total O VII column density per LoS. We see that the bulk of the LoSs lie between  $10^{11.5} \text{ cm}^{-2}$  and  $10^{14} \text{ cm}^{-2}$ . From the total number of 138 different LoSs, we find 16 (7) LoSs in which the total O VII column density is higher than  $10^{14.5} \text{ cm}^{-2}$  ( $10^{15} \text{ cm}^{-2}$ ). The observational threshold for O VII column densities is currently around a few times  $10^{15} \text{ cm}^{-2}$ , with rare exceptions reaching down to a few times  $10^{14} \text{ cm}^{-2}$ . With upcoming future missions this threshold could be pushed to  $10^{14} \text{ cm}^{-2}$  (Nicastro et al. 2022). Since Hydrangea was designed to study massive galaxy clusters with masses  $M_{200,c}$  between  $10^{14} M_{\odot}$  and  $10^{15.4} M_{\odot}$ , it is natural to expect that our studies will be biased towards more massive filaments and therefore higher O VII (and O VIII) column densities. Due to the patchy nature of the gas in the cosmic web filaments, the LoS pointed towards the cluster centre does not have to be fully representative of the column densities in the selected directions. Therefore, we also create O VII column density maps for all 138 directions (see Sec. 2.2.2.1).

### 2.2.2.1 O VII column density maps

We expand our search for projections where the total O VII column density per LoS is higher than  $10^{14.5} \text{ cm}^{-2}$  by creating column density maps for all 138 possibilities which cover a region with radius of 300 kpc around the galaxy cluster centre using 2 kpc pixels. With this

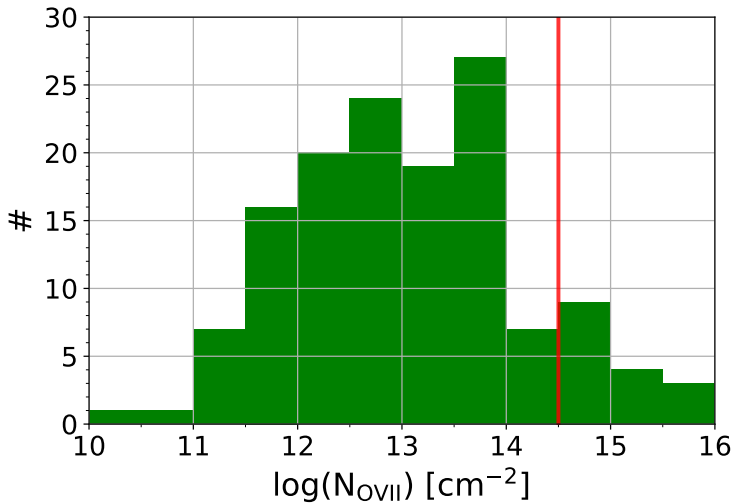


**Figure 2.1:** Histogram of the number of sightlines (out of the total number of 138 through Hydrangea cluster centres) as a function of O VII total column density per line of sight. The width of the column density bins is 0.5 dex. The red solid line represents the cut for all LoSs with O VII total column density higher than  $10^{14.5} \text{ cm}^{-2}$ . This cut selects 16 directions of lines of sight that are later discussed in the paper.

we confirm that no other directions were found in addition to the 16 Hydrangea absorbers shown in Fig. 2.1.

In Fig. 2.2 we show an example of three different orientations for three different clusters with halo identifiers: CE-7  $x$ –, CE-25  $x$ + and CE-29  $z$ +. In Sec. 2.A and Fig. 2.9 and Fig. 2.10 we show column density maps of the remaining 13 directions. In the maps we exclude gas within the central galaxy cluster halo ( $r < r_{200,c}$ ) and for plotting purposes we impose a lower threshold on the column densities of  $N_{\text{O VII}} \geq 10^{14.5} \text{ cm}^{-2}$ . To create these column density maps, we exclude the star forming gas by removing all SPH particles that fall on the equation of state (see Sec. 4.3 in Schaye et al. 2015 for more details). We also exclude the gas that was directly heated by supernovae and AGN feedback (Wijers et al. 2019).

### 2.2.2.2 Spatial properties of the O VII and O VIII absorbers

Next, we create a Cartesian grid of  $20 \times 20$  equidistantly spaced LoSs and select those that are within  $R < 100 \text{ kpc}$  of the projected centre of the cluster. This yields a total number of 276 LoSs, 10 kpc apart, which we used to probe the absorbing gas. We verified that this number is sufficient in order to probe the spatial substructures of the gas in Hydrangea volumes. Decreasing the number of LoSs to 200, 100, and 50 (in comparison to 276 LoSs), results to a difference of  $< 3\%$ ,  $< 6\%$ , and  $< 8\%$ , respectively.

We average all 276 LoSs for each of the 16 directions assuming each LoS adds to the final profile with an equal weight. This allows us to study the O VII and O VIII absorbers independently from the exact surface brightness of the extended background source. For the O VII absorption we take into account only the resonant line at  $21.60169 \text{ \AA}$  with the oscillator strength 0.696 and the Einstein coefficient of  $3.32 \times 10^{12} \text{ s}^{-1}$ . Since for the absorption studies

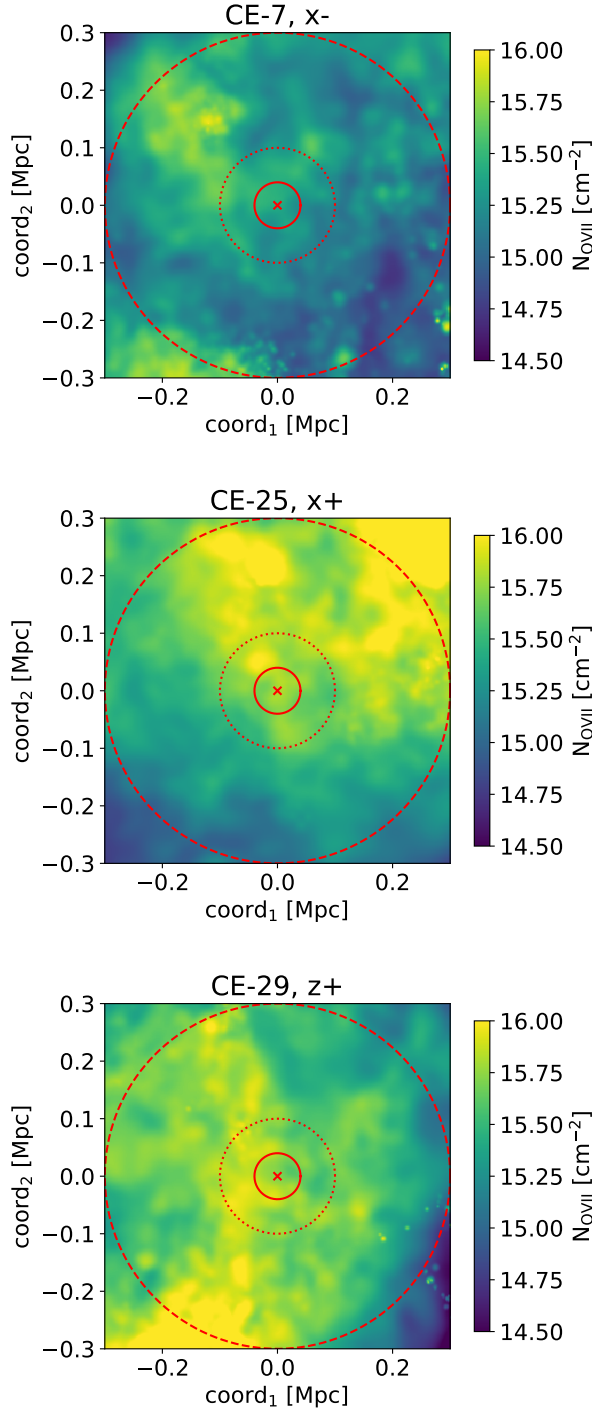


**Figure 2.2:** O VII column density maps that cover the central region with radius 300 kpc around CE-7 x-, CE-25 x+ and CE-29 z+ galaxy clusters. The maps have  $300 \times 300$  pixels with a pixel size of 2 kpc. We only plot gas with  $N_{\text{O VII}} \geq 10^{14.5} \text{ cm}^{-2}$ . The red circles show 40 kpc (solid line), 100 kpc (dotted line) and 300 kpc (dashed line) regions around the galaxy cluster centre (red cross).

the lines with the highest Einstein coefficients contribute the most to the absorption line profile, taking into account only the resonant line of O VII is sufficient. However, for O VIII there are two lines that have similarly strong Einstein coefficients: (a) the line at 18.96711 Å with oscillator strength 0.2771 and Einstein coefficient  $2.569 \times 10^{12} \text{ s}^{-1}$ , and (b) the line at 18.97251 Å with oscillator strength 0.1385 and Einstein coefficient  $2.567 \times 10^{12} \text{ s}^{-1}$ . Therefore, we combine these lines to calculate the O VIII absorption. The final O VIII wavelength of 18.96891 Å is obtained as the average of the two strongest lines weighted by their oscillator strengths. The combined oscillator strength is calculated as a sum of both oscillator strengths and results in the final value of 0.4156. Finally, the Einstein coefficient for the combined O VIII line is the larger one out of both lines:  $2.569 \times 10^{12} \text{ s}^{-1}$ . This step of combining two lines into one is done just because the *Specwizard* code itself can only take into account (in its short spectra mode) one line at a time. Because the X-ray detectors considered here have a spectral resolution of 2.5 eV (Athena X-IFU, see Sec. 2.3.1.4) and 0.9 eV (LEM, see Sec. 2.4.3), this approximation does not affect our main conclusions (the wavelengths of these two lines are separated by  $\Delta\lambda = 0.0054 \text{ Å} = 0.02296 \text{ eV}$ .)

In Fig. 2.3 we show for all 16 cases the flux depletion in O VII and in O VIII as a function of the position along the LoS  $d$ , shown as a fraction of  $r_{200}$ . For clusters where multiple projections had  $N_{\text{O VII}} \geq 10^{14.5} \text{ cm}^{-2}$ , we specify the projection ( $\pm x, \pm y, \pm z$ ) in addition to the halo identifier. Otherwise, only the halo identifier is shown. The four most prominent absorptions are for clusters CE-29  $z+$ , CE-25, CE-1  $x+$  and CE-3, where the absorption in O VII is more than 50%. In almost all 16 cases there is more than just one absorption line per direction. The sizes of the most prominent absorbers (e.g. CE-25 or CE-29  $z+$ ) along the line of sight are on average  $\sim 2 \times r_{200}$ . Some absorbers as e.g. CE-3 or CE-7 have two prominent lines along the LoS. The same holds true for O VIII absorption, however, the overall depth of the absorption features does not exceed 50% and the profiles are shallower in comparison with O VII. This is expected since the cosmic web filaments are not hot enough to ionise a dominant fraction of oxygen to its O VIII state.

### 2.2.2.3 Addition of ion-weighted peculiar velocities

An important aspect of the detectability of filaments in addition to their density, temperature, metallicity, and the total column density in the line of sight, is also how redshifted these absorption lines are in comparison with absorption lines from the ISM of the Milky Way as well as the emission lines from the galaxy cluster itself (relevant mainly for O VIII because of its brightness in the cluster centre). The velocity difference in the LoS between the gas in the galaxy cluster and the gas in filaments can be calculated by taking into account the ion-weighted peculiar velocities computed by *Specwizard* as well as the peculiar velocity of the galaxy cluster. We define the galaxy cluster peculiar velocity as the centre-of-mass velocity of the central subhalo<sup>2</sup>.

Fig. 2.4 shows the flux depletion in O VII and in O VIII as a function of the total velocity  $v_{\text{TOT}}$  along the line of sight, which is the sum of the Hubble flow velocity and the peculiar velocity of the individual SPH particles that contribute to LoSs. The peculiar velocity of the galaxy cluster is subtracted from the total velocity  $v_{\text{TOT}}$ . These profiles were calculated by taking an arithmetic average of the full sample of 276 LoSs for each direction. The total velocities of O VII and O VIII absorbers with respect to the cluster range from  $-1000 \text{ km/s}$  to approximately  $2000 \text{ km/s}$ . For most of the O VII absorbers the addition of the peculiar

<sup>2</sup>We define the centre-of-mass velocity of the central subhalo as the zero-momentum-frame velocity of the subhalo with index 0.

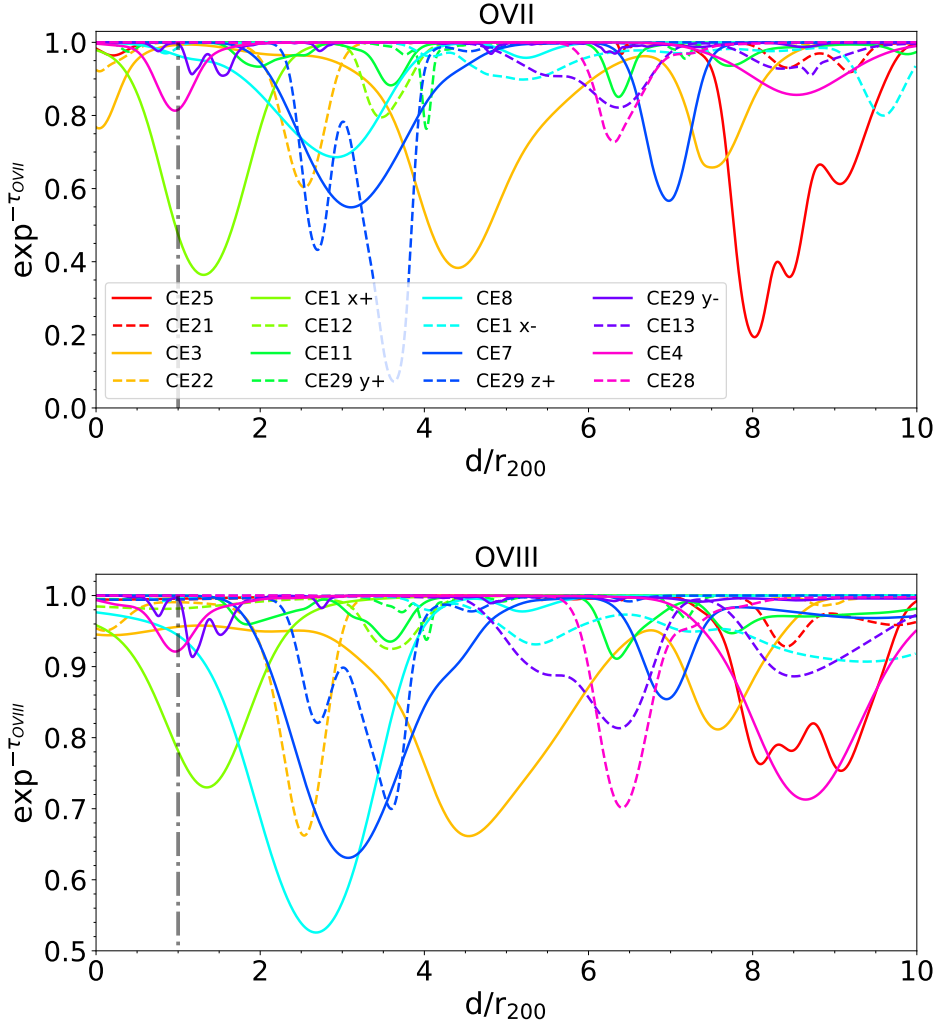


**Figure 2.3:** Equally weighted average O VII (top panel) and O VIII (bottom panel) absorption profiles within the radius 100 kpc from the cluster centre as a function of the position along the LoS  $d$ . Different colours and line styles represent different projections and Hydrangea clusters. The grey dash-dotted vertical line shows the position of  $r_{200}$ . For clusters where multiple projections had  $N_{\text{O VII}} \geq 10^{14.5} \text{ cm}^{-2}$ , we specify the projection ( $\pm x, \pm y, \pm z$ ) in addition to the halo identifier. Otherwise, only the halo identifier is shown. We see that the sizes of the most prominent absorbers (as e.g. CE-25 or CE-29  $z+$ ) along the line of sight are on average  $\sim 2 \times r_{200}$ . Some cases, e.g. CE-3 or CE-7, have two prominent absorption lines along the LoS.



Cluster	$z_{\text{cluster}}$	$r_{500}$ [kpc]	$N_{\text{H,TOT}}^{\text{neutral}} [\text{cm}^{-2}]$	100 kpc at $z_{\text{cluster}}$
A2390	0.2302	$1416 \pm 48$	$8.38 \times 10^{20}$	$0.45'$
A383	0.1883	$944 \pm 32$	$3.88 \times 10^{20}$	$0.53'$
A1413	0.1429	$1299 \pm 43$	$1.97 \times 10^{20}$	$0.66'$
A2029	0.0779	$1362 \pm 43$	$3.70 \times 10^{20}$	$1.13'$
A1795	0.0622	$1235 \pm 36$	$1.24 \times 10^{20}$	$1.39'$
A262	0.0162	$650 \pm 21$	$7.15 \times 10^{20}$	$5.05'$

**Table 2.1:** Redshift  $z_{\text{cluster}}$  and  $r_{500}$  of the clusters used in our study taken from Vikhlinin et al. (2006).  $N_{\text{H,TOT}}$  is the total hydrogen column density in the direction of the galaxy cluster (see Sec. 2.3.1.3 for more details).

velocities mainly results in a different shape of the absorption features compared to the profiles shown in Fig. 2.3, and it also slightly affects the overall depth of the absorption lines. The addition of peculiar velocities seems to affect the strength of the absorption lines more significantly for O VIII.

## 2.3 Observational predictions

### 2.3.1 Methods

#### 2.3.1.1 Galaxy cluster sample selection

For a detection of absorption originating from the cosmic web filaments against extended background sources like galaxy clusters, these background galaxy clusters need to be very bright in their cores. This makes cool-core (CC) clusters perfect candidates due to their centrally peaked surface brightness profiles.

A shortcoming that Hydrangea simulations and most cosmological hydrodynamical simulations have is their inability to properly simulate cool-core clusters due to the large entropy values in the cluster cores, which results in flat entropy profiles. An attempt to solve this issue in EAGLE-like simulations has been done by e.g. Altamura et al. (2022), however, the issue with the flat entropy profile has not yet been solved completely. Therefore, for the purpose of calculating the background emission, we replace the galaxy clusters in the Hydrangea simulations by observational profiles taken from the sample of cool-core clusters from Vikhlinin et al. (2006). We select 6 relaxed bright cool-core galaxy clusters (see Table 2.1), which span a range of redshifts, masses, and temperatures. Although our method can in principle be used with any extended source, these galaxy clusters should be among the most promising background sources for our study. Vikhlinin et al. (2006) provide the best-fitting parameters for the density and temperature profiles for these galaxy clusters as observed by the Chandra observatory, which were used to calculate the SB profiles as well as SEDs using the galaxy cluster model in SPEX described in the following section (Sec. 2.3.1.2).

#### 2.3.1.2 Galaxy cluster model in SPEX

To simulate the spectral energy distribution of the selected background galaxy clusters (used for an approximation of the backlight source), together with their SB profiles (used for weighting the optical depth profiles from the simulations), we use the *cluster* model in SPEX.

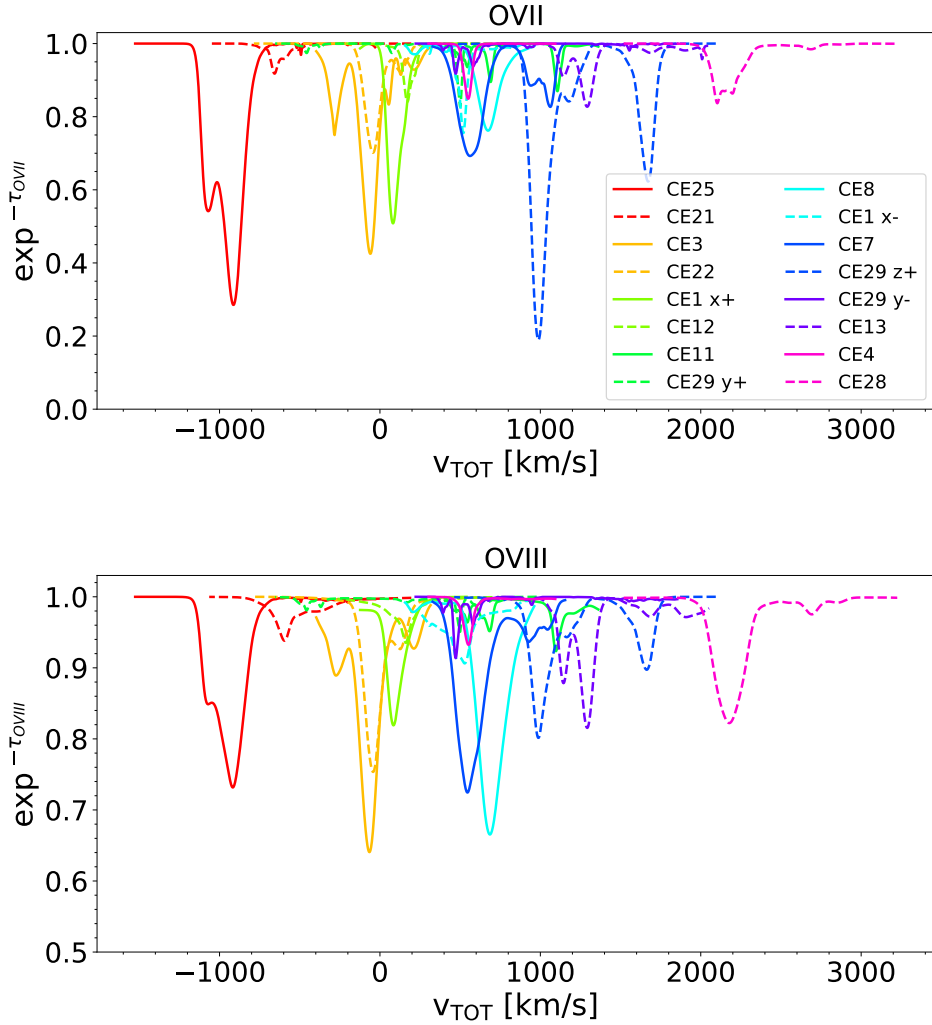


**Figure 2.4:** O VII (top panel) and O VIII (bottom panel) average absorption profiles (equally weighted) as a function of the total velocity along the line of sight  $v_{\text{TOT}}$ , which is the sum of the Hubble flow velocity and the peculiar velocity of the individual SPH particles that contribute to LoSs. The peculiar velocity of the galaxy cluster is subtracted from the total velocity  $v_{\text{TOT}}$ . Different colours and line styles represent different projections and Hydrangea clusters. The velocity difference between the strongest absorption lines and the galaxy cluster centre is on average  $\pm 1000$  km/s.

SPEX, the SPEctral X-ray and extreme ultraviolet software package (Kaastra et al. 1996; Kaastra et al. 2018, 2020), is a software package with its own atomic database SPEXACT (The SPEX Atomic Code & Tables) which includes around  $4.2 \times 10^6$  lines from 30 different chemical elements (H to Zn). It is used for the modelling and analysis of high-resolution X-ray spectra. In this paper we use SPEX version 3.07.02<sup>3</sup>. Unless stated otherwise, we use the Urdampilleta et al. (2017) ionisation balance and the protosolar abundances by Lodders et al. (2009).

The *cluster* model, which has been newly implemented in SPEX, calculates the spectrum and radial profiles for a spherically symmetric approximation of a cluster of galaxies. It takes as input parametrised 3D radial profiles of the gas density, temperature, metal abundance, and turbulent velocities. Given these parametrised profiles, the emission in multiple 3D shells, each approximated as a single temperature model in collisional ionisation equilibrium (CIE), is computed and projected onto the sky. The cluster model can then be run in different modes, where the output is either the SED within a user-defined projected spatial region, or a radial SB profile in a user-requested energy band.

More specifically, the assumed shapes of the underlying 3D profiles used as input to the cluster model follow:

- a two  $\beta$  model for the density distribution (with the additional possibility to introduce a jump or break in the slope at a given radius),
- the same functional form for the temperature profile as that proposed in Vikhlinin et al. (2006), again with a possible additional jump (although this latter capability was not used in this work),
- the abundance profile functional form defined in Mernier et al. (2017).

For more details about this model we refer to Štofanová et al. (in preparation) as well as the SPEX manual page<sup>4</sup>.

We can therefore directly use the fitted parameters already reported in Vikhlinin et al. (2006) to describe the 3D temperature profiles of clusters in our sample. For the density profile, on the other hand, the functional form defined in SPEX is different from that adopted in Vikhlinin et al. (2006). Thus, for each target, we attempted to approximate the 3D density profile reported in Vikhlinin et al. (2006) with the new functional form available in the *cluster* model. For all six clusters, we were able to match the two functional forms, with differences of at most 15% for all radii up to  $2 \times r_{500}$ . We additionally assume that the metallicity of each cluster follows the average abundance profile of the sample investigated in Mernier et al. (2017). The turbulent velocity is assumed to be 100 km/s, which is the current default in the *cluster* model.

### 2.3.1.3 Model for the Milky Way absorption

In order to realistically simulate the observation of gas in filaments, we need to take into account the absorption by our own Galaxy. The interstellar medium of the Milky Way is a multiphase gas that can not be simply modelled as a neutral gas. Therefore we adopt a model from Gattuzz & Churazov (2018), which assumes the ISM to have three components: (a) a neutral/cold component at temperature  $10^4$  K ( $9 \times 10^{-4}$  keV), (b) a warm component at

<sup>3</sup>For the most recent version see <https://spex-xray.github.io/spex-help/changelog.html>.

<sup>4</sup>For now the details of the *cluster* model can be found in the SPEX manual <https://var.sron.nl/SPEX-doc/spex-help-pages/models/clus.html>.

temperature  $10^{4.7}$  K ( $4.3 \times 10^{-3}$  keV), and lastly (c) a hot component at temperature  $10^{6.3}$  K (0.17 keV). We simulate all of these components with the *hot* model in SPEX. However, we set our neutral component to temperature  $1 \times 10^{-6}$  keV, which is lower than in Gatuuz & Churazov (2018). The reason is that in SPEX versions 3.06.00, 3.06.01 and higher, the database includes charge exchange processes which affect the ionisation at low temperatures, and in such cases the plasma would not be completely neutral.

The total hydrogen column densities that we use for the neutral component of the ISM,  $N_{\text{H,TOT}}^{\text{neutral}}$ , were taken from Willingale et al. (2013)<sup>5</sup> (see Table 2.1). For all galaxy clusters in this paper we assume that the warm and hot components of the ISM have a total hydrogen column density  $N_{\text{H,TOT}}^{\text{warm}} = 0.5 \times 10^{20} \text{ cm}^{-2}$  and  $N_{\text{H,TOT}}^{\text{hot}} = 0.2 \times 10^{20} \text{ cm}^{-2}$ , respectively. These hydrogen column densities were taken from Fig. 4 of Gatuuz & Churazov (2018), which shows that most of the extragalactic sources have quite similar hydrogen column densities.

Fig. 2.5 shows the effects of a neutral-only and three-component model of Galactic ISM. For illustration purposes, we plot the effects of absorption on a power-law shaped spectrum; however, for our final analysis the same absorption model was folded with the more complex SED of each cluster. The absorption profile regions represented by shaded rectangles (determined by the total velocity of the strongest absorbers - CE-25 and CE-29  $z_+$ ) are overplotted for the different cluster redshifts taken from Table 2.1. As we can see, the galaxy cluster redshift and the velocity difference between the galaxy cluster and the absorbing gas in filaments are crucial factors for the O VII detectability, together with the spectral resolution of the detector. Continuous improvements in determining the column densities for the Galactic ISM are needed to distinguish between the ISM and the O VII absorption lines.

### 2.3.1.4 Athena X-ray Integral Field Unit (X-IFU)

Unlike the grating spectroscopic X-ray instruments that were used to search for the WHIM until now, non-dispersive micro-calorimeters uniquely allow high resolution X-ray spectroscopy of extended sources.

The Athena X-ray observatory (Advanced Telescope for High Energy Astrophysics) is an L(large)-class mission selected by the European Space Agency (ESA) which plans to study the hot and energetic parts of the Universe, including baryons in the cosmic web that are the focus of this paper. On board it will carry the Wide Field Imager (WFI, Meidinger et al. 2014, 2018) and the X-ray Integral Field Unit (X-IFU, Barret et al. 2018), which is a micro-calorimeter based on a large format array of super-conducting molybdenum-gold Transition Edge Sensors (TESs). The X-IFU will operate in the energy band 0.2–12 keV and it is expected to have an unprecedented combination of a large effective area of  $5900 \text{ cm}^2$  at 0.5 keV (and an even larger effective area of  $1.4 \text{ m}^2$  at 1 keV) and a large field of view (FoV) of 5 arcminutes combined with an angular resolution of 5 arcseconds, and a spectral resolution of 2.5 eV at 0.5 keV. For the simulation of data with X-IFU we used the 2018 response files that can be downloaded here <http://x-ifu.irap.omp.eu/resources/for-the-community> (Barret et al. 2022).

### 2.3.1.5 Summary of the methods and the fitting procedure

In order to study the detectability of the O VII and O VIII absorption lines, we first calculate the surface brightness weighted optical depth profiles of three Hydrangea absorbers: CE-7, CE-25, and CE-29  $z_+$ . The CE-25, and CE-29  $z_+$  absorbers are the strongest absorbers out of

<sup>5</sup>We used the online tool created by the SWIFT team <https://www.swift.ac.uk/analysis/nhtot/>.

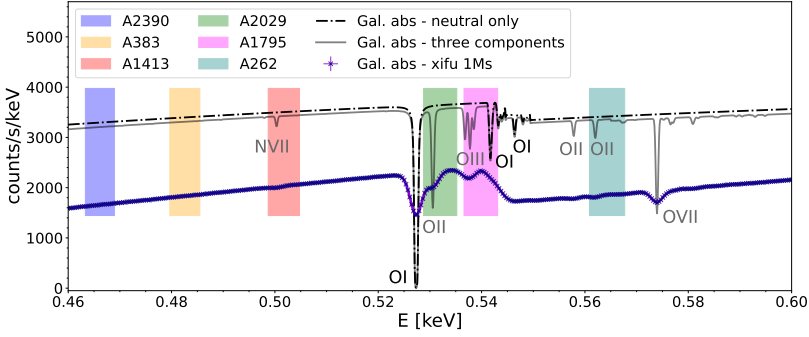


**Figure 2.5:** Absorption spectrum of the Galactic ISM for a completely neutral gas (black dash-dotted line) and for the three-component model of ISM (neutral, warm, and hot phases, solid grey line). In the energy range we are interested in (0.46–0.60 keV), the neutral component contributes to the spectrum with O I lines, while the three-component model adds O II, O III, O VII and N VII lines to the spectrum. The violet solid line with dark blue points (with lower normalization) shows the three-component ISM model folded through the Athena X-IFU response. To demonstrate the effect of the neutral and three-component Galactic absorption model, we simulate the background source of light in this figure as a power law with an arbitrary normalisation and exposure time. The coloured shaded rectangles represent the minimum and maximum energy ranges ( $v_{\text{TOT}} \sim \pm 1000$  km/s) of the strongest absorption line profiles from our sample (CE-25 and CE-29  $z_+$ ) for different galaxy cluster redshifts given in Table 2.1. This figure demonstrates that the ISM lines which might compromise the detection of O VII cosmic web filaments are N VII, O I, O II, O III, and O VII.

our sample, and additionally to these we also select CE-7 in order to simulate less prominent absorptions. For these absorbers we have a full sample of 276 LoSs which we combine into one final absorption profile by weighting every LoS contribution by the surface brightness profile (in the bolometric energy range) of a given background galaxy cluster. These LoSs were drawn from the circular area with radius 100 kpc from the cluster core. We calculate the SB profiles using the *cluster* model, which gives us the bolometric energy flux for every projected shell (the user can specify the energy range in which the flux is calculated). The optical depth in O VII, and O VIII, is given by

$$\tau_{\text{O VII, O VIII}} = \frac{\sum_{m=0}^{276} \text{SB}(R) \times \tau_{\text{O VII, O VIII}}^m(R)}{\sum_{m=0}^{276} \text{SB}(R)}, \quad (2.1)$$

where index  $m$  represents the individual LoSs, and  $R$  is the projection radius. We convolve the final weighted Hydrangea absorption profile with the galaxy cluster SEDs (also calculated for the projected radius of 100 kpc). We take into account the three-component absorption model for the ISM of the Milky Way and redshift the O VII and O VIII Hydrangea absorption lines with respect to the redshift of the background galaxy clusters. These spectra are then folded through the response files of the Athena X-IFU to simulate the observations with different exposure times (100 ks, 250 ks, and 500 ks) for different absorbers.

We fit the simulated spectra in SPEX in a narrow energy band around the absorption line, which is typically 0.4 – 0.6 keV. For simplicity, we fit the background continuum with a power law. We can afford this assumption, since in this narrow energy band the clusters do not seem to have many emission lines. If the spectrum of a specific cluster (as e.g. A262

or A383) has strong emission lines in the energy band  $0.4 - 0.6$  keV, we exclude the energy intervals corresponding to these emission lines during the fitting procedure. Since the shape of the Hydrangea absorption profiles is unresolved by X-IFU ( $2.5$  eV), we fit the absorption lines from Hydrangea with a gaussian line. If the Hydrangea absorption lines are not sufficiently separated from Galactic lines of the local ISM and the peaks of the lines cannot be clearly resolved, we discard these simulated observations from our sample. If the Hydrangea absorption line is sufficiently separated from the ISM lines but within  $2 - 6$  eV from each other, we leave the abundance of the element in that particular ISM component free during the fitting procedure (e.g. as in case of Abell 2029 and Abell 262). In such cases we do not only calculate the errors on the normalisation of the absorption line, but also the errors on the fitted abundance of that particular element. The errors are estimated by using the Levenberg-Marquardt algorithm and represent the standard deviation of  $1\sigma$ . We use C-statistics (Cash 1979), which can be briefly summarised as the maximum likelihood estimation in the limit of Poissonian statistics. SPEX uses modified C-statistics based on Baker & Cousins (1984), which is described in detail in Kaastra (2017). The fit is considered good, if the C-statistics value of the fit is within/close to the range of the expected C-statistics value and its errors.

## 2.3.2 Results: Simulations with the Athena X-IFU

### 2.3.2.1 Significance of the O VII detection

In Fig. 2.6 we show X-IFU simulated spectra of the O VII Hydrangea absorption profiles for the CE-29 Hydrangea absorber and A383 background galaxy cluster at redshift  $z = 0.1883$  (also referred to as CE-29 & A383) for an exposure time of 250 ks. We also show CE-25 & A2029 at redshift  $z = 0.0779$  and 100 ks exposure time. These two cases represent the 'best' and the 'worst' scenarios for O VII observations that are still possible with X-IFU. The left panels in Fig. 2.6 are Chandra images of A383 (top left panel, Chandra observations ID 2321<sup>6</sup>) and A2029 (bottom left panel, Chandra observations ID 4977<sup>7</sup>).

The 'best' possible scenario for O VII observations is when the Hydrangea absorption line is sufficiently separated from any of the ISM lines. We show as an example X-IFU simulated spectra of the CE-29 absorber projected in front of the galaxy cluster A383. For all three chosen Hydrangea absorbers (CE-7, CE-25, and CE-29  $z+$ ) and for A383 and A2390, the O VII Hydrangea absorption line is sufficiently separated from the ISM lines and can potentially be observed with X-IFU.

The 'worst' possible scenario for O VII observations that is still feasible with X-IFU is when the Hydrangea absorption line is blended with ISM lines, but its peak is sufficiently separated from the ISM lines and can be resolved with X-IFU. This is the case for, for example, CE-25 & A2029, where the Hydrangea O VII absorption line is close to the complex of oxygen lines from the Galactic ISM as shown in Fig. 2.6. These lines are the O I line from the neutral component, and the O II and O III lines from the warm component. In this case we fit the O VII absorption line while allowing the abundance of oxygen in the neutral as well as the warm component of the ISM to be free during fitting. For two other Hydrangea absorbers, CE-7 and CE-29, the velocity difference between the galaxy cluster A2029 and the gas in the filaments is not 'favourable' and the Hydrangea absorption lines are not sufficiently separated from the O II ISM line.

<sup>6</sup>A383 Chandra observations with ID 2321 can be downloaded from <https://doi.org/10.25574/02321>.

<sup>7</sup>A2029 Chandra observations with ID 4977 can be downloaded from <https://doi.org/10.25574/04977>.

As already seen from Fig. 2.5, for A1795 the O VII line lies close to the O I or O III ISM lines, as well as close to the oxygen absorption edge. With the X-IFU simulations we confirm that none of the three chosen examples of Hydrangea absorbers are sufficiently separated from the ISM lines and we discard these cases from our sample.

For the case of A1413 one needs to be careful about the N VII line from the hot component of the ISM at 0.5 keV. Two of the three absorbers considered here (CE-7 and CE-29) are too close to this line to be resolved with the X-IFU. The column density of the hot component is not high enough for the N VII line to be significant in the Athena spectrum, which makes fitting this line even more difficult. Therefore, while fitting the O VII line of the third absorber (CE-25), we fix the nitrogen abundance to the initial input value (which is equal to unity for the Lodders et al. 2009 proto-solar abundances) during the fitting procedure. However, the column density of the hot phase ISM is not well known and in reality the N VII line may be more significant in the observed spectra of the galaxy cluster.

Table 2.2 contains the results of fitting for three Hydrangea absorbers and all galaxy cluster background sources mentioned in Table 2.1. From this table we see that even in the case of the less prominent absorbers (here represented by CE-7), for which the flux in O VII does not decrease by more than 40% (see Fig. 2.4), O VII can be detected with X-IFU with at least  $5\sigma$  significance. This is possible with an exposure time of 385 ks for Abell 2390 and 195 ks for Abell 383 (see Table 2.3). Unfortunately, for closer and brighter galaxy clusters in our sample, the CE-7 absorption line of O VII cannot be resolved from the N VII, O II or O III ISM lines.

More prominent absorbers, which show depletion of the flux in O VII of more than 70%, and which have a significant velocity difference between the gas in the filaments and the galaxy cluster core (in our studies this difference is  $v_{\text{TOT}} \sim \pm 1000$  km/s), can almost all (besides CE-25 & A2390 and CE-29 & A1413) be detected with more than  $5\sigma$  significance with exposure time  $\leq 250$  ks (for high redshifts, such as Abell 383) or even 100 ks for the lower-redshift galaxy clusters, such as Abell 2029 or Abell 262. The CE-25 absorber in our study is always resolved from the ISM lines while CE-29 can potentially be observed only for high-redshift clusters such as A2390 and A383.

The exposure times needed to get a  $5\sigma$  detection in O VII with Athena X-IFU for CE-7, CE-25, and CE-29  $z$ -absorbers are summarized in Table 2.3.

### 2.3.2.2 Significance of the O VIII detection

The detection of the cosmic web filaments against galaxy cluster background sources in O VIII is significantly more difficult than for O VII. Firstly, the depletion of flux in O VIII is comparable to the less prominent O VII absorbers, which as we have shown in Table 2.2, require more exposure time for a significant detection (more than 200 ks or 300 ks). For most of these absorbers the flux in O VIII decreased by 10 – 20% relative to the continuum (see Fig. 2.4). For some absorbers, as e.g. CE-3, CE-8, the line flux decreased by 35%. Secondly, due to high temperatures and densities in the intracluster medium (ICM), the galaxy cluster spectra contain a strong O VIII emission line. Even though the velocity difference between ICM and the gas in the cosmic web filaments is similar for O VII and O VIII absorption (see Fig. 2.4), the wings of the O VIII emission line are too bright for the O VIII absorption line to be sufficiently separated with the X-IFU resolution of 2.5 eV. In Sec. 2.4.3 we discuss how these results would be affected if we used a detector with an even higher spectral resolution.

		<b>CE-7</b>	<b>CE-25</b>	<b>CE-29</b>
<b>Abell 2390</b>	$t_{\text{exp}}$ [ks]	500	250	250
	normalisation [ $\times 10^{49}$ ph/s]	$-8.6 \pm 1.5$	$-8.5 \pm 2.0$	$-15.9 \pm 2.1$
	C-statistics	829	799	757
	expected C-statistics	$791 \pm 40$	$791 \pm 40$	$791 \pm 40$
	significance $\sigma$	<b>5.7</b>	<b>4.3</b>	<b>7.6</b>
<b>Abell 383</b>	$t_{\text{exp}}$ [ks]	500	250	250
	normalisation [ $\times 10^{49}$ ph/s]	$-4.8 \pm 0.6$	$-4.5 \pm 0.9$	$-6.4 \pm 0.9$
	C-statistics	653	649	669
	expected C-statistics	$588 \pm 34$	$588 \pm 34$	$588 \pm 34$
	significance $\sigma$	<b>8.0</b>	<b>5.0</b>	<b>8.0</b>
<b>Abell 1413</b>	$t_{\text{exp}}$ [ks]		250	
	normalisation [ $\times 10^{49}$ ph/s]		$-4.1 \pm 0.5$	
	C-statistics	blended with N VII	415	blended with N VII
	expected C-statistics		$419 \pm 29$	
	significance $\sigma$		<b>8.2</b>	
<b>Abell 2029</b>	$t_{\text{exp}}$ [ks]		100	
	normalisation [ $\times 10^{49}$ ph/s]		$-9.1 \pm 0.5$	
	abundance O (neutral)		$1.01 \pm 0.02$	
	abundance O (warm)	blended with O II	$1.06 \pm 0.05$	blended with O II
	C-statistics		150	
	expected C-statistics		$172 \pm 19$	
	significance $\sigma$		<b>18.2</b>	
<b>Abell 1795</b>		blended with O III	blended with O I	blended with O III
<b>Abell 262</b>	$t_{\text{exp}}$ [ks]		100	
	normalisation [ $\times 10^{49}$ ph/s]		$-0.23 \pm 0.02$	
	abundance O (hot)	blended with O II	$1.3 \pm 0.2$	blended with O II
	C-statistics		408	
	expected C-statistics		$430 \pm 29$	
	significance $\sigma$		<b>11.5</b>	

**Table 2.2:** X-IFU simulations for the CE-7, CE-25, and CE-29  $z+$  Hydrangea O VII absorbers and the A2390, A383, A1413, A2029, A1795, and A262 background galaxy clusters.  $t_{\text{exp}}$  is the exposure time and the normalisation of the Gaussian line is given in units of  $\times 10^{49}$  ph/s. We also provide the values of the C-statistics, the significance of the detection  $\sigma$ , as well as the value of the expected C-statistics (see Sec. 2.3.1.5 and Sec. 2.3.2.1 for more details). The radius of interest was assumed to be 100 kpc and the final absorption profiles were weighted by the surface brightness of the respective galaxy cluster. The errors represent the standard deviation  $1\sigma$ .



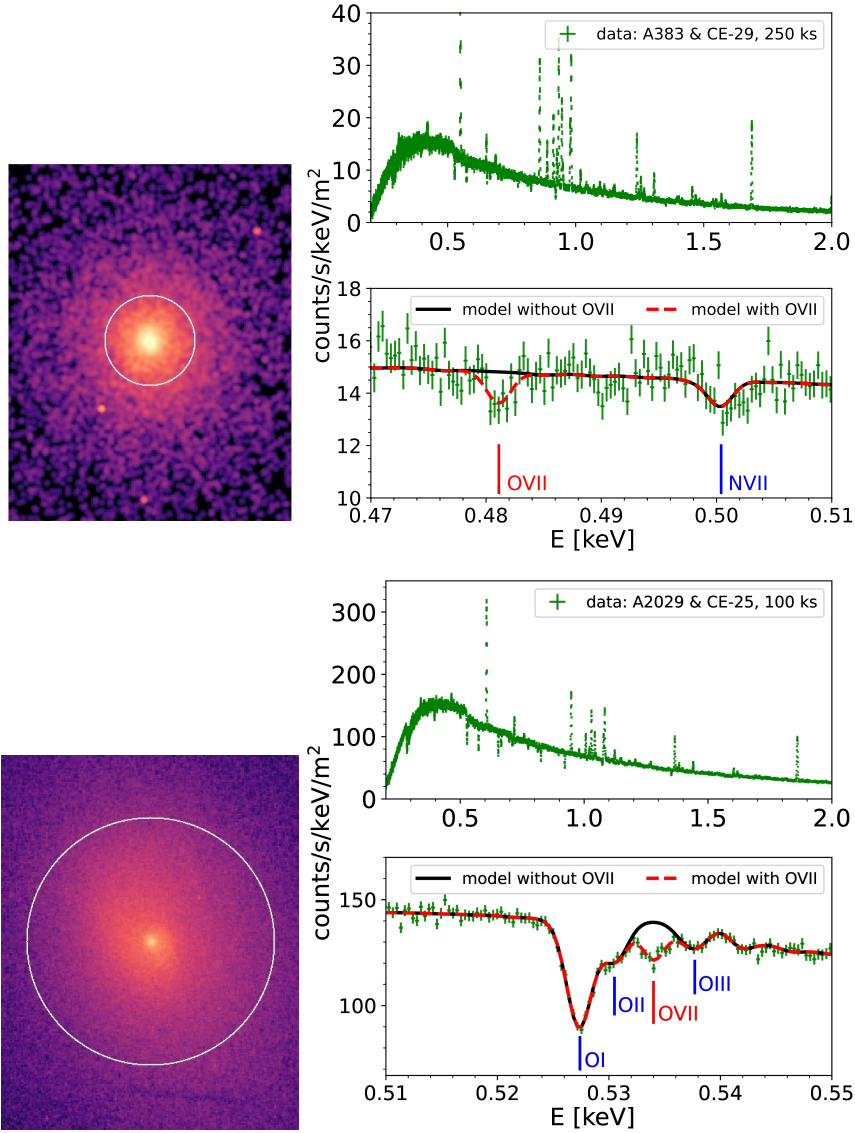


**Figure 2.6:** Broad band simulated spectrum for Athena X-IFU in the energy range 0.2 – 2 keV and a zoom-in to 0.47 – 0.51 keV of the CE-29  $z$ + Hydrangea absorber and A383 (top two right panels, 250 ks exposure time,  $z = 0.1883$ ) and the CE-25 and A2029 (bottom two right panels, 100 ks exposure time,  $z = 0.0779$ ), where the zoom-in for CE-25 and A2029 shows the energy band 0.51 – 0.55 keV. The black solid line represents the spectral model (folded through the response of X-IFU) together with the three-component absorption model of the Milky Way ISM as described in Sec. 2.3.1.3. The absorption lines of the local ISM are indicated in all panels with blue vertical lines. The red dashed line represents the same spectral model as the black solid line but with an addition of the Hydrangea O VII absorption line (solid red vertical lines) according to the best-fitting parameters described in Table 2.2. Left panels show the Chandra images of A383 (top left panel) and A2029 (bottom left panel). The white circle has a radius of 100 kpc as used in all calculations in this paper. The errors shown in the spectra represent the standard deviation  $1\sigma$ .

$t_{\text{exp}}$ [ks]	CE-7	CE-25	CE-29
Abell 2390	385	338	108
Abell 383	195	250	98
Abell 1413	–	93	–
Abell 2029	–	8	–
Abell 1795	–	–	–
Abell 262	–	19	–

**Table 2.3:** Exposure time  $t_{\text{exp}}$  in ks for X-IFU (2018 baseline response matrices) simulations for CE-7, CE-25, and CE-29  $z+$  Hydrangea O VII absorbers and A2390, A383, A1413, A2029, A1795, and A262 background galaxy clusters for a detection of  $5\sigma$ . The radius of interest was assumed to be 100 kpc and the final absorption profiles were weighted by the surface brightness profile of the respective galaxy cluster.

## 2.4 Discussion

We have shown above that detecting the WHIM in absorption against bright cluster cores is possible (and perhaps even promising) with future, high-resolution, non-dispersive X-ray spectrometers. Below, we discuss in more detail various additional aspects that can affect the detectability of O VII and O VIII absorption lines, such as the optimal size of the spectral extraction region, the effect of using background sources with different underlying surface brightness distributions, the impact of the detector’s spectral resolution, the impact of the O VII emission from the cosmic web filaments, and possible blending with emission lines from low-temperature gas in cluster cores.

### 2.4.1 The optimal size of the spectral extraction region

Until now, we focused our calculations on a circular aperture with a fiducial radius of 100 kpc. However, it is not clear if this is the optimal choice for the spectral extraction region. To answer the question of how the selection of the radius of interest affects our results, we did a new set of calculations with *Specwizard* for the CE-25 Hydrangea absorber for two additional radii: 40 kpc and 300 kpc. As already shown in Table 2.2, this absorber was detected with Athena for most of the background sources, and therefore we chose to show the results of this subsection for this absorber. How CE-25 looks like on these scales can be seen in Fig. 2.2 (red lines with different line styles).

The shaded areas in Fig. 2.7 show the 10th and 90th percentile scatter between different individual sightlines (from the full sample of 276 LoSs) covering each radius. Our results indicate that the absorption profiles are deeper for a smaller radius of interest; for larger radii, the scatter among different sightlines increases, and their average absorption profile becomes shallower. The relatively small scatter between individual sightlines probing the central 40 kpc radius (shaded blue area in Fig. 2.7) suggests that the projected properties of the CE-25 absorber are not very patchy over this spatial scale, while their spatial substructure increases considerably when considering a larger, 300 kpc region. Fig. 2.7 also provides a comparison to quasar-like studies, where the absorbers would be probed along a single line of sight. In this case, the absorption profile could lie anywhere in the plotted shaded area, whereas the absorption profile for an extended source would follow the solid line.

For calculating the significance of the O VII detection with X-IFU and quantifying the

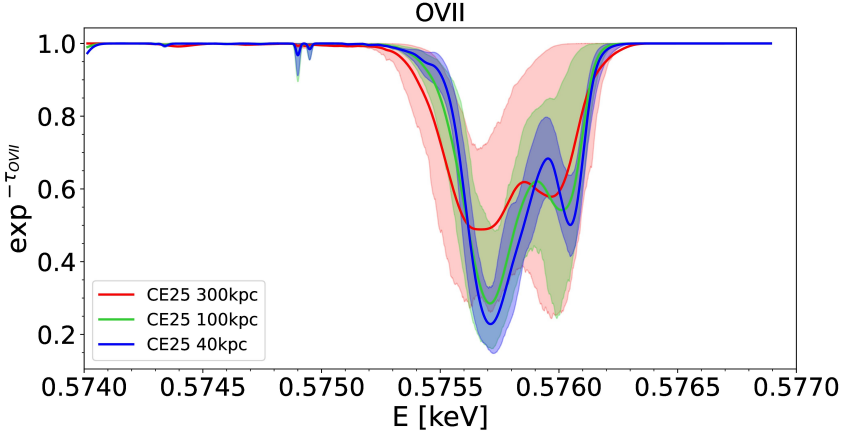


**Figure 2.7:** CE-25 O VII absorption profile (equally weighted) at O VII rest energy for 40 kpc (blue solid line), 100 kpc (green solid line), and 300 kpc (red solid line) spectral extraction regions. In every energy bin, the shaded area represents all the data between the 10th and 90th percentiles of the full sample, which consists of 276 LoSs for each radius. The larger spectral extraction region with  $R = 300$  kpc results in shallower absorption profiles in comparison with  $R = 40$  kpc.

comparison of different radii of interest, we chose as an example CE-25 (SB weighted profile) and A1413 as a background source. We again assumed that the absorption profile can be fitted with a gaussian. The results can be found in Table 2.4 for an exposure time of 250 ks.

In conclusion, there is a clear trade-off in choosing the size of the spectral extraction region: the smaller the region, the deeper the absorption profile is likely to be (see Fig. 2.7). When the region of interest increases, we start to average over a larger variety of sightline properties, which dilutes the average signal. However, larger regions of interest also mean a larger number of counts from the extended background source, and therefore better statistics in determining the continuum level with respect to which the line is measured, increasing the significance of the detection. Our study suggests that, at least out to the radii of interest considered in our study, the latter effect is more important, i.e. the significance of O VII detection increases with the size of the radius (see Table 2.4). However, we would like to point out that calibration uncertainties (such as gain variation across the detector) may play an additional role when determining the significance of the O VII detection for various spectral extraction regions.

### 2.4.2 Impact of weighting by different surface brightness profiles

In this paper, we demonstrated the method of observing cosmic web filaments against bright cool-core galaxy clusters. We selected a few galaxy clusters which span a range of redshifts, masses, and temperatures. However, one could potentially use any bright cool-core cluster. What would change is the SB profile that is used for weighting of the LoSs that are used for the final Hydrangea absorption profile.

To assess the impact of this weighting, we compare the final weighted profiles for two cases: (a) equally weighted profiles (the arithmetic mean), and (b) surface brightness weighted

radius [kpc]	40	100	300
normalisation [ $\times 10^{49}$ ph/s]	$-1.17 \pm 0.25$	$-4.1 \pm 0.5$	$-9.3 \pm 0.8$
C-statistics	482	415	399
expected C-statistics	$419 \pm 29$	$419 \pm 29$	$419 \pm 29$
significance $\sigma$	<b>4.7</b>	<b>8.2</b>	<b>11.6</b>

**Table 2.4:** X-IFU simulations for CE-25 and the A1413 background galaxy cluster for three different spectral extraction regions: 40 kpc, 100 kpc, and 300 kpc. The final absorption profiles were weighted by the surface brightness of A1413 and fitted with a gaussian profile. The errors represent the standard deviation of  $1\sigma$ . The exposure time for all radii was 250 ks. In conclusion, even though the larger radius of interest,  $R = 300$  kpc, results in shallower absorption profiles in comparison with 40 kpc, the increase in the number of counts for the larger area improves the significance of the O VII detection.

profiles (see Eq. (2.1) in Sec. 2.3.1.5). The difference between the equally weighted profiles and the SB weighted profiles is mostly  $< 5\%$  and maximally 10% for all 16 absorbers and all galaxy clusters, with the exception of three Hydrangea absorbers which show a difference larger than 10%: CE-1  $x+$ , CE-22 and CE-25. For these three outliers the difference between the weights depends on the background galaxy cluster, and is the highest for A383: 17% for CE-1  $x+$ , and 36% for CE-22.

As already seen from the column density maps, the cosmic web filaments in O VII can be very patchy in the projection on the sky, and they do not have to homogeneously cover the whole spectral extraction region, from which we draw the LoSs for the final absorption profiles. Even though the difference between the arithmetic mean and SB weighting is not as significant, we chose to use the SB weighting for the results obtained in Sec. 2.3.2.

### 2.4.3 Prospects for detectors with a different spectral resolution and effective area

In the case of the Athena mission, which is planned for the second half of the 2030s, one needs to keep in mind that it might still undergo changes in the mission requirements. This could possibly result in the degradation of the effective area or spectral resolution. The change in the effective area would affect mainly the amount of exposure time needed for a detection above  $5\sigma$ , however, the observations would still be possible and the method and the results presented in this paper would not be affected. The more concerning would be the degradation of the spectral resolution. In the case of O VII, we tried to simulate data with a spectral resolution of 4 eV instead of 2.5 eV. For the background sources at a redshift similar to A2029, where the Hydrangea absorbers are blended with the O I, O II, and O III ISM lines, such a resolution is no longer enough to sufficiently separate the O VII Hydrangea line from the ISM lines. We also simulated two other cases from Table 2.2: (a) CE-25 and A1413 for a 250 ks exposure time, and (b) CE-25 and A262 for a 100 ks exposure time. In the case of A1413, the significance of the detection of O VII decreased from  $8.2\sigma$  to  $6.3\sigma$ . For A262 the significance of the detection decreased from  $10\sigma$  to  $6\sigma$ . This means that if the spectral resolution is degraded from 2.5 eV to 4 eV, the exposure time for a  $5\sigma$  detection of the CE-25 O VII absorber would increase from 93 ks to 174 ks in the case of the background galaxy cluster A1413, and from 25 ks to 63 ks in the case of A262. Nevertheless, it is encouraging that such studies would remain feasible.

Another detector that we discuss in this section is the Integral Field Unit (IFU) micro-calorimeter of the Line Emission Mapper (LEM, Kraft et al. 2022). LEM is a mission concept to be submitted to the National Aeronautics and Space Administration (NASA) 2023 Astrophysics Probes call for proposals. It is an X-ray probe that will, among other applications, focus on galaxy formation and evolution by probing the circumgalactic and intergalactic media. It will consist of an X-ray mirror with an effective area of  $1600 \text{ cm}^2$  at  $0.5 \text{ keV}$ , and a cryocooled array of Transition-Edge Sensor (TES) micro-calorimeters, whose technology will be built on Athena X-IFU and the Lynx X-ray observatory concept (Vikhlinin 2018).

LEM's biggest advantage considering our scientific interest lies in its spectral resolution of approximately  $0.9 \text{ eV}$  for extended sources. In Fig. 2.8, we plot LEM simulated spectrum for CE-25 & A2029 O VII absorption line for a 100 ks exposure time and CE-25 & A2029 O VIII absorption line for a 1 Ms exposure time. In comparison with X-IFU (see Fig. 2.6), the O I, O II, and O III Galactic absorption lines are completely separated from the O VII Hydrangea absorption line. We compared these simulated results to the X-IFU results given in Table 2.2. The significance of the O VII detection decreased from  $18.2\sigma$  to  $15.4\sigma$ , which is caused mainly by the fact that the exposure time was the same for both instruments, even though the effective area is smaller for LEM. In general, the observations with LEM might need more observing time to reach the same significance of detection, however, its unprecedented spectral resolution can increase the number of detections by distinguishing more easily between the absorption from cosmic web filaments and the absorption by the Galactic ISM. In the case of O VIII (see the bottom panel of Fig. 2.8), a spectral resolution comparable to that of LEM can distinguish between galaxy cluster O VIII emission line and the cosmic web filament O VIII absorption line. According to our simulations, a detection of  $10\sigma$  is possible in 1 Ms. Therefore, a  $5\sigma$  detection would be feasible with LEM for an exposure time of 250 ks.

#### 2.4.4 Impact of potential sources of O VII emission

Due to the centrally peaked density profiles in relaxed galaxy clusters, the radiative cooling times of the diffuse gas trapped in the potential wells of these objects can become shorter than the Hubble time (typically less than 1 Gyr). It is now understood that the energy input from AGN feedback largely compensates for this gas cooling, keeping the ICM hot (for a review, see McNamara & Nulsen 2007). However, the heating-cooling balance is rarely perfect, and local thermal instabilities can often develop, forming narrow strands of multi-phase gas (see e.g. Sharma et al. 2012; Li & Bryan 2014). The coolest X-ray emitting phases of this gas should be visible through their soft X-ray line emission, for instance as O VII or Fe XVII (Sanders & Fabian 2011; Pinto et al. 2014).

In order to investigate whether the potential X-IFU detection of this emission from cool gas would affect the analysis and results presented in this paper, we add an additional CIE component to our model. The typical temperatures for this cool CIE component as reported by Pinto et al. (2014) are between  $0.45 - 0.85 \text{ keV}$ , while its normalisation is about 10–50 times lower than the normalisation of the model describing the bulk of the intracluster medium.

For our calculations we chose CE-29 & A383 X-IFU observations (with exposure time 250 ks) as an example. We added an additional CIE component with temperature  $0.6 \text{ keV}$ , with a normalization that corresponds to a flux (in the  $0.2 - 1 \text{ keV}$  energy band) which is 10 times lower than the flux of the original model as described in Sec. 2.3.1. After simulating the new X-IFU spectra and fitting the spectra in the same manner as described in Sec. 2.3.1.5, the significance of the O VII detection decreased from  $8\sigma$  to  $\approx 7.5\sigma$ .

Therefore we can conclude that, for the strongest absorbers like CE-25 and CE-29, even a

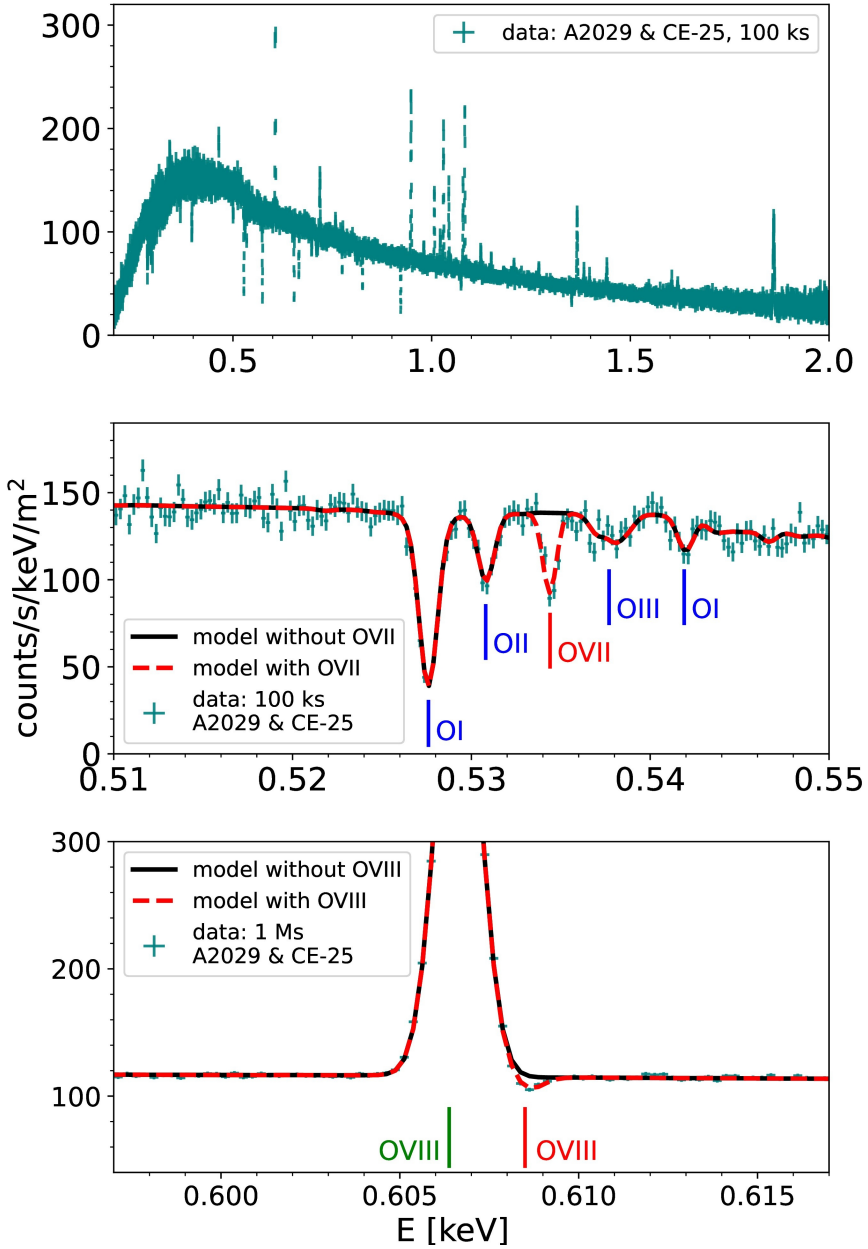


**Figure 2.8:** LEM simulated broad band spectrum in the energy range 0.2 – 2 keV (top panel) and a zoom in to 0.51 – 0.55 keV (middle panel) and 0.6 – 0.615 keV (bottom panel) of the CE-25 Hydrangea absorber and backlight cluster A2029. The black solid line represents the spectral model (folded through the response of LEM) together with the three-component absorption model of the Milky Way ISM as described in Sec. 2.3.1.3. The absorption lines of the local ISM are indicated in all panels with blue vertical lines. The red dashed line represents the same spectral model as the black solid line but with an addition of the Hydrangea OVII or OVIII absorption line (labelled with solid red vertical lines) according to the best-fitting parameters described in Sec. 2.4.3. The green vertical line in the bottom panel shows the OVIII galaxy cluster emission line.

10% contribution in flux from the cooling gas would not matter, while for smaller  $N_{\text{O VII}}$  (like CE-7), caution should be taken with this cooling gas. If present, gas cooling will probably happen along patchy small-scale filaments that can be excluded from the spectral extraction to test the robustness of the O VII absorption signal in case both phenomena are seen simultaneously.

Furthermore, we estimated the effects of O VII emission from gas belonging to the filament itself, by approximating the volume of the filament as a cylinder with a 100 kpc radius (same as our typical spectral extraction region), and a length of  $2 \times r_{200}$  (corresponding to one of the largest absorbers, i.e. CE-29  $z_+$ ; see Fig. 2.3). For a rough estimate, we convert the number of O VII ions into a hydrogen number density by assuming an O/H metallicity of 0.2 Solar, and that all oxygen is in the O VII ionization state, and averaging over all LOSs in the central 100 kpc. This yields an emission measure of the CE-29  $z_+$  filament that is 4 orders of magnitude lower than that of the potential cool gas in the cluster core, considered earlier in this section. We therefore conclude that the intrinsic O VII emission from the filament does not affect the absorption signal.

## 2.5 Conclusions

In this paper we studied the prospects of observing cosmic web filaments in absorption against diffuse X-ray emission of cool-core galaxy clusters.

We extended the study of Simionescu et al. (2021), which simplified the WHIM as a single temperature absorbing gas cloud in collisional ionisation equilibrium. We projected 23 galaxy clusters from the Hydrangea cosmological hydrodynamical simulations along the  $\pm x$ ,  $\pm y$ , and  $\pm z$  simulation axes and out of the total number of 138 directions we found 16 directions with a column density sufficiently high that it could potentially be observed in O VII absorption against galaxy clusters with the X-IFU instrument of the Athena X-ray Observatory (Fig. 2.1, Fig. 2.2, Fig. 2.9 and Fig. 2.10).

We obtained the absorption profiles for all 16 directions by averaging over 276 sightlines in the simulation volumes, which were probing the area of a circle with radius 100 kpc in the plane of the sky. In Fig. 2.3 and Fig. 2.4 we showed the spatial properties and the velocity structure for all 16 directions.

For three absorbers (CE-7, CE-25, and CE-29  $z_+$ ) we simulated the Athena X-IFU spectra, where all sightlines were weighted by the surface brightness profile of the chosen background galaxy clusters. Our simulations also took into account a three-component model for Galactic ISM absorption. The CE-7 galaxy cluster is at the low mass end of the galaxy cluster sample with mass  $M_{200c} \approx 10^{14.34} M_{\odot}$ , while the CE-25, and CE-29  $z_+$  are among the three most massive Hydrangea clusters, with masses  $M_{200c} \approx 10^{15.15} M_{\odot}$ , and  $M_{200c} \approx 10^{15.38} M_{\odot}$ , respectively.

Our main results can be summarized as follows:

- Out of the massive clusters from the Hydrangea cosmological simulations, 16 out of 138 directions have on average O VII column densities above  $10^{14.5} \text{ cm}^{-2}$ . The strongest of these absorbers can be detected with at least  $5\sigma$  significance in reasonable exposure times with the Athena X-IFU ( $T_{\text{exp}} \leq 250 \text{ ks}$ ), provided that the Galactic foreground absorption at the observed line energy permits it. Table 2.3 summarizes the exposure times for O VII detection for three example absorbers: CE-7  $x_-$ , CE-25  $x_+$ , and CE-29  $z_+$ . Unfortunately, O VIII absorption from the WHIM cannot be detected with Athena since the wings of the O VIII galaxy cluster emission line are too

bright for O VIII absorption line to be sufficiently separated with the X-IFU resolution of 2.5 eV.

- Under the assumption that the ISM of the Milky Way can be represented by a three-component model as described in Sec. 2.3.1.3, the ISM lines that might intervene with the O VII cosmic web filaments detection are N VII, O I, O II, O III, and O VII (Fig. 2.5).
- From our studies, the most promising clusters for the detection of the O VII WHIM absorption against extended sources seem to be the higher redshift clusters, e.g. A2390 ( $z = 0.2302$ ) and A383 ( $z = 0.1883$ ), for which all three Hydrangea absorbers with different total velocity along the line of sight  $v_{\text{TOT}}$  and different optical depths could be detected with X-IFU. Lower redshift clusters give even more significant detections, but suffer more from the presence of foreground ISM lines, and the detection or non-detection depends on the combination of the galaxy cluster redshift and the velocity  $v_{\text{TOT}}$ .
- The velocity difference between the strongest absorbers and the galaxy cluster centre is on average  $\sim \pm 1000$  km/s (Fig. 2.4). The maximum  $v_{\text{TOT}}$  that we found in the Hydrangea absorbers was  $\approx 2200$  km/s for CE-28.
- Even though the larger spectral extraction region with  $R = 300$  kpc results in shallower absorption profiles in comparison with  $R = 40$  kpc, the increase in the photon number count for the larger area improves the significance of the O VII detection (Fig. 2.7).
- If the spectral resolution of LEM is approximately 1 eV for extended sources, then it can additionally probe the WHIM O VII line which is closer in energy to Galactic foreground lines (see Fig. 2.8). The unprecedented spectral resolution of LEM could even distinguish the O VIII emission line from the galaxy cluster and the O VIII absorption line from the WHIM. According to our simulations, a  $5\sigma$  significance of the O VIII WHIM detection for cases like CE-25 & A2029 would be feasible in 250 ks (see Sec. 2.4.3).
- If the Athena X-IFU resolution was degraded to 4 eV, cases similar to O VII absorption from CE-25 and the A2029 background galaxy cluster would be lost due to blending with ISM absorption lines. For CE-25 and background clusters A1413 and A262 this would result in an increase of the required exposure time from 93 ks to 174 ks and from 25 ks to 63 ks for a detection of at least  $5\sigma$ , respectively.

**Acknowledgements:** The authors acknowledge the financial support from NOVA, the Netherlands Research School for Astronomy. L.Š. is supported by NWO grant Athena 184.034.002. A.S. is supported by the Women In Science Excel (WISE) programme of the Netherlands Organisation for Scientific Research (NWO), and acknowledges the Kavli IPMU for the continued hospitality. SRON Netherlands Institute for Space Research is supported financially by NWO. N.A.W. is supported by a CIERA Postdoctoral Fellowship. Y.B. acknowledges funding from the Dutch Research Organisation (NWO) through Veni grant number 639.041.751 and financial support from the Swiss National Science Foundation (SNSF) under project 200021\_213076. This work used the DiRAC@Durham facility managed by the Institute for Computational Cosmology on behalf of the STFC DiRAC HPC Facility ([www.dirac.ac.uk](http://www.dirac.ac.uk)). The equipment was funded by BEIS capital funding via STFC capital grants ST/K00042X/1, ST/P002293/1 and ST/R002371/1, Durham University and STFC operations grant ST/S003908/1. DiRAC is part of the National e-Infrastructure.



**Data Availability:** The dataset generated and analysed during this study is available in the ZEN-ODO repository (Štofanová 2023).

## Appendix

### 2.A Total column density maps

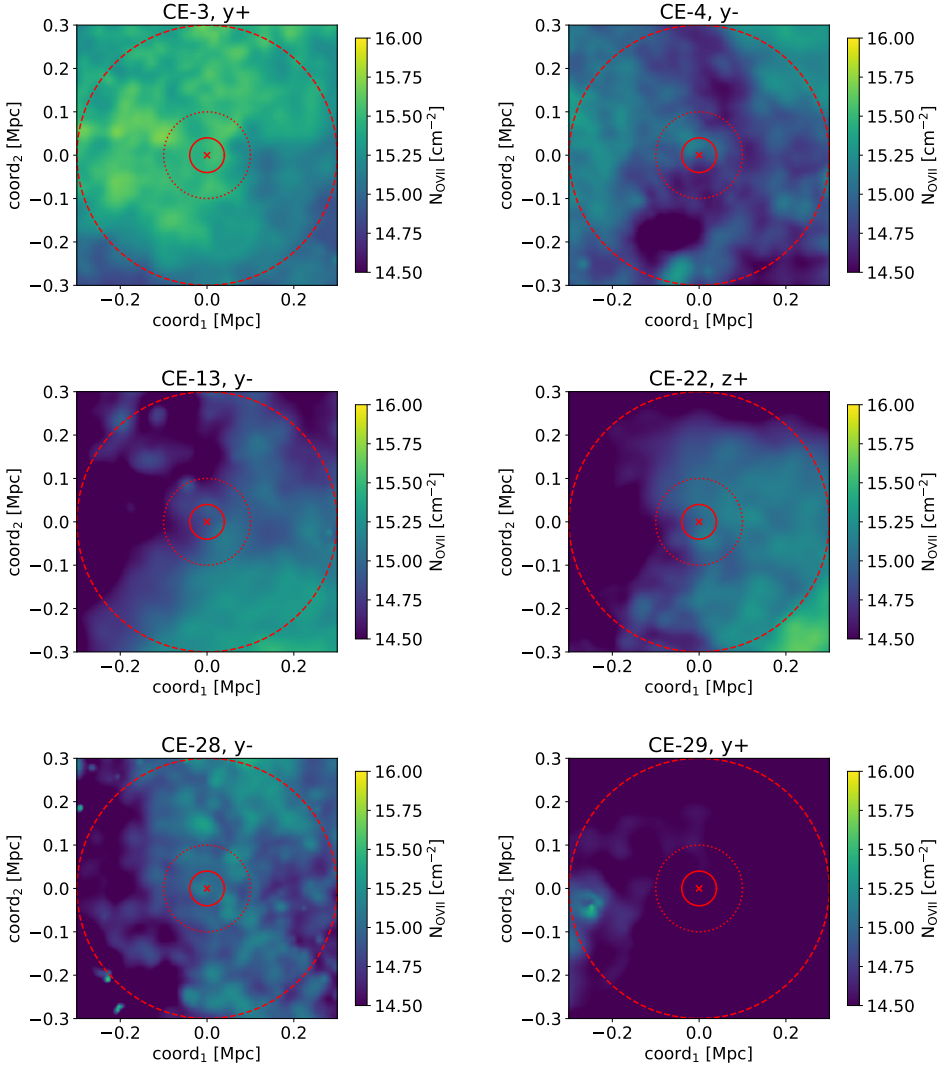


**Figure 2.9:** Continuation of Fig. 2.2 for CE-3 y+, CE-4 y-, CE-13 y-, CE-22 z+, CE-28 y-, and CE-29 y+.

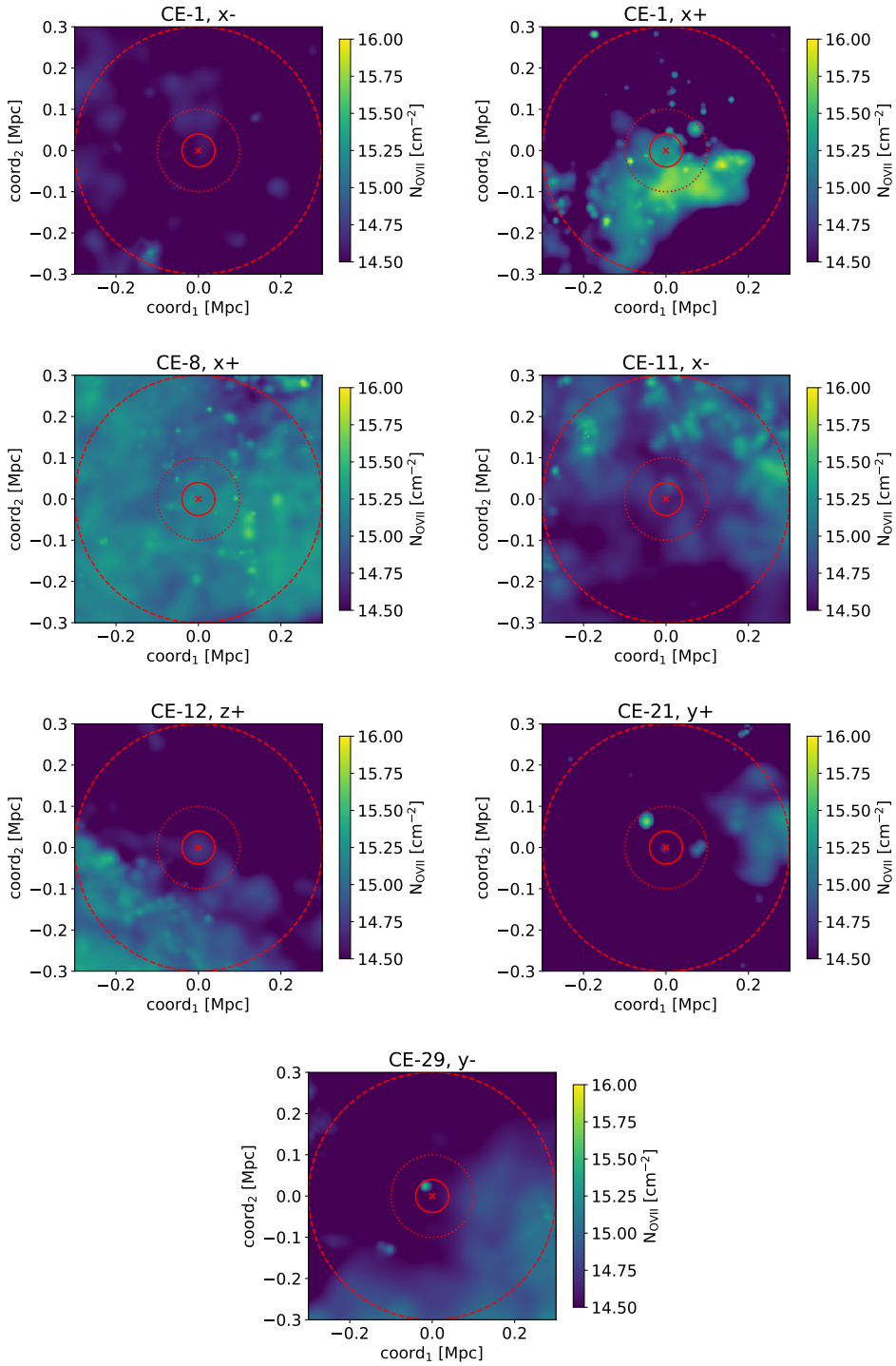


**Figure 2.10:** Continuation of Fig. 2.2 for CE-1  $x^-$ , CE-1  $x^+$ , CE-8  $x^+$ , CE-11  $x^-$ , CE-12  $z^+$ , CE-21  $y^+$ , and CE-29  $y^-$ .



# 3

## Galaxy cluster photons alter the ionisation state of the nearby warm-hot intergalactic medium

---

Lýdia Štofanová, Aurora Simionescu, Nastasha A. Wijers, Joop Schaye, and Jelle S. Kaastra

*Published in Monthly Notices of the Royal Astronomical Society, 2021, Volume 515, Issue 3, pp.3162-3173.*

### ABSTRACT

---

The physical properties of the faint and extremely tenuous plasma in the far outskirts of galaxy clusters, the circumgalactic media of normal galaxies, and filaments of the cosmic web, remain one of the biggest unknowns in our story of large-scale structure evolution. Modelling the spectral features due to emission and absorption from this very diffuse plasma poses a challenge, as both collisional and photo-ionisation processes must be accounted for. In this paper, we study the ionisation by photons emitted by the intra-cluster medium in addition to the photo-ionisation by the cosmic UV/X-ray background on gas in the vicinity of galaxy clusters. For near massive clusters such as A2029, the ionisation parameter can no longer describe the ionisation balance uniquely. The ionisation fractions (in particular of C IV, C V, C VI, N VII, O VI, O VII, O VIII, Ne VIII, Ne IX, and Fe XVII) obtained by taking into account the photoionisation by the cosmic background are either an upper or lower limit to the ionisation fraction calculated as a function of distance from the emission from the cluster. Using a toy model of a cosmic web filament, we predict how the cluster illumination changes the column densities for two different orientations of the line of sight. For lines of sight passing close to the cluster outskirts, O VI can be suppressed by a factor of up to 4.5, O VII by a factor of 2.2, C V by a factor of 3, and Ne VIII can be boosted by a factor of 2, for low density gas.

---

### 3.1 Introduction

For almost three decades, scientists have been trying to find the ‘missing baryons’ in the Universe. The ‘missing baryons’ problem originates from the comparison of the amount of baryons detected in the high redshift Universe ( $z > 2$ ) with the amount detected in the local Universe from  $z = 0$  to  $z = 1 - 2$ . At redshift  $z > 2$ , these baryons reside in much cooler gas and can predominantly be detected in the so called Lyman  $\alpha$  forest (e.g. Lynds 1971; Sargent et al. 1980; Cen et al. 1994; Zhang et al. 1995; Weinberg et al. 1997; Schaye 2001). To predict where to find them in the local Universe, one needs to rely on cosmological hydrodynamical simulations (e.g. Bristow & Philipps 1994; Cen & Ostriker 1999), which show that baryons are heated to higher temperatures, mainly via shock-heating due to the gravitational collapse and the hierarchical growth of structures in the Universe. In addition, processes such as supernova feedback, active galactic nuclei feedback, radiative cooling, or photoionisation can heat up this gas (e.g. Tepper-García et al. 2012). Most of the diffuse baryons in the present epoch have not yet been converted into stars and can be found in groups of galaxies – intragroup medium (IGrM), in the haloes of galaxy clusters – intracluster medium (ICM), or in the space between them – intergalactic medium (IGM). A subset of the IGM is the warm-hot intergalactic medium (WHIM) permeating large-scale structure filaments, while another component of the IGM is comprised of gas found in the haloes of galaxies – the so-called circumgalactic medium (CGM).

In this work we focus on the WHIM, which at low redshift contains around 30% up to 60% of all baryons of the Universe (e.g. Fukugita et al. 1998; Davé et al. 2001; Tepper-García et al. 2012; Shull et al. 2012; Martizzi et al. 2019; Tuominen et al. 2021). These baryons reside predominantly in the filamentary structures of the cosmic web (e.g. Martizzi et al. 2019; Tuominen et al. 2021) and can be detected mostly in the ultraviolet (UV, see e.g. Nicastro et al. 2003) and X-ray wavebands/energies (e.g. Hellsten et al. 1998; Fang et al. 2002a; Wijers et al. 2019; Wijers & Schaye 2022) because of its relatively high temperatures of  $10^5 - 10^7$  K. Due to its high temperatures, low electron densities ( $10^{-6} - 10^{-4}$  cm $^{-3}$ ), and high ionisation state, the observations of this very diffuse and tenuous gas are extremely challenging with currently available UV and X-ray missions. Since the emission decreases as density squared, and absorption decreases linearly with density, it is more feasible to detect the WHIM in absorption against very bright, point like sources (e.g. quasars). Since oxygen is the most abundant element after hydrogen and helium in Universe, it is common to look for the WHIM gas in O VII and O VIII absorbers, but also in Ne IX or N VII (e.g. Perna & Loeb 1998; Fang et al. 2003; Rasmussen et al. 2003; Fujimoto et al. 2004; Nicastro et al. 2005b; Takei et al. 2007; Nicastro et al. 2018; Ahoranta et al. 2021). Observations of the WHIM in emission, however, are possible, though mostly through stacking methods to obtain higher signal-to-noise to distinguish the WHIM detection from the background. Since we focus on absorption studies in this paper, we only list few of the publications regarding the emission studies (e.g. Kull & Böhringer 1999; Zappacosta et al. 2002; Finoguenov et al. 2003; Kaastra et al. 2003; Werner et al. 2008). The IGM can also be detected in the UV. Typical UV absorbers are coming particularly from warm CGM and can be observed in e.g. O VI, C IV, N V or Ne VI (see e.g. Tumlinson et al. 2011; Werk et al. 2014). For more details we refer to the CGM review paper by Tumlinson et al. (2017).

The WHIM gas is typically modelled with collisional ionisation equilibrium (CIE) models (assuming the gas has only one temperature) and with photoionisation models that take into account the photoionisation by the UV and X-ray background (e.g. Nicastro et al. 2005a). The sources of this background are known to include star forming galaxies and quasars. The modelling of this background can be very complex, and has been described in many previous works, including e.g. Haardt & Madau (2012); Faucher-Giguère (2020).

The presence of the photoionising radiation causes a suppression of the cooling rates in comparison with the CIE case. In a CIE plasma, the lighter elements such as hydrogen, carbon, and helium are the dominant coolants for temperatures below  $\sim 10^{-2}$  keV (for a plasma with roughly proto-solar metallicities). In highly photoionised gas, these elements are significantly less efficient coolants. The relative contributions of different coolants to the total cooling rate, however, also depend strongly on the shape of the spectrum of the ionising source. The suppression of cooling rates in photoionised plasma leads to longer cooling times and can affect star/galaxy formation over time. This has been already noted by

Cluster	$z$	$r_{500}$ [kpc]	$T_{\text{spec}}$ [keV]
A262	0.0162	$650 \pm 21$	$2.08 \pm 0.06$
A1795	0.0622	$1235 \pm 36$	$6.12 \pm 0.05$
A2029	0.0779	$1362 \pm 43$	$8.47 \pm 0.09$

**Table 3.1:** Redshift  $z$ ,  $r_{500}$  and  $T_{\text{spec}}$  of the clusters used in our study taken from Vikhlinin et al. (2006).

e.g. Silk (1985); Dekel & Rees (1987); Babul & White (1991), which show how quasars can ionise the gas in their surroundings and inhibit the formation of galaxies in their neighbourhood. This can propagate through time and even affect the large-scale structure seen in the galaxy distribution. This was also shown in Efstathiou (1992) for the gas of primordial composition (H and He plasma) where the paper explores how the presence of photoionisation caused by the extragalactic UV background can inhibit the formation of dwarf galaxies, most prominently in the gas temperature range  $10^4$ – $10^5$  K (see also Quinn et al. 1996; Thoul & Weinberg 1996). Wiersma et al. (2009a) showed how UV/X-ray radiation from galaxies and quasars can significantly suppress the cooling rates for gas enriched with metals as well and how this affects the gas with temperatures even up to  $10^7$  K.

In this paper, we explore how an additional source of photoionisation, in this case caused by the photons originating in galaxy clusters in addition to the photoionisation by cosmic UV and X-ray background, can change the ionisation balance of the WHIM. In Section 3.2 we model the spectral energy distribution of three different cool-core galaxy clusters together with the cosmic UV/X-ray background, which serves as the ionisation source to the photoionisation model. In Section 3.3.1, we describe the main changes to the ionisation state of the WHIM by focusing on the most massive galaxy cluster in our sample. We make the comparison to the other two, less massive clusters in Section 3.3.2. In Section 3.4.1 we use a simplified model of a filament and predict column densities in two different orientations: perpendicular and parallel to the line of sight, and provide a comparison to the column densities calculated for the photoionisation by the cosmic UV/X-ray background only. In Section 3.4.2 we show how the cooling rates of the WHIM can be affected by an additional source of photoionisation from the galaxy cluster. And finally, Section 3.5 summarizes our main conclusions. Throughout the paper, we assume a cosmology with total matter density  $\Omega_m = 0.3$ , dark energy density  $\Omega_\Lambda = 0.7$ , radiation density  $\Omega_r = 0$ , curvature  $\Omega_k = 0$  and Hubble constant  $H_0 = 70$  km/s/Mpc.

## 3.2 Methods

### 3.2.1 Galaxy cluster selection

For the purpose of our study, we select three relaxed cool-core clusters with different masses and temperatures (A262, A1795 and A2029). We chose these clusters to estimate the effect of the cluster emission on its surrounding medium for a range of cluster parameters. We summarize the main properties of these clusters as reported by Vikhlinin et al. (2006) in Table 3.1: redshift  $z$ , radius  $r_{500}$ <sup>1</sup> and observational average temperature  $T_{\text{spec}}$ , which is obtained from the single-temperature fit to the cluster spectrum (without the central 70 kpc region).

### 3.2.2 Density and temperature profiles

Density and temperature profiles for the galaxy cluster sample used in our study are taken from Vikhlinin et al. (2006). The emission measure profile  $n_p n_e(r)$  follows

---

<sup>1</sup> $r_{500}$  denotes the radius of a sphere within which the mean overdensity is 500 times the critical density of the Universe.

$$n_p n_e(r) = n_0^2 \frac{(r/r_c)^{-\alpha}}{(1 + r^2/r_c^2)^{3\beta-\alpha/2}} \frac{1}{(1 + r^\gamma/r_s^\gamma)^{\epsilon/\gamma}} + \frac{n_{02}^2}{(1 + r^2/r_{c2}^2)^{3\beta_2}}, \quad (3.1)$$

where  $n_p$  and  $n_e$  are the proton and electron number density, respectively. Parameters  $n_0$ ,  $r_c$ ,  $r_s$ ,  $\alpha$ ,  $\beta$ ,  $\epsilon$ ,  $n_{02}$ ,  $r_{c2}$  and  $\beta_2$  are taken from Table 2 in Vikhlinin et al. (2006) and  $\gamma = 3$ .

The temperature profile  $T_{3D}(r)$  is expressed as a product of  $t_{\text{cool}}(r)$  and  $t(r)$

$$T_{3D}(r) = T_0 \times t_{\text{cool}}(r) \times t(r); \quad (3.2)$$

where

$$t_{\text{cool}}(r) = \frac{\left(\frac{r}{r_{\text{cool}}}\right)^{a_{\text{cool}}} + \frac{T_{\text{min}}}{T_0}}{\left(\frac{r}{r_{\text{cool}}}\right)^{a_{\text{cool}}} + 1}, \quad (3.3)$$

$$t(r) = \frac{(r/r_t)^{-a}}{\left[1 + \left(\frac{r}{r_t}\right)^{b\gamma^{c/b}}\right]}.$$

Parameters  $T_0$ ,  $r_t$ ,  $a$ ,  $b$ ,  $c$ ,  $T_{\text{min}}$ ,  $r_{\text{cool}}$  and  $a_{\text{cool}}$  for individual clusters are taken from Table 3 of Vikhlinin et al. (2006). Both the emission measure profile and the temperature profile as defined by equations (3.1) and (3.2), respectively, are three-dimensional.

### 3.2.3 SPEX

In this study we use the SPEctral X-ray and EUV (SPEX) software package (Kaastra et al. 1996; Kaastra et al. 2018, 2020) v. 3.06<sup>2</sup> which is used for modelling and analysis of high-resolution X-ray spectra. With its own atomic database SPEXACT (The SPEX Atomic Code & Tables) it includes around  $4.2 \times 10^6$  lines from 30 different chemical elements (H to Zn). More specifically, we use a model for collisional ionisation equilibrium *cie* and the *pion* model for photoionisation equilibrium (PIE) (described in Mehdipour et al. 2016, for the most recent updates see Štofanová et al. 2021). Unless stated otherwise, we use the protosolar abundances by Lodders et al. (2009) and assume that the ICM has solar metallicities<sup>3</sup>.

### 3.2.4 Total photon flux seen by an absorbing particle

To calculate spectra of selected clusters, we treat them as extended sources. The clusters are divided into radial bins while setting the outermost radius to  $r_{500}$  (we checked that the contribution to the cluster flux from  $r_{500} < r < r_{200}$  is small in comparison with  $r < r_{500}$ ). For the integration we use the QUAD function from the SciPy library (Virtanen et al. 2020), where the number of shells is set using an adaptive algorithm<sup>4</sup>. For each shell at distance  $r$  we calculate the density and temperature following equations 3.1 and 3.2, respectively. Knowing the temperature of each shell we simulate the spectrum of the shell with the collisional ionisation equilibrium (CIE) model in SPEX. The normalization in SPEX

<sup>2</sup>For the most recent version see <https://spex-xray.github.io/spex-help/changelog.html>

<sup>3</sup>In practice, the contribution from line emission is subdominant to the bremsstrahlung continuum for the sources we study in this paper (hot and massive galaxy clusters, for which most of the emission comes from cluster cores).

<sup>4</sup>This algorithm sets by default the upper bound of the number of subintervals in each integration step to 50. The algorithm is described in detail at <https://docs.scipy.org/doc/scipy/reference/generated/scipy.integrate.quad.html>. We checked the integration for higher as well as lower number of subintervals and the change in comparison with the default number of 50 subintervals is negligible (relative differences of order of  $10^{-4}$  and lower for the comparison between 50 and 10 subintervals).

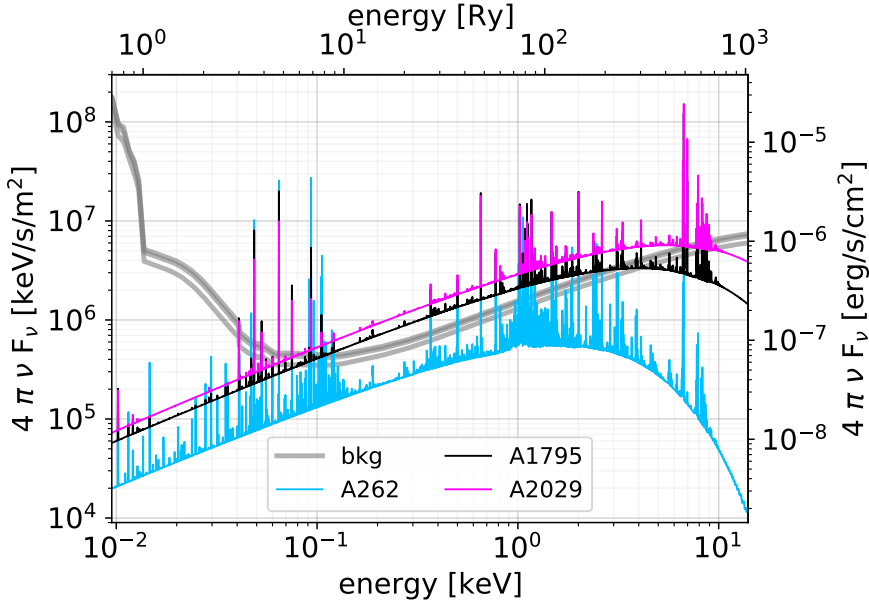


**Figure 3.1:** Spectra of the intra-cluster media of A262 (blue), A1795 (black) and A2029 (pink) and the corresponding cosmic UV/X-ray background at the cluster redshift (grey) as calculated by Faucher-Giguère (2020). We plot spectra for all clusters at a distance of  $2 \times r_{500}$ . The galaxy cluster spectra are treated as extended sources and their spectrum is a result of summation of CIE models of different temperatures (see the main text for more details).

is defined as the emission measure  $EM = n_e n_H V$ , where  $V$  is the volume of the CIE source. Each CIE model is then renormalized by  $n_p n_e$  following equation (3.1).

We estimate the photon flux seen by any absorbing particle for a set of distances  $R_{\text{abs}}$  between  $r_{500}$  and 13 Mpc (for distances greater than 13 Mpc, cluster emission is negligible in comparison with the cosmic UV/X-ray background). The photon flux contribution of the infinitesimally small cluster shell (with a thickness  $dr$ ) to the total photon flux can be written as the surface integral:

$$\frac{dF_{\text{shell}}^{\text{ph}}}{dr} = \iint \frac{\varepsilon_r}{4\pi (\mathbf{R}_{\text{abs}} - \mathbf{r})^2} r^2 \sin \theta d\theta d\varphi, \quad (3.4)$$

where  $\mathbf{r}$  is a vector from the cluster centre to the cluster shell and  $\mathbf{R}_{\text{abs}}$  is the vector from the centre of the cluster to the absorbing particle.  $\varepsilon_r$  is the photon specific emissivity at given  $r$ . If we rewrite equation (3.4) by defining  $L_{\text{shell}} = \varepsilon_r 4\pi r^2 dr$ , the integral has an analytic solution given by

$$F_{\text{shell}}^{\text{ph}} = \frac{1}{8\pi r R_{\text{abs}}} L_{\text{shell}}(r) \ln \left( \frac{R_{\text{abs}} + r}{R_{\text{abs}} - r} \right), \quad (3.5)$$

which holds for  $R_{\text{abs}} > r$ . The total photon flux seen by an absorbing particle placed at distance  $R_{\text{abs}}$  from the galaxy cluster center is then the integral of equation 3.5 over radius  $r$  from zero to  $r_{500}$ .

The spectra of individual clusters are shown in Fig. 3.1 for A262 (blue), A1795 (black) and A2029 (magenta) at a distance of  $2 \times r_{500}$ . To account for the effect of photoionisation by unresolved background sources, we add the cosmic UV/X-ray background to the spectrum of the cluster. We use the model presented by Faucher-Giguère (2020) (hereafter referred to as *bkg*). For the redshifts of the cluster sample presented in this paper, the background does not differ much. Therefore, we plot all three profiles for the background in Fig. 3.1 in grey. The final spectrum that we use as an ionising background in our calculations is then the sum of the cluster spectrum and the cosmic UV/X-ray background.



### 3.2.5 Photoionisation model

To model the effect of the galaxy cluster emission on the absorbing medium in its vicinity, we assume the medium is in ionisation equilibrium, accounting for collisional ionisation and photo-ionisation. We describe this plasma with the photoionisation model *pion*.

In photoionised plasmas it is common to define the ionisation parameter  $\xi$  (Tarter et al. 1969; Krolik et al. 1981) as

$$\xi \equiv \frac{L_{1-1000 \text{ Ry}}}{n_{\text{H}} R_{\text{abs}}^2}, \quad (3.6)$$

where the ionising source is described by the luminosity  $L_{1-1000 \text{ Ry}}$  over the energy band 1–1000 Rydbergs ( $\approx 1.36 \times 10^{-2}$ –13.6 keV),  $n_{\text{H}}$  is the hydrogen number density of a photoionised plasma and  $R_{\text{abs}}$  is the distance of the photoionised plasma to the source of ionisation.

It is common to tabulate ionisation fractions as a function of temperature and the ionisation parameter  $\xi$ . However, in the model that we are describing in this paper, this does not suffice. The reason is that the shape of the spectrum changes with the distance, because the relative contributions of different cluster shells and the relative contribution of the background all depend on the distance. This means that the ionisation balance can no longer be described solely as a function of  $\xi$  and temperature, but it needs to be described as a function of  $n_{\text{H}}$ ,  $R_{\text{abs}}$  and temperature.

To account for this effect, we calculate  $\xi$  based on a prescribed array of densities  $n_{\text{H}}$  and distances  $R_{\text{abs}}$  while taking into account the "correct" shape of the spectrum for each of these distances as described in Sec. 3.2.4. For that we select 30 points for  $n_{\text{H}}$  and 30 points for  $R_{\text{abs}}$  which are evenly distributed on a logarithmic scale. Densities  $n_{\text{H}}$  range from  $10^{-6} \text{ cm}^{-3}$  to  $10^{-1} \text{ cm}^{-3}$  and  $R_{\text{abs}}$  goes from  $r_{500}$  to approximately 13 Mpc.

In this paper, we use the *pion* model in its temperature mode, which allows us to assume a range of temperatures for the photoionised plasma. This, however, means that instead of solving the ionisation balance and the energy balance equations simultaneously, we only solve the ionisation balance equation. The consequence of this is that although we assume ionisation equilibrium, the plasma is allowed to be out of thermal equilibrium and the equilibrium temperature is only one of the temperatures in the range of the temperatures we used in our studies. This is reasonable for the gas we are probing, since this gas is shock-heated and tends to be out of thermal equilibrium because of its long cooling times. For our studies, we select 15 different temperatures in the range  $10^{-3}$ –1 keV ( $\sim 10^4$ – $10^7$  K) evenly distributed on a logarithmic scale.

## 3.3 Results

To demonstrate the effect of the additional source of photoionisation other than the cosmic UV and X-ray background, in subsection 3.3.1 we focus on the case of the cluster A2029. This cluster has the highest luminosity and alters the ionisation balance the most out of all selected clusters. In subsection 3.3.2 we show the comparison of A2029 to the less massive and less hot clusters A1795 and A262.

While we calculated the effect of the cluster emission for the entire grid of electron density, temperature, and  $R_{\text{abs}}$  as described in Section 3.2.5, for illustration purposes we present here our results for a limited, representative subset of these parameters.

### 3.3.1 A2029

#### 3.3.1.1 The effect of the cluster emission on the total photoionisation and ionisation rates

The top panel of Fig. 3.2 shows the total ionisation rate for the background spectral energy distribution (SED) in comparison to that for the A2029+*bkg* SED as a function of temperature. The total ionisation rates are shown for the example of a hydrogen number density of  $2.4 \times 10^{-5} \text{ cm}^{-3}$  at a distance  $2 \times r_{500}$  of the photoionised gas from the galaxy cluster centre. The bottom panel of Fig. 3.2 shows the ratio of

solid and dash-dotted lines in the top panel but for the example set of X-ray and UV ions: C IV, C V, C VI, N V, N VII, O VI, O VII, O VIII, Ne VIII, Ne IX and Fe XVII. We note that the total ionisation and photoionisation rates are defined as number of ionisations/photoionisations per second per ion.

We can see from the plot that for low temperatures (below 20 eV for O VI and below 90 eV for O VII) photoionisation is the dominant ionisation process. The addition of the cluster emission increases both the ionisation and the photoionisation rate. However, above a specific ion-dependent temperature, the plasma starts to be dominated by collisions with free electrons and the contribution of the cluster emission to the total ionisation rate decreases. At high temperatures, the plasma is in its CIE limit and the addition of the cluster emission does not have any effect on the total ionisation rate. The total photoionisation rate does not change as a function of  $kT$ , but it increases by a factor of few if A2029 is added to the background spectrum (e.g. by a factor of 2.8 for O VI and a factor of 2.9 for O VII). Since the WHIM gas may not always reach temperatures sufficiently high to be fully in CIE, taking into account the photoionisation from the galaxy cluster is important, mainly at lower gas temperatures, and should not be neglected.

To study the behaviour with the hydrogen number density, we compare plasmas close to the temperature of the CIE temperature peak ( $kT \approx 0.2$  keV) of O VII, and approximately 10 times lower than that ( $kT \approx 0.02$  keV). The total photoionisation rate does not change either with density, or with temperature (the photoionisation cross-section is a constant with temperature and density), it only changes with the distance to the cluster.

The total ionization rates, plotted in Fig. 3.3, increase with density because of the increasing contribution from collisional ionisation, however, the details again depend on the temperature and the ion we study. As we see in the top panel of Fig. 3.3, at temperature 0.02 keV the total ionisation rate of O VI is higher for A2029+*bkg* in comparison with the background for densities  $n_H < 10^{-3} \text{ cm}^{-3}$ . As the density increases, the curves for A2029+*bkg* and *bkg*-only converge to the same value. However, for O VII, the temperature is too low for collisional ionisation to contribute and all the ionisations come from photoionisation, which in this case is the same as when we described the behaviour of the photoionisation rate. For the higher temperature of  $\approx 0.2$  keV (bottom panel of Fig. 3.3), the addition of the cluster emission can generally be neglected.

In equation (3.6) we defined the ionisation parameter  $\xi$ . As already mentioned in Sec. 3.2.5, it often suffices to parametrize the ionisation balance with this ionisation parameter and the temperature. However, in the model where we include the light from the cluster as well as the ionising background, the ionisation balance can no longer be parametrized solely with  $\xi$  and temperature  $T$ , but needs to be expressed as a function of  $(n_H, R_{\text{abs}}, T)$ . We demonstrate this behaviour in Fig. 3.4, where we plot ion fractions of O VI as a function of the ionisation parameter  $\xi$  for all  $n_H$  and  $R_{\text{abs}}$  values we used for the calculations and for two different temperatures. As Fig. 3.4 clearly shows, at a fixed value of  $\xi$ , many values of the ion fractions of O VI are possible. The spread of possible values then depends on the density  $n_H$  of the ionising plasma and the distance  $R_{\text{abs}}$  from the ionisation source as well as its temperature  $kT$ .

### 3.3.1.2 The effect of the additional cluster emission on the ionisation balance

In Figures 3.5 and 3.6 we show how ion fractions of different ions (C IV, C V, C VI, N VII, Ne VIII, Ne IX, O VI, O VII, O VIII, Fe XVII) change as a function of temperature and the distance from the ionisation source (A2029+*bkg*) and compare the results with the ion fractions calculated for the case when the ionisation source is only the UV/X-ray background (*bkg*, green solid line). We plot these ion fractions for density  $n_H = 2.4 \times 10^{-5} \text{ cm}^{-3}$ . For each distance in Figures 3.5 and 3.6, Table 3.2 lists a value of the ionisation parameter  $\xi$  as well as the dimensionless ionisation parameter for hydrogen  $U$ , defined as the ratio of the ionising photon flux (in photons per unit area per unit time) to  $cn_H$ , where  $c$  is the speed of light and  $n_H$  is the total hydrogen number density (Davidson & Netzer 1979). In SPEX this parameter is calculated from the SED and the ionisation parameter  $\xi$ .

We can see that depending on temperature, the green line representing the results of the background SED (without the contribution of the cluster) forms an upper or lower boundary for the ion fractions. Other lines with different colours represent the ion fractions for the A2029+*bkg* SED for

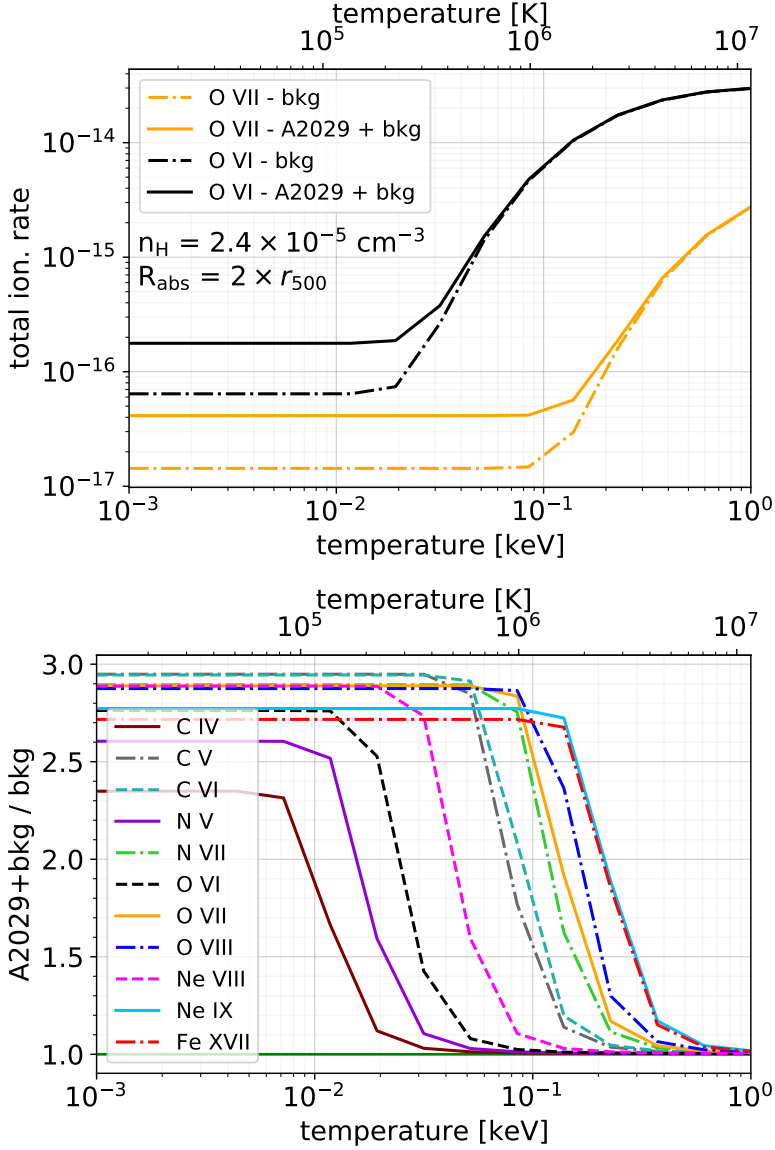


**Figure 3.2:** *Top panel:* The total ionisation rate (number of ionisations per second per ion) plotted as a function of photoionised plasma temperature for O VI and O VII. The dashed-dotted lines represent the total ionisation rate for the Faucher-Giguère (2020) cosmic background at the redshift of cluster A2029 ( $z = 0.0779$ ). The solid lines represent the total ionisation rate if the SED of A2029 plus the Faucher-Giguère (2020) background is taken into account. The distance of the photoionised gas from the cluster center is  $2 \times r_{500}$  and the hydrogen number density is set to  $2.4 \times 10^{-5} \text{ cm}^{-3}$ . *Bottom panel:* ratio of the total ionisation rate for A2029+bkg (solid lines in the top panel) and only the background bkg (dash-dotted lines in the top panel) for a representative set of UV and X-ray ions.

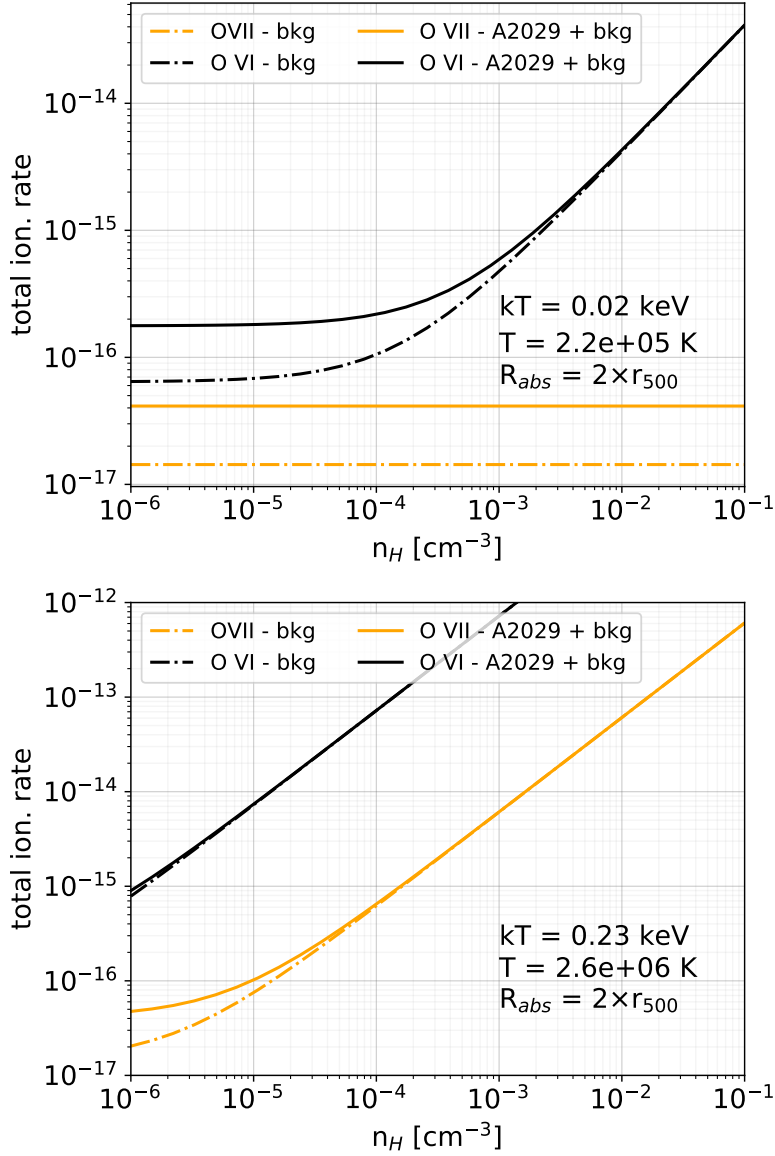


**Figure 3.3:** The total ionisation rate (number of ionisations per second per ion) plotted as a function of hydrogen number density for O VI and O VII. The dashed-dotted lines represent the total ionisation rate for the Faucher-Giguère (2020) cosmic background at the redshift of cluster A2029 ( $z = 0.0779$ ). The solid lines represent the total ionisation rate if the SED of A2029 plus the Faucher-Giguère (2020) background is taken into account. The distance of the photoionised gas from the cluster center is  $2 \times r_{500}$ . In the top panel we show plasma with temperature 0.02 keV (close to the CIE peak temperature of O VI) and in the bottom panel we show plasma with temperature 0.23 keV (close to the CIE peak temperature of O VII).

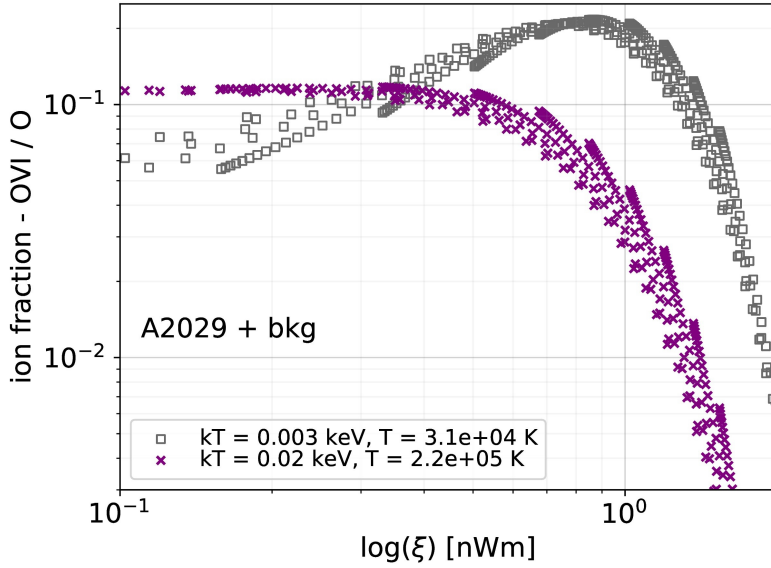


**Figure 3.4:** Ion fraction of O VI as a function of the ionisation parameter  $\xi$  for two chosen temperatures:  $2.2 \times 10^5$  K (CIE peak temperature) and  $3.1 \times 10^4$  K for a subset of distances  $R_{\text{abs}}$  and densities  $n_{\text{H}}$  selected in our studies. The figure illustrates how multiple ion fraction values are possible for a fixed value of  $\xi$  as a consequence of including photoionisation by the SED of A2029+bkg.

$R_{\text{abs}}$ [Mpc]	$\log(\xi)$ [ $10^{-9}$ Wm]	$U$ [ $\times 10^{-2}$ ]
$r_{500}$	0.87	4.20
1.7	0.70	3.59
2.2	0.56	3.22
2.7	0.45	3.00
3.5	0.36	2.86
4.4	0.29	2.77
5.5	0.24	2.72
bkg	0.14	2.63

**Table 3.2:** Distance  $R_{\text{abs}}$ , ionisation parameter  $\xi$ , which is defined in equation (3.6), and ionisation parameter for hydrogen  $U$  (defined in Sec. 3.3.1.2).

different distances from the cluster centre. In grey we show the distances that are smaller than  $r_{200}$  of A2029<sup>5</sup>. The temperature at which the background SED fractions transition from a lower to an upper limit is different for different ions. Depending on the temperature we also see that for some ions the differences between the A2029+*bkg* and *bkg* can exceed an order of magnitude (see e.g. O VII, O VIII).

The ion fractions and the effect of the additional emission from the cluster photons also depend on the density of the plasma as well as the distance from the cluster. Therefore we plot the ion fractions as a function of the distance to the cluster, colour coded by the hydrogen number density in Fig. 3.7, and choose O VI and O VII ions as examples. In the collisional ionisation equilibrium (dashed black line), the ion fractions depend only on temperature and do not change with distance, nor density of the gas.

Fig. 3.7 shows the ion fractions of O VI and O VII for two different temperatures: the peak temperature in CIE (left panels), and a temperature 10 times lower (right panels). Coloured solid lines represent the ion fractions of O VI and O VII for A2029+*bkg*. All the lines asymptote to the ion fractions for the UV/X-ray background. In this plot, the background would be represented by horizontal lines, where the value would be a constant close to the values where the solid lines flatten towards larger distances.

One can, however, argue that gas at densities as low as  $10^{-6} \text{ cm}^{-3}$  is unlikely to exist at a distance of  $r_{500}$  from the cluster centre. Therefore, we calculate how the hydrogen number density is expected to change as a function of distance from the cluster using a theoretical curve from Walker et al. (2013) (their equation (20) without scaling factors). This curve can be expressed as

$$n_H(r) = \frac{1}{1.2} [P(r)]^{3/5} [K(r)]^{-3/5}; \quad (3.7)$$

where  $P(r)$  and  $K(r)$  are the pressure and entropy profiles, respectively. Within  $r_{200}$  the cluster is virialized and we can assume that the universal pressure profile  $P(r)$  follows a generalized Navarro-Frenk-White (GNFW) profile as proposed by Nagai et al. (2007) (in this paper we use parameters taken from Planck Collaboration et al. 2013) and that the entropy profile  $K(r)$  follows a power-law as described in Pratt et al. (2010). For all distances  $r \leq r_{200}$  we indicate the densities which fall below the theoretical prediction with dotted lines in Fig. 3.7.

We see that depending on the temperature, the ion fractions can differ significantly (by more than a factor of 10) if cluster emission is taken into account. Depending on the plasma properties and the species, the ion fractions can be higher or lower in comparison with the ionisation by the background. For the temperatures close to the CIE peak, the *bkg* model behaves as an upper limit on the ion fractions, however, if we consider a lower temperature, this only holds true for lower densities while for higher densities the background model acts as a lower limit on the ion fractions instead. Fig. 3.7 also shows how the effect of photoionisation by the galaxy cluster emission is stronger for smaller distances from the galaxy cluster and the difference between A2029+*bkg* and only the background decreases towards larger distances. In our calculations, the difference between these two models was negligible for distances larger than 13 Mpc.

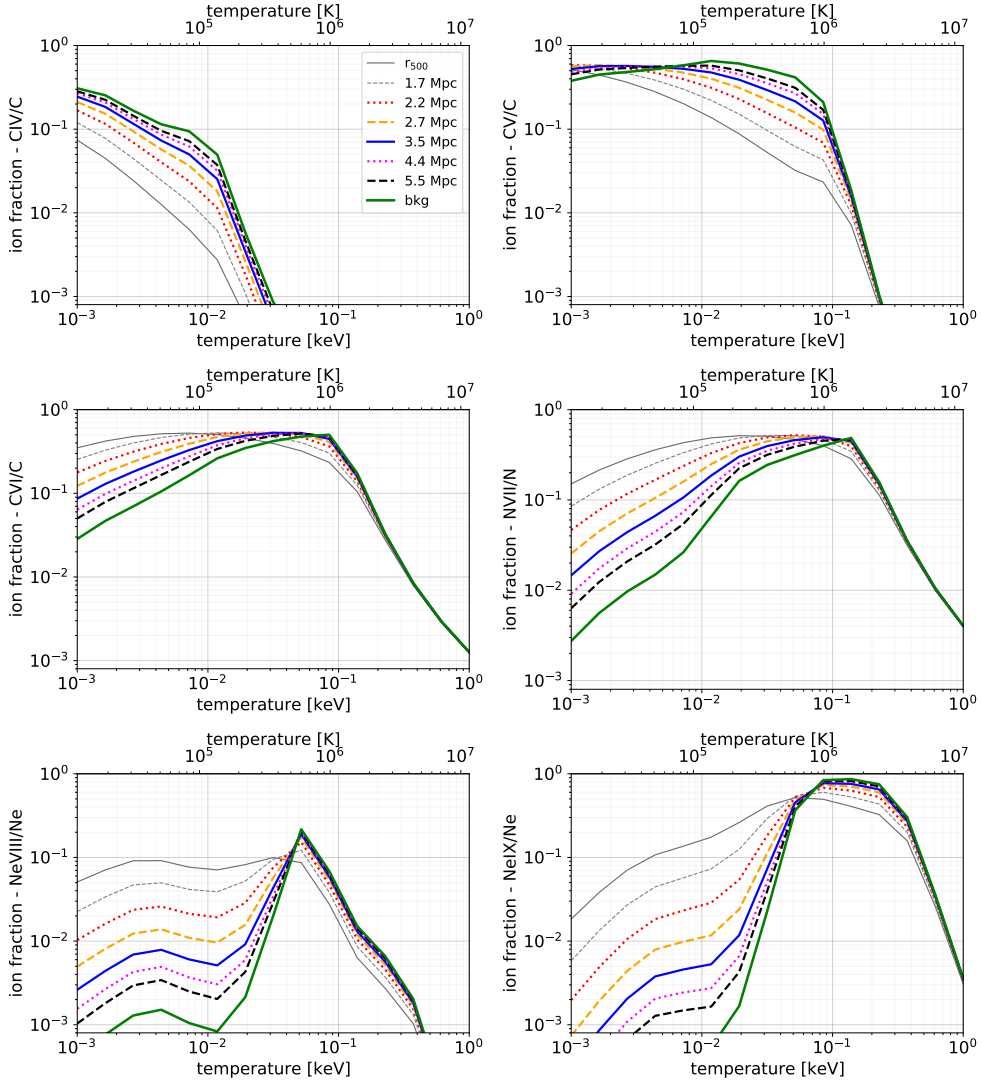
### 3.3.2 Comparison to A262 & A1795

Fig. 3.8 shows the same calculation as in the top panel of Fig. 3.2 for O VI (black lines) and O VII (orange lines) with the addition of the less massive clusters A1795 (dashed line) and A262 (dotted line). We see that less massive galaxy clusters have a smaller impact on the photoionization of nearby WHIM compared to more massive clusters.

More quantitatively, let us focus on the O VII ion fractions as an example. For A2029, the biggest differences between the SED of cluster+*bkg* and *bkg* only are seen for a WHIM temperature  $kT = 0.23 \text{ keV}$  and density  $10^{-6} \text{ cm}^{-3}$  (black line in Fig. 3.7, top left panel). In this case, at  $r_{200}$  the ion fractions for A2029+*bkg* in comparison with *bkg*-only differ by 162%. At the distance of 5 Mpc, this difference drops to 52%, and for distances bigger than 8 Mpc the difference is approximately 17.4%. If we do the same comparison for A262, the differences between ion fractions of O VII drop to 90% (at  $r_{200}$ ), 4.5% (at 5 Mpc) and 3.1% (at 8 Mpc).

---

<sup>5</sup>We use the scaling relation  $r_{200} \approx \frac{3}{2} r_{500}$ , which is approximately 2.04 Mpc for A2029.



**Figure 3.5:** Ion fractions of C IV, C V, C VI, N VII, Ne VIII, Ne IX as a function of plasma temperature for A2029+*bkg* and the cosmic X-ray/UV background by Faucher-Giguère (2020). Different colors represent ion fractions for different distances from the cluster center as indicated in the legend and the green solid line shows the ion fractions for only the background. The hydrogen number density is assumed to be  $2.4 \times 10^{-5} \text{ cm}^{-3}$ . The ionisation parameters  $U$  and  $\xi$  which correspond to distances shown in this plot are listed in Table 3.2.

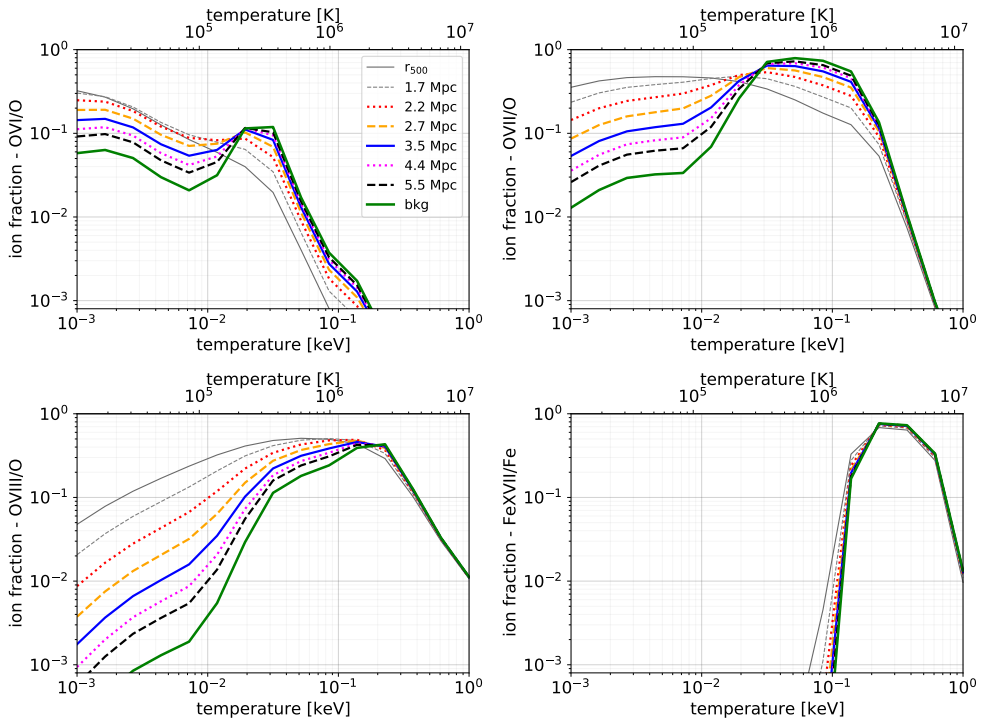


**Figure 3.6:** Same as Fig. 3.5 but for O VI, O VII, O VIII and Fe XVII.



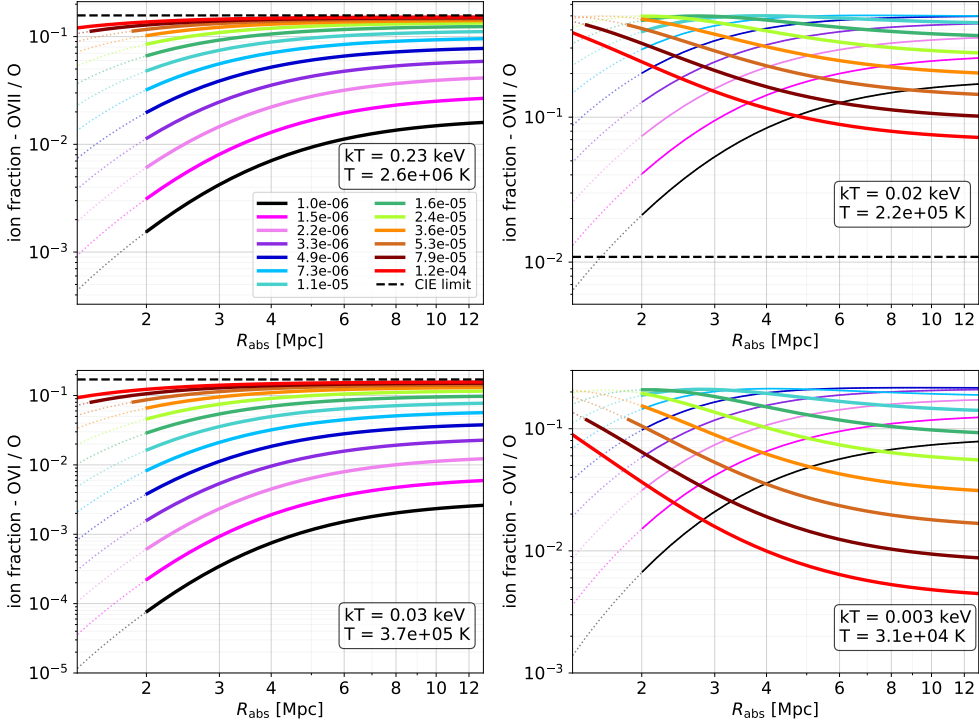


**Figure 3.7:** Ion fractions of O VII (top row) and O VI (bottom row) as a function of distance  $R_{\text{abs}}$  colour coded by the hydrogen number density in units of  $\text{cm}^{-3}$ . Coloured solid lines account for photoionisation by the cluster A2029 and the background, the black dashed line shows O VI and O VII ion fractions in CIE. Left panels show temperatures, for which the O VI and O VII ion fractions peak in CIE, right panels show temperatures 10 times lower. Values that do not satisfy the conditions described in Sec. 3.3.1.2 are shown by dotted lines.

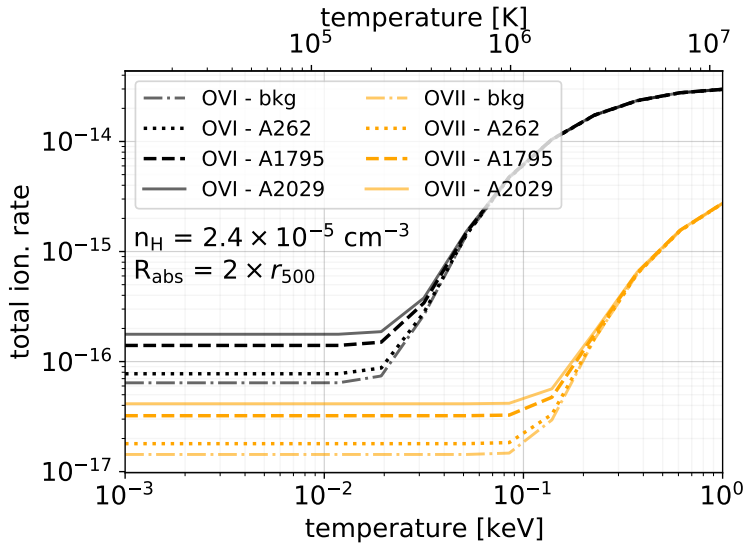


**Figure 3.8:** Same as the top panel of Fig. 3.2 but for ionisation by the background (dash-dotted lines) and by the background plus A2029 (solid lines), A1795+*bkg* (dashed lines) and A262+*bkg* (dotted lines). Black lines show the total ionisation rate for O VI, orange lines show O VII. The distance of the photoionised gas from the cluster center is  $2 \times r_{500}$  and the hydrogen number density is assumed to be  $2.4 \times 10^{-5} \text{ cm}^{-3}$ .

In conclusion, the less massive clusters have lower luminosities, and therefore the change in ionisation parameter  $\xi$  (between *bkg*-only and cluster+*bkg*) is also smaller. They, however, still alter the ionisation balance and cause a similar effect as we described in Sec. 3.3.1. More generalized conclusions are difficult to provide since the ionisation balance is a function of 5 parameters: density and temperature of the photoionised gas, distance of the photoionised gas from the galaxy cluster/group core and the cluster/group mass, and last but not least redshift as well. However, our research suggests that, if WHIM signals are detected in the future in the vicinity of massive clusters of galaxies, the effect of photoionization from the cluster itself should be modelled carefully.

## 3.4 Discussion

As we already mentioned in Sec. 3.2.5, due to the addition of the cluster emission, the ionisation balance can no longer be parametrized by the ionisation parameter  $\xi$  and the temperature of the photoionised plasma, but it needs to be expressed as a function of the density, temperature, *and* distance of the photoionised plasma to the galaxy cluster.

In this section we discuss two applications where this behaviour can be demonstrated: firstly, we calculate the column densities of a large scale structure WHIM filament using a toy model in section 3.4.1 and secondly, we show how the cooling rates are suppressed in section 3.4.2.

### 3.4.1 Impact on the predicted column densities

In this section, we consider a filament and calculate the column densities for two different orientations: a) when the line of sight (LoS) is parallel to the spine of the filament, and b) when LoS is perpendicular to the spine of the filament. In both scenarios we use A2029 as a cluster emission source and assume

the filament has the shape of a cylinder. We describe the problem in cylindrical coordinates, where  $z$  is parallel to the spine of the filament.

In general, we calculate the ionic column density by integrating the ion number density (for a specific orientation) expressed as

$$n_i(r, z) = \frac{Y_i}{Y}(T, n_H, R_{\text{abs}}(r, z)) \times 0.3Z_{\odot} \times \rho(r) \times \frac{X_H}{m_p}, \quad (3.8)$$

where  $Y_i/Y = Y_i/Y(T, n_H, R_{\text{abs}}(r, z))$  are the ion fractions as calculated in Sec. 3.3 (e.g. O VII/O),  $\rho(r)$  is the density of the photoionised plasma,  $m_p$  is the mass of a proton and the hydrogen mass fraction  $X_H$  is set to 0.752. The metallicity is set to  $0.3 Z_{\odot}$ , where  $Z_{\odot}$  is the solar metallicity taken from Lodders et al. (2009) (since we calculate the column density of O, Ne and C, this means that  $Z_{\odot} = [\text{O}/\text{H}]_{\odot} = 10^{8.76}/10^{12}$  for oxygen,  $Z_{\odot} = [\text{Ne}/\text{H}]_{\odot} = 10^{8.05}/10^{12}$  for neon and  $Z_{\odot} = [\text{C}/\text{H}]_{\odot} = 10^{8.39}/10^{12}$  for carbon). For both orientations (parallel and perpendicular), we select two different sets of densities and temperatures according to phase diagrams from the EAGLE cosmological simulations (Schaye et al. 2015) shown in Wijers et al. (2019):  $n_H = 10^{-6} \text{ cm}^{-3}$  and  $T = 10^5 \text{ K}$  and  $n_H = 10^{-5} \text{ cm}^{-3}$  and  $T = 10^{5.5} \text{ K}$ . We also consider a density typical for CGM gas:  $n_H = 10^{-4} \text{ cm}^{-3}$  and  $T = 10^{6.5} \text{ K}$ . For simplicity, we set the temperature and density of the filament to constant values in both chosen orientations.

In the first scenario, the LoS is parallel to the spine of the filament and centered on the galaxy cluster core. We calculate the column density (in a pencil beam) of O VI, O VII, O VIII, C V and Ne VII by integrating the ion number density  $n_i$  as expressed in equation (3.8) along the coordinate  $z$  from  $r_{200}$  to  $r_{200} + 20 \text{ Mpc}$ , where 20 Mpc is our chosen length of the filament. We note that the filament length is still a point of discussion. For example, the maximum filament spine length found in the EAGLE simulation by Tuominen et al. (2021) is  $\approx 35 \text{ Mpc}$ , while Tanimura et al. (2020) reports a range of filament lengths between 30 Mpc up to 100 Mpc, which is not surprising given that the EAGLE simulation box is only 100 Mpc on a side. Malavasi et al. (2020) shows a distribution of filament lengths between 0–100 Mpc obtained from the galaxy distribution using SDSS measurements.

In the second scenario, the LoS is perpendicular to the spine of the filament and located at a distance of  $z = 2 \times r_{500}$  from the center of A2029. In this scenario, we integrate equation (3.8) along the  $r$  coordinate from zero to the Jeans length  $R_{\text{Jeans}}$ , which is an indicative size for overdense absorbers in any given line of sight (Schaye 2001). We set the mean molecular weight to  $\mu = 0.625$ . Columns 2 and 3 in Table 3.3 show the total and ionic column densities for the parallel orientation, columns 4 and 5 show the column densities for the perpendicular orientation. Column 6 shows the column densities for CGM-like properties of the studied gas, equally assuming the depth along the line of sight to be the Jeans length. For each ion we compare the ionic column densities for gas exposed to A2029+*bkg* and to only the background.

We see that in most of the cases, the addition of the cluster emission to the X-ray/UV background reduces the column densities. The biggest changes are seen for densities  $10^{-6} \text{ cm}^{-3}$  and  $10^{-5} \text{ cm}^{-3}$  and can be up to almost factor of 5 (O VI). However, in the case of O VIII and Ne VIII, we see an enhancement of column densities, which can be 15–20% for the parallel orientation, and 60–70% for the perpendicular orientation (for these ions the biggest enhancements are seen for the density  $n_H = 10^{-5} \text{ cm}^{-3}$ ).

The results of our toy model show that the changes in column densities are bigger for the perpendicular orientation, and in the case of parallel orientation, these changes do not exceed 50%. This is, however, dependent on the length of the filament. If we reduce this length to 10 Mpc from 20 Mpc, the difference between A2029+*bkg* and *bkg* is almost twice as large.

The detection of the effect reported in our studies can be challenging with current X-ray missions, however, not impossible. The column densities, currently reported in the literature are approximately of the order of  $10^{15} \text{ cm}^{-2}$ , more specifically,  $N_{\text{O VII}} = (1.4 \pm 0.4) \times 10^{15} \text{ cm}^{-2}$  (Kovács et al. 2019);  $N_{\text{O VIII}} \sim 9.5 \times 10^{15} \text{ cm}^{-2}$  (Fang et al. 2002b); Williams et al. (2007) provides measurements for a set of different ions:  $N_{\text{C V}} \sim 10^{15.22} \text{ cm}^{-2}$ ,  $N_{\text{C VI}} \sim 10^{15.16} \text{ cm}^{-2}$ ,  $N_{\text{O VII}} \sim 10^{16.09} \text{ cm}^{-2}$ ,  $N_{\text{O VIII}} \sim 10^{15.80} \text{ cm}^{-2}$ ,  $N_{\text{Ne IX}} \sim 10^{15.83} \text{ cm}^{-2}$ ,  $N_{\text{N VI}} < 10^{15.39} \text{ cm}^{-2}$ ,  $N_{\text{N VII}} < 10^{15.39} \text{ cm}^{-2}$ , and  $N_{\text{O V}} \sim (10^{13.59} - 10^{14.06}) \text{ cm}^{-2}$ . Ahoranta et al. (2020) report column densities of Ne IX and O VIII to be  $N_{\text{Ne IX}} \sim 10^{15.4} \text{ cm}^{-2}$  and  $N_{\text{O VIII}} \sim 10^{15.5} \text{ cm}^{-2}$ , respectively. All of these measurements probe WHIM in absorption against bright

A2029	parallel orientation		perpendicular orientation		CGM
$n_{\text{H}}$ [ $\text{cm}^{-3}$ ]	$10^{-6}$	$10^{-5}$	$10^{-6}$	$10^{-5}$	$10^{-4}$
$T$ [K]	$10^5$	$10^{5.5}$	$10^5$	$10^{5.5}$	$10^{6.5}$
$kT$ [keV]	0.009	0.03	0.009	0.03	0.27
$R_{\text{Jeans}}$ [Mpc]	3.34	1.88	3.34	1.88	1.88
$N_{\text{H}}$ [ $\text{cm}^{-2}$ ]	$6.17 \times 10^{19}$	$6.17 \times 10^{20}$	$1.03 \times 10^{19}$	$5.79 \times 10^{19}$	$5.79 \times 10^{20}$
$N_{\text{O}}$ [ $\text{cm}^{-2}$ ]	$1.07 \times 10^{16}$	$1.07 \times 10^{17}$	$1.78 \times 10^{15}$	$1.00 \times 10^{16}$	$1.00 \times 10^{17}$
$N_{\text{C}}$ [ $\text{cm}^{-2}$ ]	$4.54 \times 10^{15}$	$4.54 \times 10^{16}$	$7.59 \times 10^{14}$	$4.27 \times 10^{15}$	$4.27 \times 10^{16}$
$N_{\text{Ne}}$ [ $\text{cm}^{-2}$ ]	$2.08 \times 10^{15}$	$2.08 \times 10^{16}$	$3.47 \times 10^{14}$	$1.95 \times 10^{15}$	$1.95 \times 10^{16}$
$N_{\text{O VI}}^{\text{A2029+bkg}}$ [ $\text{cm}^{-2}$ ]	$2.33 \times 10^{14}$	$7.64 \times 10^{15}$	<b><math>1.10 \times 10^{13}</math></b>	<b><math>3.42 \times 10^{14}</math></b>	$4.11 \times 10^{13}$
$N_{\text{O VI}}^{\text{bkg}}$ [ $\text{cm}^{-2}$ ]	$2.95 \times 10^{14}$	$8.68 \times 10^{15}$	<b><math>4.93 \times 10^{13}</math></b>	<b><math>8.15 \times 10^{14}</math></b>	$4.24 \times 10^{13}$
$N_{\text{O VII}}^{\text{A2029+bkg}}$ [ $\text{cm}^{-2}$ ]	$3.19 \times 10^{15}$	$6.47 \times 10^{16}$	<b><math>2.75 \times 10^{14}</math></b>	$4.48 \times 10^{15}$	$1.45 \times 10^{16}$
$N_{\text{O VII}}^{\text{bkg}}$ [ $\text{cm}^{-2}$ ]	$3.67 \times 10^{15}$	$6.85 \times 10^{16}$	<b><math>6.13 \times 10^{14}</math></b>	$6.43 \times 10^{15}$	$1.52 \times 10^{16}$
$N_{\text{O VIII}}^{\text{A2029+bkg}}$ [ $\text{cm}^{-2}$ ]	$5.02 \times 10^{15}$	$2.81 \times 10^{16}$	$8.44 \times 10^{14}$	$4.18 \times 10^{15}$	$4.44 \times 10^{16}$
$N_{\text{O VIII}}^{\text{bkg}}$ [ $\text{cm}^{-2}$ ]	$4.92 \times 10^{15}$	$2.41 \times 10^{16}$	$8.22 \times 10^{14}$	$2.26 \times 10^{15}$	$4.53 \times 10^{16}$
$N_{\text{C V}}^{\text{A2029+bkg}}$ [ $\text{cm}^{-2}$ ]	$2.17 \times 10^{14}$	$1.13 \times 10^{16}$	<b><math>1.53 \times 10^{13}</math></b>	<b><math>0.43 \times 10^{15}</math></b>	$4.50 \times 10^{13}$
$N_{\text{C V}}^{\text{bkg}}$ [ $\text{cm}^{-2}$ ]	$2.72 \times 10^{14}$	$1.33 \times 10^{16}$	<b><math>4.54 \times 10^{13}</math></b>	<b><math>1.25 \times 10^{15}</math></b>	$4.58 \times 10^{13}$
$N_{\text{Ne VIII}}^{\text{A2029+bkg}}$ [ $\text{cm}^{-2}$ ]	$2.30 \times 10^{14}$	$11.35 \times 10^{14}$	$2.49 \times 10^{13}$	<b><math>1.79 \times 10^{14}</math></b>	$1.37 \times 10^{14}$
$N_{\text{Ne VIII}}^{\text{bkg}}$ [ $\text{cm}^{-2}$ ]	$2.56 \times 10^{14}$	$9.33 \times 10^{14}$	$4.28 \times 10^{13}$	<b><math>0.88 \times 10^{14}</math></b>	$1.44 \times 10^{14}$

**Table 3.3:** Total column densities of hydrogen, oxygen, carbon and neon and ionic column densities of O VI, O VII, O VIII, C V, Ne VIII for a toy model of a cosmic filament oriented parallel (columns 2 and 3) and perpendicular (columns 4 and 5) at a distance of  $2 \times r_{300}$  to the line of sight as described in Sec. 3.4.1 for gas exposed to the SED of the background compared to the SED of A2029+bkg. Column 6 shows the column densities for CGM-like properties of the studied gas, equally assuming the depth along the line of sight to be the Jeans length. For the parallel orientation, the length of the filament is assumed to be 20 Mpc, and for the perpendicular orientation its thickness is the Jeans scale. If the column densities for the background and A2029+bkg differ by more than a factor of two, we highlight them in the bold face.

point-like sources, which would be a suggested method for the detection of the photoionisation of WHIM by galaxy clusters, as reported in this paper. As we can see from Table 3.3, our reported column densities that have the biggest differences between cluster+bkg and bkg are typically of the same order or slightly lower than the column densities currently observed with the X-ray or UV missions. Nicastro et al. (2022) show that the Athena X-IFU will be able to probe absorbing column densities down to  $N_{\text{O VII}} \sim 1.6 \times 10^{15} \text{ cm}^{-2}$ , before problems related to systematic uncertainties on the continuum level become important. A few of the scenarios/geometries listed in our Table 3.3 can be probed with this limiting sensitivity. However, in order to access the typical column densities where the cluster photoionization has the largest effect ( $N_{\text{O VII}} \sim$  a few of  $10^{14} \text{ cm}^{-2}$ , see column 4 of Table 3.3), grating spectrometers with a higher resolving power and which can thus probe lower line equivalent widths robustly, are needed. Missions such as *Arcus* and *Lynx* would therefore be ideal, since their resolving power at 0.5 keV is 2500 and  $> 5000$ , respectively. Let us take as an example a resonant line of O VII at 573.95 eV. Scaling from equations (4) and (13) of Nicastro et al. (2022), for an absorption against a bright Seyfert galaxy with flux of 1 mCrab, it would take *Arcus* approximately 500 ks and *Lynx/XGS* 50 ks to probe column densities of  $N_{\text{O VII}}^{\text{A2029+bkg}} = 2.75 \times 10^{14} \text{ cm}^{-2}$ . A detailed feasibility simulation is deferred to future work.

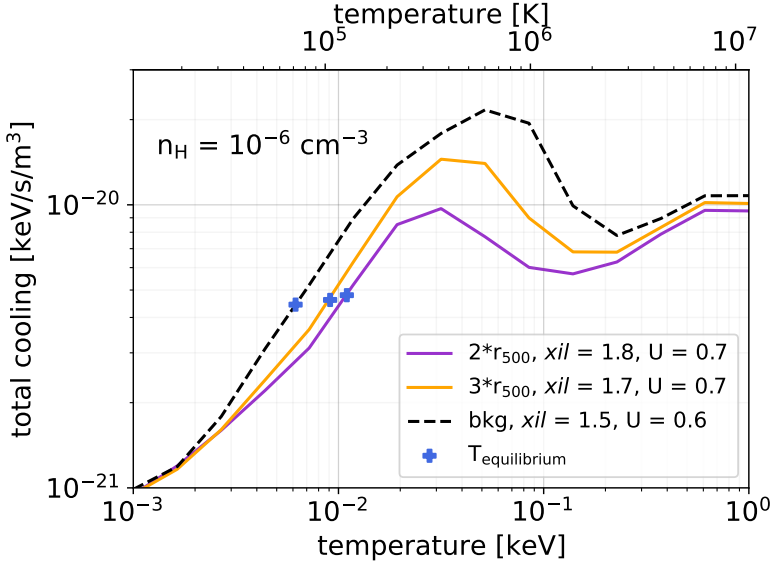


**Figure 3.9:** *Left panel:* total cooling rate for the gas with density  $n_H = 10^{-6} \text{ cm}^{-3}$  at distance  $R_{\text{abs}} = 2 \times r_{500}$  (purple solid line) and  $R_{\text{abs}} = 3 \times r_{500}$  (orange solid line). The dashed black line represents the total cooling rate for the SED of the background. The equilibrium temperature for each curve is marked by the blue plus sign. Parameter  $xil$  is defined as  $xil = \log \xi$  in units of  $10^{-9} \text{ Wm}$ . The metallicity is set to  $0.3 Z_{\odot}$  for carbon up to nickel.

### 3.4.2 Suppression of cooling rates

In the case of CIE, when no external radiation is present, the cooling rates depend only on the temperature of the CIE plasma, but do not depend on its density after normalisation by  $n_e n_H$ . However, in the presence of the cluster, as we have shown in the previous sections, the normalised cooling rates also depend on a distance  $R_{\text{abs}}$  and a density  $n_H$ .

The presence of the photoionising radiation causes a suppression of the cooling rates in comparison with the CIE case (as described in Sec. 3.1). In Fig. 3.9 we show the total cooling in  $\text{keV/s/m}^3$  for the background SED (black dashed line) and for the SED of A2029+bkg for two different distances:  $2 \times r_{500}$  (purple solid line) and  $3 \times r_{500}$  (orange solid line) for density  $n_H = 10^{-6} \text{ cm}^{-3}$  and metallicities of  $0.3 \times Z_{\odot}$ , where similarly to Sec. 3.4.1,  $Z_{\odot}$  is taken from Lodders et al. (2009). As expected, the total cooling rates are suppressed in comparison with only the background, and the closer we get to the cluster, the lower the total cooling rate is. The biggest differences can be seen for temperatures of a few times  $10^{-3} \text{ keV}$  to  $0.2 \text{ keV}$ . The total cooling rates change at most by a factor of 3 for temperatures around  $0.09 \text{ keV}$  and densities around  $10^{-6} \text{ cm}^{-3}$ . When we check individual contributions to the total cooling, the biggest change between background and A2029+bkg is in dielectronic recombination by almost a factor of 7 (at  $kT = 0.05 \text{ keV}$ ) and for collisional excitation by a factor of 6 (at  $kT = 0.09 \text{ keV}$ ).

Even though we see that the cooling rates are suppressed once the cluster emission is taken into account, it is also important to calculate on what time scales such cooling happens and whether this change could be relevant. For that we calculate the cooling time  $t_{\text{cool}}$  for the two most prominent cases from our column density calculations in Sec. 3.4.1: a)  $n_H = 10^{-6} \text{ cm}^{-3}$ ,  $T = 10^5 \text{ K}$ , and b)  $n_H = 10^{-5} \text{ cm}^{-3}$ ,  $T = 10^{5.5} \text{ K}$ . The cooling time  $t_{\text{cool}}$  is expressed as

$$t_{\text{cool}} = \frac{3n_{\text{tot}}k_B T}{2n_{\text{tot}}^2 \Lambda}, \quad (3.9)$$

where  $n_{\text{tot}} = n_i + n_e$  is the total particle number density of gas consisting of the sum of the ion number

density  $n_i$  and the electron number density  $n_e$ , and  $\Lambda$  is the normalized cooling rate in  $\text{keV m}^3 \text{s}^{-1}$ . The denominator in equation (3.9)  $n_{\text{tot}}^2 \Lambda$  then represents the total cooling rate of the gas in  $\text{keV m}^{-3} \text{s}^{-1}$  which we plot along the y-axis of Fig. 3.9.

In the case a) we obtain  $t_{\text{cool}} = 255.5 \text{ Gyr}$ , and in the case b)  $t_{\text{cool}} = 10.1 \text{ Gyr}$ . By comparing  $t_{\text{cool}}$  to the Hubble time ( $\approx 14.4 \text{ Gyr}$ ), we see that the suppression of cooling rates will not be important for the gas with density  $10^{-6} \text{ cm}^{-3}$ , but can potentially affect gas with density of  $10^{-5} \text{ cm}^{-3}$ , when the cooling time is around 10 Gyr. We note, however, that in our calculations we do not include adiabatic cooling due to the Hubble expansion. The addition of cluster emission causes an increase in the thermal equilibrium temperature of approximately 38% ( $3 \times r_{500}$ ) or 56% ( $2 \times r_{500}$ ) for  $n_{\text{H}} = 10^{-6} \text{ cm}^{-3}$  in comparison with the *bkg* model.

If we increase the metallicity to  $Z_{\odot}$  instead, which might be relevant for the CGM, the biggest differences can be seen again for temperatures of a few times  $10^{-3} \text{ keV}$  to  $0.2 \text{ keV}$ . The total cooling rates change by a factor of 5 for temperatures around  $0.09 \text{ keV}$  and densities around  $10^{-6} \text{ cm}^{-3}$ . When we check individual contributions to the total cooling, the biggest change between cooling for the *bkg* model and A2029+*bkg* is in dielectronic recombination and collisional excitation by almost factor of 7 for both processes at the same temperature as for the metallicity  $0.3 \times Z_{\odot}$ . The addition of cluster emission causes an increase in equilibrium temperature of approximately 67% ( $3 \times r_{500}$ ) or 80% ( $2 \times r_{500}$ ) for  $n_{\text{H}} = 10^{-6} \text{ cm}^{-3}$  in comparison with the *bkg* model.

### 3.5 Conclusions

This paper studies the impact of the radiation emitted by the intra-cluster gas in galaxy clusters on their environment. In particular, we show how the addition of photons from galaxy clusters alters the ionisation balance of the surrounding warm-hot intergalactic medium relative to models considering any photoionisation by the cosmic UV and X-ray background.

We model the spectra of the intra-cluster gas from three different cool-core clusters (A262, A1795, and A2029) using the SPEX software package. These spectra, together with the emission from the cosmic UV/X-ray background, are used as ionising sources for the photoionisation model to realistically describe the WHIM. We examine the effect on the ionisation balance for a set of densities and temperatures of the WHIM gas, as well as distances of the WHIM to the galaxy clusters (Sec. 3.3). In Sec. 3.4 we discuss the effect on the column densities for a toy model WHIM filament and calculate how much the cooling rates are suppressed by adding the galaxy cluster to the ionising source.

Due to the changing spectrum of the radiation that the absorbing gas receives at different distances from the galaxy cluster, the ionisation balance can no longer be solely described as a function of the ionisation parameter  $\xi$  and the temperature of the photoionised gas. Instead, the ionisation balance needs to be parametrised as a function of the temperature and density of the photoionised gas, as well as the distance to the galaxy cluster (Fig. 3.4).

We see that more massive clusters alter the ionisation balance of the plasma in their vicinity more than the less massive clusters and cause bigger differences in the total ionisation rate (Fig. 3.8).

Our main results can be summarised as follows:

- For massive, relaxed clusters such as A2029, the addition of the galaxy cluster emission to the UV and X-ray background emission increases the total ionisation rate, especially in the regime of lower densities and temperatures, where photoionisation dominates over collisional ionisation (Figs. 3.2 and 3.3).
- The ion fractions obtained from the photoionisation by the cosmic UV and X-ray background represent either an upper or lower limit (depending on the plasma properties) on the ion fractions calculated as a function of distance using the cluster+*bkg* emission as opposed to *bkg*-only emission (Figs. 3.5 and 3.6).
- The effect of the photoionisation by cluster+*bkg* emission is strongest towards the galaxy cluster outskirts and decreases at larger distances from the cluster (Fig. 3.7). The differences between *bkg* and cluster+*bkg* are negligible for distances larger than 13 Mpc.

- The addition of the galaxy cluster emission affects the column densities of our toy filament. For lines of sight passing close to the cluster outskirts, O VI can be suppressed by a factor of up to 4.5 ( $n_{\text{H}} = 10^{-6} \text{ cm}^{-3}$ ) or a factor of 2.4 ( $n_{\text{H}} = 10^{-5} \text{ cm}^{-3}$ ), O VII by a factor of 2.2 ( $n_{\text{H}} = 10^{-6} \text{ cm}^{-3}$ ), C V by a factor of 3 (for both densities  $10^{-6}$  and  $10^{-5} \text{ cm}^{-3}$ ), and Ne VIII can be boosted by a factor of 2 ( $n_{\text{H}} = 10^{-5} \text{ cm}^{-3}$ ) (Sec. 3.4.1 and Table 3.3).
- The addition of the cluster emission to the model suppresses the total cooling rates at maximum by a factor of 3 for the metallicities  $0.3 \times Z_{\odot}$ , and by a factor of 5 for  $Z_{\odot}$ . In both cases, this change is most significant for temperatures ranging from a few times  $10^{-3} \text{ keV}$  to  $0.2 \text{ keV}$  (for a gas with  $n_{\text{H}} = 10^{-6} \text{ cm}^{-3}$ ).

In conclusion, our work emphasises that the impact of the cluster photoionization on the column densities should be considered when interpreting future detections of the IGM near galaxy clusters in absorption.

**Acknowledgements:** The authors acknowledge the financial support from NOVA, the Netherlands Research School for Astronomy. A.S. is supported by the Women In Science Excel (WISE) programme of the Netherlands Organisation for Scientific Research (NWO), and acknowledges the Kavli IPMU for the continued hospitality. SRON Netherlands Institute for Space Research is supported financially by NWO.

**Data Availability:** The dataset generated and analysed during this study is available in the ZENODO repository (Štofanová et al. 2022).

# 4

## The *clus* model in SPEX: projection and resonant scattering effects on the iron abundance and temperature profiles of galaxy clusters

---

Lýdia Štofanová, Aurora Simionescu, and Jelle S. Kaastra

*submitted to A&A*

---

### ABSTRACT

In this paper we introduce the *clus* model, which has been newly implemented in the X-ray spectral fitting software package SPEX. Based on the 3D radial profiles of the gas density, temperature, metal abundance, turbulent, and inflow/outflow velocities, the *clus* model creates spectra for a chosen projected region on the sky. Additionally, it can also take into account the resonant scattering. We show a few applications of the *clus* model on simulated spectra of the massive elliptical galaxy NGC 4636, and galaxy clusters A383, A2029, A1795, A262, and the Perseus cluster. We quantify the effect of projection, as well as resonant scattering on inferred profiles of the iron abundance and temperature, assuming the resolution similar to Chandra ACIS-S and XRISM Resolve. Our results show that, depending on the mass of the object, as well as the projected distance from its core, neither a single-temperature, double-temperature, nor the Gaussian-shaped differential emission measure models can accurately describe the input emission measure distribution of these massive objects. The largest effect of projection as well as resonant scattering is seen for projected profiles of iron abundance of NGC 4636, where we are able to reproduce the observed iron abundance drop in its inner-most few kiloparsecs. Furthermore, we find that projection effects also influence the best-fit temperature, and the magnitude of this effect varies depending on the underlying hydrodynamical profiles of individual objects. In the core, the projection effects are the largest for A1795 and NGC 4636, while in the outskirts the largest difference between 2D and 3D temperature profiles are for Perseus and A1795, regardless of the instrumental resolution. These findings might potentially have an impact on cross-calibration studies between different instruments, as well as on the precision cosmology.

---



## 4.1 Introduction

Galaxy clusters, galaxy groups, and massive elliptical galaxies appear as diffused sources of light at X-ray wavelengths (Forman et al. 1972; Kellogg et al. 1972). Plasma revealed by this X-ray emission is referred to as the intra-cluster medium (ICM), the intra-group medium (IGrM), or the circum-galactic medium (CGM), and forms a major fraction of the baryonic matter in these objects. It emits mostly through the free-free continuum (thermal bremsstrahlung), and through line emission. The X-ray spectroscopy of these sources can be used to derive many of their properties, as for example their electron temperature, electron density, turbulent velocities, or metal abundances (Böhlinger & Werner 2010).

In the last few decades, the capabilities of X-ray spectroscopy were showcased mainly through CCD and grating spectrometers. The Chandra X-ray Observatory, XMM-Newton, and Suzaku allowed great progress thanks to their improved spectral and spatial resolution, as well as larger effective area and low background. Another milestone that X-ray spectroscopy reached was in 2016, when a micro-calorimeter was launched on board of the Hitomi satellite, which offered an unprecedented spectral resolution of 5 eV at the energy of 6 keV. XRISM, which was launched to its orbit in September 2023, and which carries on the legacy of Hitomi, will continue observing the Universe through high-resolution spectroscopy.

Among many discoveries enabled with Chandra, XMM-Newton, and Suzaku, these observatories provided detailed measurements of the metal distribution in galaxy clusters, galaxy groups, and giant elliptical galaxies. Many of these objects show flattened, or peaky metal (mostly iron) abundance profiles towards their cores, however, X-ray observations of some of them revealed a steep decrease (sometimes by as much as 50% of their global maximum) of metal abundances in the few innermost kiloparsecs (Churazov et al. 2003; Johnstone et al. 2002; Sanders & Fabian 2002, 2007; Million et al. 2010; Rafferty et al. 2013; Mernier et al. 2017).

A few possible scenarios have arisen to explain these central abundance drops, but their origin has not yet been established. For example, metals can be transported to larger distances by the mechanical energy powered by the active galactic nucleus (AGN) feedback (Simionescu et al. 2008, 2009), or by galactic winds (Schindler et al. 2005). Studies by Panagoulia et al. (2013, 2015) suggested instead that iron might get depleted into dust grains in the cores of these massive objects, and therefore it becomes ‘invisible’ in X-rays. If this scenario is true, and if the elements such as iron, silicon, sulphur, magnesium or calcium would show the central abundance drop, the noble gasses such as neon or argon should be indifferent to this process. Such behaviour has been confirmed with Chandra in Lakhchaura et al. (2019), who reported that in the central 10 kpc of the Centaurus galaxy cluster, elements such as Fe, Si, S, Mg, and Ca show an abundance drop, however, no abundance drop was found in Ar. Liu et al. (2019) concluded similar results for 10 cool-core clusters. Contrary to these conclusions, measurements with XMM-Newton suggested that the observed abundance drop in the Centaurus cluster could be partly caused by systematic uncertainties in the atomic data and response matrices, rather than the depletion of iron into dust (Fukushima et al. 2022). Future XRISM observations of metals in the Centaurus galaxy cluster promise to resolve this mystery. Other scenarios originate from incompleteness in the spectral fitting models, as for example projection effects (Sanders & Fabian 2007), modelling of the central brightest cluster galaxy (BCG), or a simplification of the multi-temperature plasma with a single-temperature fitting model, which is also known as the “iron bias” (Buote 2000). Another scenario suggests sedimentation of helium nuclei in the cluster cores, which could potentially raise the helium abundance values above the solar one, and therefore overestimate the continuum, and underestimate all other abundances (Ettori & Fabian 2006). This scenario is, however, impossible to test directly in X-rays, since He does not have transitions in X-ray wavelengths.

An alternative explanation arose from an idea proposed in Gilfanov et al. (1987), which shows that the radial X-ray surface brightness profile of galaxy clusters can be distorted by the scattering of X-ray photons in the resonant lines of highly charged and heavy-metal ions. Some lines in the ICM have optical depths larger than unity, and undergo the resonant scattering (RS) process. If a photon is resonantly scattered, it gets absorbed and almost immediately re-emitted in a different direction.

This causes the flux in the resonant line to drop in the cluster cores, however, in the outskirts the flux of the same resonant line is enhanced. Since the optical depth of each spectral line depends, among other things, also on the turbulent velocity, RS has been used as an independent proxy to measure gas motions and turbulent velocities in the ICM and IGrM, in addition to the gas velocities obtained from the line broadening (see e.g. Churazov et al. 2004; Werner et al. 2009; de Plaa et al. 2012; Zhuravleva et al. 2013; Ogorzalek et al. 2017; Gu et al. 2018). Recent study of Nelson et al. (2023b) showed that RS could be used to observe CGM around galaxies with future X-ray observatories. Additionally, RS has been studied in relation to the abundance drop in the Centaurus galaxy cluster, however, Sanders & Fabian (2006) showed that accounting for RS does not remove the central dip in its abundance profile. In case of the massive elliptical galaxy NGC 4636, Werner et al. (2009) concluded that neglecting the effect of RS underestimates the chemical abundances of iron and oxygen by  $\sim 10 - 20\%$ .

In this paper we present the *clus* model, which has been newly implemented in the SPEX-ray and EUV (SPEX) software package, and which calculates the spectrum and radial profiles for a spherically symmetric approximation of a cluster or a group of galaxies, or even massive elliptical galaxies. In section 4.2 we describe details of this model, our sample selection, and the fitting procedure. In section 4.3 we provide an application of the *clus* model to the Chandra ACIS-S and XRISM Resolve simulated data, and we address whether the *clus* model can help with understanding the origin of the iron abundance drops in the cores of some galaxy clusters, groups, or giant elliptical galaxies. We also discuss the effects on the projected temperature profiles. In section 4.4 we discuss our results and compare our findings to existing literature studies. Lastly, section 4.5 summarizes our main conclusions.

## 4.2 Methods

### 4.2.1 SPEX

We use the SPEX software package (Kaastra et al. 1996; Kaastra et al. 2018, 2020) in version 3.08<sup>1</sup> for modelling and analysis of high-resolution X-ray spectra. With its own atomic database SPEXACT (The SPEX Atomic Code & Tables) it includes around  $4.2 \times 10^6$  lines from 30 different chemical elements (H to Zn). Since the first version of SPEX, many updates have been made, including the implementation of the *clus* model which is described in more details in this paper. Unless stated otherwise, we use the proto-solar abundances by Lodders et al. (2009).

### 4.2.2 The *clus* model

The *clus* model takes as input parametrised 3D radial profiles of the gas density, temperature, metal abundance, turbulent, as well as inflow/outflow velocities. Given these parametrised profiles, the emission in multiple 3D shells, each approximated as a single temperature model in collisional ionisation equilibrium (CIE), is computed and projected onto the sky. The number of shells can be adjusted and is set by a user through the parameters *nr* (number of 3D shells for which the model is evaluated) and *npro* (number of projected annuli). The 3D model is evaluated on a logarithmically spaced grid, which is defined by the inner radius  $r_{\text{in}}$  and outer radius  $r_{\text{out}}$ , where at radius  $r_{\text{out}}$  the density is set to zero. Radius  $r_{\text{in}}$  is taken as 1% of  $r_{500}$ , or if it is smaller, 10% of the smallest of the core radii in the density profile (see Sec. 4.2.2.1). For the innermost shell, the inner boundary  $r_{\text{in}}$  is replaced by zero. The *clus* model can then be run in different modes, where the output is either the spectral energy distribution within a user-defined projected spatial region, or a radial surface brightness profile in a user-requested energy band.

More specifically, the assumed shapes of the underlying 3D profiles used as input to the *clus* model follow:

---

<sup>1</sup>For the most recent version see <https://spex-xray.github.io/spex-help/changelog.html>.

- a two  $\beta$  model for the density distribution (with the additional possibility to introduce a jump or a break in the slope at a given radius, see Sec. 4.2.2.1),
- the same functional form for the temperature profile as that proposed in Vikhlinin et al. (2006), again with a possible additional jump (see Sec. 4.2.2.2),
- the universal abundance profile as defined in Mernier et al. (2017) (see Sec. 4.2.2.3).

The hydrodynamical profiles such as density or temperature are evaluated for the middle radius of each shell using analytical parametrization of the 3D profiles, and it is assumed that these quantities are constant within the shell. Therefore, the emission measure of each shell is simply evaluated as the product of electron and hydrogen density at the central radius of the shell, multiplied by the volume of the shell. In case the user introduces a density discontinuity in the model, the radius of the density discontinuity is also chosen as an additional grid point (if it is close to an existing grid point, that existing grid point is moved to the discontinuity).

The *clus* model takes a linear grid for the projected 2D profiles, which emulates real detectors that are designed with a linear scale. For the 3D profiles, the quantities are evaluated at the shell central radii, while for the 2D projected profiles the quantities are evaluated at sub-shell resolution (typically using 20 points for each shell). Within the shell it is assumed that the emission measure as a function of radius follows a power-law. The power-law slope is determined by comparing the emission measures of the neighbouring shells.

The *clus* model also has two ascii-output options: (a) the output *clus* gives the radius, hydrogen density, temperature, gas pressure, emission measure, turbulent velocity, outflow velocity and relative abundances, and (b) the output *clup* provides the projected radial profile of the number of photons and energy flux, in an energy band which is specified with parameters  $E_{\min}$  and  $E_{\max}$  (given in units of keV). The *clus* model has in total 80 different parameters which are summarized in Table 4.1.

#### 4.2.2.1 Radial density profile

The hydrogen density distribution  $n_H(r)$  is parametrised as the sum of two beta-models (Cavaliere & Fusco-Femiano 1976; Mohr et al. 1999), modified by a possible density jump:

$$n_H(r) = [n_1(r) + n_2(r)] \times f(r) . \quad (4.1)$$

Densities  $n_i(r)$ , where  $i = 1, 2$ , are defined as

$$n_i(r) = \frac{n_{0,i}}{[1 + (r/r_{c,i})^2]^{1.5\beta_i}} , \quad (4.2)$$

where  $n_{0,1}$  and  $n_{0,2}$  are the central densities,  $r_{c,1}$  and  $r_{c,2}$  are the core radii, and  $\beta_1$  and  $\beta_2$  are the slopes of the beta profiles. The optional density jump  $f(r)$  is defined as

$$\begin{aligned} r < r_s : f(r) &= 1 , \\ r > r_s : f(r) &= \Delta_d (r/r_s)^{\gamma_d} , \end{aligned} \quad (4.3)$$

where  $r_s$  is the discontinuity radius and  $\Delta_d$  is the density jump at  $r_s$ . For  $\Delta_d > 1$  the density increases outside  $r_s$  relative to the undisturbed profile, while for  $\Delta_d < 1$  it decreases. Please note that, in the case of no jump (i.e.  $\Delta_d = 1$ ), the term  $f(r)$  is ignored. Further fine-tuning of this thermodynamic discontinuity (which can represent e.g. a shock, or a cold front) can be achieved by changing the power-law parameter  $\gamma_d$ . If  $\gamma_d > 0$  ( $\gamma_d < 0$ ) the values are increasing (decreasing) at large radii, while  $\gamma_d = 0$  means a constant jump.

#### 4.2.2.2 Radial temperature profile

The temperature profile  $T(r)$  can be written as

$$T(r) = T_1(r) \times f_1(r) \times f_2(r) , \quad (4.4)$$

where  $T_1(r)$  is based on Vikhlinin et al. (2006) (Eq. 6), and is re-written to a different but equivalent form following Eq. 10 in Kaastra et al. (2004)

$$\begin{aligned} T_1(r) &= T_c + (T_h - T_c) \frac{(r/r_{ic})^\mu}{1 + (r/r_{ic})^\mu}, \\ f_1(r) &= \frac{(r/r_{to})^{-a}}{[1 + (r/r_{to})^b]^{c/b}}. \end{aligned} \quad (4.5)$$

The central and outer temperatures  $T_c$  and  $T_h$ , respectively, are not the actual temperatures, but the temperatures that would exist without the  $f_1(r)$  and  $f_2(r)$  terms. The temperature jump  $f_2(r)$  is defined as

$$\begin{aligned} r < r_s : f_2(r) &= 1, \\ r > r_s : f_2(r) &= \Delta_t (r/r_s)^{\gamma_t}, \end{aligned} \quad (4.6)$$

where  $\Delta_t$  and  $\gamma_t$  are the temperature jump and the power-law parameter, which are defined similarly to the density jump, and the discontinuity radius  $r_s$  is the same as for the jump in the density profile. We assume that the ion temperature is equal to the electron temperature for each shell.

If one aims to relate the *clus* model temperature parameters to those of Vikhlinin et al. (2006), then

$$T_c = T_{\min}, T_h = T_0, \mu = a_{\text{cool}}, r_{ic} = r_{\text{cool}}, r_{to} = r_t, \quad (4.7)$$

where  $T_{\min}$ ,  $T_0$ ,  $a_{\text{cool}}$ ,  $r_{\text{cool}}$ , and  $r_t$  are parameters from Eq. 4 and Eq. 5 in Vikhlinin et al. (2006).

#### 4.2.2.3 Radial abundance profile

The relative metal abundances from hydrogen to zinc (parameters 01 to 30 in the *clus* model) are given in proto-solar units, where the user can specify which set of abundance tables is used (see the SPEX command *abundance*). By default, the reference element which serves as a scaling atom is hydrogen, but it can be also specified by the user. These abundances can be modified by a multiplicative radial scaling law  $f_{\text{abu}}(r)$ , whose form is a modified version of Eq. 6 taken from Mernier et al. (2017)

$$f_{\text{abu}}(r) = \frac{A}{(1 + r/B)^C} \left[ 1 - D \exp^{-(r/F) \times (1+r/E)} \right] + G, \quad (4.8)$$

where the default values for parameters ( $A = 1.34$ ,  $B = 0.021$ ,  $C = 0.48$ ,  $D = 0.414$ ,  $E = 0.163$ , and  $F = 0.0165$ ) are set to the universal abundance profile values from Mernier et al. (2017). If the abundances are meant to be constant as a function of radius, the user should take care that  $f(r) \equiv 1$  for all radii. This can be achieved for instance by setting  $A = 0$  and  $G = 1$ . The constant term  $G$  was not included in Mernier et al. (2017), but may be useful for some applications. The radial scaling works the same way for all chemical elements (i.e. all elements are assumed to have the same radial profile shape); the abundances themselves can be different. The radial scaling is only done for elements with nuclear charge 3 or more (i.e., lithium and higher). Hydrogen and helium are excluded from the scaling. It is therefore highly recommended to keep the reference atom to its default (hydrogen) for this model.

#### 4.2.2.4 Turbulent velocity and radial motions of plasma

The turbulent velocity  $v_{\text{turb}}$  is defined as

$$v_{\text{turb}}^2(r) = v_a^2 + \frac{v_b |v_b| \times (r/r_v)^2}{1 + (r/r_v)^2}, \quad (4.9)$$

and is equivalent to the root-mean-square velocity  $v_{\text{rms}}$ , which is related to the micro-turbulent velocity  $v_{\text{mic}}$  following a relation

$$v_{\text{mic}} = \sqrt{2} v_{\text{rms}} = \sqrt{2} v_{\text{turb}}. \quad (4.10)$$

The Doppler broadening  $\Delta E_D$  of a line with a rest frame energy  $E_0$  is then expressed as

$$\Delta E_D = \frac{E_0}{c} \sqrt{\left( \frac{2k_B T_{\text{ion}}}{A m_p} + v_{\text{mic}}^2 \right)} \quad (4.11)$$

where  $c$  is the speed of light,  $k_B$  is the Boltzmann constant,  $A$  is the atomic weight,  $m_p$  is the mass of a proton, and  $T_{\text{ion}}$  is the ion temperature. The term  $\sqrt{\frac{2k_B T_{\text{ion}}}{A m_p}}$  represents the thermal broadening.

At the center,  $v_{\text{turb}}$  is given by  $v_{\text{turb}} = v_a$ , at large distances it is given by  $v_{\text{turb}}^2 = v_a^2 + v_b |v_b|$ . Positive values of  $v_b$  mean increasing turbulence for larger radii, while negative values of  $v_b$  mean decreasing turbulence for larger radii. The turbulent velocity as defined in Eq. (4.9) is only the component due to microscopic or macroscopic motions of the gas cells. In addition, the thermal motions of the ion are added in quadrature using the relevant (ion) temperature. Note that for negative values of  $v_b$  with  $v_b < -v_a$ , the turbulent velocity would become imaginary ( $v^2 < 0$ ). To avoid a crash, SPEX cuts these values off to zero, and continues its calculations.

In addition to turbulence, the model allows for systematic radial motion (inflow or outflow), which is defined as

$$v_{\text{rad}}(r) = v_c + \frac{(v_h - v_c) \times (r/r_z)^2}{1 + (r/r_z)^2}, \quad (4.12)$$

where parameter  $v_c$  corresponds to the flow velocity at the core,  $v_h$  is the flow velocity at large distances. Positive values of  $v_{\text{rad}}$  correspond to the inflow, negative values correspond to the outflow. Radii  $r_r$  and  $r_z$  are typical radii where the velocity fields ( $v_{\text{turb}}$ ,  $v_{\text{rad}}$ ) change.

#### 4.2.2.5 Projection of the radial profiles

The *clus* model projects the spectra of all shells onto the sky. Instead of the spectrum for the full cluster, users can also specify calculation of the spectrum within a projected annulus, which is given by the inner ( $r_{\text{min}}$ ) and outer ( $r_{\text{max}}$ ) radii given in units of  $r_{\text{out}}$ . As previously mentioned, at radius  $r_{\text{out}}$  the density is set to zero. Thus, for  $r_{\text{min}} = 0$  and  $r_{\text{max}} = 1$ , the full cluster spectrum is obtained.

If the user wants to calculate the spectrum or profile in a more complex region and not a simple annulus, for instance the projection of a square detector (pixel), the *clus* model provides this option by using the parameter *azim*. For *azim*=0, the full annulus is used, while for *azim*=1, a more complex region can be used. In this latter case, the user must specify the name of an ascii-file through the parameter called *fazi*, which describes the covered azimuthal fraction of the desired region as a function of radius. For a more detailed description of the specific format of this ascii-file, we refer the reader to Sec. 4.1.6.10 of the SPEX manual<sup>2</sup>.

#### 4.2.2.6 Resonance scattering

The resonance scattering (RS) is calculated using Monte Carlo simulations: for the most important spectral lines affected by RS, random photons are drawn per each spectral line. From the 3D emissivity profiles for the relevant lines,  $N \times nr$  random photons are drawn, where  $nr$  is the number of 3D shells (introduced in Sec. 4.2.2) and  $N$  is an integer which can be set by the user. Each of these individual photons are followed. The calculation for the photon stops when it is either absorbed in the continuum, or when it leaves the cluster. Alternatively, it can be absorbed and then (a) re-emitted in a new random direction (the resonance scattering), or (b) it decays to a non-ground level, resulting in two or more photons until the atom reaches the ground state again. Such photons are followed until they are destroyed or they escape. At the end of the calculation, statistics is collected on the history of the photon. Note that the *clus* model assumes that all ions are in their ground state when they absorb a photon. Under the assumption of spherical symmetry, the magnitude of RS is the same throughout each spherical shell.

<sup>2</sup>SPEX manual for *clus* model can be found here: <https://var.sron.nl/SPEX-doc/speex-help-pages/models/clus.html>.

The user can include the calculation of the resonant scattering by setting the parameter *rsca* to unity. There are two available modes for this calculation:

- mode 1: The number of initial photons is distributed according to the emissivity of individual shells. This mode is more suitable for the overall spectrum of the galaxy cluster, and its accuracy is higher in the cluster cores, from where the bulk of the photons is emitted.
- mode 2: There is the same number of photons in each shell, while the final result is weighted with the shell emissivity. This mode is more accurate (in comparison with mode=1) when analyzing radial line profiles of the resonant lines in the outskirts, where the emissivity is small.

The RS calculations include the most relevant 666 transitions for H-like to Na-like ions. We use a simple scaling law  $N_{\text{hydrogen}} = 10^{25} \sqrt{T}$ , where  $N_{\text{hydrogen}}$  is the total hydrogen column density from the core of the cluster to infinity (in units of per square meter), and  $T$  is the temperature (in keV). This matches approximately the Perseus cluster at a temperature of 4 keV. It is based on the simple scaling laws for cluster mass  $M$ , radius  $R$  and density  $\rho$ :

$$\begin{aligned} M &\sim R^3 \rho, & \rho &= \text{constant}, \\ M &\sim T^{1.5}, & N_{\text{hydrogen}} &\sim \rho R. \end{aligned} \tag{4.13}$$

We calculated the optical depths of all ground-state absorption lines in SPEX using the *hot* absorption model for a grid of temperatures  $T$  ranging from 0.25 keV to 16 keV with a step size of a factor of 2 while assuming no turbulence (i.e., the highest possible optical depths) and a column density of 5 times higher than the scaling relation  $N_{\text{hydrogen}} = 10^{25} \sqrt{T}$ . From this list, we selected all lines with energy larger than 0.1 keV, optical depth larger than 0.03, and optical depth larger than 1% of the strongest line of that ion at that temperature. For each resonance line, we only considered the most important decay channels from the excited state (typically stronger than 1% of the total decay rate) in order to limit the number of decay routes to the ground to a manageable number. In practice, the number of decay routes was thus limited to a maximum of 7 (including the main resonance line), and we limited the number of lines to a maximum of 3 per route (ignoring the lowest energy lines in a few cases, which were always at much lower energy than the X-ray band). Transition energies, oscillator strengths and branching ratios were thus obtained from the current atomic database of SPEX. When this database is updated, the same transitions will be used for the resonance scattering, but branching ratios, oscillator strengths and line energies will automatically be adjusted; these quantities are initialised each time upon the first call of the *clus* model.

If the resonant scattering is included in the SPEX *clus* model calculation, the user has an option to output three diagnostic files with information on the resonant lines. These files have an ascii format and are named: *cluslin1*, *cluslin2* and *cluslin3*. In particular, *cluslin1* includes a summary of all spectral lines where resonance scattering is taken into account, and *cluslin2* and *cluslin3* give the projected properties and 3D radial properties of all the lines summarized in *cluslin1*, respectively. For more details about these ascii files, we refer the reader to the SPEX manual.

### 4.2.3 Sample selection and *clus* model simulations

In Table 4.2 we provide a sample of objects that were used in this study. The redshift and  $r_{500}$  values of A383, A2029, A1795 and A262 were taken from Vikhlinin et al. (2006), for the Perseus galaxy cluster from Hitomi Collaboration et al. (2018b), and for the massive elliptical galaxy NGC 4636 from Pinto et al. (2015). We note that this sample is not fully representative of all galaxy clusters, groups nor massive elliptical galaxies, but rather serves as demonstrative example of the capabilities of the *clus* model and its potential applications.

We simulate spectra of these objects using the *clus* model for two different types of X-ray detectors: (a) ACIS-S CCD (charged coupled device) spectrometer on board of the Chandra X-ray observatory, and (b) Resolve micro-calorimeter on board of the recently launched XRISM observatory. We obtain the input parameters for the density and temperature profiles by fitting the functional form defined in sections 4.2.2.1 and 4.2.2.2 to the profiles given in Vikhlinin et al. (2006) for galaxy clusters A383,

Acronym	Variable	Units	Acronym	Variable	Units
r500	$r_{500}$	$1e+22$ m	dfe	D	–
rou	$r_{out}$	$r_{500}$	efe	E	$r_{500}$
nr	Number of 3D shells	–	ffe	F	$r_{500}$
npro	Number of projected annuli	–	gfe	G	–
hd1	$n_{0,1}$	$m^{-3}$	av	$v_a$	km/s
rc1	$r_{c,1}$	$r_{500}$	bv	$v_b$	km/s
bet1	$\beta_1$	–	rv	$r_v$	$r_{500}$
hd2	$n_{0,2}$	$m^{-3}$	zc	$v_c$	km/s
rc2	$r_{c,2}$	$r_{500}$	zh	$v_h$	km/s
bet2	$\beta_2$	–	rz	$r_z$	$r_{500}$
rsh	$r_s$	$r_{500}$	emin	$E_{min}$	keV
dfac	$\Delta_d$	–	emax	$E_{max}$	keV
dgad	$\gamma_d$	–	rmin	$r_{min}$	$r_{out}$
tc	$T_c$	keV	rmax	$r_{max}$	$r_{out}$
th	$T_h$	keV	azim	–	–
rtc	$r_{tc}$	$r_{500}$	fazi	–	–
mu	$\mu$	–	rsca	Resonant scattering	–
rto	$r_{to}$	$r_{500}$	nif0	N	–
at	a	–	rmod	Mode of resonant scattering	–
bt	b	–	out1	Output 1	–
ct	c	–	out2	Output 2	–
tfac	$\Delta_t$	–	out3	Output 3	–
dgat	$\gamma_t$	–	ref	Reference element	–
afe	A	–	01 ... 30	Abundances H to Zn in proto-solar units	–
bfe	B	$r_{500}$	file	Filename for non-thermal electron distribution	–
cfe	C	$r_{500}$			

**Table 4.1:** The complete set of all 80 parameters of the *clus* model. The acronyms of the parameters are their names as used in the SPEX interface and all variables are described in Sec.4.2.2.

Cluster	$z_{\text{cluster}}$	$r_{500}$ [kpc]	$N_{\text{H,TOT}}^{\text{neutral}}$ [ $\text{cm}^{-2}$ ]	1 kpc [']
A383	0.1883	944	$3.88 \times 10^{20}$	0.005
A2029	0.0779	1362	$3.70 \times 10^{20}$	0.011
A1795	0.0622	1235	$1.24 \times 10^{20}$	0.014
Perseus	0.01790	1245	$20.7 \times 10^{20}$	0.046
A262	0.0162	650	$7.15 \times 10^{20}$	0.051
NGC 4636	0.0037	350	$2.07 \times 10^{20}$	0.218

**Table 4.2:** Redshift  $z_{\text{cluster}}$  and  $r_{500}$  of the clusters used in our study. Values of redshift  $z_{\text{cluster}}$  and radius  $r_{500}$  were taken from Vikhlinin et al. (2006) for A383, A2029, A1795 and A262, from Hitomi Collaboration et al. (2018b) for the Perseus cluster, and from Pinto et al. (2015) for NGC 4636.  $N_{\text{H,TOT}}$  is the total hydrogen column density in the direction of the galaxy cluster, which was taken from Willingale et al. (2013)<sup>a</sup>.

**Notes.** <sup>(a)</sup> We used the online tool created by the SWIFT team, which is available here <https://www.swift.ac.uk/analysis/nhtot/>.

A2029, A1795, and A262. For NGC 4636 we use data from Baldi et al. (2009), and for the Perseus cluster we use data from Zhuravleva et al. (2015) corrected for Lodders et al. (2009) proto-solar abundances (for more details see section 5.1 in Hitomi Collaboration et al. 2018b). Fig. 4.1 shows the comparison of density and temperature profiles for these objects. For the abundance profiles of all objects considered in this study we assume a universal abundance profile taken from Mernier et al. (2017). Such a profile does not have an abundance drop in the innermost few kpc.

In all simulations we leave the turbulent velocity at its default value of 100 km/s, and we assume no Poisson noise, which means that the photons are not randomised. This produces correct uncertainties on the parameters, and its advantage lies in the fact that only one simulation is needed, and the result of such simulation can be fully reproducible since the random fluctuations are not taken into account. We also take into account the absorption by our Milky Way (simulated with the *hot* component in SPEX), which is simplified to the absorption by neutral gas only, whose temperature is set to  $1 \times 10^{-6}$  keV. The total hydrogen column densities that we use for the neutral component of the ISM  $N_{\text{H,TOT}}^{\text{neutral}}$  are taken from Willingale et al. (2013) (see Table 4.2). We make two different types of calculations: (a) we neglect the RS effect, and therefore take into account only the projection effects and multi-phase structure of the gas, and (b) we add RS to simulations assuming mode 1 (see Sec. 4.2.2.6). The parameter  $r_{\text{out}}$  is set to  $2 \times r_{500}$ . In summary, the complete model with which all data in this study is simulated, includes three components: redshift component, hot component and the *clus* model. Unless stated otherwise, all other parameters of the *clus* model are set to their default values in SPEX.

#### 4.2.4 Fitting procedure

The gas in galaxy clusters, groups and massive elliptical galaxies is known to be multi-phase, and unless one fits only the high-energy part of the spectra around the Fe-K complex, single-temperature models can not sufficiently describe the temperature structure in these objects (Buote 2000; Kaastra et al. 2004; Simionescu et al. 2009; Sanders 2023). More complex models, which are usually fitted to X-ray spectra, are either a double-temperature model, or the so-called *gdem* model. Some earlier works preferred the *wdem* model instead (Kaastra et al. 2004; Werner et al. 2006; de Plaa et al. 2010). Note that the *clus* model accounts not only for multi-temperature, but also multi-metallicity and multi-velocity structure projected along the LOS. In our results we neglect the multi-velocity structure but we take into account the presence of multiple temperatures and abundances in the 3D profiles of studied clusters.

A single-temperature model (1T) assumes the gas has just one temperature and that it is in CIE, while a double-temperature model (2T) is a superposition of two CIE models with two different tem-



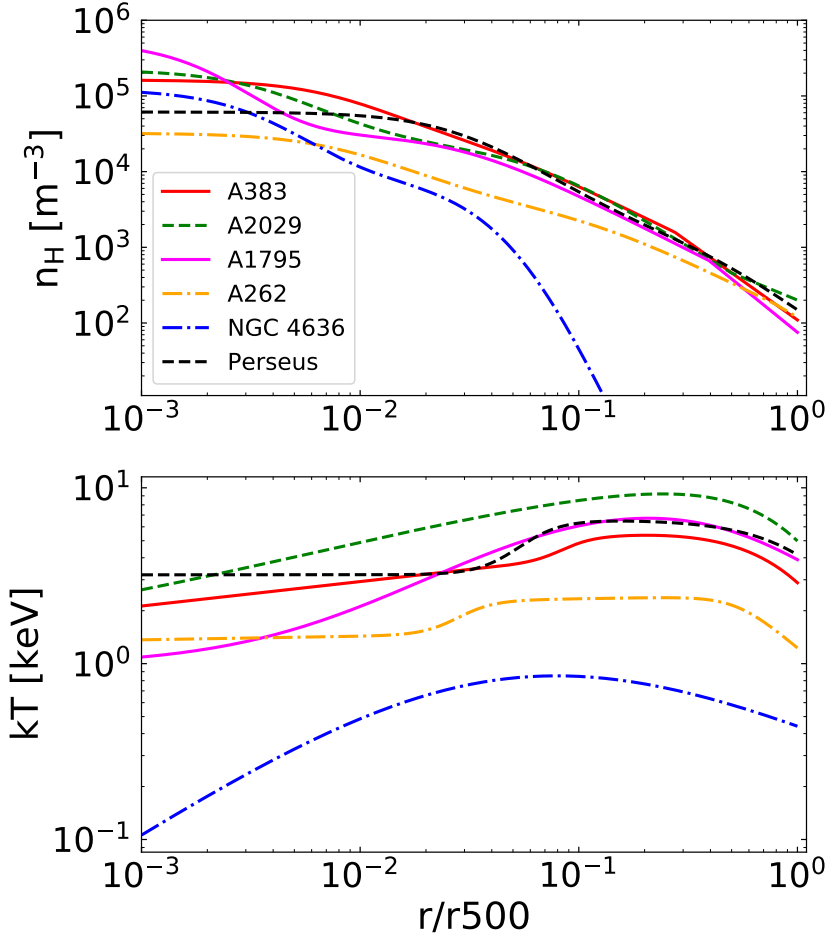


**Figure 4.1:** Input radial profiles of hydrogen density  $n_H$  (top panel) and temperature  $kT$  (bottom panel) for the sample selection from Table 4.2. These profiles are obtained by fitting the functional forms of density and temperature profiles as defined in sections 4.2.2.1 and 4.2.2.2 to the profiles given in Vikhlinin et al. (2006) (for galaxy clusters A383, A2029, A1795, and A262), to data from Baldi et al. (2009) (for NGC 4636), and data from Zhuravleva et al. (2015) (for the Perseus cluster).

peratures. The *gdem* model assumes that the emission measure  $\text{EM}(T)$ <sup>3</sup> as a function of temperature  $T$  follows a Gaussian distribution, and can be described as

$$\frac{d \text{EM}(x)}{dx} = \frac{\text{EM}_0}{\sqrt{2\pi} \sigma_x} \exp\left(-\frac{(x - x_0)^2}{2\sigma_x^2}\right), \quad (4.14)$$

where  $\text{EM}_0$  is the total, integrated emission measure;  $x_0 = \log(k_B T_0)$ , where  $T_0$  is the average temperature of the plasma; and  $\sigma_x$  is the width of the Gaussian distribution, which in this case is in units of  $x = \log(k_B T)$ . To quantify the discrepancies between these three models (1T, 2T, *gdem*) and the *clus* model, we simulate the spectra following Sec. 4.2.3, and fit them with 1T, 2T and *gdem* models (including the redshift and *hot* components). For Chandra ACIS-S we use the 2004 response files, created for the central 100 kpc of A2029 (Chandra observations ID 4977<sup>4</sup>). We choose to use the response files from 2004 observations because the ACIS detectors did not suffer as much from the contamination<sup>5</sup> at low-energies (around and below 1 keV). For XRISM Resolve we use the 2019<sup>6</sup> response files assuming 5 eV spectral resolution. For spectra simulated with Chandra ACIS-S we ignore energies outside the 0.6 – 7 keV energy bins, and for XRISM Resolve we ignore energies outside energy bins between 0.6 – 12 keV while assuming a gate valve open configuration. The data for Chandra ACIS-S CCD are simulated for an exposure time of 500 ks, while the XRISM Resolve micro-calorimeter data are simulated for an exposure time of 200 ks (except for Fig. 4.7, which was simulated with exposure time of 500 ks). For all spectra in these energy ranges we use optimal binning following Kaastra & Bleeker (2016). We evaluate the goodness of the fit by using C-statistics (Cash 1979), which can be summarised as the maximum likelihood estimation in the limit of Poissonian statistics. In SPEX, we use modified C-statistics based on Baker & Cousins (1984), which is described in detail in Kaastra (2017). The fit is considered good, if the  $\Delta\text{C}$ -statistics value of the fit is close to the expected C-statistics value. Because we do not include Poisson noise in our spectral simulations, the expected C-statistics for a model exactly matching the one which is used for the simulated data is identical to zero. The C-statistics of each of our fits therefore stem from the mismatches between the exact input model and the best-fit model, and for the rest of this work we will denote this as  $\Delta\text{C}$ -statistics.

For calculations using the 1T model, three parameters are let to vary: normalization, temperature, and the iron abundance. The iron abundance is coupled to abundances from carbon to zinc. The *gdem* model has an additional free parameter  $\sigma$ , which defines the width of the Gaussian emission measure distribution (see equation (4.14), if  $\sigma = 0$ , the *gdem* model is identical to 1T model in SPEX).

For the 2T model we first fit the spectra with the 1T model, and only after finding the best-fit parameters of the 1T model we add the second CIE component. The initial value for the normalization of the second CIE component is assumed to be 10% of the best-fit normalization of the first CIE component, and the temperature of the second CIE component is assumed to be 0.5 times the best-fit temperature of the first CIE component. Only if the normalization of the second component is significant, we free the temperature of the second component. The iron abundance of the first component is coupled to all abundances from carbon to zinc of the first component, and also to the abundances of the second CIE component. In case of the 2T model, the best-fit values of temperature are then weighted by the emission measure (the normalization of CIE models in SPEX is equal to the emission measure). The EM weighted temperature is defined as

$$T_{\text{EM,weighted}} = \frac{\text{EM}_{\text{CIE1}} \times T_{\text{CIE1}} + \text{EM}_{\text{CIE2}} \times T_{\text{CIE2}}}{\text{EM}_{\text{CIE1}} + \text{EM}_{\text{CIE2}}}. \quad (4.15)$$

We calculate the error on  $T_{\text{EM,weighted}}$  using the error propagation equation. Unless stated otherwise, all errors in this study are reported at the  $1\sigma$  level. The best-fit values of the 2T model, for which the

<sup>3</sup>EM is defined as a product of  $n_e n_H dV$ , where  $n_e$  is the electron density,  $n_H$  is the hydrogen density, and  $dV$  is the volume filled by the emitting gas.

<sup>4</sup>A2029 Chandra observations with ID 4977 can be downloaded from <https://doi.org/10.25574/04977>.

<sup>5</sup>For more details about this contamination of the ACIS detectors or the optical blocking filters, and its effect on quantum efficiency and effective areas see <https://cxc.cfa.harvard.edu/ciao/why/acisqcontamN0010.html>.

<sup>6</sup>For more details see <https://heasarc.gsfc.nasa.gov/docs/xrism/proposals/index.html>.

second CIE component was not significant (its normalization was zero within  $2\sigma$  level), were removed from our sample.

## 4.3 Results

### 4.3.1 Simulations with the Chandra ACIS-S CCD

The angular resolution of Chandra allows us to simulate spectra for the objects in Table 4.2 for multiple radial bins, and therefore create radial profiles of the iron abundance and temperature. For all objects besides NGC 4636, we define an array of radii between 5 – 110 kpc, which are equally distributed on a logarithmic scale. Due to the low redshift, as well as low mass of NGC 4636, we chose its radial bins between 0.3 – 35 kpc, which are also equally spaced on a logarithmic grid. Our results for the Perseus cluster, NGC 4636, A2029, A1795, A262, and A383 are plotted in Fig. 4.2, Fig. 4.3, Fig. 4.8, Fig. 4.9, Fig. 4.10, and Fig. 4.11, respectively. In these figures we plot an upper limit to the expected value of C-statistics (purple dashed line in bottom left panels). The values of  $\Delta C$ -statistics, which lie below the purple curve, all indicate an acceptable fit.

Fig. 4.4 shows the results of fitting 1T, 2T and *gdem* models to spectra simulated with the *clus* model which were extracted for the inner-most and outer-most radial bins (labelled in the caption). We plot the ratio of the best-fit values of the iron abundance and temperature to their input 3D values as defined in equations (4.8) and (4.4), respectively. Values of 3D profiles of the iron abundance and temperature are evaluated at the centres of these shells. On the  $x$  ( $y$ ) axis we plot the best-fit values to the spectra simulated without (with) RS. Deviations from the vertical line at  $x = 1$  (along purple arrows in the bottom right panel) indicate the magnitude of projection effects, deviations from the diagonal line  $x = y$  (along coral arrows) indicate the magnitude of RS effect, while deviations from the horizontal line at  $y = 1$  (along teal arrows) indicate a combination of projection and RS effects. Due to the low count rate and large statistical uncertainties, we make the inner-most and outer-most shells of NGC 4636 in Fig. 4.4 thicker in comparison with shells chosen for the radial profiles shown in Fig. 4.3.

#### 4.3.1.1 Temperature profile

In the cores of all studied objects, the projected temperature is higher in comparison with the input 3D temperature. For A262, A383, and Perseus this difference is at most by 10 – 13% and for A2029 at most by 20 – 25%. A1795 shows the largest difference out of all studied clusters, where we see an increase in the projected temperature by a factor of 1.5 (1T), 1.63 (*gdem*), and 1.8 (2T) in comparison with the input 3D temperature. The inferred temperatures are significantly higher for  $r_{\text{in}}$ . This is expected since the 3D temperature profile as a function of radius increases towards the core, and therefore there is hotter gas projected in front of and behind the inner region. However, it is worth noting that, depending on the underlying profiles, some cool-core clusters are affected considerably more than others.

In the outskirts, the projected temperature is higher than its 3D value by at most 5 – 6% for most of the clusters. Perseus shows a slightly higher value of the projected temperature (by 7.5%). A262 and NGC 4636 (1T and *gdem*) show a lower projected value of the temperature in comparison with the input 3D value by maximally 4%.

For all galaxy clusters studied in this paper, including or neglecting the RS effect does not make a difference when obtaining the projected temperature profiles in the their cores, but also in their outskirts.

#### 4.3.1.2 Iron abundance profile

As seen from top left panel of Fig. 4.4, the iron abundance of most of the clusters in our sample can be lower or higher by 5 – 10% in their cores due to the projection effects, with an exception of 1T and *gdem* fits to the A1795 spectrum, which shows higher values by approximately 10 – 20% due to the projection effects. After fitting 1T, 2T and *gdem* models to the simulated spectra of the Perseus cluster,

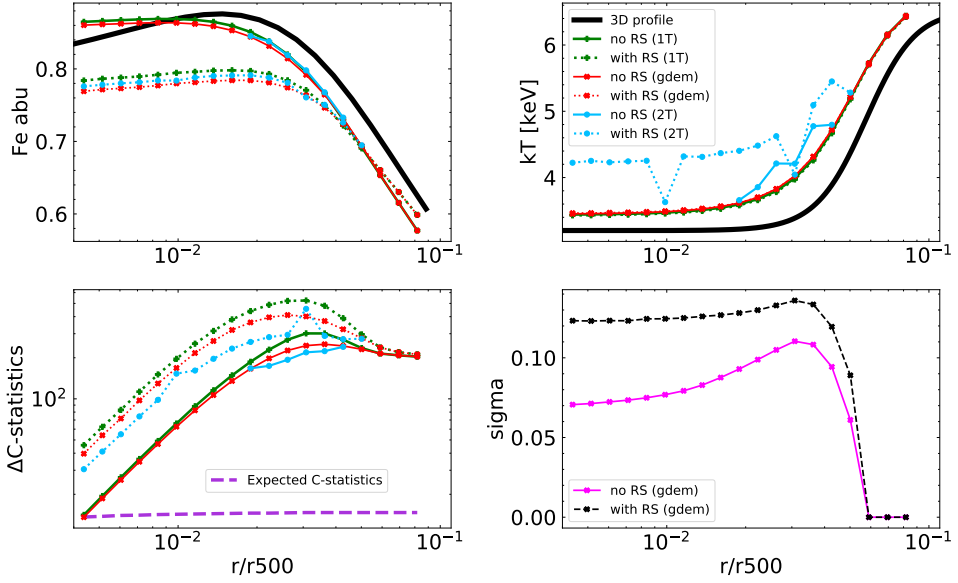


**Figure 4.2:** Best-fit values of the iron abundance and temperature for spectra of the Perseus cluster simulated with Chandra ACIS-S. Spectra without RS (solid lines) and with RS (dotted lines) are fitted with 1T (green lines), 2T (blue lines), and *gdem* (red lines) models as described in Sec. 4.2.4. The top panels show the best-fit iron abundance values (top left) and best-fit temperature values (top right) together with the 3D profiles (black lines) defined in equations (4.8) and (4.4), respectively. The bottom left panel shows the values of  $\Delta C$ -statistics and the expected value of C-statistics (purple dashed line, see Sec. 4.2.4 for more details). The bottom right panel shows the best-fit value of the  $\sigma$  parameter, which is defined in the *gdem* model as the width of the gaussian distribution of the emission measure as a function of temperature. Since the simulated data does not include the Poisson noise, the values of  $\Delta C$ -statistics which are below the purple curve, indicate an acceptable fit. Spectra for every radial bin were simulated assuming 500 ks exposure time.

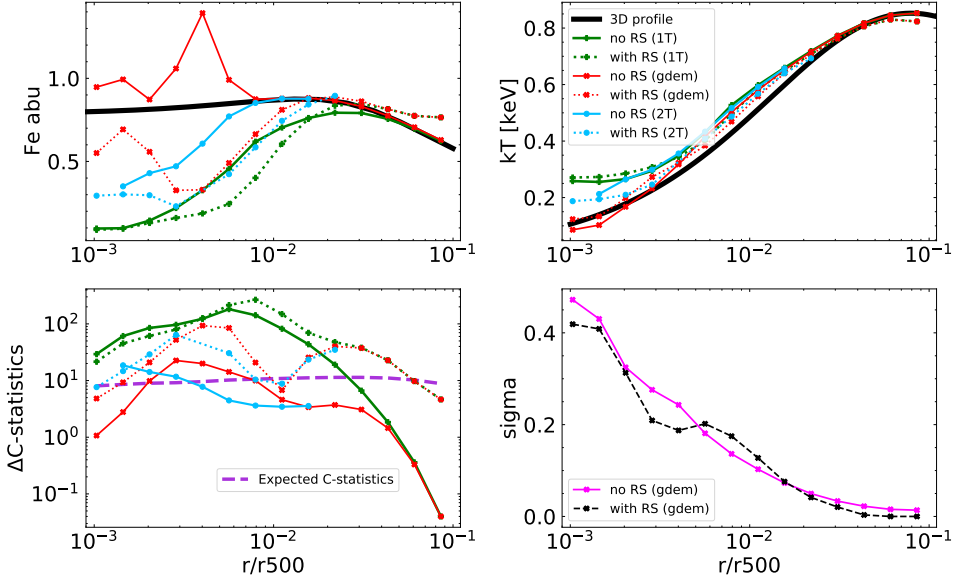


**Figure 4.3:** Same as Fig. 4.2 but for NGC 4636.

A2029 and A383, we notice similar behaviour of the best-fit iron abundance profiles in their cores. The projected iron abundance profiles show a clear separation between data simulated with and without RS. If constrained, all three models (1T, 2T, and *gdem*) predict lower iron abundance values in the cores of these clusters if the RS is present in their simulated spectra. Contrary to results for the Perseus cluster, A2029 and A383, the projected profiles of the iron abundance in the cores of A1795 and A262 do not show such differences between fitting the data simulated with or without RS. The  $\Delta C$ -statistics values are worse if RS is taken into account. This result is not surprising since the RS is not included in 1T, 2T, nor *gdem* models.

In the outskirts, the projected iron abundance of the more massive galaxy clusters (A2029, A1795, A383 and the Perseus cluster) in our sample is lower by approximately 10% due to the projection effects, while for the less massive object A262 this difference between the projected value and the input iron abundance value rises to  $\sim 14 - 20\%$ . The projected values of iron abundance in the outskirts of all clusters in our sample are lower than their 3D input profiles.

#### 4.3.1.3 NGC 4636

The differences between 2D and 3D iron abundance and temperature profiles in the core ( $r_{\text{in}} \in 0.3 - 1.2$  kpc) and outskirts ( $r_{\text{out}} \in 12.6 - 35$  kpc) of NGC4636 are shown in Fig. 4.4.

The best-fit projected temperature in the core of NGC 4636 is higher by factor  $\sim 1.5$  for 1T and 2T models, while the *gdem* model shows smaller difference between 2D and 3D temperatures (an increase by approximately 10%). This difference is caused by the projection effects. In the outskirts, the projected temperature is lower by 3.5% for 1T and *gdem* model, while the 2T model is statistically not significant. The effect of RS on inferred temperature profile is the largest in the core and in the case of the *gdem* (increase by approximately 18%) and 2T models (decrease by approximately 17%), and the smallest in case of the 1T model (increase by  $\sim 6\%$ ). In the outskirts, the effect of RS on the projected temperature is within  $< 2\%$ .

The massive elliptical galaxy NGC 4636 shows the biggest differences in the recovered shape of the iron abundance profile. Out of all considered objects in this paper, this is the only case where we can

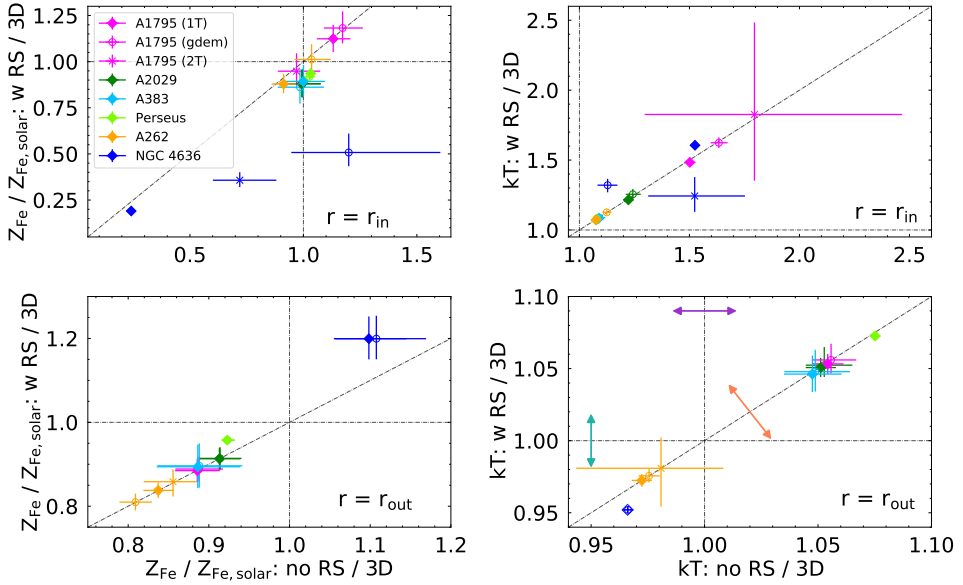


**Figure 4.4:** Best-fit values of 1T (diamond points), 2T (cross) and *gdem* (empty circles) models to the Chandra ACIS-S simulated data with and without the effect of RS for an exposure time of 500 ks. The left panels show the best-fit iron abundance values, whereas the right panels show the best-fit values for temperature. The top and bottom panels show the best-fit values for the most inner and the most outer shells, respectively. The shells thickness for most of the objects are approximately between 5–6 kpc for  $r_{\text{in}}$ , and 80–110 kpc for  $r_{\text{out}}$ , with exception of A383 ( $r_{\text{in}} \in 5 - 8.5$  kpc,  $r_{\text{out}} \in 66 - 110$  kpc) and NGC 4636 ( $r_{\text{in}} \in 0.3 - 1.2$  kpc,  $r_{\text{out}} \in 12.6 - 35$  kpc). All best-fit values are divided by their corresponding input (3D) values. The best-fit values of the 2T model, for which the second CIE component was not significant were removed from this plot (see last paragraph of section 4.2.4). 1T results of NGC 4636 for  $kT(r_{\text{out}})$  are plotted with an empty diamond point for visualisation purposes.

reproduce a drop in the iron abundance profile in the inner-most few kpc, which has been observed with XMM-Newton (see section 4.4 for more details). Due to projection, the iron abundance in the core drops by  $\approx 80\%$  (1T) and  $\approx 30\%$  (2T), respectively. In the case of fitting its simulated spectra with the *gdem* model, we see an increase in the projected value of iron abundance by  $\approx 20\%$  in comparison with the input iron abundance value. For the 1T model, there is almost no difference between the best-fit iron abundance values with and without RS. On the other hand, if RS is present in the simulated data, the iron abundance inferred from fitting 2T and *gdem* models to simulated spectra shows a decrease by approximately 50% and 58%, respectively.

#### 4.3.1.4 Comparison of the input and fitted emission measure distributions

In Fig. 4.5 we plot the input emission measure as a function of temperature for the Perseus cluster (left panels) and NGC 4636 (right panels), and compare it to the Gaussian distribution retrieved from the best-fit *gdem* model following equation (4.14). We inspected two shells while making sure that in one of these shells the sigma parameter reached its maximum (see the bottom right panel in Fig. 4.2 and Fig. 4.3). We calculate the distribution of EM as a function of temperature in each shell (plotted with histogram bars) following the 3D profiles of density and temperature as defined in equations (4.1) and (4.4), respectively.

Our results show that for both targets, the *gdem* model does not represent accurately the shape of the input EM. The smallest difference between the best-fit *gdem* model and the input EM distribution is for the shells with  $\sigma \approx 0.14$  (Perseus) and  $\sigma \approx 0.2$  (NGC 4636). Even in this case one might argue that a model which could represent the input EM distribution of these shells more accurately might not be the *gdem* model, but rather a decreasing power-law or a skewed *gdem* model.

In the inner-most projected shell of the Perseus cluster, the input EM is skewed towards a single temperature, whose value coincides with the 3D value in its core ( $\approx 3.3$  keV). Both best-fit *gdem* models (with and without RS) overestimate the amount of gas with temperatures below and above this peak temperature.

In the case of NGC 4636, the best-fit *gdem* model (no RS) peaks at a slightly different temperature in comparison with the input EM distribution, which results in overestimating the amount of gas with temperatures below 0.1 keV, and underestimating the gas at higher temperatures. The tail of the EM distribution of this massive elliptical galaxy (above 0.4 keV) agrees well with the *gdem* results (no RS). In the case of the best-fit *gdem* values including RS, the *gdem* model peaks at the same temperature as the input EM distribution, however, it overestimates the amount of gas with temperatures lower/higher than this peak. The tail of this *gdem* best-fit distribution agrees well with the input EM distribution for temperatures above  $\approx 0.6$  keV. The input EM distribution could again be described more accurately by a different model, as for example the skewed *gdem* model.

In the outskirts of both objects, the best-fit *gdem* values of  $\sigma$  were either identical with zero, or very close to zero. We would like to stress that the plotted histograms in Fig. 4.5 take into account only the effect of projection. When we refer to the gas as being multi-phase, we mean considering its 3D temperature profile as defined in Fig. 4.1, and we neglect other effects that can also change the phase of the gas (e.g. cooling instabilities).

### 4.3.2 Simulations with the XRISM Resolve micro-calorimeter

The design of the XRISM Resolve micro-calorimeter in combination with its  $3' \times 3'$  FoV and the angular resolution of 1.7 arcminutes limits our simulations to only two radial bins, from which the spectra of studied objects are extracted:

- $r_{\text{in}} = 0 - 0.75'$ , which corresponds to a  $1.5' \times 1.5'$  array, and
- $r_{\text{out}} = 0.75' - 1.5'$ , which corresponds to the rest of the  $3' \times 3'$  array.

In Fig. 4.6 we show the results of fitting 1T, 2T and *gdem* models to spectra extracted for the inner and outer radial bins as defined in the figure caption. We plot the best-fit values of the iron abundance and temperature for two cases: with and without the effect of resonant scattering. The values of 3D profiles of the iron abundance and temperature are evaluated at the centres of these shells following equations (4.8) and (4.4), respectively. Our simulations are done assuming the response files for an open gate valve, however, at the moment the gate valve opening attempts have not been successful. In case that the gate valve remains closed for an extended period of time, we plan to redo our simulations in the future with the updated response files.

#### 4.3.2.1 Temperature profile

In the inner shells, the differences between the 3D temperatures and the best-fit projected values are slightly larger in comparison with the outer shells due to the same reason as we discussed in section 4.3.1.1. As shown in Fig. 4.6, the best-fit values for  $r_{\text{in}}$  are larger by at most 6% (Perseus) to 26% (A1795, 2T), with an exception of A383, for which the best-fit temperature is lower by 2% in comparison with the input temperature. In the outer shells, the best-fit values are higher at most by  $\sim 3\%$  (A2029, 1T) to 23% (Perseus, 2T) for most of the studied objects. For A383, the 2D temperature is lower by  $\sim 6\%$ . For all objects besides A383, the best-fit temperatures are always higher than the input 3D temperatures for both inner and outer shells.

From Fig. 4.6 we see that the presence or absence of RS in spectra of almost all objects considered in this study does not affect the projected temperature (within error bars) recovered from fitting simulated

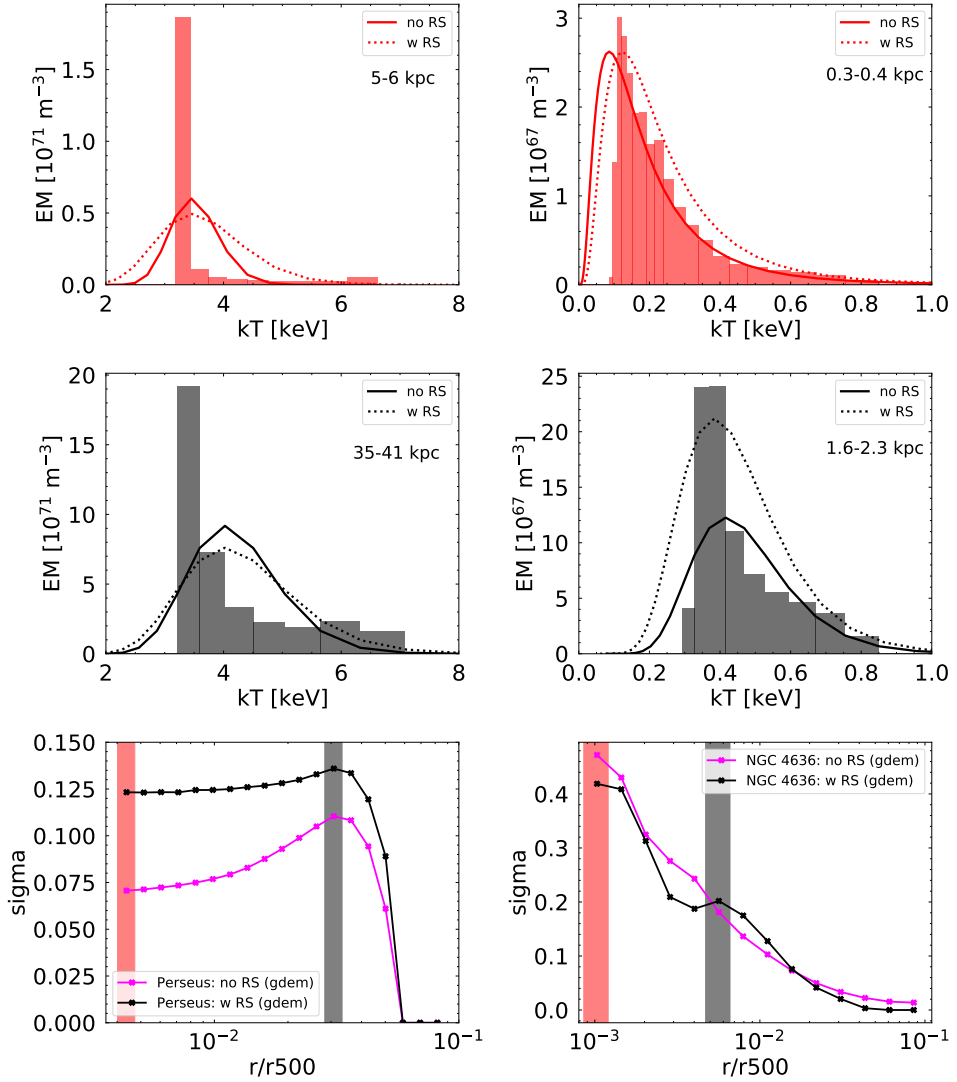


**Figure 4.5:** Emission measure (EM) distribution as a function of temperature for the Perseus cluster (left panels) and NGC 4636 (right panels). Different colours represent different shells which were used to extract the input emission measure distribution as described in Sec. 4.3.1.4 (plotted with histograms). The Gaussian functions in each plot were obtained following equation (4.14), and by using the best-fit values obtained and described in more details in Sec. 4.3.1. The bottom row shows the radial profile of best-fit values of  $\sigma$  for the Perseus cluster and NGC 4636, where the red and black bars correspond to radial bins used for deriving the EM distribution in the first two rows of this figure.



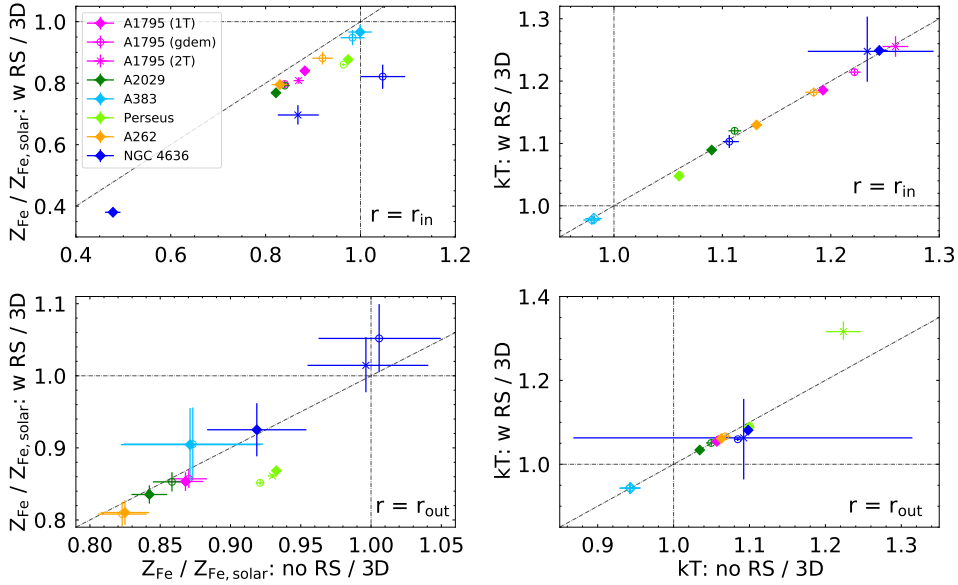


**Figure 4.6:** Same as Fig. 4.4 but for data simulated with XRISM Resolve micro-calorimeter. The exposure time was assumed to be 200 ks. The physical sizes of inner shells are approximately (0-3) kpc for NGC 4636, (0-16) kpc for Perseus and A262, (0-54) kpc for A1795, (0-66) kpc for A2029, and (0-142) kpc for A383. The physical sizes of outer shells are approximately (3-7) kpc for NGC 4636, (16-33) kpc for Perseus and A262, (54-108) kpc for A1795, (66-133) kpc for A2029, and (142-283) kpc for A383. The errors represent the standard deviation  $1\sigma$ . Similar to Fig. 4.4, the best-fit values of the 2T model, for which the second CIE component was not significant, were removed from this plot (see the last paragraph of section 4.2.4). 1T results of A383 for kT in both radial bins are plotted with an empty diamond point for visualisation purposes.

spectra with models like 1T, 2T or *gdem* (the data points lie on the diagonal black solid line). This is true for both radial bins ( $r_{\text{in}}$  and  $r_{\text{out}}$ ). The only exception is the 2T fit in the outer radial bin of the Perseus cluster, where the projected temperature increased by approximately 7% due to the presence of RS in the simulated data.

#### 4.3.2.2 Iron abundance profile

In comparison with Chandra results, XRISM results yield slightly higher values for the effect of projection, as well as resonant scattering, on the iron abundance in the inner shell of galaxy clusters. The projection effects make the iron abundance in the cores of the galaxy clusters lower by  $\sim 1 - 20\%$  when compared to the input 3D values. These effects are the lowest ( $\sim 1 - 5\%$ ) for the Perseus cluster, A383, and A262 (the *gdem* model). For A2029, A1795, and A262 (1T), the projection effects make the iron abundance in the core of these clusters lower by approximately  $8 - 20\%$  in comparison with the input abundance. In the outer shells the projection effects make the inferred iron abundance lower by  $13 - 20\%$ , with an exception of the Perseus cluster, for which we see an effect of approximately  $6 - 8\%$ .

The effect of RS on the inferred iron abundance is slightly higher in the cores of galaxy clusters in comparison with their outskirts, however, for all clusters studied in this paper we see an effect of maximally 10% in both radial bins. Fitting 1T, 2T and *gdem* models to spectra simulated with RS causes a decrease in the projected iron abundance for all clusters from our sample besides the outskirts of A383. The largest effect of RS is in the case of the Perseus cluster ( $\sim 11\%$  in the core, and  $\sim 8\%$  in the outer shell). We summarize these results (together with NGC 4636 which is discussed in a separate section) in Table 4.3.

#### 4.3.2.3 NGC 4636

Temperature in the core of NGC 4636 inferred from the *gdem* model is affected the least by the projection ( $\sim 10\%$ ), while in the case of 1T and 2T models this value rises to  $\sim 24\%$ . In the outskirts, all three models yield similar results, and the projection effects cause an increase in temperature by maximally 10% in comparison with 3D values. In both radial bins, the RS does not significantly affect the projected temperature obtained from 1T, 2T and *gdem* models.

Similar to our conclusions in Sec. 4.3.1, the best-fit values of the iron abundance in the core of NGC 4636 are affected the most by fitting 1T, 2T, and *gdem* models to the spectra simulated with the *clus* model. The projection effects make the iron abundance in the core lower by 55% and 15% for 1T and 2T models, respectively. In the case of the *gdem* model, the projected iron abundance is higher by 5% in comparison with the input 3D profile. If the RS is taken into account in the simulated spectrum, the iron abundance decreases by approximately 10% (1T), 17% (2T), and 22% (*gdem*). In the outskirts, the 1T model shows the largest sensitivity to the projection effects, while the *gdem* model shows the largest sensitivity if RS is taken into account. Both of these effects are below 10%.

In Fig. 4.7 we show NGC 4636 simulated spectra (with RS) for a shell from 0.3-7 kpc (full FOV) for 500 ks XRISM/Resolve observation. We compare data simulated with the *clus* model (black points) to the best-fit 1T (blue solid line), 2T (green solid line), and *gdem* (red solid line) models. We plot the residuals between the simulated data and the 1T, 2T and *gdem* models in the bottom three panels. These residuals show that 1T, 2T and *gdem* models can not fully describe the richness of the NGC 4636 spectra, especially if the resolution of the observed spectrum is similar to XRISM Resolve. Additionally, the discrepancy between 2D and 3D profiles for XRISM is slightly lower in comparison with our Chandra results, which is mostly due to the difference in their spatial resolution.

	RS	$r_{\text{in}}$ 3D	1T	2T	$g_{\text{dem}}$	$r_{\text{out}}$ 3D	1T	2T	$g_{\text{dem}}$
A2029	✗ ✓	0.86 0.86	$0.70 \pm 0.01$ $0.66 \pm 0.01$	– –	$0.72 \pm 0.01$ $0.68 \pm 0.01$	0.65 0.65	$0.55 \pm 0.01$ $0.54 \pm 0.01$	– –	$0.56 \pm 0.01$ $0.56 \pm 0.01$
A1795	✗ ✓	0.86 0.86	$0.76 \pm 0.01$ $0.73 \pm 0.01$	$0.75 \pm 0.01$ $0.70 \pm 0.01$	$0.73 \pm 0.01$ $0.69 \pm 0.01$	0.68 0.68	$0.59 \pm 0.01$ $0.58 \pm 0.01$	– –	$0.59 \pm 0.01$ $0.58 \pm 0.01$
A383	✗ ✓	0.65 0.65	$0.65 \pm 0.02$ $0.62 \pm 0.02$	– –	$0.63 \pm 0.02$ $0.61 \pm 0.02$	0.41 0.41	$0.36 \pm 0.02$ $0.37 \pm 0.02$	– –	$0.36 \pm 0.02$ $0.37 \pm 0.02$
Perseus	✗ ✓	0.85 0.85	$0.83 \pm 0.004$ $0.75 \pm 0.004$	– –	$0.82 \pm 0.004$ $0.73 \pm 0.004$	0.87 0.87	$0.81 \pm 0.003$ $0.75 \pm 0.003$	$0.80 \pm 0.003$ $0.75 \pm 0.003$	$0.80 \pm 0.003$ $0.74 \pm 0.004$
A262	✗ ✓	0.87 0.87	$0.72 \pm 0.02$ $0.69 \pm 0.01$	– –	$0.80 \pm 0.02$ $0.77 \pm 0.02$	0.81 0.81	$0.67 \pm 0.01$ $0.66 \pm 0.01$	– –	$0.67 \pm 0.01$ $0.66 \pm 0.01$
NGC 4636	✗ ✓	0.84 0.84	$0.40 \pm 0.01$ $0.32 \pm 0.01$	$0.73 \pm 0.04$ $0.59 \pm 0.03$	$0.88 \pm 0.04$ $0.69 \pm 0.03$	0.88 0.88	$0.80 \pm 0.03$ $0.81 \pm 0.03$	$0.87 \pm 0.04$ $0.89 \pm 0.03$	$0.88 \pm 0.04$ $0.92 \pm 0.04$

**Table 4.3:** XRISM Resolve best-fit iron abundance values for 1T, 2T and  $g_{\text{dem}}$  models with (✓) and without (✗) RS for the inner ( $r_{\text{in}}$ ) and outer shells ( $r_{\text{out}}$ ) as defined in the caption of Fig. 4.6. The errors are reported at  $1\sigma$  level. The exposure time was assumed to be 200 ks.

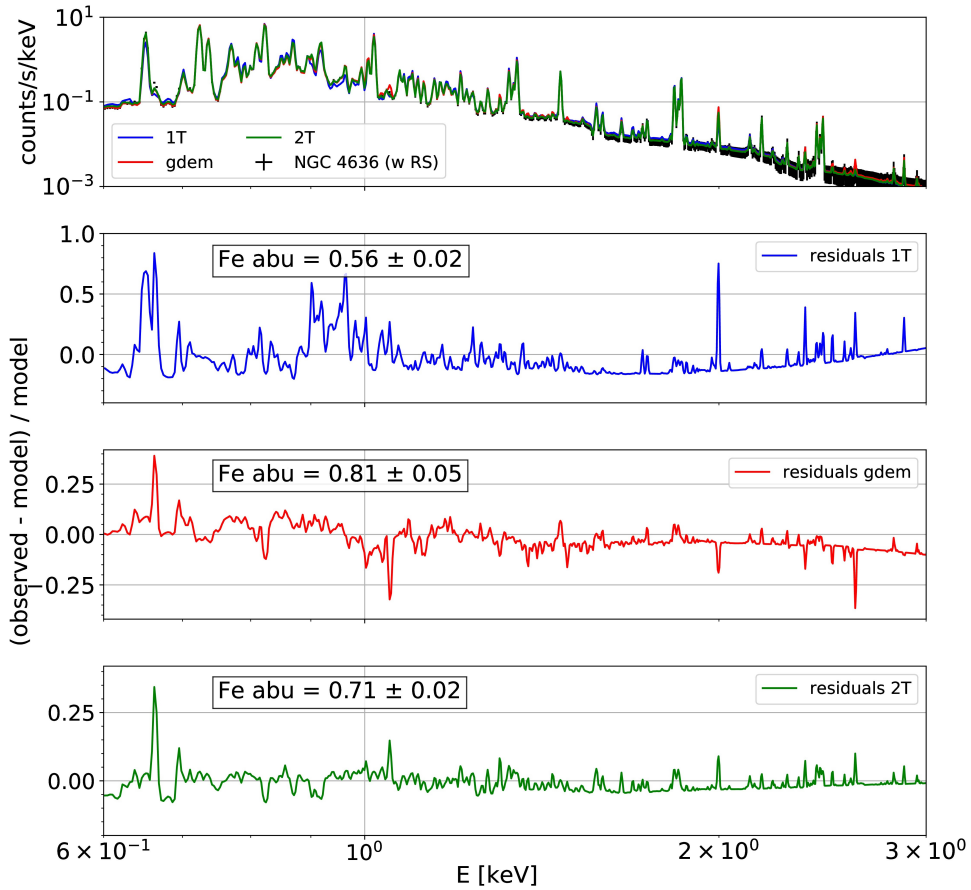


**Figure 4.7:** XRISM Resolve spectra in the energy range 0.6 – 3 keV simulated with the *clus* model (including RS) for the 0.3 – 7 kpc aperture region of NGC 4636 (black points), while assuming the gate valve is open. The best-fit 1T, 2T and *gdem* models are plotted with blue, green and red solid lines together with the residuals which are shown in bottom three panels. The best-fit values of the iron abundance are given in the plots together with  $1\sigma$  errors. The exposure time was assumed to be 500 ks.

## 4.4 Discussion

### 4.4.1 Multi-temperature and multi-metallicity structure of the ICM

Our results show that even if the temperature and gas density distribution is smooth, and at every shell the gas is isothermal, while no thermal instabilities are present in the ICM, the projection effects influence the best-fit temperatures obtained from fitting the complex spectra of galaxy clusters and NGC 4636 with models such as 1T, 2T, and *gdem*. In Fig. 4.4 we showed that in cores of some cool-core clusters the projected temperature is within 8 – 12% from the input temperature (see e.g. core of A262), while in other cool-core clusters, as for example the core of A1795, the projection effects caused a difference between the input temperature and the projected temperature which is as large as a factor of 1.5 – 1.8. In case of the core of NGC 4636 (1T and 2T models) this factor is 1.5, while the temperature inferred from the *gdem* model is 10% higher in comparison with the input value. For all objects studied in this paper, the 2D temperature is higher in comparison with the 3D input temperature.

The temperature in the inner radius inferred from XRISM simulations is less affected by the projection effects (for most of the clusters) in comparison with Chandra results (see Fig. 4.6). On the other hand, the temperature inferred from XRISM simulations in  $r_{\text{out}}$  is affected slightly more by projection in comparison with Chandra simulations.

It is well known that the 1T model can not describe the multi-temperature structure of galaxy clusters accurately, and leads to an “iron bias” (Buote 2000) for the low-temperature objects, and to an “inverse iron bias” for the high-temperature objects (Rasia et al. 2008; Simionescu et al. 2009; Gastaldello et al. 2010). Simionescu et al. (2009) concluded that for the cool-core cluster Hydra A, one needs a broad emission measure distribution such as the *gdem* model to fit simultaneously the lines of the Fe-K and Fe-L complexes, which indicate a multi-temperature origin of the gas. E.g. Kaastra et al. (2004) concluded that the 2T model can in most cases sufficiently describe the spectra of cool-core clusters. However, as our results show, neither 2T nor *gdem* model can in many cases accurately describe the underlying emission measure distribution as shown in Fig. 4.5, even when the fit is statistically acceptable (see all values of  $\Delta C$ -statistics which lie below the purple dashed curve in bottom left panels of Fig. 4.3, Fig. 4.8, Fig. 4.9, Fig. 4.10, and Fig. 4.11). This shows the difficulty of reconstructing the input temperature profile from the projected values, even for a smooth temperature profile assuming a set of isothermal shells and neglecting any cooling instabilities. Such findings might impact the cross-calibration studies between different instruments, which in return might affect the inferred masses of galaxy clusters, and therefore also the cosmological parameters (see e.g. Wallbank et al. 2022; Migkas et al. 2024).

### 4.4.2 Measured Fe abundance drop in the cores

As we already mentioned in the introduction of this paper, some galaxy clusters, galaxy groups, and massive elliptical galaxies show a sharp decrease in the radial profiles of the metal content in their inner-most few kiloparsecs. A unified theory explaining the reason behind this abundance drop has not yet been established. In this paper, we investigated whether projection effects and the resonant scattering process can potentially explain the measured abundance profiles in some of these objects.

Out of the objects studied in this paper, only the cores of the Perseus cluster and the massive elliptical galaxy NGC 4636 have a confirmed abundance drop in their projected profiles, e.g. in the XMM-Newton observations (Werner et al. 2009 for NGC 4636, and Mernier et al. 2017 for NGC 4636 and the Perseus cluster). We compare our results to the work of Mernier et al. (2017) since the authors used the same set of proto-solar abundances by Lodders et al. (2009). The iron abundance was measured by fitting *gdem* to the XMM-Newton data, resulting in a decrease from  $0.9 Z_{\text{Fe}}/Z_{\text{Fe},\odot}$  at  $\sim 0.02 r_{500}$  to  $0.5 Z_{\text{Fe}}/Z_{\text{Fe},\odot}$  at  $\sim 0.003 r_{500}$  for NGC 4636, while for the Perseus cluster the iron abundance drops from  $0.8 Z_{\text{Fe}}/Z_{\text{Fe},\odot}$  at  $\sim 0.03 r_{500}$  to  $0.6 Z_{\text{Fe}}/Z_{\text{Fe},\odot}$  at  $\sim 0.004 r_{500}$ . The authors find no abundance drop in A2029 and in A1795, while A262 shows a sharp increase from  $0.6 Z_{\text{Fe}}/Z_{\text{Fe},\odot}$  at  $\sim 0.1 r_{500}$  to  $1.4 Z_{\text{Fe}}/Z_{\text{Fe},\odot}$  at  $\sim 0.007 r_{500}$ . Similar conclusions of no significant abundance drop in the inner-most few kpc were reached for A2029 with Chandra ACIS-S observations (Figure 4 of Lewis et al. 2002), for A1795 with

XMM-Newton observations (Figure 1 of Tamura et al. 2001) and with Chandra ACIS observations (Figure 7 of Ettori et al. 2002), and for A262 with Suzaku observations (Figure 3 of Sato et al. 2009). Besides a global abundance value reported for A383 in Morandi et al. (2010), which reaches  $0.52 \pm 0.07$  of the solar value for Grevesse & Sauval (1998) abundances, we could not find the radial profile of the iron abundance in currently existing literature.

A few previous works such as Rasmussen & Ponman (2007) or Russell et al. (2008) concluded that projection effects do not affect the measured iron abundance profiles significantly. Depending on the mass of the simulated objects, as well as the projected distance from the core, we find different conclusions from our simulations.

#### 4.4.2.1 Perseus

For the core of the Perseus cluster Churazov et al. (2004) and Gastaldello & Molendi (2004) concluded that there is no evidence for resonant scattering based on XMM-Newton data. However, measurements with the Hitomi SXS micro-calorimeter showed that the resonant scattering suppresses the flux measured in the Fe xxv He $\alpha$  line by a factor of  $\sim 1.3$  in the inner  $\sim 30$  kpc (Hitomi Collaboration et al. 2018b). From our simulations with Chandra ACIS-S as well as XRISM Resolve we can conclude that

- the projection effects can not explain the abundance drop in the core of the Perseus cluster, and all used models (1T, 2T, and *gdem*) cause an increase (decrease) in the iron abundance maximally by 5% based on simulations with Chandra (XRISM).
- the effect of resonant scattering can only partly explain the iron abundance drop in the core of Perseus, and according to our results, the measured iron abundance can maximally decrease by 10 – 15%.

Similar conclusions were reported in Sanders & Fabian (2006), who showed that resonant scattering can not remove the central drop in the Chandra CCD spectra of galaxy clusters (namely Centaurus and A2199), and that this effect can change the measured metallicities at most by 10%. Additionally, the Perseus cluster is not a perfectly symmetric system, and faint X-ray cavities, as well as weak shocks, ripples, and radio lobes around its central galaxy NGC 1275 are present in its ICM (see e.g. McNamara et al. 1996; Fabian et al. 2011; Hitomi Collaboration et al. 2018a). Such effects are, however, neglected in our simulations. We defer the simulations of non-spherically symmetric systems as well as additional clusters known to host abundance dips to future work.

#### 4.4.2.2 NGC 4636

The massive elliptical galaxy NGC 4636 is known for showing resonant scattering in its core, which changes the flux ratio between the resonant line at  $15.01\text{\AA}$  and forbidden lines at  $17.05\text{\AA}$  and  $17.10\text{\AA}$  of Fe xvii (Xu et al. 2002; Kahn et al. 2003; Hayashi et al. 2009; Werner et al. 2009; Ahoranta et al. 2016). As we mentioned earlier in this paper, it also has a steep abundance drop measured in its core, which makes it a perfect candidate to test the theory whether accounting for the RS effect can remove this central abundance drop.

NGC 4636 was one of the five massive elliptical galaxies studied in Werner et al. (2009). The authors fitted the observed spectra with a 1T model, and concluded that more complicated models did not improve the fit, and that differential emission measure models always converged to the single-temperature approximation. This is not in agreement with our findings in Fig. 4.5, which shows that in the core, the differential emission measure should follow a decreasing power-law or perhaps a skewed *gdem* model.

Depending on the model (1T, 2T, or *gdem*) which we used to fit the simulated data of NGC 4636, we confirm that the central abundance drop in this massive elliptical galaxy can be potentially explained by RS, and in the case of the 1T model also solely by projection effects. The models like 1T, 2T, and *gdem* neglect the RS effect, which influences the measurement of fluxes in Fe xvii lines. Our results indicate larger differences between 3D and projected values (50 – 58% depending on the model) in

comparison with those reported in Werner et al. (2009), where the authors concluded that RS can lead to underestimating Fe and O abundances by 10 – 20% in its core.

As previously mentioned, in Mernier et al. (2017) the iron abundance measured using the *gdem* model drops from  $0.9 Z_{\text{Fe}}/Z_{\text{Fe},\odot}$  at  $\sim 0.02 r_{500}$  to  $0.5 Z_{\text{Fe}}/Z_{\text{Fe},\odot}$  at  $\sim 0.003 r_{500}$ . Using the same model as the authors (*gdem*) to fit the spectra we simulated with the *clus* model, while taking into account RS, we report a drop approximately from  $0.86 Z_{\text{Fe}}/Z_{\text{Fe},\odot}$  at  $\sim 0.02 r_{500}$  to  $0.33 Z_{\text{Fe}}/Z_{\text{Fe},\odot}$  at  $\sim 0.003 r_{500}$ . These findings are in agreement with observations by Mernier et al. (2017) (within statistical uncertainties).

Similar to our discussion of the results for the Perseus cluster, we would like to point out that NGC 4636 is known for its non-spherical nature. Its X-ray images show a presence of X-ray bubbles and cavities, as well as spiral arms, which are believed to originate from shocks caused by the central AGN, and its interaction with the surrounding ICM (see e.g. Jones et al. 2002; Baldi et al. 2009). The *clus* model assumes a spherical symmetry when simulating X-ray spectra. This assumption breaks down for NGC 4636, which might affect the results reported in this paper. However, we do not expect that the central abundance drop for this object would completely disappear.

## 4.5 Conclusions

This paper introduces the *clus* model, which was recently implemented in the software package SPEX. The *clus* model can be used for any X-ray emitting plasma which is in CIE, and which can be approximated with spherical symmetry. The advantage of this model lies in the forward modelling of spectra and radial profiles of selected sources, assuming their 3D temperature, density, velocity and metal abundance profiles. The X-ray emitting gas is divided into a set of spherically symmetric shells, where the emission in each shell is described with a single CIE model, and projected onto the sky. This model also includes the resonant scattering (RS) effect, which is implemented through the Monte Carlo simulations.

We used the *clus* model to simulate spectra of galaxy clusters Abell 383, Abell 2029, Abell 1795 and Abell 262, the Perseus cluster, and the massive elliptical galaxy NGC 4636. We modelled spectra of these objects with and without resonant scattering while assuming CCD-like (Chandra ACIS-S) and micro-calorimeter (XRISM Resolve) spectral resolutions. We created projected radial profiles of their metal abundance and temperature by fitting their simulated spectra with models like the single-temperature (1T), double-temperature (2T), and the gaussian-shaped differential emission measure (*gdem*) models.

As shown in this paper, the impact of projection and RS effects vary depending on the mass or temperature of the object, as well as the projected distance from its core. Our main conclusions can be summarized as follows:

- As shown by the differential emission measure for the Perseus cluster and NGC 4636 (see Fig. 4.5), the 1T, 2T, or *gdem* models are not always accurately describing the underlying EM distribution. The EM distribution changes depending on the projected distance from the cluster core as well as the thickness of the shell. Depending on these properties, different models such as e.g. skewed *gdem* model, or decreasing power-law might be more suitable to describe the EM profile. Hence fitting data with a model, which does not represent the underlying distribution, can lead to fitting biases.
- The projection effects cause an increase of temperature inferred from fitting 1T, 2T, or *gdem* models to the simulated spectra in the cores of studied objects, with the exception of XRISM results for A383. For clusters with less prominent core in their density profile, this increase is 10 – 30% (6 – 18%) for Chandra (XRISM), while for the objects with a more prominent core in the density profile, such as A1795 and NGC 4636, this increase can be as high as a factor of 1.5 – 1.8 if spectra were simulated with Chandra. For XRISM results, these factors are slightly lower  $\sim (1.2 - 1.26)$  due to lower spatial resolution. In the outskirts of galaxy clusters, the differences are below 8% for Chandra, however, XRISM results show that the projected temperature can be higher by 3 – 23% in comparison with its input value.
- Using models like the *clus* model for fitting CCD and micro-calorimeter spectra is more crucial

for obtaining the abundance profiles of low-mass and low-temperature objects (see Fig. 4.4 and Fig. 4.6). In the outskirts of A262, the projected iron abundance is 14 – 20% lower than the input profile irrespective of the model used for fitting its simulated spectra. In the core of the massive elliptical galaxy NGC 4636, the projected iron abundance is lower by almost 80% (55%) for 1T model, or higher by 20% (5%) for the *gdem* model if spectra were simulated with Chandra (XRISM). Regardless of the instrument, the *gdem* model is affected the least by the projection effects in the core of NGC 4636. However, we report non-negligible differences between the input and projected profiles also for hotter and more massive objects. For some cool-core clusters, the differences might be negligible (e.g. iron abundance in the core of A383 simulated with Chandra and XRISM), while in other cool-core clusters as for example A1795, the projected iron abundance in its core is approximately 20% higher (lower) in comparison with the input profile, if data was simulated with Chandra (XRISM).

- The resonant scattering can reduce the observed central abundance drop in galaxy clusters such as the Perseus cluster by maximally 10 – 15%, but it can not fully explain the abundance drop in the inner-most few kpc.
- In case of the massive elliptical galaxy NGC 4636, the resonant scattering can explain the abundance drop measured in its core. Depending on the model used for fitting its spectra, not accounting for the resonant scattering leads to an underestimation of the iron abundance in the core of this massive elliptical galaxy by  $\sim 50\%$  (2T) to 58% (*gdem*), if data was simulated with Chandra. In the case of the 1T model, this abundance drop can also be solely explained by projection effects. The XRISM results show that RS can make the iron abundance in the core of NGC 4636 lower by maximally 10 – 22%.

**Acknowledgements:** The authors acknowledge the financial support from NOVA, the Netherlands Research School for Astronomy. A.S. acknowledges the Kavli IPMU for the continued hospitality. SRON Netherlands Institute for Space Research is supported financially by NWO.

**Data Availability:** The dataset generated and analysed during this study will be available in the ZENODO repository.

## Appendix

### 4.A Chandra results for other clusters



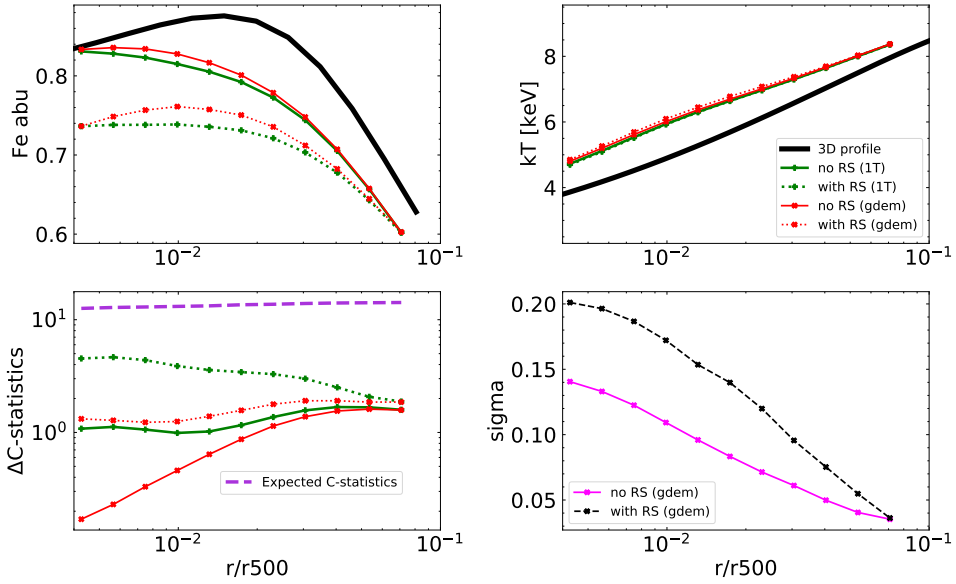


**Figure 4.8:** Same as Fig. 4.2 but for A2029.

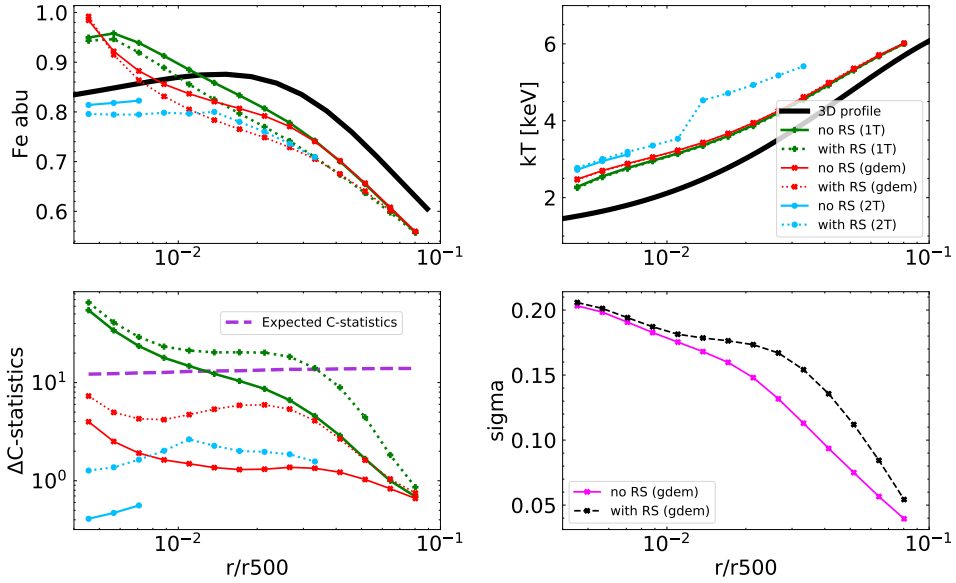


**Figure 4.9:** Same as Fig. 4.2 but for A1795.

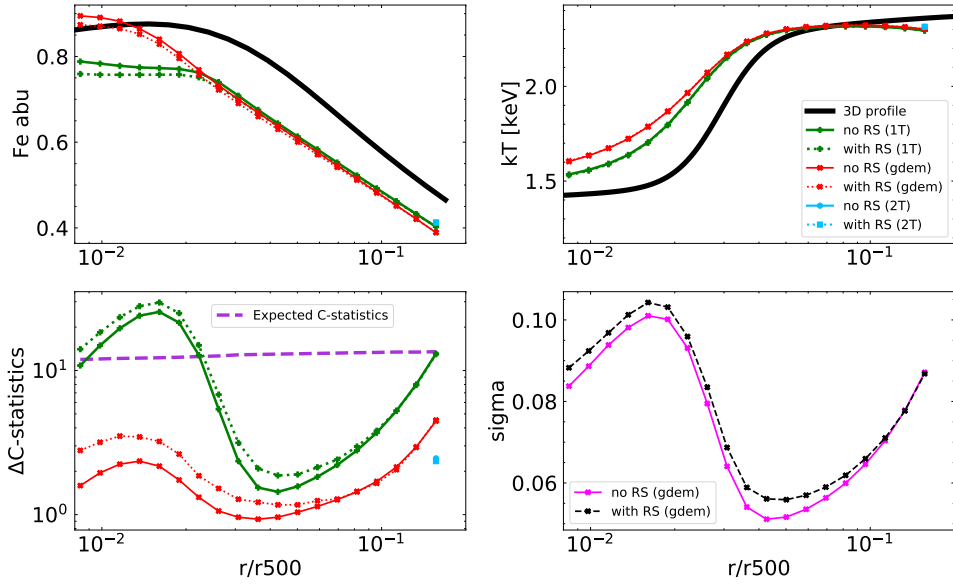


Figure 4.10: Same as Fig. 4.2 but for A262.

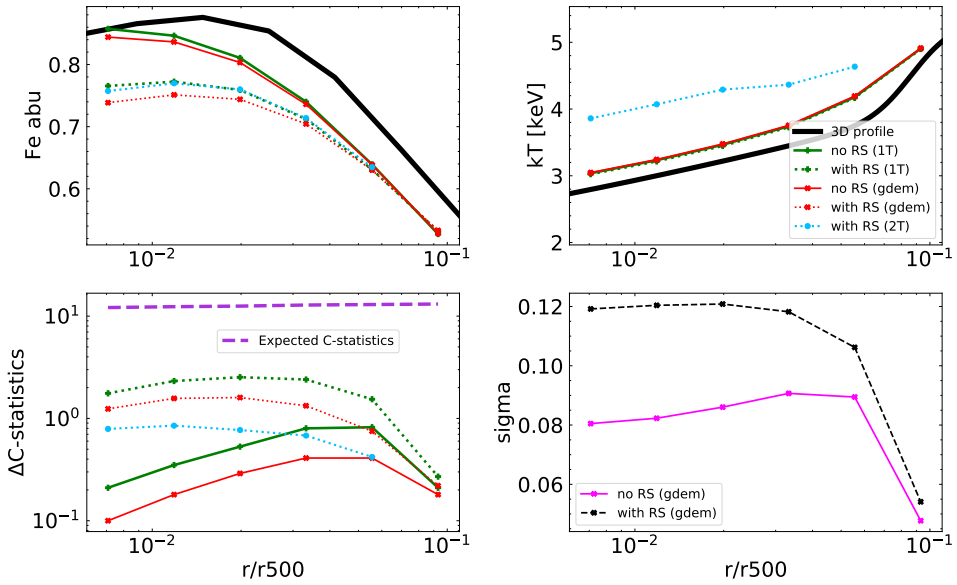


Figure 4.11: Same as Fig. 4.2 but for A383.



# 5

## New radiative loss curve from updates to collisional excitation in the low-density, optically thin plasmas in SPEX

---

Lýdia Štofánová, Jelle Kaastra, Missagh Mehdipour, and Jelle de Plaa

*Published in Astronomy & Astrophysics, 2021, Volume 655, id.A2, 17 pp.*

### ABSTRACT

---

Understanding and modelling astrophysical plasmas on atomic levels while taking into account various assumptions (for example, collisional ionisation equilibrium or photoionisation equilibrium) became essential with the progress of high-resolution X-ray spectroscopy. In order to prepare for the upcoming X-ray spectroscopy missions such as XRISM or Athena, the plasma codes with their models and the atomic databases need to be up to date and accurate. One such update for the plasma code SPEX is presented in this paper where we focus on the radiative loss due to collisional excitation in the low-density, optically thin regime. We also update the atomic data for neutral hydrogen and include the contribution of the dielectronic recombination. With all these updates being implemented in SPEX we finally present the new cooling curve. We include the comparison to other plasma codes (MEKAL, APEC, Cloudy) and other atomic databases (CHIANTI, ADAS). We show how the updated cooling impacts the stability curve for photoionised plasmas and find a new stable branch.

---

## 5.1 Introduction

Hot astrophysical plasmas heated to temperatures of around  $10^4$ – $10^8$  K can be found in a wide range of astrophysical sources at various scales throughout the Universe. Depending on the properties of the plasma (as for example, temperature, density) and its environment, different atomic processes contribute to the overall shape of the spectrum. These processes all need to be taken into account in models for X-ray emission from these hot plasmas.

Over the last couple of decades, X-ray spectroscopy has undergone significant improvements that have allowed us to obtain X-ray spectra with a high level of detail. The observations that have been made so far, however, also reveal the importance of accurate atomic data as well as the improvement of the plasma codes that are needed in order to properly understand the observed X-ray spectra. Such models in the plasma codes help us to understand the radiation coming from the X-ray sources and allow us to study their physical properties.

In general, plasma codes can be either collisional, photoionised or include both regimes at the same time. A few examples are APEC (Smith et al. 2001), CHIANTI (Dere et al. 1997), MEKAL (Mewe et al. 1995), SPEX (Kaastra et al. 1996), Cloudy (Ferland et al. 1998), Mocassin (Ercolano et al. 2003), Titan (Dumont et al. 2000), and XSTAR (Kallman & Bautista 2001). The discrepancies between different plasma codes can be relatively high, especially for lower temperatures (for instance, see Hitomi Collaboration et al. 2018c). These discrepancies can be caused by different approaches and approximations used for solving the Schrödinger (Dirac) equation or different ionisation balance and calculation of level populations (for more about atomic data in X-rays, see reviews by Smith 2005; Kallman & Palmeri 2007 and references therein).

One of many consequences of such discrepancies are the estimates of the cooling rates. Plasma can cool down via multiple processes; for example, bremsstrahlung or more complex cooling via radiative recombination, collisional excitation, ionisation, etc. The process of cooling has been extensively studied in many works such as, for example Raymond et al. (1976), Boehringer & Hensler (1989), Sutherland & Dopita (1993), Landi & Landini (1999), Schure et al. (2009), and Lykins et al. (2013). In this paper, we use the term cooling for the cooling of the population of free electrons only, which we express in units of  $\text{keV m}^3 \text{s}^{-1}$ . For more details about the terminology of cooling, we refer the reader to Gnat & Ferland (2012), for example.

The radiative loss function and the cooling function should give the same results if the collisional ionisation equilibrium (CIE) is considered since the plasma in an enclosed and non-expanding box can lose the energy only by radiating photons if for example, magnetic fields, heat conduction, radioactive processes, etc. are not taken into account. For the collisional excitation process in a low-density plasma, as discussed in the present paper, the radiative loss is the same as the cooling. This is different from radiative recombination, which leads to radiative losses equal to the cooling by that process plus the ionisation potential of the recombined ion and different from collisional ionisation of the valence electrons, which does not produce radiation at all.

This work serves as a report of the updates made in the plasma code SPEX. More specifically, we focus on the updates of electron collisional excitation rates and the impact of these updates on the cooling for the plasma in the low-density regime. Collisional excitation occurs when a free electron collides with an atom or ion and brings the bound electron into the excited state. Because these excited states are less energetically favourable, the excited electron falls down to a lower level by radiative transition.

In previous versions of SPEX, the collisional excitation rates were calculated with the codes by Mewe et al. (1985), Mewe et al. (1986) and MEKAL (Mewe et al. 1995) which originally operated in the regimes  $\lambda < 300 \text{ \AA}$ ,  $\lambda < 1000 \text{ \AA}$ , and  $\lambda < 2000 \text{ \AA}$ , respectively. Over the years, the X-ray line database of SPEX has been updated and has grown, also extending to the ultraviolet (UV), optical, and infrared (IR) bands. Since the first version of SPEX, many updates have been made and the most recent works are the updated radiative recombination rates (Mao & Kaastra 2016; Mao et al. 2017a), the updated collisional ionisation rates (Urdampilleta et al. 2017), a model for the charge exchange transfer (Gu et al. 2016), updates of the collisional excitation rates (Kaastra et al. 2017), and the updated data for the

Fe-L complex (focusing mainly on Fe xvii to Fe xxiv ions) by Gu et al. (2019). The latest version, 3.06.01, also includes the updated radiative loss function due to collisional excitation that we present in this paper and that is used in the photoionisation model pion (for a plasma in photoionisation equilibrium – PIE) and updates of the collision strengths of H I (see Section 5.3.8 for more details).

The paper is structured as follows. In Section 5.2 we describe how to calculate the radiative loss rates from the excitation rates and how the radiative loss curves for specific ions are obtained. We show our main results in Section 5.3 where we focus on the plasma in collisional ionisation equilibrium and address the accuracy as well as the role of collisional excitation, resonant excitation, metastable levels and updated atomic data for neutral hydrogen. We also discuss the discrepancies in the cooling curves obtained from different plasma codes. In Section 5.4 we implement tables created for the radiative loss rates due to collisional excitation to the photoionisation model in SPEX and study the effect of the updated cooling on the stability curves. We discuss the results in Section 5.5 and give the main conclusions in Section 5.6.

## 5.2 Methods

### 5.2.1 Radiative loss due to collisional excitation in low-density plasmas

The radiative loss rate for collisional excitation quantifies the energy loss of plasma due to collisions of free electrons with atoms or ions (we consider the radiative loss by the population of free electrons only). To calculate this radiative loss rate, we first define the excitation rate  $S_{ij}(T)$  for the excitation from level  $i$  to level  $j$  (while assuming the Maxwellian velocity distribution for electrons) as

$$S_{ij}(T) = \frac{S_0 \bar{\Omega}(y)}{\sqrt{T} w_i e^y}, \quad y = \frac{E_{ij}}{kT}, \quad (5.1)$$

where  $T$  is the temperature of plasma (electron temperature),  $w_i$  is the statistical weight of level  $i$ ,  $\bar{\Omega}(y)$  is the effective collision strength (Hebb & Menzel 1940, also called the Upsilon value),  $E_{ij}$  is the excitation energy for the transition  $i \rightarrow j$  and  $S_0$  is the constant defined as

$$S_0 = h^2 (2\pi m_e)^{-3/2} k^{-1/2}, \quad (5.2)$$

where  $m_e$  is the electron mass and  $h$  and  $k$  represent the Planck constant and the Boltzmann constant, respectively. The units of  $S_{ij}$  are  $\text{m}^3 \text{s}^{-1}$ , such that the total number of excitations per second in a volume  $V$  with electron density  $n_e$  and ion density  $n_i$  is given by  $n_e n_i V S_{ij}$ . As the temperature approaches lower values, the excitation rate decreases exponentially, while for higher temperatures the excitation rate decreases as  $1/\sqrt{T}$ . The total radiative loss function due to collisional excitation only per specific atom or ion from the lower level  $i$  is then obtained by summation of the product of the excitation rate and the excitation energy over all transitions in the atom or ion:

$$\Lambda_{i,\text{exc}}(T) = \sum_j S_{ij}(T) E_{ij}. \quad (5.3)$$

We note that the Equation (5.3) is valid only in the low-density plasmas. That allows us to ignore the effect of the collisional de-excitation when the collision of an ion with a free electron or another ion results in the bound electron being brought into the lower energy orbit.

### 5.2.2 Radiative loss curves in SPEX, MEKAL and CHIANTI

Throughout the years, SPEX (Kaastra et al. 1996) has been extended up to the UV/IR regime, and its atomic database SPEXACT is still under development. The number of elements present in the SPEX atomic database increased from 15 (H, He, C, N, O, Ne, Na, Mg, Al, Si, S, Ar, Ca, Fe, Ni) to 30, and now

SPEX includes all elements up to and including zinc. It contains all ions of the hydrogen and helium iso-electronic sequences and most of the ions of lithium, beryllium, and boron iso-electronic sequences up to Na-like ions. For all ions where we do not yet have data in our SPEXACT database, we used the MEKAL code to calculate line fluxes when available. Originally, the MEKAL code took into account approximately 5500 lines, while the new updated SPEXACT database contains around  $4.2 \times 10^6$  lines. One of the biggest differences between these two codes lies in calculating the line fluxes, for which MEKAL uses temperature-dependent parametrisation (see Mewe et al. 1985 and references therein, mainly Mewe (1972) and Eq. (10) and Eq. (11)), whereas SPEX calculates the line fluxes by obtaining the level populations from the transition rate balance equations. Then, the total line power in SPEX is calculated using the radiative transition probabilities.

To calculate the radiative loss rates in SPEX we used version 3.05.00 (Kaastra et al. 1996; Kaastra et al. 2018) and made these rates public as a part of SPEX version 3.06.00 and higher. The most updated version 3.06.01 includes, among others, updates of the radiative loss rates in the SPEXACT database as well as the cooling rates in the photoionisation model *pion*<sup>1</sup> (which we describe in this paper). Unless stated otherwise, we used the Urdampilleta et al. (2017) ionisation balance and the protosolar abundances by Lodders et al. (2009).

For comparison, we also calculated the radiative loss rates in version 9.0 of the CHIANTI database (Dere et al. 1997; Dere et al. 2019) using version 0.9.1 of the python package ChiantiPy. The excitation energies of individual transitions are considered to be theoretical values (due to more complete dataset of line energies for different ions), and we used the observed values only if the theoretical values were not available. The choice of using theoretical values does not have a significant impact on the final radiative loss rates for the vast majority of available ions. We comment on these differences in more detail in Section 5.5.1.

To estimate the uncertainties in different databases, we also used the *upsilon* values from ADAS (Summers 2004), for which we used the free electron excitation data from the ion data collections of OPEN-ADAS<sup>2</sup>. We calculated the radiative loss rates for a set of oxygen ions and prioritized the most complete datasets with the highest number of levels (if multiple data files contain the same number of levels, we prioritized the data file with the widest temperature range that can be compared to our calculations). The ADAS datasets together with references, number of levels, and temperature range for oxygen ions are shown in Table 5.1. We then calculated the total radiative loss rate on the temperature grid available for each ion (significantly narrower than the temperature grid we choose for SPEX, MEKAL, and CHIANTI).

## 5.3 Results

The excitation rate  $S_{ij}$  and the excitation energy  $E_{ij}$  for all the transitions from the ground level to upper levels allows us calculate the total radiative loss rate due to collisional excitation for individual ions using Eq. (5.3). In the following sections, we calculate the radiative loss rates in SPEX and show the comparison to different databases or codes. We also address other aspects that need to be considered while obtaining these rates.

### 5.3.1 Effect of the maximum principal quantum number

The highest energy loss and therefore the strongest emission lines in the case of the collisional excitation come from the lowest levels of the atom or ion. But with the improvement of the X-ray spectroscopy, the emission lines originating from the higher levels become visible in measured spectra as well. To quantify the effect of the maximum principal quantum number  $n$  used in the calculations we studied the dependency of the cumulative radiative loss rate (due to the collisional excitation only) on various  $n$  for a set of ions (as well as temperatures) for which the SPEX database includes the tran-

<sup>1</sup><https://spex-xray.github.io/spex-help/>

<sup>2</sup><https://open.adas.ac.uk/>

ion	number of levels	file name in OPEN-ADAS	temperature range [eV]	reference
O I	554	ic#o0.dat	0.009 – 172	[1]
O II	668	ic#o1.dat	0.034 – 689	[1]
O III	590	clike_jm19#o2.dat	0.155 – 1551	[2]
O IV	204	blike_lgy12#o3.dat	0.276 – 2757	[3]
O V	238	belike_lfm14#o4.dat	0.431 – 4308	[4]
O VI	204	lilike_lgy10#o5.dat	0.620 – 6204	[5]
O VII	49	ic#o6.dat	0.422 – 8444	[1]
O VIII	25	ic#o7.dat	0.551 – 11030	[1]

**Table 5.1:** Summary of O I–O VIII data files used for calculation of the radiative loss rates due to collisional excitation in ADAS.

**References.** [1] Giunta 2012 (available online); [2] Mao et al. (2020); [3] Liang et al. (2012); [4] Fernández-Menchero et al. (2014); [5] Liang & Badnell (2011).

iso-electronic sequence	number of levels in SPEX			
	C	O	Si	Fe
H-like	284	284	284	284
He-like	678	678	678	678
Li-like	885	885	885	889
Be-like	753	727	753	808
B-like	719	973	972	1100
C-like	1199	1218	1218	1525

**Table 5.2:** Number of levels included in the SPEX database for C, O, Si, and Fe from H-like to C-like iso-electronic sequences.

sitions up to the principal quantum number 20. In particular, these ions are C VI, O VIII, Si XIV and Fe XXVI. We calculated the difference between the cumulative radiative loss rate for transitions  $n \leq 5$  and compared it to the radiative loss rate when all transitions with  $n \leq 20$  are taken into account. For all mentioned ions, the difference between  $n \leq 5$  and  $n \leq 20$  cumulative radiative loss rates for low temperatures is less than 1%, while for higher temperatures this difference increases up to 5–6% (see Fig. 5.1). Therefore, not including the transitions for  $n > 5$  introduces uncertainties in the radiative loss rates that are smaller than 6%. A similar conclusion was obtained in Hitomi Collaboration et al. (2018c).

Fig. 5.1 only considers H-like (one-electron) systems. If more complex systems are taken into account, the number of levels that are included in the calculations can affect the resulting radiative loss rate. This is discussed in Lykins et al. (2013) for the case of collisional plasma as well as photoionised plasma. Authors show that, in general, more levels are needed in the collisional case in comparison with the photoionised case. The final optimal number of levels that is considered is 100 (25) for iron ions and 50 (25) for other ions in the collisional (photoionised) case. If such a number of levels is included in the calculations, the cooling rates can be reproduced within 1% (0.1%) up to maximum of 5% for the collisional (photoionised) case. As we show in Table 5.2 for a selection of ions, SPEX includes a sufficient number of levels and fulfills this requirement.



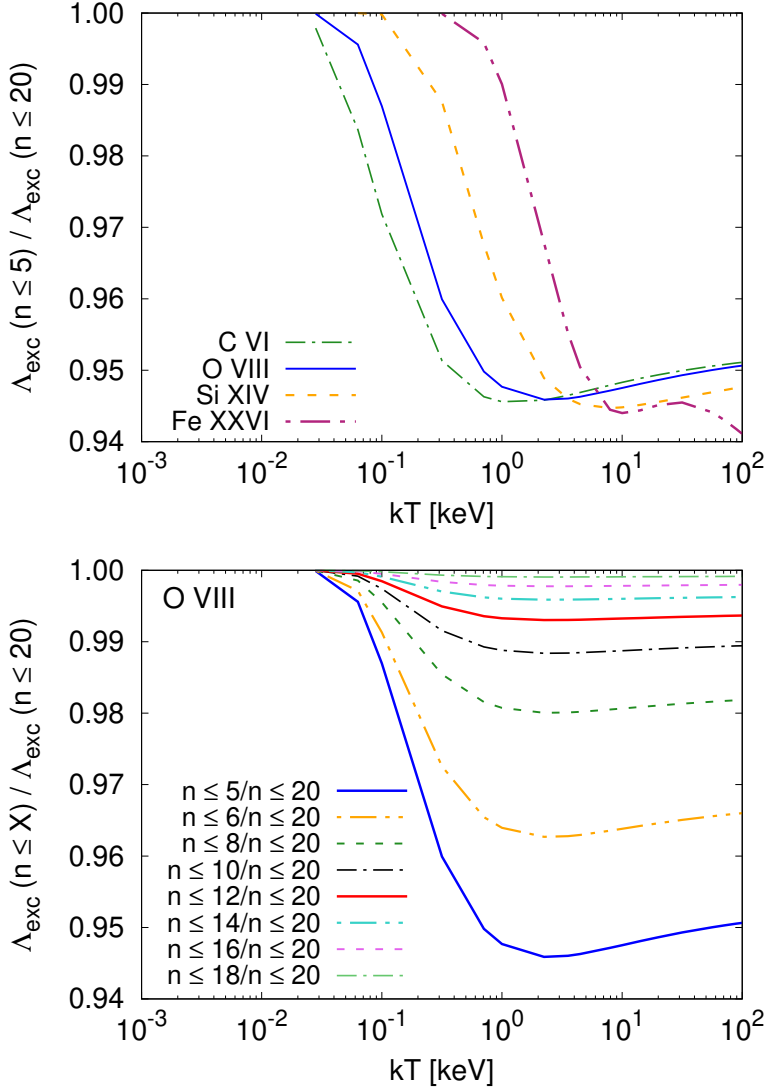


**Figure 5.1:** *Top panel:* Cumulative radiative loss rate for all transitions up to the principal quantum number 5  $\Lambda_{\text{exc}}(n \leq 5)$  for H-like ions plotted relatively to the cumulative radiative loss rate for all transitions up to the principal quantum number 20  $\Lambda_{\text{exc}}(n \leq 20)$  as a function of temperature. *Bottom panel:* Cumulative radiative loss rates for O VIII up to various values of  $n$  relative to  $\Lambda_{\text{exc}}(n \leq 20)$ .

### 5.3.2 Contribution of resonant excitation

In the process of a dielectronic recombination, a free electron is captured while exciting a bound electron. This creates a doubly excited state that is not stable and can be followed by a radiation-free transition to a non-ground level and a loss of an electron. This process is called resonant excitation (RE). As a result, the ion gets to the excited state using less energy in comparison with the energy that would have been needed in the case of direct excitation.

The SPEX database for resonant excitation is currently incomplete but it contains a significant amount of resonances for the whole H-like iso-electronic sequence and almost all He-like ions (besides He I, Li II, Be III and B IV). If lines produced by RE are available in the SPEX database, they are already accounted for in the total excitation rate. To quantify the difference between the radiative loss rates including or excluding RE (for transitions to the ground level), we calculated the total radiative loss curve per ion for both scenarios. By calculating the ratio of the total radiative loss rate with RE and the total radiative loss rate without RE, we found that if RE was taken into account, the radiative loss rates were higher than the radiative loss rates excluding RE, and its effect was typically  $\sim 15\%$  (for example, for Si XIV and  $kT \sim 0.2$  keV).

### 5.3.3 Comparison of radiative loss function for SPEX and MEKAL

First, we calculated the radiative loss rates for SPEX (version 3.06.01) and compared them to the radiative loss rates obtained with MEKAL (Mewe et al. 1985, 1986), and (Mewe et al. 1995). In this paper, we showed the comparison to Schure et al. (2009), which is the latest work regarding the updates of the radiative loss function in SPEX. SPEX version 2.00.11 was based on the MEKAL line-emission model (for all elements including oxygen shown in this work as an example, except for iron, which was calculated using the HULLAC code Bar-Shalom et al. 2001) with the addition of new lines in the 200–2000 Å band (Mewe et al. 1995). The main rationale for comparing our results to MEKAL is the fact that the data generated by MEKAL are still widely used while analysing the X-ray spectra. We showed how the update of the collisional excitation affected the radiative loss function. Later in the paper (see Section 5.4), we also show the impact on the cooling curve in the photoionisation model pion in which the cooling by collisional excitation used to be calculated based on the MEKAL code (for SPEX version 3.05.00 and earlier).

In SPEX, we obtained the excitation rates and the excitation energies from the SPEXACT database, and we calculated total radiative loss curves using the Eq. (5.3) (we remind the reader that we only consider excitations from the ground level for now). In the case of MEKAL, we obtained the excitation energy and the emission rate (in photons/s) for each transition by excluding the contributions from other processes (such as radiative and dielectronic recombination, inner shell ionisation, proton excitations and dielectronic satellite lines), and we only took into account the contribution from the electron excitations. The total radiative loss rate for each ion was then calculated as the sum of the product of the excitation energy and the emission rate over all transitions.

A comparison of the total radiative loss rates per ion can be seen in Fig. 5.2. We see that the updated radiative loss curves either have similar shapes but different normalisations (see Be-like ions C III, O V, Ne VII for which the MEKAL code overestimated the cooling rates at temperatures below 10 keV but underestimated the cooling rates for temperatures above 10 keV) or the shapes of the curves vary, as can be seen for C II and Si VIII. Updated radiative loss curves for ions such as Ne VI, Mg VII, and Al IX differ from MEKAL by a few orders in the range  $10^{-3}$ – $10^{-2}$  keV, which arises from the extension of the energy band to the UV and IR regimes (in comparison with the MEKAL code, which is focused on purely X-ray regime).

More specifically, for Be-like ions C III, O V, and Ne VII the main difference between the SPEX and MEKAL radiative loss rates at low temperatures is caused by a single line for the transition from  $2s2p\ ^1P_1$  to the ground state  $2s^2\ ^1S_0$ . We illustrate this with the example of C III, where the line occurs at 977 Å. In Table 5.3, we show the values for the Maxwellian-averaged collision strengths  $\bar{\Omega}(T)$  of C III at 0.01 keV for some spectral codes.

From Table 5.3, we can see that different codes arrive at values up to two times larger or smaller

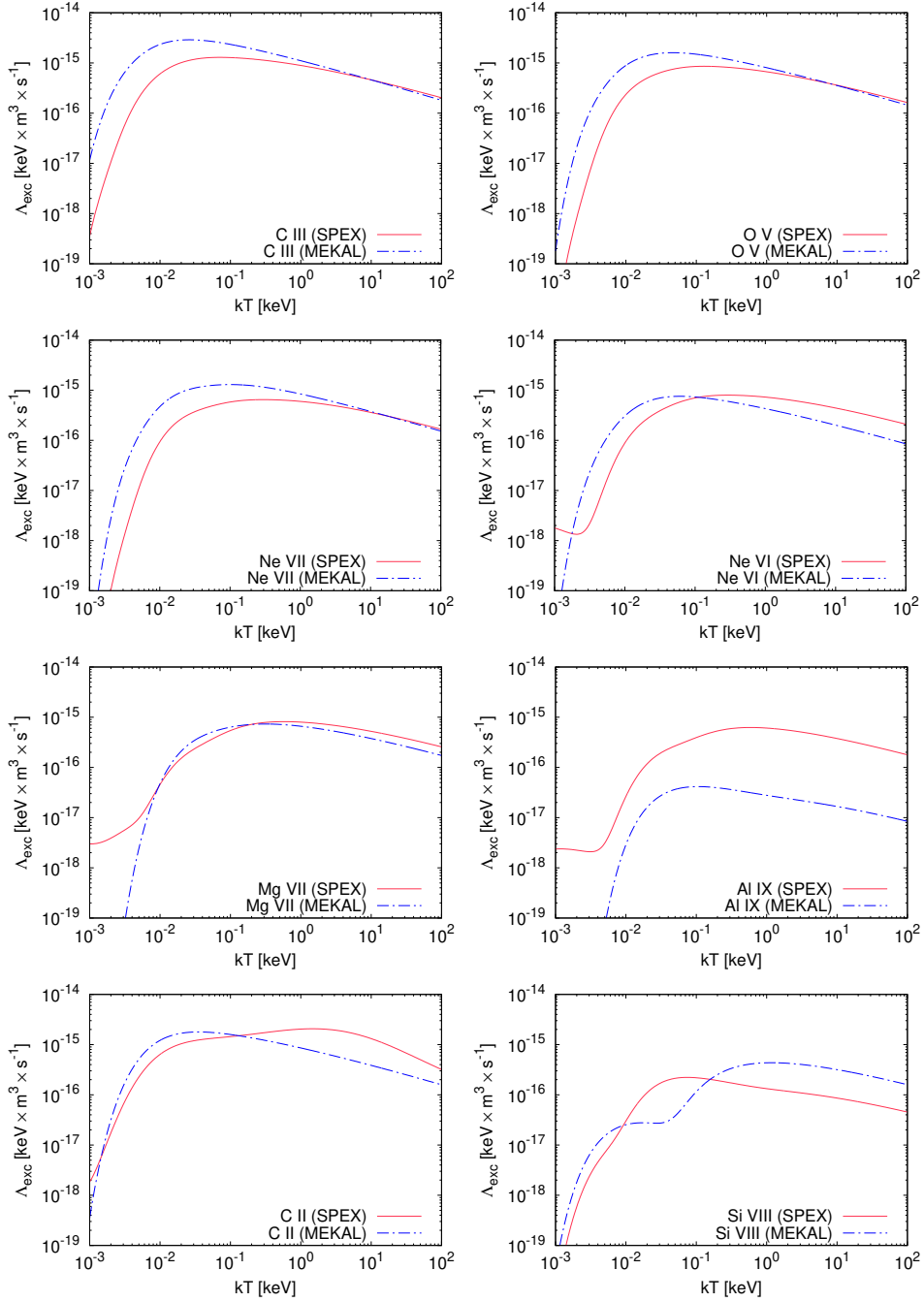


**Figure 5.2:** Comparison of collisional excitation radiative loss rates from SPEX version 3.06.01 (red solid line) and MEKAL (blue dash-dotted line) for a representative sample of ions. We refer the reader to Section 5.3.3 for a detailed description of differences between SPEX and MEKAL for these ions.

code	$\bar{\Omega}(T)$	remarks
MEKAL	10.48	Based on [1] which uses a scaled value from the Fe results given by [2] using $A = 0.5$ , $B = 0.3$ and $E = 0.276$ in Eq. A7 of that paper. This paper cites the distorted wave calculations of [3].
SPEX	5.93	Based on older FAC <sup>a</sup> calculations made by A.J.J. Raassen.
CHIANTI v. 9.0	4.93	R-matrix calculations [4].
OPEN ADAS	4.51	R-matrix calculations in combination with an intermediate coupling frame transformation [5].
AtomDB v. 3.0.9	2.71	Refers to CHIANTI 6 [6], [7].

**Table 5.3:** Comparison of the Maxwellian-averaged collision strengths  $\bar{\Omega}(T)$  at  $T = 0.01$  keV of the C III line at 977 Å (transition from  $2s2p\ ^1P_1$  to the ground state  $2s^2\ ^1S_0$ ) between different plasma codes and atomic databases.

**References.** [1] Landini & Monsignori Fossi (1990); [2] Mewe et al. (1985); [3] Bhatia & Mason (1981); [4] Berrington et al. (1985); [5] Fernández-Menchero et al. (2014); [6] Dere et al. (1997); [7] Dere et al. (2009).

**Notes.** <sup>(a)</sup> Flexible Atomic Code described by Gu (2002, 2008) <https://github.com/flexible-atomic-code/fac>.

than the adopted SPEX value. A more careful analysis of the best available data for this transition for a broad range of temperatures is clearly needed, but it is beyond the scope of this paper.

For Ne VI at low temperatures, most cooling in the SPEX code is caused by the  $2p\ ^2P_{1/2} - 2p\ ^2P_{3/2}$  transition at 75622 Å (magnetic dipole transition); this transition is not present in the MEKAL code. At high temperatures, the main difference comes from the  $2p\ ^2P_{1/2} - 3d\ ^2D_{3/2}$  transition; the excitation energy of this transition is only 101 eV, so at high temperatures the excitation cross-section is dominated by the high-energy limit proportional to the logarithm of the energy; in the SPEX code, which is based on calculations with the FAC code, the constant of proportionality is about two times larger than the default value of 0.276 adopted for MEKAL.

For Mg VII and Al IX, similarly to the case of Ne VI at low temperatures, infrared transitions between the  $2p^2\ ^3P_1$  and  $2p^2\ ^3P_0$  ground state dominate the cooling at low temperatures for SPEX, but these transitions are absent from the MEKAL code. In addition, the MEKAL code only contains two transitions of Al IX so the lack of flux at higher temperatures is not surprising.

In C II, the MEKAL code only contains six spectral lines, while the SPEX code has thousands of lines, making it more complete and rendering more flux in most cases. Finally, for Si VIII, the MEKAL code concentrates a lot of flux in the so-called N1 line at 61.05 Å, which is a conglomerate of all  $2p$  to  $3d$  transitions in this ion, including non-ground state transitions.

### 5.3.4 Comparison with the CHIANTI and ADAS databases

For the series of oxygen ions (O I – O VIII) plotted in Fig. 5.3, we showed how the radiative loss rates obtained from different atomic databases and codes (SPEX/MEKAL/ADAS) differed from CHIANTI (except for O I and O II ions, which are not in the SPEX database). We summarised the references for oxygen ions in Tables 5.1 (ADAS) and 5.4 (SPEX and CHIANTI).

For cases of highly ionised oxygen (O VI to O VIII) and higher temperatures, SPEX and CHIANTI agree within 10%, but for O V the discrepancies rise to  $\sim 30\%$ . For lower temperatures around  $10^{-3}$  keV, radiative loss rates differ by 75% for O V and 26% for O VI<sup>3</sup>. The discrepancies between SPEX and CHIANTI at high temperatures are slightly bigger for O III and O IV. To understand where these differ-

<sup>3</sup>Data for radiative loss rates at these temperatures for O VII and O VIII are below the threshold of  $10^{-20}$  keV m<sup>3</sup> s<sup>-1</sup> that we introduced due to numerical uncertainties.

ion	levels <sub>SPEX</sub>	<i>n</i> <sub>SPEX</sub>	reference <sub>SPEX</sub>	levels <sub>CHIANTI</sub>	<i>n</i> <sub>CHIANTI</sub>	reference <sub>CHIANTI</sub>
O I	–	–	–	7	3	[1], [2], [3]
O II	–	–	–	35	3	[4], [5]
O III	1003	5	[6]	46	3	[7], [8], [9], [10]
O IV	627	5	[6]	204	4	[11]
O V	219	6	[6]	166	5	[12], [13]
O VI	282	5	[6], [14]	923	8	[15]
O VII	247	10	[6], [16]	49	5	[17]
O VIII	164	20	[6], [18]	25	5	[19]

**Table 5.4:** References, number of levels included in the database and the maximum principal quantum number *n* for O I–O VIII data files used for calculation of the radiative loss rates in SPEX and CHIANTI.

**References.** [1] Bell et al. (1998); [2] Zatsarinny & Tayal (2003); [3] Froese Fischer & Tachiev (2004); [4] Tayal (2007); [5] Kisieliu et al. (2009); [6] T. E. Raassen<sup>a</sup> using FAC code; [7] Aggarwal (1983); [8] Aggarwal (1985); [9] Bhatia & Kastner (1993); [10] Lennon & Burke (1994); [11] Liang et al. (2012); [12] Kato et al. (1990)<sup>b</sup>; [13] Landi et al. (2013); [14] Zhang et al. (1990); [15] Liang & Badnell (2011); [16] Sampson et al. (1983); [17] Whiteford et al. (2001); [18] Aggarwal & Kingston (1991a); [19] Ballance et al. (2003).

**Notes.** <sup>(a)</sup> Data are public as a part of the SPEX plasma code and can be downloaded here <https://spex-xray.github.io/spex-help/>. <sup>(b)</sup> These data were updated by Berrington, K.A. More information can be found in Landi et al. (2006).

ences between SPEX and CHIANTI are coming from, we summarised the collision strengths data and origins in Table 5.4. We see that the data comes from different types of calculations (for example, FAC versus R-matrix calculations), and different approaches were used to solve the Schrödinger equation (see for example, Section III of Kallman & Palmeri 2007 for more details about these approximations). The databases of SPEX and CHIANTI also include different numbers of lines and differ in the maximum principal quantum number *n* that is available for the calculations.

When it comes to O I, MEKAL radiative loss rates are lower than CHIANTI radiative loss rates for the whole temperature range, while for O II and temperatures above 0.003 keV we see that the MEKAL radiative loss rates are higher than in the case of CHIANTI. For O I MEKAL agrees with CHIANTI within 30% for all temperatures above 0.01 keV, whereas for O II it overestimates the radiative loss rates by factor of 3 above 0.01 keV. MEKAL is also an outlier for the case of higher ionised oxygen as the dataset used in MEKAL is less complete and is outdated. For O IV, the MEKAL values differ substantially from the CHIANTI values, because, as for other ions, several multiplets at long wavelengths are treated as a single line and the MEKAL code has only 11 lines for this ion.

For all ions besides O I and O II, the ADAS radiative loss rates agree with CHIANTI within 10% (for O VI and temperatures around  $10^{-3}$  keV the agreement is within 20%). In the case of lower ionisation states of oxygen at low temperatures, we see that ADAS overestimates the radiative loss rates in comparison with CHIANTI by a factor of 2 and 5 for O II and O I, respectively.

Overall, we see many discrepancies between SPEX, MEKAL, CHIANTI, and ADAS databases, which might be caused by several factors, for instance different approaches for calculation of the collision strengths, not accurate or even missing atomic data, different values of line energies or the amount of transitions used in the atomic database. This shows that the constant updates of the atomic physics codes and the atomic databases is needed in order to prepare for unprecedented level of details provided by the upcoming X-ray missions, namely XRISM and Athena.

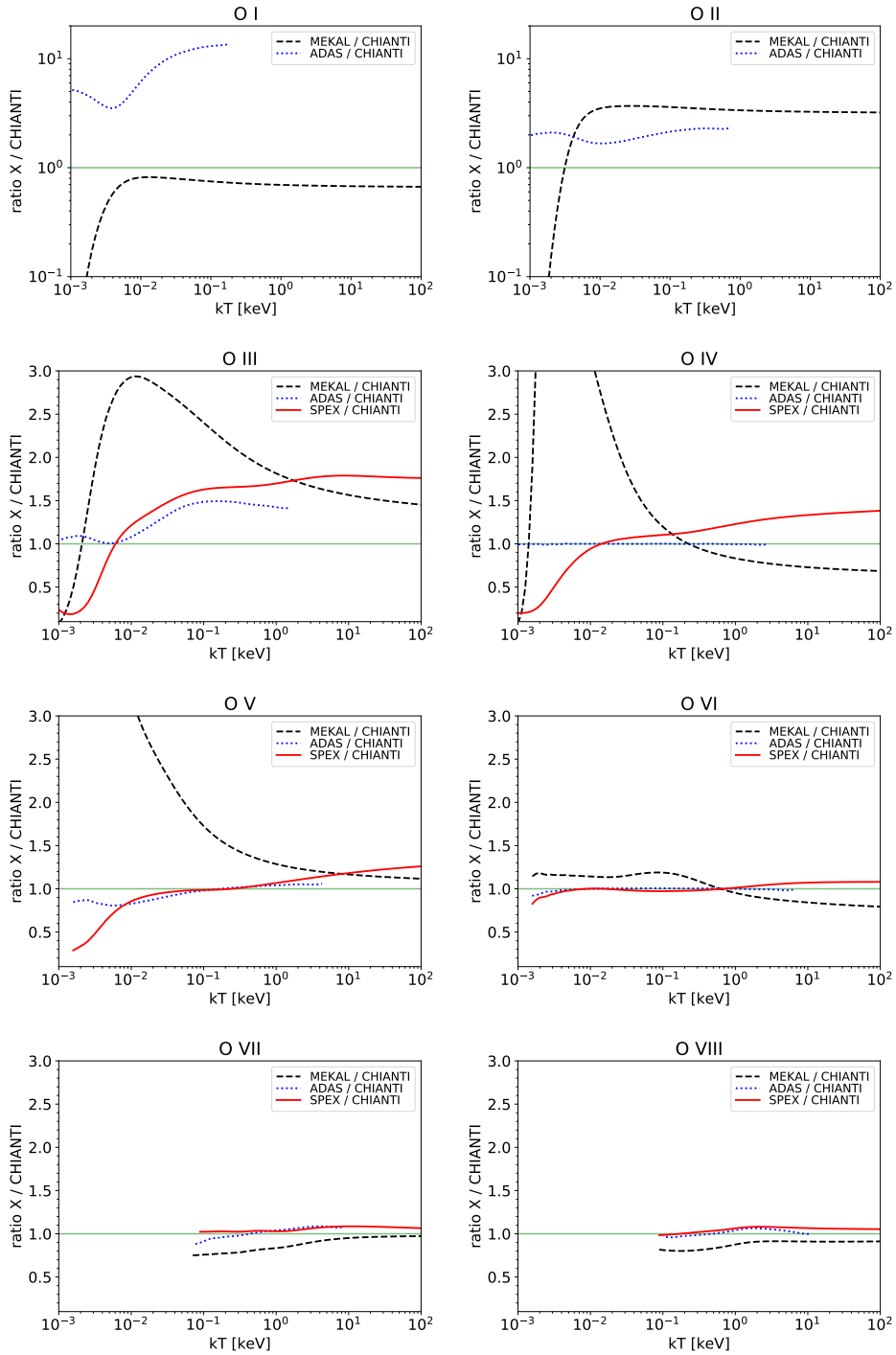


**Figure 5.3:** Radiative loss rates due to collisional excitation for SPEX (red solid line), MEKAL (black dashed line), and ADAS (blue dotted line) plotted relative to CHIANTI for O I – O VIII ions. We refer the reader to Section 5.3.4 and Tables 5.1 (ADAS) and 5.4 (SPEX and CHIANTI) for more detailed descriptions of the differences seen in these databases.

### 5.3.5 Updated dielectronic recombination and its contribution to overall cooling

In this paper, we put emphasis on the role of cooling due to radiative losses caused by collisional excitation. In order to quantify its role in astrophysical situations, we also studied the plasmas in photoionisation equilibrium in Section 5.4, where we described the plasma by the photoionisation model pion. However, a fraction of the total cooling may also be carried by dielectronic recombination (DR), which was ignored in the previous versions of pion (Mehdipour et al. 2016). Since then, we have included the radiative losses caused by DR in the pion model. For other processes that lead to cooling and are included in SPEX, we invite the reader to consult Section 5.4.2.

We implemented the radiative loss rates from DR in SPEX as follows: for ions for which the new collisional calculations were available, the radiative loss rate was obtained from the product of the DR rate that was used for the computation of the occupation of the excited levels and the corresponding energy of the auto-ionising level. For all other ions, we used the DR contribution as taken from the MEKAL code.

In all practical cases presented in this paper, we found that the DR did not contribute by more than a few percent to the total cooling rate.

### 5.3.6 Implementation of updates to PIE model in SPEX

In SPEX versions 3.05.00 and earlier, in the photoionisation model pion the radiative loss by collisional excitation was calculated using the MEKAL code. Now we update these calculations by applying the results from the previous sections assuming the plasma is in the low-density regime. This new model is then used for calculations in Section 5.4, where the sample of ions used for the updated radiative loss by collisional excitation is shown in Fig. 5.4. We prioritised ions from the SPEX database and extended our sample with ions from the CHIANTI database. The ions such as Ne I, Ar VI, Ca IV, Ni X were included from the MEKAL database. In order to facilitate the interpolation, we rescaled  $\Lambda_{\text{exc}}$  according to the following expression:

$$f(T) = \Lambda_{\text{exc}} \sqrt{kT} \exp\left(\frac{E_{\text{eff}}}{kT}\right), \quad (5.4)$$

where  $E_{\text{eff}}$  is the excitation energy from the ground level to the second level. These rescaled radiative loss rates per ion were then used for the final interpolation to get the total radiative loss curve expressed on a chosen temperature grid. We interpolated  $\log f$  as a function of  $\log T$  using three-point Lagrangian interpolation for a grid with spacing 0.05 in  $\log T$  between  $10^{-3}$  keV and 100 keV and linear extrapolation in  $\log f - \log T$  space outside this range in order to secure an accurate interpolation.

### 5.3.7 Contribution from metastable levels

In the previous sections, we analysed the radiative loss rates by the collisional excitation for the transitions from the ground level to upper levels in the low-density plasma regime.

In this section, we discuss the contribution of the metastable levels to the overall radiative loss. This plays an important role in the high-density plasmas. We showed how the radiative loss by collisional excitation from the metastable levels differed in comparison to the radiative loss by collisional excitation from the ground level. If the density of plasma is high enough, the metastable levels can be highly populated and may contribute to the total radiative loss significantly, even more so than the ground level. For example, Mao et al. (2017b) found that if the hydrogen number density  $n_{\text{H}} \gtrsim 10^{14} \text{ m}^{-3}$ , the first three excited levels of Be-like ions ( $2s2p\ ^3\text{P}_{0-2}$ ) are significantly populated ( $\gtrsim 1\%$  of the ground level population). However, for the same density the metastable levels of Be-like ions are less populated than the metastable levels of B-like and C-like ions.

SPEX can be used in the high-density regime for the calculation of spectra in collisional ionisation equilibrium, but it has not been updated yet to include the high-density regime in the calculation of the ionisation balance. Therefore, the present calculations of the radiative loss rates from the metastable levels are not yet used in the current version of SPEX. We note here that, for higher densities, the

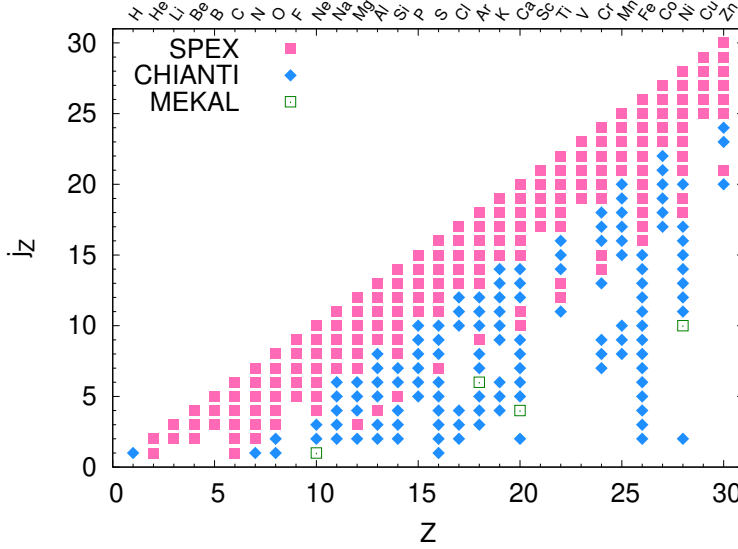


**Figure 5.4:** Final set of ions used for the tables implemented to SPEX model pion. Atomic number  $Z$  is plotted on the x-axis, while the y-axis represents the ionisation stage  $j_z$  (e.g. H I is neutral hydrogen).

iso-electronic sequence		levels
Be-like	Mg-like	1–4
B-like	Al-like	1–2
C-like	Si-like	1–5
N-like	P-like	1–5
O-like	S-like	1–5
F-like	Cl-like	1–2

**Table 5.5:** Metastable levels (in energy order) for which the radiative loss rates were calculated (level 1 represents the ground level).

effect of collisional de-excitation in the radiative loss should be taken into account. The radiative loss by collisional excitation (either from the ground level or from the metastable levels) in this paper was calculated only in the low-density limit.

In Table 5.5, we list all the lower levels from which the radiative loss rates by collisional excitation were calculated for the set of Be-like to Cl-like iso-electronic sequences besides Ne and Na (level 1 represents the ground level). For example, if we calculate the radiative loss rates from level 2, this effectively means taking into account transitions from the second level to all upper levels available in the SPEX database.

In Fig. 5.5, we show the contributions from metastable levels relatively to the contribution from the ground level using the SPEX database in the example of O v (the definition of metastable levels for O v can be found in Table 5.6). For  $kT \sim 0.002$  keV, the contribution from the second and third levels is higher by more than a factor of two in comparison with the contribution from the ground level and on contrary the contribution from the fourth level is lower than the contribution from the ground level. Towards higher temperatures, the ratios decrease with a local minimum around  $kT \sim 0.01$ – $0.02$  keV. At very high temperatures above 3 keV, the curves indicate a higher contribution to the radiative loss



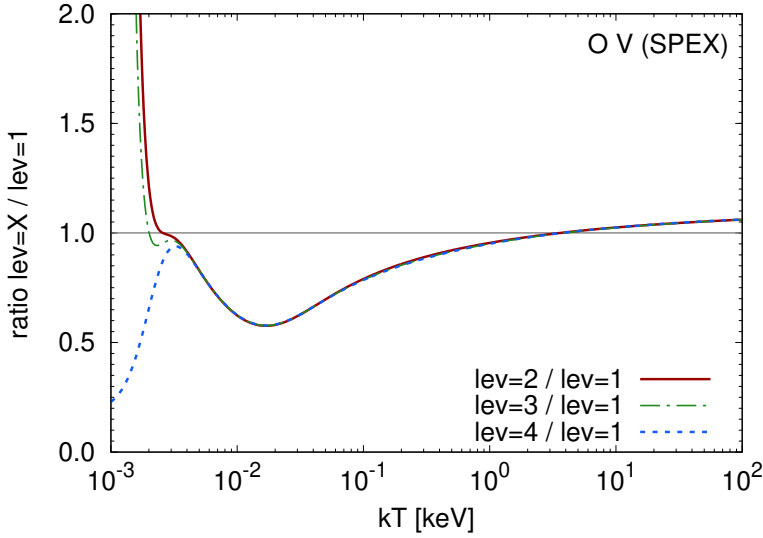


**Figure 5.5:** Contribution of metastable levels to the radiative loss rates shown relatively to the radiative loss rates only from the ground level for Be-like oxygen. The red solid line, green dash-dotted line, and blue dotted line represent the ratio of the total radiative loss rate from the second level (lev=2), the third level (lev=3), and the fourth level (lev=4) relatively to the radiative loss from the ground level (lev=1), respectively. The definition of metastable levels can be found in Table 5.6.

from metastable levels than from the ground level.

### 5.3.8 Calculation of the total cooling curve in SPEX and the comparison to MEKAL, Cloudy, and APEC

Fig. 5.6 shows the difference between the SPEX version 3.06.01 and the MEKAL code for the total radiative loss due only to line radiation (solid blue line) and for both line and continuum radiation (black dashed line). We can divide the figure into four sections: (a)  $kT > 10$  keV, where the updates of the radiative recombination were already done by Mao et al. (2017a); (b)  $2 \times 10^{-3} < kT < 10^{-1}$  keV, with the most significant difference caused by the updated database for collisional excitation (this paper); (c)  $kT < 10^{-3}$  keV, where the difference is mainly caused by resonant excitation; and (d)  $kT \sim 1.5 \times 10^{-3}$  keV, where the updates of H I collision strengths considering data from Anderson et al. (2000) and revised by Anderson et al. (2002) are included in the latest SPEX version. The Be-like ions

level	configuration	term	energy [ $\times 10^{-2}$ keV]
1	$1s^2 2s^2$	$^1S_0$	0.000
2	$1s^2 2s^1 2p^1$	$^3P_0$	1.038
3	$1s^2 2s^1 2p^1$	$^3P_1$	1.039
4	$1s^2 2s^1 2p^1$	$^3P_2$	1.043

**Table 5.6:** Definition of the ground level (level 1) and metastable levels (levels 2–4) and the energies for O V in SPEX.

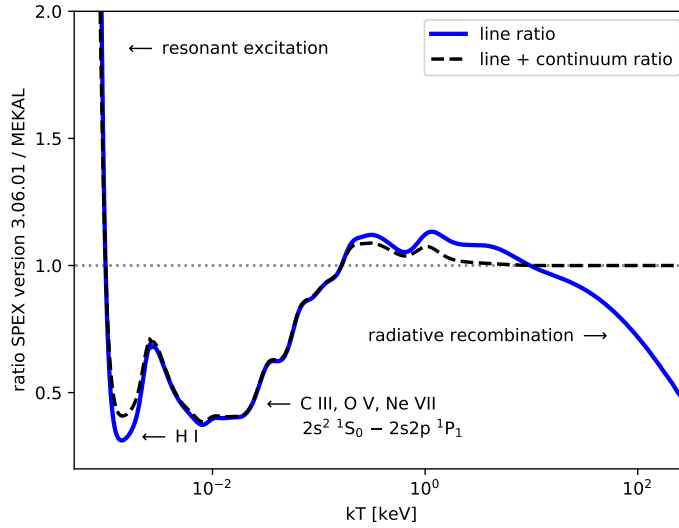


**Figure 5.6:** Ratio of radiative loss rates due only to line radiation for the SPEX version 3.06.01 and MEKAL as a function of temperature (blue solid line) and for both line and continuum radiation (black dashed line). The four biggest differences are pointed out by black arrows and are caused by updates of resonant excitation ( $kT < 10^{-3}$  keV), collisional excitation ( $2 \times 10^{-3} < kT < 10^{-1}$  keV), radiative recombination ( $kT > 10$  keV), and H I collision strengths ( $kT \sim 1.5 \times 10^{-3}$  keV).

C III, O V and Ne VII (more specifically transitions from  $2s^2$  to  $2s2p$ ) account for the most significant contributions to the dip in the  $2 \times 10^{-3}$ – $10^{-1}$  keV range, where for this energy range the MEKAL calculations overestimate the total radiative loss by approximately 60% in comparison with SPEX.

We present the final updated total cooling curve in SPEX as well as individual contributions to this curve from different elements in Fig. 5.7. We note that this is not a radiative loss curve as discussed in the sections before. We also include all transitions from lower to upper levels (as opposed to the previous calculations that considered the transitions only from the ground state to the upper levels) and continuum emission. The calculation assumes Lodders et al. (2009) abundances and the Urdampilleta et al. (2017) ionisation balance. We plot contributions from the 15 most abundant elements (H, He, C, N, O, Ne, Na, Mg, Al, Si, S, Ar, Ca, Fe, Ni) that are present in the MEKAL and SPEX database.

In Fig. 5.8 we compare the updated total cooling curve from SPEX to the total radiative loss curve from Schure et al. (2009). We also plot the total cooling curve from Cloudy and the total radiative loss curve from APEC. The total radiative loss curve by Schure et al. (2009) uses MEKAL calculations and assumes Anders & Grevesse (1989) abundances and the ionisation balance from Arnaud & Rothenflug (1985) for all present elements in MEKAL besides iron, for which the Arnaud & Raymond (1992) ionisation balance is used. The radiative loss curve from APEC (Smith et al. 2001) is calculated using PyATOMDB<sup>4</sup> version 0.10.8, Lodders et al. (2009) abundances, and the Bryans et al. (2009) ionisation balance. We also include the total cooling curve from Cloudy for which the calculations were performed with version 17.01, last described by Ferland et al. (2017). To obtain the Cloudy curve that can be directly compared to SPEX (therefore we discuss the cooling curve and not the radiative loss curve in the following text), we carefully rescale the Cloudy cooling rates and divide them by the product of the hydrogen and the electron density. For that, we obtain the hydrogen density for the specific

<sup>4</sup><https://github.com/AtomDB/pyatomdb>

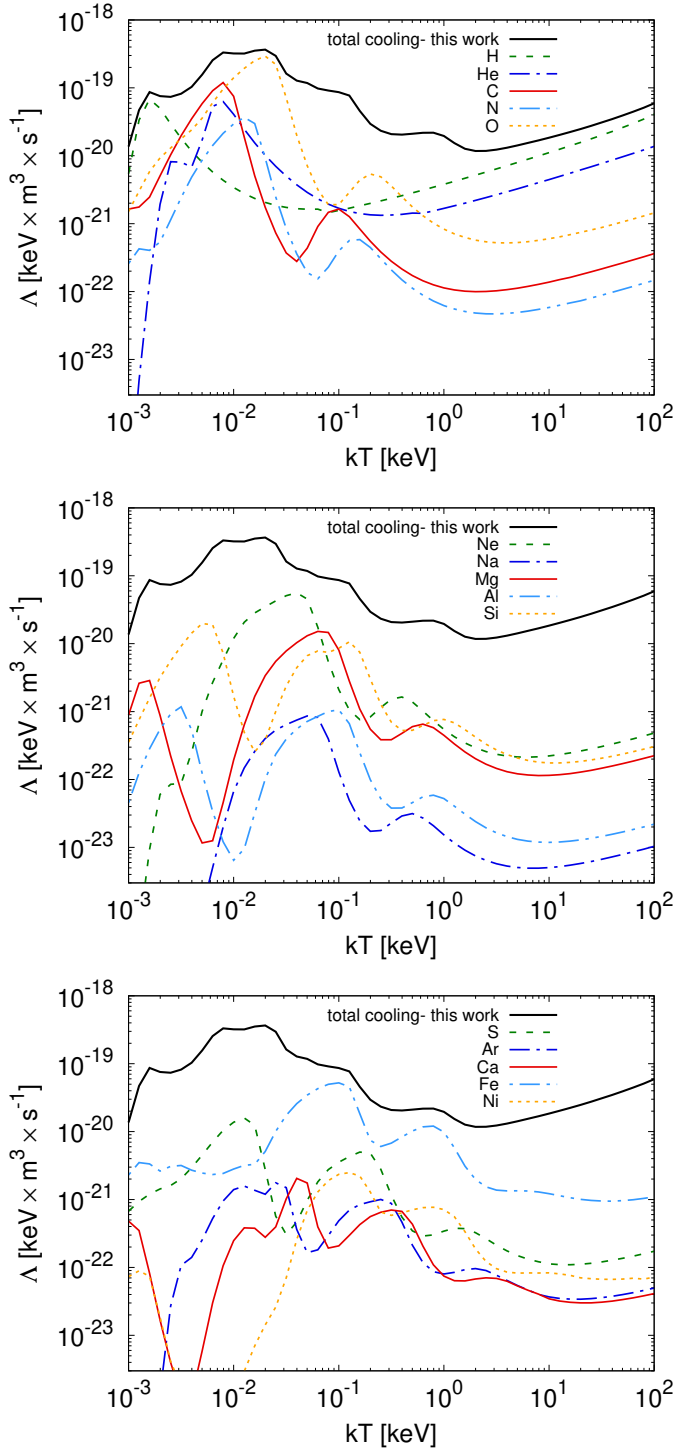


**Figure 5.7:** Total cooling curve obtained in this work (black solid line) and individual contributions to the total cooling from different elements.

temperature from SPEX, use it as an input to Cloudy calculations, and as an output we get the Cloudy cooling rates as well as the electron density that Cloudy assumes for the assumed hydrogen density (for Cloudy it is necessary to give the hydrogen density to run the calculations, whereas SPEX needs the electron density for version 3.06.00 and lower). These quantities are used for rescaling the Cloudy cooling rates from units of  $[\text{erg} \times \text{cm}^{-3} \times \text{s}^{-1}]$  to units of  $[\text{keV} \times \text{m}^3 \times \text{s}^{-1}]$  which are used in the graphs throughout this paper.

In the energy range from  $2 \times 10^{-2}$  to 30 keV, APEC and SPEX are in reasonable agreement. For higher energies, the differences are negligible (approximately 2% at 86 keV), even though SPEX and APEC use different treatments of relativistic corrections to the Bremsstrahlung emission (free-free emission). SPEX uses the correction described in Eq. (B4) in Kylafis & Lamb (1982) (based on Gluckstern et al. (1953)). On the other side, APEC (to be more precise, its PyAtomDB module) offers the user to use either a non-relativistic (Hummer 1988), semi-relativistic (Kellogg et al. 1975), or relativistic (Nozawa et al. 1998) version of Bremsstrahlung. In Fig. 5.8, we plot the relativistically corrected Bremsstrahlung using (Nozawa et al. 1998).

The cooling curves from SPEX (this work) and Cloudy agree reasonably well for all temperatures besides very low ones around 2 eV (cooling due to neutral hydrogen) and higher temperatures above 10 keV, where the main differences come from the relativistic corrections to Bremsstrahlung, where Cloudy uses van Hoof et al. (2015). Even though both codes use the Born approximation, we still see significant differences in the relativistic corrections to Bremsstrahlung (by approximately 28% at 100 keV). However, these energies are not the main interest of our paper and therefore we did not investigate the differences in specific treatments of the relativistic corrections to Bremsstrahlung in more detail.

Our new cooling curve is now more in agreement with Cloudy, especially at temperatures around  $10^{-2}$  keV ( $\sim 10^5$  K). This is mainly due to the updates of carbon, oxygen, and neon ions. This agrees well with the findings of Lykins et al. (2013), which states that Schure et al. (2009) finds significantly more cooling in this regime in comparison with Cloudy and that the most probable reasons for that are the differences in the atomic data for oxygen and carbon, since these are the main coolants for these temperatures.

We also improve the cooling for the temperatures around 2.5 eV where we find significant discrepancies between SPEX and other codes. For this temperature, the bulk of the difference between Cloudy and SPEX comes from the cooling by H I from which 71% is produced by Lyman  $\alpha$  lines and 8% is produced by Lyman  $\beta$  (considering a CIE plasma). The SPEX data for H I in version 3.06.00 and older were based on the extrapolations of R-matrix calculations of C VI (Aggarwal & Kingston 1991a), Ne X (Aggarwal & Kingston 1991b), Si XIV (Aggarwal & Kingston 1992b), and Ca XX (Aggarwal & Kingston 1992a) with an assumption that the Gaunt factor does not strongly depend on the atomic number  $Z$  and is more or less constant along the iso-electronic sequence. This assumption, however, breaks for the neutral atoms (van Regemorter 1962) and influences the collision strength calculations. Due to this assumption, there was a significant difference between cooling in SPEX and Cloudy around 2.5 eV.

After a careful comparison of various calculations that are available in the literature, we replaced the collision strengths for neutral hydrogen with data from CHIANTI in SPEX version 3.06.01 (which is used in this paper). This data is based on Anderson et al. (2000) and revised by Anderson et al. (2002). The update resulted in a decrease in SPEX cooling due to neutral hydrogen by a factor of three for temperatures around 2.5 eV and now shows a better agreement of SPEX and other plasma codes. For our final updated cooling curve based on the calculations and discussions in this paper (including the updates of the radiative loss rates due to collisional excitation and the updates of the collision strengths of neutral hydrogen), we invite the reader to check the black line in Fig. 5.7 and Fig. 5.8.

Lastly, Fig. 5.9 shows the comparison of the radiative loss curve obtained with MEKAL (the same as presented in Schure et al. (2009)) and the radiative loss curve obtained from the cie model in SPEX (version 3.06.01), as well as the cooling curve obtained from the pion model used in its CIE limit (ionisation parameter is set to zero). As we already mentioned in the introduction, unless the processes such as heat conduction or magnetic fields are taken into account, for the low-density CIE plasma in an enclosed, non-expanding box, the total cooling is the same as the energy radiated away. This holds true if the cooling is defined as the energy loss of the population of free electrons. However, if we

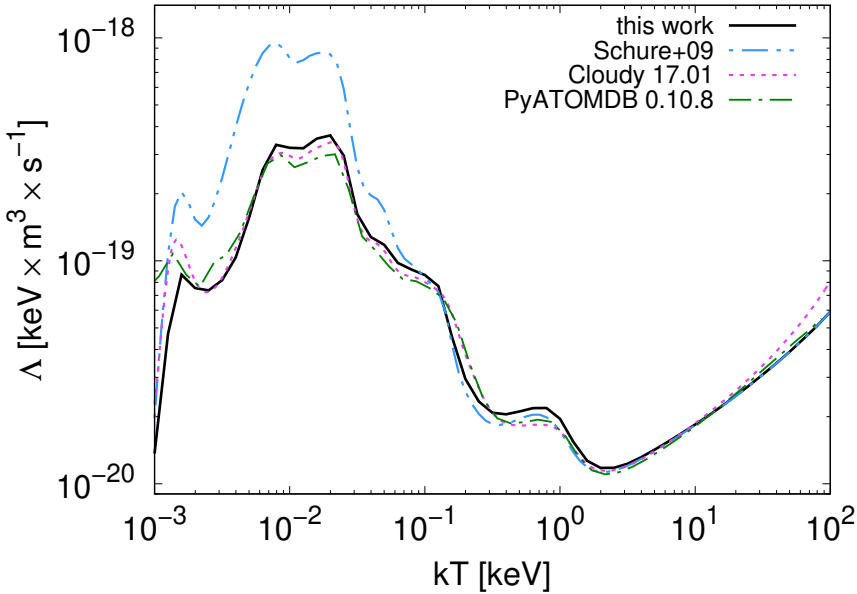


**Figure 5.8:** Comparison of the updated total cooling curve from SPEX (black solid line) and Cloudy (purple dashed line) to the total radiative loss curve from Schure et al. (2009) (blue dash-double-dotted line) and APEC (green dash-dotted line).

consider individual atomic processes, the cooling and the radiative loss do not have to be the same, as in the case of collisional ionisation or radiative recombination, for example. For collisional ionisation the cooling is greater than the radiative loss (the cooling by the free electron is equal to the ionisation potential of the relevant ion, nothing is radiated away, and the energy loss is zero), whereas for radiative recombination the cooling is less than the radiative loss; the contribution to the cooling comes from the kinetic energy of the free electron that is being captured, while the contribution to the total radiative loss is the kinetic energy of the free electron plus the ionisation potential of the ion into which the free electron is captured. However, since in the balanced plasma the number of ionisations is equal to the number of recombinations, these differences between cooling and radiative loss for the ionisation and the recombination processes (for instance also dielectronic recombination) cancel out. However, if we pay a close attention to the red and black curves in Fig. 5.9, we see that the total cooling curve is not the same as the total radiative loss curve for CIE plasma such as that described above. The reason is that the spectral calculation in the CIE model in SPEX still lacks the relevant complete and updated atomic data for several ions, in particular the ions for which we used Chianti data for the cooling contribution (see Fig. 5.4). Correcting for this discrepancy at low temperatures is out of the scope of this paper and will be addressed in the future releases of SPEX.

## 5.4 Application: Stability curve for photoionised plasmas

In the previous sections, we focused on a CIE plasma when no additional source of excitation or ionisation other than collisions with free electrons played a role in exciting (ionising) the plasma. In this section, we examine plasma that is exposed to such external source of ionisation, and we assume the plasma is in photoionisation equilibrium.

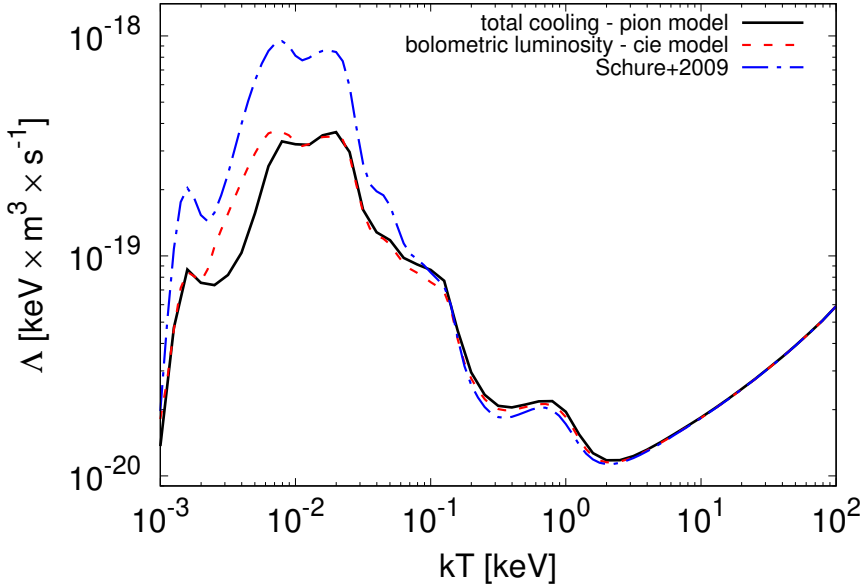


**Figure 5.9:** Comparison of the radiative loss curve obtained from Schure et al. (2009) (blue dash-dotted line), the radiative loss curve obtained from the cie model (red dashed line) in SPEX version 3.06.01, and the cooling curve obtained from the pion model (black solid line) in its CIE limit (zero ionisation parameter).

We updated the cooling function of the photoionisation model pion according to Section 5.3.6 (specifically the contribution to the cooling by the collisional excitation described in Sections 5.2 and 5.3.3, dielectronic recombination described in Section 5.3.5, and the update of the collision strengths of neutral hydrogen discussed in Section 5.3.8) and quantified the changes between the most recently updated SPEX (this work, SPEX version 3.06.01), and the previous one, SPEX version 3.05.00. We calculate the stability curve for plasma (the so called S-curve) and compare the results of our new updated cooling to the cooling in SPEX version 3.05.00, which uses the MEKAL code to calculate the cooling by collisional excitation. We remind the reader that the cooling/heating we refer to in SPEX relates to the cooling/heating of the population of free electrons only.

### 5.4.1 Thermal stability curve

While determining the ionisation equilibrium in PIE plasma, it is convenient to define the ionisation parameter  $\xi$  (Tarter et al. 1969; Krolik et al. 1981)

$$\xi \equiv \frac{L}{n_{\text{H}} r^2}, \quad (5.5)$$

where the ionising source is described by the luminosity  $L$  over the energy band 1–1000 Rydbergs,  $n_{\text{H}}$  is the hydrogen density, and  $r$  is the distance of the plasma from the source of ionisation. To obtain the thermal stability curve, we need to define the ionisation parameter in its dimensionless pressure form  $\Xi$ :

$$\Xi \equiv \frac{1}{4\pi c k} \frac{\xi}{T}, \quad (5.6)$$

where  $c$  is the speed of light,  $k$  is the Boltzmann constant, and  $T$  is the electron temperature. On the S-curve, the total cooling rate is equal to the total heating rate. Based on the slope of the S-curve

(positive or negative), one can tell whether the plasma is thermally stable ( $dT/d\Xi > 0$ ) or thermally unstable ( $dT/d\Xi < 0$ ).

### 5.4.2 Obtaining the S-curve in SPEX

After updating the cooling rates for the pion model, we compared new S-curves (following the updates in Section 5.2 and 5.3) with the S-curves obtained from SPEX version 3.05.00 for three different spectral energy distributions (SEDs) based on Mehdipour et al. (2016): (a) a power-law continuum (labelled PL) in the energy band  $10^{-4}$ – $10^3$  keV, with the photon index assumed to be  $\Gamma = 2$ ; (b) an unobscured active galactic nucleus (AGN) that corresponds to NGC 5548 (Mehdipour et al. 2015, labelled AGN1); and (c) an obscured version of AGN1 (labelled AGN2). We described plasma photoionised by such SEDs in SPEX with the pion model. The transmitted spectrum was then calculated when the photons emitted from the ionising source ionised the plasma and by using the plasma routines in SPEX; the photoionisation equilibrium (ionisation and energy balance) was calculated self-consistently. In SPEX, the atomic processes that contribute to the total cooling are: inverse Compton scattering, electron ionisation, radiative recombination, free-free emission, collisional excitation, dielectronic recombination, and adiabatic expansion. The atomic processes that contribute to the total heating are: free-free absorption, photo-electrons, Compton ionisation, Auger electrons, collisional de-excitation, and external sources of ionisation.

We selected the grid for the ionisation parameter  $\xi$  in the  $10^{-7}$ – $10^{10}$  nWm range, and for each  $\xi$  we obtained the equilibrium electron temperature  $T$ . The pressure form of the ionisation parameter  $\Xi$  was then calculated using Eq. (5.6).

### 5.4.3 A new stable branch

We show the ratio of the total cooling rate as a function of equilibrium temperature  $kT$  for SPEX version 3.06.01 (this work) and SPEX version 3.05.00 in Fig. 5.10 for all SEDs mentioned in Section 5.4.2. We show a similar comparison for the radiative loss curve for the CIE case in Fig. 5.6, where we compared SPEX version 3.06.01 to its precursor, MEKAL. In Fig. 5.10, we make a comparison to the latest previously published update by Mehdipour et al. (2016).

The biggest difference between SPEX 3.06.01 and 3.05.00 can be seen for equilibrium temperatures from  $10^{-3}$ – $2 \times 10^{-2}$  keV (apart from the resonant excitation around  $10^{-3}$  keV, which is not the main focus of this paper) where the total cooling decreased by almost 30%. This result is expected since the updates of the collisional excitation and the H I collision strengths caused a decrease in the total radiative loss curve, as we show in Fig. 5.6, Fig. 5.8, and Fig. 5.9.

Knowing the equilibrium temperature and the ionisation parameter makes it possible to calculate the dependence of  $\Xi = \Xi(kT)$  using Eq. (5.6) and obtain the stability curves. The S-curves for all three SEDs before and after the updates are plotted in the top panel of Fig. 5.11, where for values of  $\Xi > 20$  the S-curves do not change their shape or normalization, while for  $\Xi < 10^{-1}$  the equilibrium temperature decreases significantly towards lower values of  $\Xi$ .

If we look at the bottom panel of Fig. 5.11, where we see a zoomed-in view of the upper panel for  $\Xi \in (1, 20)$  and  $kT \in (10^{-3}, 1)$  keV, we notice a different behaviour and the change of the slope in two specific cases: (a) AGN1,  $kT \sim 10^{-1}$  keV and  $\Xi \sim 7$ , where the S-curve is almost vertical; and (b) AGN2,  $kT \sim (1.43\text{--}1.82) \times 10^{-2}$  keV and  $\Xi \in (10.17\text{--}10.96)$ , where an additional stable branch is found. We address the ionic column densities that are peaking on these stable branches in the following subsection.

### 5.4.4 Ionic column densities

In Fig. 5.12 and Fig. 5.13, we show where the individual ionic column densities  $N_{\text{ion}}$  peak on the S-curve in  $(kT, \Xi)$  phase space for AGN1 and AGN2 SEDs, where we find the changes in the S-curve slope (see Section 5.4.3). As an example, we show the maximum ionic concentrations for C, O, Ne, Mg, Al, Si,

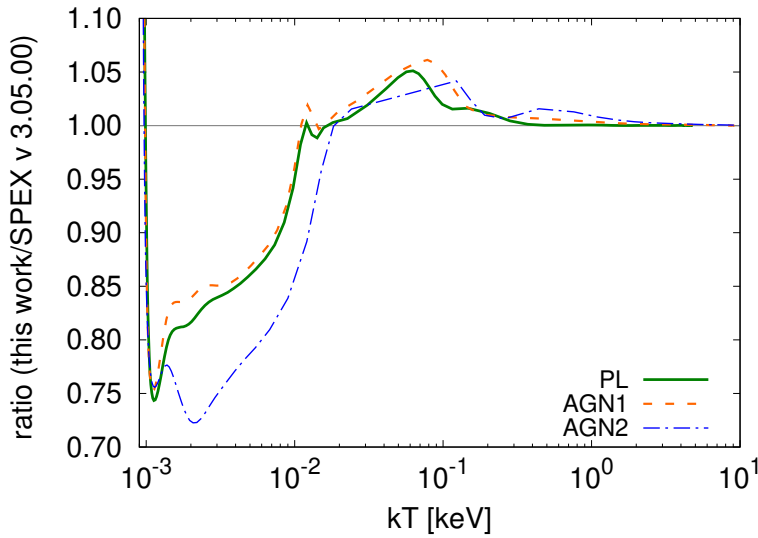


**Figure 5.10:** Ratio of the total cooling curve for the updated pion model (this work) and the previous version calculated with SPEX v 3.05.00 as a function of the equilibrium temperature  $kT$ .

and Fe. For AGN1, we find that Al xiii, Si xiv, Fe xx, and Fe xxv ions peak at the branch that changed from positive (stable) to almost vertical. In the case of AGN2, the ions which peak on the new stable branch are O viii, Ne x, Mg x, Mg xi, Al x, Al xi, Al xii, Si x, Si xi, Si xii, Fe x, Fe xi, Fe xii, Fe xiii, and Fe xiv. For the case of AGN2, before the updates these ions were peaking on the unstable branch. After the updated cooling is implemented to pion these ions are found on the new stable branch and could be potentially observed (based on the column densities) in the photoionised gas with equilibrium temperature around  $1\text{--}2 \times 10^{-2}$  keV.

From Fig. 5.12 and Fig. 5.13, one might infer, for instance, that there is no highly ionised iron at all (Fe xix to Fe xxvi) because most of it would fall on the unstable branch of the S-curve. This is not the case, because these ions are formed over a broad range of ionisation parameters or temperatures (in these figures, we only show where the ionic column densities peak). For example, Fe xxv and Fe xxvi have concentrations larger than 10% of their peak concentration over a range spanning a factor of 20 in temperature. Similarly, for the lower ionised ions of iron, the stable regions can offer sufficient Fe xix to Fe xxiv to be detectable. Obviously, the total measured column density for these ions might be reduced because contributions from the unstable regions are missing.

## 5.5 Discussion

### 5.5.1 Theoretical calculations

Because radiative cooling occurs on various scales throughout the Universe, the importance of understanding the details and atomic processes that lead to gas cooling down are central to our knowledge of astrophysical plasmas. Many line complexes and spectral features are still hardly resolved with nowadays instruments and therefore in many cases we need to rely on theoretical calculations of transition probabilities and line energies.

These theoretical calculations cannot be done without approximations used to solve the Schrödinger equation. These include independent-particle approximation, variational principle, many-body perturbation theory (Brueckner 1955; Goldstone 1957), Born (Born 1926), Born-Oppenheimer (Born & Oppen-



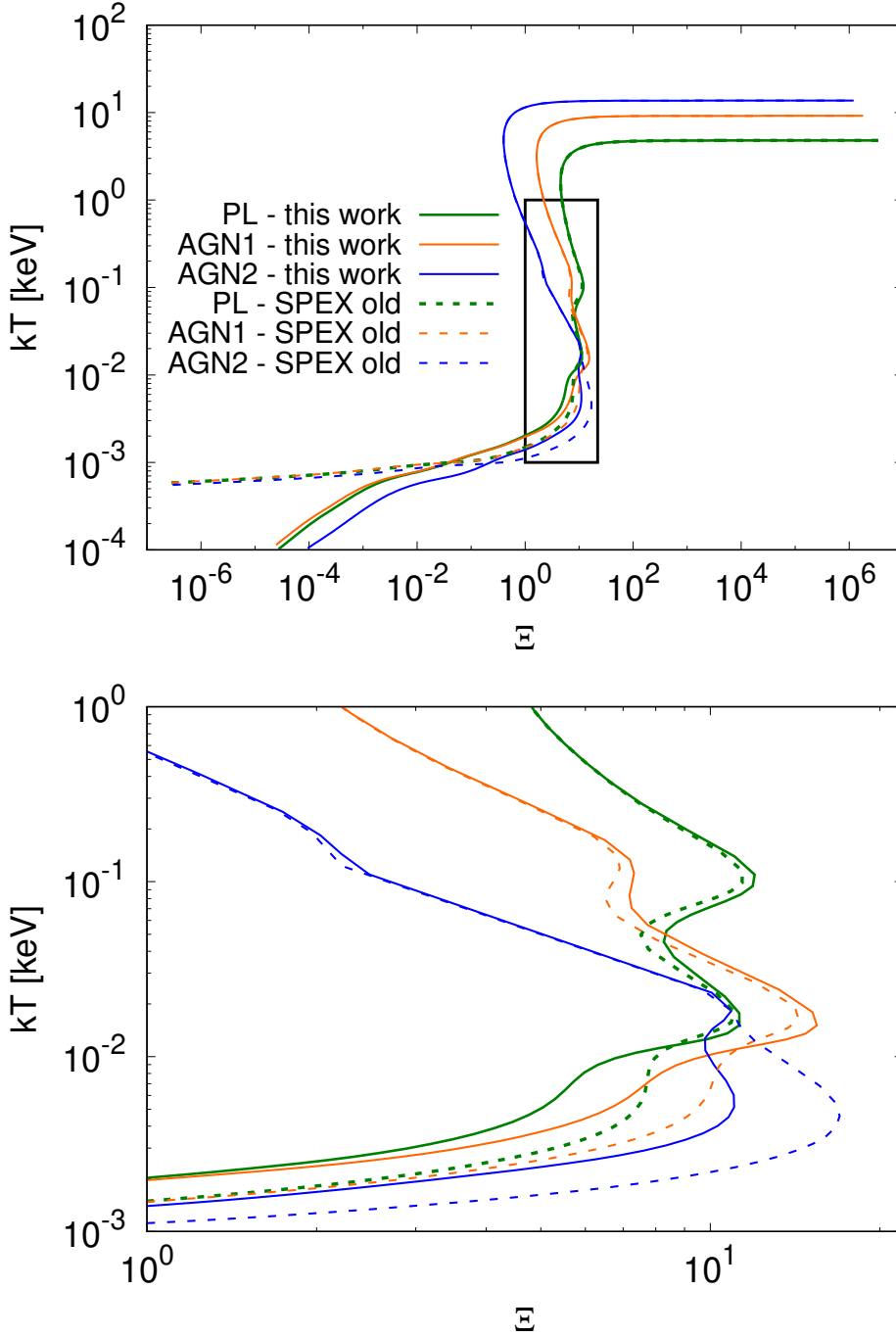


**Figure 5.11:** Stability curves for new (this work) and SPEX version 3.05.00 (labelled as SPEX old) calculations after implementing the updates of the collisional excitation, dielectronic recombination and collision strengths of neutral hydrogen (top panel), and a zoomed-in view for  $\Xi \in (1, 20)$  and  $kT \in (10^{-3}, 1)$  keV (bottom panel).

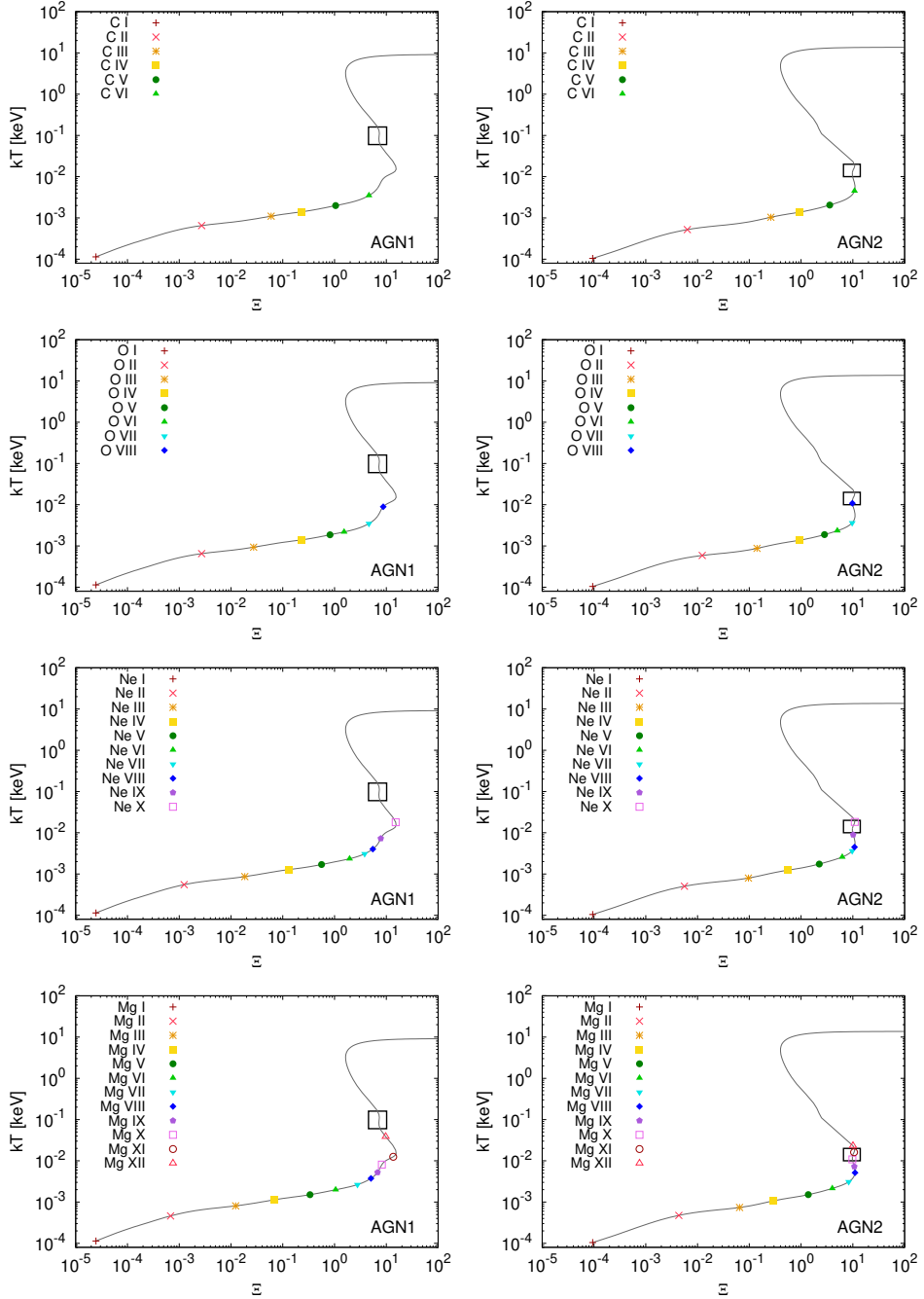


**Figure 5.12:** Stability curves for AGN1 (left panel) and AGN2 (right panel), with coloured points indicating the points in  $(kT, \Xi)$  phase space, where the column densities of C, O, Ne, and Mg peak. The rectangles represent new stable branches found after implementing the updates (described in this paper) to the photoionisation model pion in SPEX.

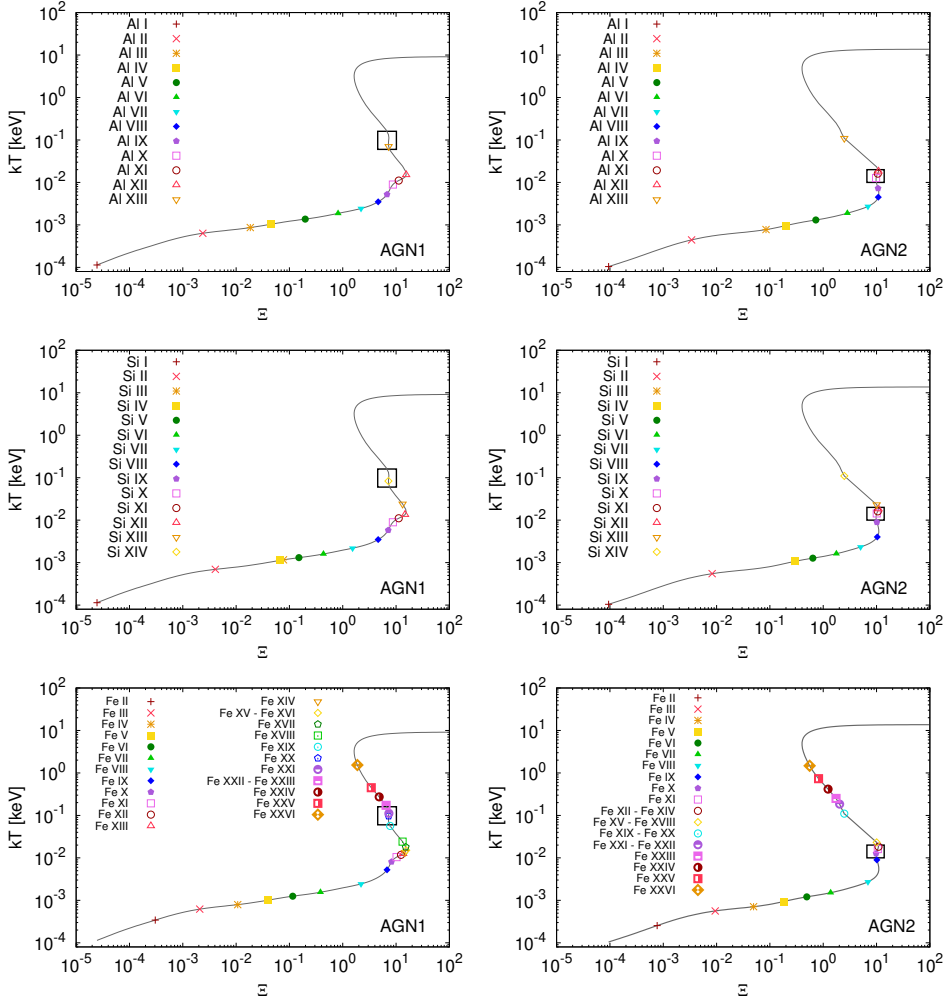


Figure 5.13: Same as Fig. 5.12 but for Al, Si, and Fe ions.

heimer 1927), the Coulomb-Born-Oppenheimer or widely used distorted wave (Mott & Massey 1933), and R-matrix approximations (Burke & Berrington 1993b).

Theoretical line energies can also differ from measured line energies. For example, for the calculations made with CHIANTI (see the ions in Fig. 5.4), and depending on the ion and the complexity of the system, we find differences as low as  $<1\%$  but also as high as  $10\%$ . For most ions, the difference between the radiative loss rate (per ion) using theoretical or observational line energies is less than a few percent, with only a few exceptions when the difference can be up to  $200\%$  (for instance,  $\text{Cl II}$ ,  $\text{Ar III}$ ,  $\text{Ar V}$ ,  $\text{Ca V}$ ). On the other hand, the wavelengths of the dominant lines in the SPEX code are in general very well benchmarked with observational data, and the energy uncertainties affect the corresponding ionic cooling rates by a much smaller amount than the uncertainties in the collision strengths.

All differences in the above-mentioned approximations then contribute to discrepancies between plasma codes and atomic databases. On top of that, the calculation of spectra depends on physical processes that are very complex and often treated in a simplified manner or are neglected completely (for example, before our updates presented in this paper, the radiative loss by collisional excitation was calculated in the pion model using MEKAL, and the potassium-to-zinc iso-electronic sequences were missing). This only shows the importance of constant updates of atomic data and supports independent development of the plasma codes that can then be compared to measurements.

## 5.5.2 Comparison of SPEX to other plasma codes

Such a comparison of differences between plasma codes is also shown in our results in Section 5.3. First, we considered the radiative loss curves for collisional excitation in SPEX and compared them with the radiative loss curves obtained from its precursor MEKAL, which is still being used by the community to analyse the X-ray spectra. The shapes and normalisations of these curves vary from ion to ion. As seen from Fig. 5.6, the significant difference between MEKAL and SPEX lies in the updates of the collisional excitation rates for  $\text{C III}$ ,  $\text{O V}$ , and  $\text{Ne VII}$  ions. The updates resulted in a decrease of the total radiative loss, especially for temperatures between  $2 \times 10^{-3}$ – $10^{-1}$  keV. This is also valid for the total cooling curve, as we showed in the comparison to Schure et al. (2009), where the total cooling in the same temperature range decreased by almost  $70\%$  (for the temperatures around  $0.01$  keV). For this temperature range, the updates of the collisional excitation resulted in a closer agreement of the total cooling curve of SPEX with other codes such as Cloudy or APEC.

As already discussed in Section 5.3.8, we found that due to incorrect collision strengths for neutral hydrogen in SPEX up to version 3.06.00, the SPEX cooling rates were significantly overestimated for temperatures around  $\sim 2.5$  eV, which is the temperature at which neutral hydrogen is a dominant coolant. After detailed examination, we decided to adopt the collision strength values for neutral hydrogen from the CHIANTI database and used this atomic data in SPEX. This led to a decrease in SPEX cooling at this temperature and resulted in a closer agreement between SPEX, Cloudy, and APEC.

### 5.5.3 Metastable levels

With Be-like oxygen, we demonstrated the importance of the radiative loss from metastable levels, which can be even higher than the radiative loss from the ground level for temperatures such as those below  $2 \times 10^{-3}$  keV and above  $3$  keV. However, the radiative loss from metastable levels is not yet included in SPEX, because to have a fully self-consistent model the ionisation and recombination rates from and to these metastable levels also need to be taken into account in the ionisation balance. Although we show only the metastable levels in the case of collisional ionisation equilibrium, many works point out how these metastable levels are also important for the plasma in photoionisation equilibrium (see for example, Osterbrock 1974; Sutherland & Dopita 1993; Ferland et al. 1998 or one of the recent works of Bertone et al. 2013, where in general the cooling gas is studied via cosmological hydrodynamical simulations in which the cooling rates become an essential ingredient for understanding the Universe on large scales. The processes that become important at temperatures below  $10^6$  K ( $0.09$  keV) are mainly the radiative recombination and two-photon decays of the metastable levels).

### 5.5.4 Update of the pion model in SPEX

In Section 5.3.6, we presented an updated model for the cooling due to collisional excitation only that was applied to pion model. The updated radiative loss due to collisional excitation lead to a different contribution from specific processes included in the overall heating/cooling balance of the photoionised plasmas. For three different SEDs, we plotted the stability curve for the updated PIE model and noticed two main differences: (a) at low values of  $\Xi$ , the slope of the S-curve became steeper in comparison with old calculations; and (b) for  $\Xi \in (1, 20)$ , where the behaviour of the S-curves changed (mainly for AGN1 and AGN2 SEDs): in the case of AGN1, the S-curve changed its slope to almost vertical, while for AGN2 we found a new stable branch. By calculating where the ionic column densities peak, we showed which ions lie in the regions of new stability branches. These ions are then expected to exist under such conditions in the photoionised plasmas (AGN1: Al XIII, Si XIV, Fe XX, Fe XXI; AGN2: O VIII, Ne x, Mg x, Mg xi, Al x, Al xi, Al xii, Si x, Si xi, Si xii, Fe x, Fe xi, Fe xii, Fe xiii, Fe xiv).

The S-curves for the same sample of SEDs were also studied in Mehdipour et al. (2016), where the authors showed the comparison of SPEX (version 3.02.00) to other photoionisation codes such as Cloudy (version 13.01) and XSTAR (version 2.3). In this older version of SPEX, no stable branch for AGN2 was found for  $\Xi \sim 10$ , whereas Cloudy and XSTAR showed a different behaviour (slope of the S-curves is positive). This shows that by updating the cooling via collisional excitation, which also affects the total cooling in the photoionisation model, the new version of the pion model in SPEX predicts S-curves that are in better agreement with the predictions from Cloudy and XSTAR, mainly for the AGN2 case where Cloudy and XSTAR already predicted the stable branch for  $\Xi \sim 10$ . This stable branch was found in SPEX after the updates of the radiative loss curve presented in this paper (see Fig. 5.11).

In general, the S-curve can be more complicated and can have multiple stable or unstable branches that depend on the source of ionisation and its SED as well as chemical composition and density of the absorbing gas along the line of sight (for instance, see Hess et al. 1997; Rózańska et al. 2008; Chakravorty et al. 2009; Lee et al. 2013). For example, as Chakravorty et al. (2012) showed, this can be caused by the strength of the soft excess as well as changes in the temperature of the accretion disc. Among the fairly recent observational papers showing such S-curves are Mehdipour et al. (2015), and Mehdipour et al. (2016), which shows a very unusual S-curve found for ultra-fast outflow in the quasar PDS 456 (Boissay-Malaquin et al. 2019).

Understanding these stable or unstable branches of S-curves can be important for studying the surroundings of AGN. Mehdipour et al. (2015) show how the obscurer in NGC 5548 shields the ionising radiation and creates a significant unstable branch on the S-curve. They studied the source in multiple epochs, and by calculating the S-curves and the peaking ionic column densities they found that highly ionised states of iron (Fe XXIII and Fe XXVI) fell on the unstable branches for all five epochs, which lead to the conclusion that these ions might be lacking in the photoionised gas regardless of the obscured or unobscured scenario.

Updating photoionisation models is also important for the estimation of the so-called absorption measure distribution (AMD), which describes the ionisation structure of the AGN wind (the density radial profile of the AGN wind is constrained by the slope of AMD Behar 2009) and depends on the ionisation parameter  $\xi$  and the hydrogen column density  $N_H$ . AMD is defined as (Holczer et al. 2007)

$$\text{AMD} = \frac{dN_H}{d \log \xi} . \quad (5.7)$$

Such AMD often shows a deep minimum in the column density profile, corresponding most often to  $\log \xi$  roughly between 1 and 2 (but this can differ from source to source). This is interpreted as the thermally unstable gas (for instance, see Behar 2009; Detmers et al. 2011; Stern et al. 2014; Adhikari et al. 2015 and references therein). If different timescales (for example, recombination, cooling or dynamical timescales) are obtained, the limits to the hydrogen column density and to the distance of the absorber from the ionising source can be obtained (for example, see Mehdipour et al. (2018) for more details).

## 5.6 Conclusions

In this work, we highlight the differences of excitation rates among different plasma codes (MEKAL, APEC, Cloudy) and other atomic databases (CHIANTI, ADAS). We show how the updates, mainly of collisional excitation, impact the radiative loss rates as well as the cooling rates in SPEX. Our main findings are as follows:

- The comparison between MEKAL and the newest version of SPEX (presented in this paper, version 3.06.01) shows that the updates of collisional excitation affect the total radiative loss curve mainly in the temperature range between  $2 \times 10^{-3} - 10^{-1}$  keV, where a significant decrease by 70% is found (Fig. 5.6).
- We calculate the total cooling curve (Fig. 5.7) considering the most updated version of SPEX (version 3.06.01), which includes the updated contribution to the cooling by the collisional excitation and dielectronic recombination. Additionally, we describe an update of the collision strengths of neutral hydrogen, which mainly affects the cooling for temperatures around 2.5 eV. All considered updates result in a better agreement of the SPEX cooling curve and the cooling curves obtained by other plasma codes such as Cloudy and APEC (Fig. 5.8).
- We implement the new cooling to the SPEX photoionisation model pion and demonstrate the impact of the updates on the stability curve of photoionised plasmas. By using the updated cooling tables we find new stable branches on the stability curves (Fig. 5.11) and associate them with an example set of ions for which the ionic column densities peak on these stability branches (Fig. 5.12 and 5.13).

With this work we show the importance of constant updates of atomic databases and plasma codes in order to understand more precisely the high-resolution spectroscopic data that will be obtained by upcoming missions, such as XRISM and Athena. These updates are also crucial for the calculation of the cooling curve, which is an important ingredient for the cooling processes in various astrophysical objects (in this paper we used AGN as an example).

**Acknowledgements:** The authors acknowledge the financial support from NWO, the Netherlands Organisation for Scientific Research and NOVA, the Netherlands Research School for Astronomy. We thank Ton Raassen, Junjie Mao and Liyi Gu for very useful and detailed discussions about atomic data and various aspects of the calculation of the collision strengths. We thank CHIANTI, PyAtomDB and Cloudy teams for the support they provide to the users of their atomic databases and plasma codes. We thank the astrophysics group at SRON and Joop Schaye's group at the Leiden University for the support throughout the various stages of this project. Last but not least, we thank the referee of this paper for the detailed referee report which helped us to improve this paper.



## Bibliography

---

- Adhikari S., Dalal N., Chamberlain R. T., 2014, *J. Cosmology Astropart. Phys.*, 2014, 019
- Adhikari T. P., Róžańska A., Sobolewska M., Czerny B., 2015, *ApJ*, 815, 83
- Aggarwal K. M., 1983, *ApJS*, 52, 387
- Aggarwal K. M., 1985, *A&A*, 146, 149
- Aggarwal K. M., Kingston A. E., 1991a, *Journal of Physics B Atomic Molecular Physics*, 24, 4583
- Aggarwal K. M., Kingston A. E., 1991b, *Phys. Scr.*, 44, 517
- Aggarwal K. M., Kingston A. E., 1992a, *Journal of Physics B Atomic Molecular Physics*, 25, 751
- Aggarwal K. M., Kingston A. E., 1992b, *Phys. Scr.*, 46, 193
- Aggarwal K. M., Berrington K. A., Burke P. G., Kingston A. E., Pathak A., 1991, *Journal of Physics B Atomic Molecular Physics*, 24, 1385
- Ahoranta J., Finoguenov A., Pinto C., Sanders J., Kaastra J., de Plaa J., Fabian A., 2016, *A&A*, 592, A145
- Ahoranta J., et al., 2020, *A&A*, 634, A106
- Ahoranta J., Finoguenov A., Bonamente M., Tilton E., Wijers N., Muzahid S., Schaye J., 2021, *A&A*, 656, A107
- Akamatsu H., et al., 2017, *A&A*, 606, A1
- Allen C. W., 1973, *Astrophysical quantities*
- Allen S. W., Evrard A. E., Mantz A. B., 2011, *ARA&A*, 49, 409
- Altamura E., Kay S. T., Bower R. G., Schaller M., Bahé Y. M., Schaye J., Borrow J., Towler I., 2022, *arXiv e-prints*, p. arXiv:2210.09978
- Anders E., Grevesse N., 1989, *Geochimica Cosmochimica Acta*, 53, 197
- Anderson H., Ballance C. P., Badnell N. R., Summers H. P., 2000, *Journal of Physics B Atomic Molecular Physics*, 33, 1255
- Anderson H., Ballance C. P., Badnell N. R., Summers H. P., 2002, *Journal of Physics B Atomic Molecular Physics*, 35, 1613
- Arnaud M., Raymond J., 1992, *ApJ*, 398, 394
- Arnaud M., Rothenflug R., 1985, *A&AS*, 60, 425
- Arnaud M., Pratt G. W., Piffaretti R., Böhringer H., Croston J. H., Pointecouteau E., 2010, *A&A*, 517, A92
- Asplund M., Grevesse N., Sauval A. J., Scott P., 2009, *ARA&A*, 47, 481
- Babul A., White S. D. M., 1991, *MNRAS*, 253, 31P
- Bahé Y. M., et al., 2017, *MNRAS*, 470, 4186



- Baker S., Cousins R. D., 1984, *Nuclear Instruments and Methods in Physics Research*, 221, 437
- Baldi A., Forman W., Jones C., Kraft R., Nulsen P., Churazov E., David L., Giacintucci S., 2009, *ApJ*, 707, 1034
- Ballance C. P., Badnell N. R., Smyth E. S., 2003, *Journal of Physics B Atomic Molecular Physics*, 36, 3707
- Bar-Shalom A., Klapisch M., Oreg J., 2001, *J. Quant. Spectrosc. Radiative Transfer*, 71, 169
- Barnes D. J., et al., 2017, *MNRAS*, 471, 1088
- Barret D., et al., 2018, in den Herder J.-W. A., Nikzad S., Nakazawa K., eds, *Society of Photo-Optical Instrumentation Engineers (SPIE) Conference Series Vol. 10699, Space Telescopes and Instrumentation 2018: Ultraviolet to Gamma Ray*. p. 106991G (arXiv : 1807 . 06092), doi:10.1117/12.2312409
- Barret D., et al., 2022, arXiv e-prints, p. arXiv:2208.14562
- Behar E., 2009, *ApJ*, 703, 1346
- Bell K. L., Berrington K. A., Thomas M. R. J., 1998, *MNRAS*, 293, L83
- Berrington K. A., Burke P. G., Dufton P. L., Kingston A. E., 1985, *Atomic Data and Nuclear Data Tables*, 33, 195
- Bertone S., Schaye J., Dolag K., 2008, *Space Sci. Rev.*, 134, 295
- Bertone S., Schaye J., Dalla Vecchia C., Booth C. M., Theuns T., Wiersma R. P. C., 2010a, *MNRAS*, 407, 544
- Bertone S., Schaye J., Booth C. M., Dalla Vecchia C., Theuns T., Wiersma R. P. C., 2010b, *MNRAS*, 408, 1120
- Bertone S., Aguirre A., Schaye J., 2013, *MNRAS*, 430, 3292
- Bhatia A. K., Kastner S. O., 1993, *Atomic Data and Nuclear Data Tables*, 54, 133
- Bhatia A. K., Mason H. E., 1981, *A&A*, 103, 324
- Biffi V., Mernier F., Medvedev P., 2018, *Space Sci. Rev.*, 214, 123
- Boehringer H., Hensler G., 1989, *A&A*, 215, 147
- Boehringer H., Werner N., 2009, arXiv e-prints, p. arXiv:0907.4277
- Böhringer H., Werner N., 2010, *A&ARv*, 18, 127
- Böhringer H., et al., 2007, *A&A*, 469, 363
- Boissay-Malaquin R., Danehkar A., Marshall H. L., Nowak M. A., 2019, *ApJ*, 873, 29
- Bond J. R., Kofman L., Pogosyan D., 1996, *Nature*, 380, 603
- Booth C. M., Schaye J., 2009, *MNRAS*, 398, 53
- Born M., 1926, *Zeitschrift für Physik*, 38, 803
- Born M., Oppenheimer R., 1927, *Annalen der Physik*, 389, 457
- Briel U. G., Henry J. P., 1995, *A&A*, 302, L9
- Bristow P. D., Phillipps S., 1994, *MNRAS*, 267, 13
- Brueckner K. A., 1955, *Physical Review*, 97, 1353
- Bryans P., Landi E., Savin D. W., 2009, *ApJ*, 691, 1540
- Buote D. A., 2000, *MNRAS*, 311, 176
- Burbidge E. M., Burbidge G. R., Fowler W. A., Hoyle F., 1957, *Reviews of Modern Physics*, 29, 547

- Burke P. G., 1993, in , *Many-Body Theory of Atomic Structure and Photoionization*. Edited by CHANG T. N. Published by World Scientific Publishing Co. Pte. Ltd. pp 47–82, doi:10.1142/9789814355940\_0003
- Burke P. G., Berrington K. A., 1993b, in Burke P. G., Berrington K. A., eds, *Atomic and molecular processes : an R-matrix approach*. Bristol ; Philadelphia : Institute of Physics
- Burke P. G., Berrington K. A., 1993a. <https://api.semanticscholar.org/CorpusID:92948354>
- Butler Contreras A., Lau E. T., Oppenheimer B. D., Bogdán Á., Tillman M., Nagai D., Kovács O. E., Burkhardt B., 2023, *MNRAS*, 519, 2251
- Callaway J., 1994, *Atomic Data and Nuclear Data Tables*, 57, 9
- Cameron A. G. W., 1957, *PASP*, 69, 201
- Cash W., 1979, *ApJ*, 228, 939
- Cavagnolo K. W., Donahue M., Voit G. M., Sun M., 2009, *ApJS*, 182, 12
- Cavaliere A., Fusco-Femiano R., 1976, *A&A*, 49, 137
- Cen R., Ostriker J. P., 1999, *ApJ*, 514, 1
- Cen R., Miralda-Escudé J., Ostriker J. P., Rauch M., 1994, *ApJ*, 437, L9
- Chakravorty S., Kembhavi A. K., Elvis M., Ferland G., 2009, *MNRAS*, 393, 83
- Chakravorty S., Misra R., Elvis M., Kembhavi A. K., Ferland G., 2012, *MNRAS*, 422, 637
- Churazov E., Forman W., Jones C., Böhringer H., 2003, *Astrophysical Journal*, 590, 225
- Churazov E., Forman W., Jones C., Sunyaev R., Böhringer H., 2004, *MNRAS*, 347, 29
- Churazov E., Khabibullin I. I., Dolag K., Lyskova N., Sunyaev R. A., 2023a, arXiv e-prints, p. arXiv:2305.07579
- Churazov E., Khabibullin I. I., Dolag K., Lyskova N., Sunyaev R. A., 2023b, *MNRAS*, 523, 1209
- Connor T., et al., 2018, *ApJ*, 867, 25
- Costantini E., Zeegers S. T., Rogantini D., de Vries C. P., Tielens A. G. G. M., Waters L. B. F. M., 2019, *A&A*, 629, A78
- Crain R. A., et al., 2015, *MNRAS*, 450, 1937
- Cullen L., Dehnen W., 2010, *MNRAS*, 408, 669
- Dalla Vecchia C., Schaye J., 2012, *MNRAS*, 426, 140
- Davé R., et al., 2001, *ApJ*, 552, 473
- Davé R., Anglés-Alcázar D., Narayanan D., Li Q., Rafieeferantsoa M. H., Appleby S., 2019, *Monthly Notices of the Royal Astronomical Society*, 486, 2827
- Davidson K., Netzer H., 1979, *Reviews of Modern Physics*, 51, 715
- Dekel A., Rees M. J., 1987, *Nature*, 326, 455
- Del Zanna G., Dere K. P., Young P. R., Landi E., 2021, *ApJ*, 909, 38
- Dere K. P., Landi E., Mason H. E., Monsignori Fossi B. C., Young P. R., 1997, *A&AS*, 125, 149
- Dere K. P., Landi E., Young P. R., Del Zanna G., Landini M., Mason H. E., 2009, *A&A*, 498, 915
- Dere K. P., Zanna G. D., Young P. R., Landi E., Sutherland R. S., 2019, *The Astrophysical Journal Supplement Series*, 241, 22

- Detmers R. G., et al., 2011, *A&A*, 534, A38
- Diemer B., Kravtsov A. V., 2014, *ApJ*, 789, 1
- Diemer B., Mansfield P., Kravtsov A. V., More S., 2017, *ApJ*, 843, 140
- Dietl J., Pacaud F., Reiprich T. H., Veronica A., Migkas K., Spinelli C., Dolag K., Seidel B., 2024, arXiv e-prints, p. arXiv:2401.17281
- Dietrich J. P., Schneider P., Clowe D., Romano-Díaz E., Kerp J., 2005, *A&A*, 440, 453
- Dolag K., 2015, in *IAU General Assembly*. p. 2250156
- Donahue M., Voit G. M., O'Dea C. P., Baum S. A., Sparks W. B., 2005, *ApJ*, 630, L13
- Dopita M. A., Sutherland R. S., 2003, *Collisional Ionization Equilibrium*. Springer Berlin Heidelberg, Berlin, Heidelberg, pp 101–123, doi:10.1007/978-3-662-05866-4\_5, [https://doi.org/10.1007/978-3-662-05866-4\\_5](https://doi.org/10.1007/978-3-662-05866-4_5)
- Dubois Y., et al., 2014, *MNRAS*, 444, 1453
- Dumont A. M., Abrassart A., Collin S., 2000, *A&A*, 357, 823
- Durier F., Dalla Vecchia C., 2012, *MNRAS*, 419, 465
- Eckert D., et al., 2015, *Nature*, 528, 105
- Efstathiou G., 1992, *MNRAS*, 256, 43P
- Ercolano B., Barlow M. J., Storey P. J., Liu X.-W., 2003, *MNRAS*, 340, 1136
- Ettori S., Fabian A. C., 2006, *MNRAS*, 369, L42
- Ettori S., Fabian A. C., Allen S. W., Johnstone R. M., 2002, *MNRAS*, 331, 635
- Ezoe Y., Ohashi T., Mitsuda K., 2021, *Reviews of Modern Plasma Physics*, 5, 4
- Fabian A. C., et al., 2011, *MNRAS*, 418, 2154
- Fang T., Bryan G. L., Canizares C. R., 2002a, *ApJ*, 564, 604
- Fang T., Marshall H. L., Lee J. C., Davis D. S., Canizares C. R., 2002b, *ApJ*, 572, L127
- Fang T., Sembach K. R., Canizares C. R., 2003, *ApJ*, 586, L49
- Faucher-Giguère C.-A., 2020, *MNRAS*, 493, 1614
- Ferland G. J., Korista K. T., Verner D. A., Ferguson J. W., Kingdon J. B., Verner E. M., 1998, *PASP*, 110, 761
- Ferland G. J., et al., 2017, *Rev. Mex. Astron. Astrofis.*, 53, 385
- Fernández-Menchero L., Del Zanna G., Badnell N. R., 2014, *A&A*, 566, A104
- Finoguenov A., Briel U. G., Henry J. P., 2003, *A&A*, 410, 777
- Fisher J. D., Faltenbacher A., Johnson M. S. T., 2016, *MNRAS*, 458, 1517
- Forman W., Kellogg E., Gursky H., Tananbaum H., Giacconi R., 1972, *ApJ*, 178, 309
- Froese Fischer C., Tachiev G., 2004, *Atomic Data and Nuclear Data Tables*, 87, 1
- Fujimoto R., et al., 2004, *PASJ*, 56, L29
- Fukugita M., Hogan C. J., Peebles P. J. E., 1998, *ApJ*, 503, 518
- Fukushima K., Kobayashi S. B., Matsushita K., 2022, *MNRAS*, 514, 4222
- Gastaldello F., Molendi S., 2004, *ApJ*, 600, 670

- Gastaldello F., et al., 2010, *A&A*, 522, A34
- Gatuzz E., Churazov E., 2018, *MNRAS*, 474, 696
- Ghirardini V., et al., 2019, *A&A*, 621, A41
- Ghirardini V., et al., 2021, *A&A*, 647, A4
- Gilfanov M. R., Syunyaev R. A., Churazov E. M., 1987, *Soviet Astronomy Letters*, 13, 3
- Gluckstern R. L., Hull M. H., Breit G., 1953, U.S. AEC Report
- Gnat O., Ferland G. J., 2012, *ApJS*, 199, 20
- Goldstone J., 1957, *Proceedings of the Royal Society of London Series A*, 239, 267
- Grevesse N., Sauval A. J., 1998, *Space Sci. Rev.*, 85, 161
- Grevesse N., Noels A., Sauval A. J., 1992, in Mattok C., ed., *ESA Special Publication Vol. 348, Coronal Streamers, Coronal Loops, and Coronal and Solar Wind Composition*. pp 305–308
- Gu M., 2002, in *APS April Meeting Abstracts*. APS Meeting Abstracts. p. B17.075
- Gu M. F., 2008, *Canadian Journal of Physics*, 86, 675
- Gu L., Kaastra J., Raassen A. J. J., 2016, *A&A*, 588, A52
- Gu L., Zhuravleva I., Churazov E., Paerels F., Kaastra J., Yamaguchi H., 2018, *Space Sci. Rev.*, 214, 108
- Gu L., et al., 2019, *A&A*, 627, A51
- Gu L., et al., 2020, *A&A*, 641, A93
- Gu L., et al., 2022, *A&A*, 664, A62
- Haardt F., Madau P., 2001, in Neumann D. M., Tran J. T. V., eds, *Clusters of Galaxies and the High Redshift Universe Observed in X-rays*. p. 64 ([arXiv:astro-ph/0106018](https://arxiv.org/abs/astro-ph/0106018))
- Haardt F., Madau P., 2012, *ApJ*, 746, 125
- Halpern J. P., Grindlay J. E., 1980, *ApJ*, 242, 1041
- Hasinger G., Burg R., Giacconi R., Hartner G., Schmidt M., Trumper J., Zamorani G., 1993, *A&A*, 275, 1
- Hattori S., Ota N., Zhang Y.-Y., Akamatsu H., Finoguenov A., 2017, *PASJ*, 69, 39
- Hayashi K., Fukazawa Y., Tozuka M., Nishino S., Matsushita K., Takei Y., Arnaud K. A., 2009, *PASJ*, 61, 1185
- Hebb M. H., Menzel D. H., 1940, *ApJ*, 92, 408
- Hellsten U., Gnedin N. Y., Miralda-Escudé J., 1998, *ApJ*, 509, 56
- Hess C. J., Kahn S. M., Paerels F. B. S., 1997, *ApJ*, 478, 94
- Hirschmann M., Dolag K., Saro A., Bachmann L., Borgani S., Burkert A., 2014, *MNRAS*, 442, 2304
- Hitomi Collaboration et al., 2016, *Nature*, 535, 117
- Hitomi Collaboration et al., 2018a, *PASJ*, 70, 9
- Hitomi Collaboration et al., 2018b, *PASJ*, 70, 10
- Hitomi Collaboration et al., 2018c, *PASJ*, 70, 12
- Holczer T., Behar E., Kaspi S., 2007, *ApJ*, 663, 799
- Hopkins P. F., 2013, *MNRAS*, 428, 2840

- Hopkins P. F., Kereš D., Oñorbe J., Faucher-Giguère C.-A., Quataert E., Murray N., Bullock J. S., 2014, *MNRAS*, 445, 581
- Hummer D. G., 1988, *ApJ*, 327, 477
- Johnstone R. M., Allen S. W., Fabian A. C., Sanders J. S., 2002, *MNRAS*, 336, 299
- Jones C., Forman W., Vikhlinin A., Markevitch M., David L., Warmflash A., Murray S., Nulsen P. E. J., 2002, *ApJ*, 567, L115
- Kaastra J. S., 2017, *A&A*, 605, A51
- Kaastra J. S., Bleeker J. A. M., 2016, *A&A*, 587, A151
- Kaastra J. S., Mewe R., Nieuwenhuijzen H., 1996, in Yamashita K., Watanabe T., eds, *UV and X-ray Spectroscopy of Astrophysical and Laboratory Plasmas*. pp 411–414
- Kaastra J. S., et al., 2001, in Giacconi R., Serio S., Stella L., eds, *Astronomical Society of the Pacific Conference Series Vol. 234, X-ray Astronomy 2000*. p. 351
- Kaastra J. S., Lieu R., Tamura T., Paerels F. B. S., den Herder J. W., 2003, *A&A*, 397, 445
- Kaastra J. S., et al., 2004, *A&A*, 413, 415
- Kaastra J. S., Werner N., Herder J. W. A. d., Paerels F. B. S., de Plaa J., Rasmussen A. P., de Vries C. P., 2006, *ApJ*, 652, 189
- Kaastra J. S., Paerels F. B. S., Durret F., Schindler S., Richter P., 2008, *Space Sci. Rev.*, 134, 155
- Kaastra J. S., Gu L., Mao J., Mehdipour M., Raassen T., Urdampilleta I., 2016, *IAU Focus Meeting*, 29A, 291
- Kaastra J. S., Gu L., Mao J., Mehdipour M., Mernier F., de Plaa J., Raassen A. J. J., Urdampilleta I., 2017, *Journal of Instrumentation*, 12, C08008
- Kaastra J. S., Raassen A. J. J., de Plaa J., Gu L., 2018, *SPEX X-ray spectral fitting package*, Zenodo, doi:10.5281/zenodo.2419563, <https://doi.org/10.5281/zenodo.2419563>
- Kaastra J. S., Raassen A. J. J., de Plaa J., Gu L., 2020, *SPEX X-ray spectral fitting package*, doi:10.5281/zenodo.4384188, <https://doi.org/10.5281/zenodo.4384188>
- Kahn S. M., et al., 2003, in Bowyer S., Hwang C.-Y., eds, *Astronomical Society of the Pacific Conference Series Vol. 301, Matter and Energy in Clusters of Galaxies*. p. 23 (arXiv:astro-ph/0210665), doi:10.48550/arXiv.astro-ph/0210665
- Kaiser N., 1986, *MNRAS*, 222, 323
- Kallman T., Bautista M., 2001, *ApJS*, 133, 221
- Kallman T. R., McCray R., 1982, *ApJS*, 50, 263
- Kallman T. R., Palmeri P., 2007, *Reviews of Modern Physics*, 79, 79
- Kato T., Lang J., Berrington K. A., 1990, *Atomic Data and Nuclear Data Tables*, 44, 133
- Kay S. T., Pratt G. W., 2022, in , *Handbook of X-ray and Gamma-ray Astrophysics*. p. 100, doi:10.1007/978-981-16-4544-0\_119-1
- Kellogg E., Gursky H., Tananbaum H., Giacconi R., Pounds K., 1972, *ApJL*, 174, L65
- Kellogg E., Baldwin J. R., Koch D., 1975, *ApJ*, 199, 299
- Kisielius R., Storey P. J., Ferland G. J., Keenan F. P., 2009, *MNRAS*, 397, 903
- Kovács O. E., Bogdán Á., Smith R. K., Kraft R. P., Forman W. R., 2019, *ApJ*, 872, 83
- Kraft R., et al., 2022, *arXiv e-prints*, p. arXiv:2211.09827

- Krolik J. H., McKee C. F., Tarter C. B., 1981, *ApJ*, 249, 422
- Kühn S., et al., 2022, *Physical Review Letters*, 129, 245001
- Kull A., Böhringer H., 1999, *A&A*, 341, 23
- Kylafis N. D., Lamb D. Q., 1982, *ApJS*, 48, 239
- Lakhchaura K., Mernier F., Werner N., 2019, *A&A*, 623, A17
- Landi E., Landini M., 1999, *A&A*, 347, 401
- Landi E., Del Zanna G., Young P. R., Dere K. P., Mason H. E., Landini M., 2006, *ApJS*, 162, 261
- Landi E., Young P. R., Dere K. P., Del Zanna G., Mason H. E., 2013, *ApJ*, 763, 86
- Landini M., Monsignori Fossi B. C., 1990, *A&AS*, 82, 229
- Lau E. T., Nagai D., Avestruz C., Nelson K., Vikhlinin A., 2015, *ApJ*, 806, 68
- Leccardi A., Molendi S., 2008, *A&A*, 486, 359
- Lee J. C., et al., 2013, *MNRAS*, 430, 2650
- Lennon D. J., Burke V. M., 1994, *A&AS*, 103, 273
- Lewis A. D., Stocke J. T., Buote D. A., 2002, *ApJ*, 573, L13
- Li Y., Bryan G. L., 2014, *ApJ*, 789, 153
- Liang G. Y., Badnell N. R., 2011, *A&A*, 528, A69
- Liang G. Y., Badnell N. R., Zhao G., 2012, *A&A*, 547, A87
- Libeskind N. I., et al., 2018, *MNRAS*, 473, 1195
- Liu A., Zhai M., Tozzi P., 2019, *MNRAS*, 485, 1651
- Lodders K., 2003, *ApJ*, 591, 1220
- Lodders K., Palme H., Gail H. P., 2009, *Landolt Börnstein*, 4B, 712
- Lorimer D. R., Bailes M., McLaughlin M. A., Narkevic D. J., Crawford F., 2007, *Science*, 318, 777
- Lykins M. L., Ferland G. J., Porter R. L., van Hoof P. A. M., Williams R. J. R., Gnat O., 2013, *MNRAS*, 429, 3133
- Lynds R., 1971, *ApJ*, 164, L73
- Macquart J. P., et al., 2020, *Nature*, 581, 391
- Malavasi N., Aghanim N., Douspis M., Tanimura H., Bonjean V., 2020, *A&A*, 642, A19
- Mao J., Kaastra J., 2016, *A&A*, 587, A84
- Mao J., Kaastra J., Badnell N. R., 2017a, *A&A*, 599, A10
- Mao J., Kaastra J. S., Mehdipour M., Raassen A. J. J., Gu L., Miller J. M., 2017b, *A&A*, 607, A100
- Mao J., Badnell N. R., Del Zanna G., 2020, *A&A*, 634, A7
- Markevitch M., 1999, *ApJ*, 522, L13
- Markevitch M., et al., 2009, in *astro2010: The Astronomy and Astrophysics Decadal Survey*. p. 192 ([arXiv:0902.3709](https://arxiv.org/abs/0902.3709)), doi:10.48550/arXiv.0902.3709
- Martizzi D., et al., 2019, *MNRAS*, 486, 3766
- Mathews W. G., Ferland G. J., 1987, *ApJ*, 323, 456

- McNamara B. R., Nulsen P. E. J., 2007, *ARA&A*, 45, 117
- McNamara B. R., O’Connell R. W., Sarazin C. L., 1996, *AJ*, 112, 91
- Mehdipour M., et al., 2015, *A&A*, 575, A22
- Mehdipour M., Kaastra J. S., Kallman T., 2016, *A&A*, 596, A65
- Mehdipour M., et al., 2018, *A&A*, 615, A72
- Meidinger N., Nandra K., Plattner M., Porro M., Rau A., Santangelo A. E., Tenzer C., Wilms J., 2014, in Takahashi T., den Herder J.-W. A., Bautz M., eds, *Society of Photo-Optical Instrumentation Engineers (SPIE) Conference Series Vol. 9144, Space Telescopes and Instrumentation 2014: Ultraviolet to Gamma Ray*. p. 91442J, doi:10.1117/12.2054490
- Meidinger N., Nandra K., Plattner M., 2018, in den Herder J.-W. A., Nikzad S., Nakazawa K., eds, *Society of Photo-Optical Instrumentation Engineers (SPIE) Conference Series Vol. 10699, Space Telescopes and Instrumentation 2018: Ultraviolet to Gamma Ray*. p. 106991F, doi:10.1117/12.2310141
- Mernier F. D. M., 2017, PhD thesis, University of Leiden, Netherlands
- Mernier F., et al., 2017, *A&A*, 603, A80
- Mernier F., et al., 2018, *Space Sci. Rev.*, 214, 129
- Mewe R., 1972, *Sol. Phys.*, 22, 459
- Mewe R., Gronenschild E. H. B. M., van den Oord G. H. J., 1985, *A&AS*, 62, 197
- Mewe R., Lemen J. R., van den Oord G. H. J., 1986, *A&AS*, 65, 511
- Mewe R., Kaastra J. S., Liedahl D. A., 1995, *Legacy*, 6, 16
- Migkas K., et al., 2024, arXiv e-prints, p. arXiv:2401.17297
- Million E. T., Allen S. W., Werner N., Taylor G. B., 2010, *MNRAS*, 405, 1624
- Mitsuda K., et al., 2010, in Arnaud M., Murray S. S., Takahashi T., eds, *Society of Photo-Optical Instrumentation Engineers (SPIE) Conference Series Vol. 7732, Space Telescopes and Instrumentation 2010: Ultraviolet to Gamma Ray*. p. 773211, doi:10.1117/12.856778
- Mohr J. J., Mathiesen B., Evrard A. E., 1999, *ApJ*, 517, 627
- Molnar S. M., Hearn N., Haiman Z., Bryan G., Evrard A. E., Lake G., 2009, *ApJ*, 696, 1640
- Morandi A., Pedersen K., Limousin M., 2010, *ApJ*, 713, 491
- Morgan L. A., 1980, *Journal of Physics B Atomic Molecular Physics*, 13, 3703
- Mott N. F., Massey H. S. W., 1933, *Theory of Atomic Collisions*
- Nagai D., Kravtsov A. V., Vikhlinin A., 2007, *ApJ*, 668, 1
- Navarro J. F., Frenk C. S., White S. D. M., 1995, *MNRAS*, 275, 720
- Navarro J. F., Frenk C. S., White S. D. M., 1996, *ApJ*, 462, 563
- Navarro J. F., Frenk C. S., White S. D. M., 1997, *ApJ*, 490, 493
- Nelson D., Pillepich A., Ayromlou M., Lee W., Lehle K., Rohr E., Truong N., 2023a, arXiv e-prints, p. arXiv:2311.06338
- Nelson D., et al., 2023b, *MNRAS*, 522, 3665
- Nicastro F., et al., 2002, *ApJ*, 573, 157
- Nicastro F., et al., 2003, *Nature*, 421, 719

- Nicastro F., et al., 2005a, *Nature*, 433, 495
- Nicastro F., et al., 2005b, *ApJ*, 629, 700
- Nicastro F., et al., 2018, *Nature*, 558, 406
- Nicastro F., Fang T., Mathur S., 2022, arXiv e-prints, p. arXiv:2203.15666
- Nozawa S., Itoh N., Kohyama Y., 1998, *ApJ*, 507, 530
- Ogorzalek A., et al., 2017, *MNRAS*, 472, 1659
- Osterbrock D. E., 1974, *Astrophysics of gaseous nebulae*
- Panagoulia E. K., Fabian A. C., Sanders J. S., 2013, *MNRAS*, 433, 3290
- Panagoulia E. K., Sanders J. S., Fabian A. C., 2015, *MNRAS*, 447, 417
- Parekh V., Laganá T. F., Thorat K., van der Heyden K., Iqbal A., Durret F., 2020, *MNRAS*, 491, 2605
- Parimbelli G., Branchini E., Viel M., Villaescusa-Navarro F., ZuHone J., 2022, arXiv e-prints, p. arXiv:2209.00657
- Perna R., Loeb A., 1998, *ApJ*, 503, L135
- Persic M., Salucci P., 1992, *MNRAS*, 258, 14P
- Peterson J. R., et al., 2001, *A&A*, 365, L104
- Peterson J. R., Kahn S. M., Paerels F. B. S., Kaastra J. S., Tamura T., Bleeker J. A. M., Ferrigno C., Jernigan J. G., 2003, *ApJ*, 590, 207
- Pillepich A., et al., 2018, *MNRAS*, 475, 648
- Pinto C., et al., 2014, *A&A*, 572, L8
- Pinto C., et al., 2015, *A&A*, 575, A38
- Planck Collaboration et al., 2013, *A&A*, 558, C2
- Planck Collaboration et al., 2014, *A&A*, 571, A16
- Ponman T. J., Cannon D. B., Navarro J. F., 1999, *Nature*, 397, 135
- Pratt G. W., Böhringer H., Croston J. H., Arnaud M., Borgani S., Finoguenov A., Temple R. F., 2007, *A&A*, 461, 71
- Pratt G. W., et al., 2010, *A&A*, 511, A85
- Price D. J., 2008, *Journal of Computational Physics*, 227, 10040
- Psaradaki I., et al., 2020, *A&A*, 642, A208
- Quinn T., Katz N., Efstathiou G., 1996, *MNRAS*, 278, L49
- Rafferty D. A., Birzan L., Nulsen P. E. J., McNamara B. R., Brandt W. N., Wise M. W., Röttgering H. J. A., 2013, *MNRAS*, 428, 58
- Rasia E., Mazzotta P., Bourdin H., Borgani S., Tornatore L., Ettori S., Dolag K., Moscardini L., 2008, *ApJ*, 674, 728
- Rasmussen J., Ponman T. J., 2007, *MNRAS*, 380, 1554
- Rasmussen A., Kahn S. M., Paerels F., 2003, in Rosenberg J. L., Putman M. E., eds, *Astrophysics and Space Science Library Vol. 281, The IGM/Galaxy Connection. The Distribution of Baryons at  $z=0$* . p. 109 (arXiv:astro-ph/0301183), doi:10.1007/978-94-010-0115-1\_20
- Raymond J. C., Cox D. P., Smith B. W., 1976, *ApJ*, 204, 290



- Reiprich T. H., et al., 2021, *A&A*, 647, A2
- Rogantini D., Costantini E., Zeegers S. T., de Vries C. P., Bras W., de Groot F., Mutschke H., Waters L. B. F. M., 2018, *A&A*, 609, A22
- Rogantini D., et al., 2019, *A&A*, 630, A143
- Rogantini D., Mehdipour M., Kaastra J., Costantini E., Juráňová A., Kara E., 2022, *ApJ*, 940, 122
- Ross J. E., Aller L. H., 1976, *Science*, 191, 1223
- Rózańska A., Kowalska I., Gonçalves A. C., 2008, *A&A*, 487, 895
- Russell H. R., Sanders J. S., Fabian A. C., 2008, *MNRAS*, 390, 1207
- Ryu D., Kang H., Hallman E., Jones T. W., 2003, *ApJ*, 593, 599
- Sampson D. H., Goett S. J., Clark R. E. H., 1983, *Atomic Data and Nuclear Data Tables*, 29, 467
- Sanders J. S., 2023, arXiv e-prints, p. arXiv:2301.12791
- Sanders J. S., Fabian A. C., 2002, *MNRAS*, 331, 273
- Sanders J. S., Fabian A. C., 2006, *MNRAS*, 370, 63
- Sanders J. S., Fabian A. C., 2007, *MNRAS*, 381, 1381
- Sanders J. S., Fabian A. C., 2011, *MNRAS*, 412, L35
- Sargent W. L. W., Young P. J., Boksenberg A., Tytler D., 1980, *ApJS*, 42, 41
- Sato K., Matsushita K., Gastaldello F., 2009, *PASJ*, 61, S365
- Schaller M., Dalla Vecchia C., Schaye J., Bower R. G., Theuns T., Crain R. A., Furlong M., McCarthy I. G., 2015, *MNRAS*, 454, 2277
- Scharf C., Donahue M., Voit G. M., Rosati P., Postman M., 2000, *ApJ*, 528, L73
- Schaye J., 2001, *ApJ*, 559, 507
- Schaye J., Dalla Vecchia C., 2008, *MNRAS*, 383, 1210
- Schaye J., et al., 2010, *MNRAS*, 402, 1536
- Schaye J., et al., 2015, *MNRAS*, 446, 521
- Schaye J., et al., 2023, *MNRAS*, 526, 4978
- Schindler S., et al., 2005, *A&A*, 435, L25
- Schure K. M., Kosenko D., Kaastra J. S., Keppens R., Vink J., 2009, *A&A*, 508, 751
- Sharma P., McCourt M., Quataert E., Parrish I. J., 2012, *MNRAS*, 420, 3174
- Shull J. M., Smith B. D., Danforth C. W., 2012, *ApJ*, 759, 23
- Silk J., 1985, *ApJ*, 297, 1
- Simionescu A., Werner N., Finoguenov A., Böhringer H., Brüggen M., 2008, *A&A*, 482, 97
- Simionescu A., Werner N., Böhringer H., Kaastra J. S., Finoguenov A., Brüggen M., Nulsen P. E. J., 2009, *A&A*, 493, 409
- Simionescu A., et al., 2019, *MNRAS*, 483, 1701
- Simionescu A., et al., 2021, *Experimental Astronomy*, 51, 1043
- Smith R. K., 2005, in *X-ray Diagnostics of Astrophysical Plasmas: Theory, Experiment, and Observation*.

- Smith R. K., Brickhouse N. S., Liedahl D. A., Raymond J. C., 2001, *ApJ*, 556, L91
- Spence D., Bonamente M., Nevalainen J., Tuominen T., Ahoranta J., de Plaa J., Liu W., Wijers N., 2023, arXiv e-prints, p. arXiv:2305.01587
- Springel V., 2005, *MNRAS*, 364, 1105
- Springel V., et al., 2018, *MNRAS*, 475, 676
- Stern J., Behar E., Laor A., Baskin A., Holczer T., 2014, *MNRAS*, 445, 3011
- Summers H. P., 2004
- Sun M., Voit G. M., Donahue M., Jones C., Forman W., Vikhlinin A., 2009, *ApJ*, 693, 1142
- Sutherland R. S., Dopita M. A., 1993, *ApJS*, 88, 253
- Takei Y., Henry J. P., Finoguenov A., Mitsuda K., Tamura T., Fujimoto R., Briel U. G., 2007, *ApJ*, 655, 831
- Tamura T., et al., 2001, *A&A*, 365, L87
- Tanimura H., Aghanim N., Kolodzig A., Douspis M., Malavasi N., 2020, *A&A*, 643, L2
- Tanimura H., Aghanim N., Douspis M., Malavasi N., 2022, *A&A*, 667, A161
- Tarter C. B., Tucker W. H., Salpeter E. E., 1969, *ApJ*, 156, 943
- Tayal S. S., 2007, *ApJS*, 171, 331
- Tepper-García T., Richter P., Schaye J., Booth C. M., Dalla Vecchia C., Theuns T., Wiersma R. P. C., 2011, *MNRAS*, 413, 190
- Tepper-García T., Richter P., Schaye J., Booth C. M., Dalla Vecchia C., Theuns T., 2012, *MNRAS*, 425, 1640
- Thoul A. A., Weinberg D. H., 1996, *ApJ*, 465, 608
- Tittley E. R., Henriksen M., 2001, *ApJ*, 563, 673
- Tumlinson J., et al., 2011, *Science*, 334, 948
- Tumlinson J., Peebles M. S., Werk J. K., 2017, *ARA&A*, 55, 389
- Tuominen T., et al., 2021, *A&A*, 646, A156
- Urdampilleta I., Kaastra J. S., Mehdipour M., 2017, *A&A*, 601, A85
- Ursino E., Galeazzi M., Roncarelli M., 2010, *ApJ*, 721, 46
- Veronica A., et al., 2022, *A&A*, 661, A46
- Veronica A., et al., 2024, *A&A*, 681, A108
- Vikhlinin A., 2018, in *American Astronomical Society Meeting Abstracts #231*. p. 103.04
- Vikhlinin A., Kravtsov A., Forman W., Jones C., Markevitch M., Murray S. S., Van Speybroeck L., 2006, *ApJ*, 640, 691
- Villaescusa-Navarro F., et al., 2021, *ApJ*, 915, 71
- Virtanen P., et al., 2020, *Nature Methods*, 17, 261
- Vogelsberger M., et al., 2014, *MNRAS*, 444, 1518
- Vogelsberger M., Marinacci F., Torrey P., Puchwein E., 2020, *Nature Reviews Physics*, 2, 42
- Walker S. A., Fabian A. C., Sanders J. S., Simionescu A., Tawara Y., 2013, *MNRAS*, 432, 554
- Wallbank A. N., Maughan B. J., Gastaldello F., Potter C., Wik D. R., 2022, *MNRAS*, 517, 5594

- Wang Q. D., McCray R., 1993, *ApJ*, 409, L37
- Weinberg D. H., Miralda-Escudé J., Hernquist L., Katz N., 1997, *ApJ*, 490, 564
- Wendland H., 1995, *Advances in Computational Mathematics*, 4, 389, 1572
- Werk J. K., et al., 2014, *ApJ*, 792, 8
- Werner N., Mernier F., 2020, in , *Reviews in Frontiers of Modern Astrophysics; From Space Debris to Cosmology*. pp 279–310, doi:10.1007/978-3-030-38509-5\_10
- Werner N., de Plaa J., Kaastra J. S., Vink J., Bleeker J. A. M., Tamura T., Peterson J. R., Verbunt F., 2006, *A&A*, 449, 475
- Werner N., Finoguenov A., Kaastra J. S., Simionescu A., Dietrich J. P., Vink J., Böhringer H., 2008, *A&A*, 482, L29
- Werner N., Zhuravleva I., Churazov E., Simionescu A., Allen S. W., Forman W., Jones C., Kaastra J. S., 2009, *MNRAS*, 398, 23
- Whiteford A. D., Badnell N. R., Ballance C. P., O’Mullane M. G., Summers H. P., Thomas A. L., 2001, *Journal of Physics B Atomic Molecular Physics*, 34, 3179
- Wiersma R. P. C., Schaye J., Smith B. D., 2009a, *MNRAS*, 393, 99
- Wiersma R. P. C., Schaye J., Theuns T., Dalla Vecchia C., Tornatore L., 2009b, *MNRAS*, 399, 574
- Wijers N., 2022, PhD thesis
- Wijers N. A., Schaye J., 2022, *MNRAS*, 514, 5214
- Wijers N. A., Schaye J., Oppenheimer B. D., Crain R. A., Nicastro F., 2019, *MNRAS*, 488, 2947
- Wijers N. A., Schaye J., Oppenheimer B. D., 2020, *MNRAS*, 498, 574
- Williams R. J., Mathur S., Nicastro F., Elvis M., 2007, *ApJ*, 665, 247
- Willingale R., Starling R. L. C., Beardmore A. P., Tanvir N. R., O’Brien P. T., 2013, *MNRAS*, 431, 394
- Xu H., et al., 2002, *ApJ*, 579, 600
- York D. G., et al., 2000, *AJ*, 120, 1579
- Zappacosta L., Mannucci F., Maiolino R., Gilli R., Ferrara A., Finoguenov A., Nagar N. M., Axon D. J., 2002, *A&A*, 394, 7
- Zatsarinny O., Tayal S. S., 2003, *ApJS*, 148, 575
- Zeegers S. T., et al., 2017, *A&A*, 599, A117
- Zeegers S. T., Costantini E., Rogantini D., de Vries C. P., Mutschke H., Mohr P., de Groot F., Tielens A. G. G. M., 2019, *A&A*, 627, A16
- Zel’dovich Y. B., 1970, *A&A*, 5, 84
- Zhang H. L., Sampson D. H., Fontes C. J., 1990, *Atomic Data and Nuclear Data Tables*, 44, 31
- Zhang Y., Anninos P., Norman M. L., 1995, *ApJ*, 453, L57
- Zhuravleva I., et al., 2013, *MNRAS*, 435, 3111
- Zhuravleva I., et al., 2015, *MNRAS*, 450, 4184
- de Lapparent V., Geller M. J., Huchra J. P., 1986, *ApJ*, 302, L1
- de Plaa J., Werner N., Simionescu A., Kaastra J. S., Grange Y. G., Vink J., 2010, *A&A*, 523, A81
- de Plaa J., Zhuravleva I., Werner N., Kaastra J. S., Churazov E., Smith R. K., Raassen A. J. J., Grange Y. G., 2012, *A&A*, 539, A34

- 
- Štofanová L., Kaastra J., Mehdipour M., de Plaa J., 2021, *A&A*, 655, A2
- Štofanová L., Simionescu A., Wijers N. A., Schaye J., Kaastra J. S., 2022, *MNRAS*, 515, 3162
- van Hoof P. A. M., Ferland G. J., Williams R. J. R., Volk K., Chatzikos M., Lykins M., Porter R. L., 2015, *MNRAS*, 449, 2112
- van Regemorter H., 1962, *ApJ*, 136, 906
- van de Voort F., Schaye J., 2013, *MNRAS*, 430, 2688
- Štofanová L., 2023. Zenodo, doi:10.5281/zenodo.10031082
- Štofanová L., Simionescu A., Wijers N. A., Schaye J., Kaastra J., 2022. Zenodo, doi:10.5281/zenodo.6656840



# Nederlandse samenvatting

---

## “Het grote plaatje”

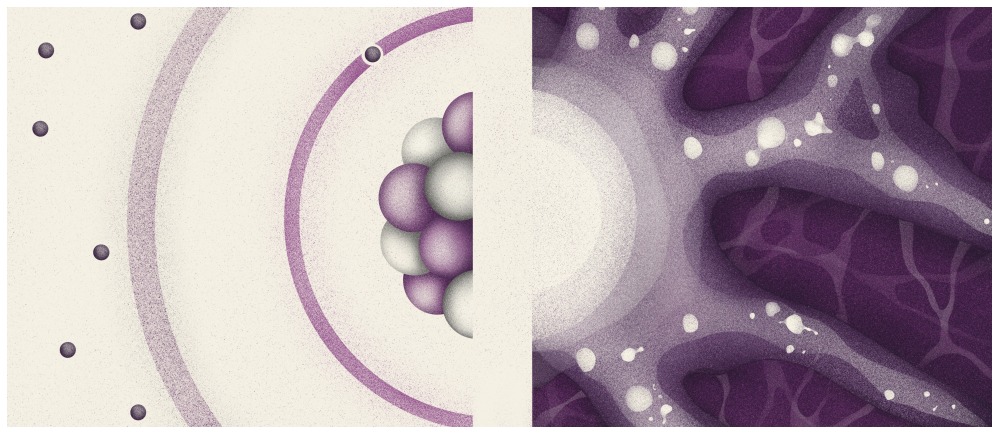
Het overgrote deel van de massa van een menselijk lichaam is opgebouwd uit slechts zes elementen: zuurstof, koolstof, waterstof, stikstof, calcium en fosfor. Vijf van deze zes elementen zijn **metalen**, een verzamelterm die astrofysici gebruiken voor alle elementen die zwaarder zijn dan waterstof en helium. *Maar hoe zijn deze metalen ontstaan, waar komen ze vandaan, en hoe hebben ze de aarde bereikt?*

Tegenwoordig is het algemeen bekend dat waterstof en helium (en kleine sporen van lithium en beryllium) van oeroude oorsprong zijn, terwijl de zwaardere elementen worden gevormd in de kernen van sterren in verschillende fasen van hun ‘leven’ (zie bijv. Cameron 1957; Burbidge et al. 1957, Mernier 2017). Wanneer deze sterren exploderen als supernova’s, stoten ze de metalen die in hun kernen zijn gevormd uit naar het medium om hen heen. Dit verrijkt de omgeving waarin de sterren zich bevinden. We vinden de metalen terug in stofdeeltjes of zelfs in grotere astrofysische objecten (bijv. asteroïden of kometen). Ze kunnen daarmee lange afstanden afleggen en mogelijk de bouwstenen van het leven vormen. Deze metalen zijn zelfs te vinden in het heelal op grote schaal: de filamenten van het kosmisch web, het intra-cluster medium van clusters en het circumgalactisch medium rond individuele sterrenstelsels. Door deze astrofysische objecten te bestuderen via spectroscopie, en de impact van verschillende terugkoppelingsprocessen op het transport van metalen op verschillende fysische schalen te onderzoeken, kunnen we de oorsprong en evolutie van metalen in enkele van de meest massieve objecten in ons universum beter begrijpen.

## De grote-schaalstructuur van het heelal

Onder de vele theorieën die de evolutie van ons Universum beschrijven, wordt het model waarin de structuur hiërarchisch groeit door veel onderzoekers geaccepteerd. Metingen van het licht van de Kosmische Microgolfachtergrond geven aan dat ons Universum is geëvolueerd uit kleine dichtheidsfluctuaties, die in de loop van de tijd uitgroeiden tot grotere systemen onder invloed van de zwaartekracht. In de huidige tijd ( $z = 0$ ) heeft ons Universum een structuur die bekend staat als het **Kosmische Web**. Veel van het gas in de filamenten van het web is nog niet gedetecteerd. Modellen voorspellen dat het temperatuur heeft tussen  $10^5 - 10^7$  K, en elektronendichtheden tussen  $10^{-6} - 10^{-4}$  cm $^{-3}$ . De verwachting is dat we met toekomstige röntgenspectroscopische missies de *filamenten* van dit kosmische web kunnen bestuderen. Tot nu toe is het erg moeilijk gebleken om dit hete, diffuse en ijle plasma te observeren, hoewel het niet onmogelijk is, zoals al besproken in sectie 1.3 van dit proefschrift.

Het beste idee van het kosmische web krijgen we tot nu toe door het bestuderen van zijn knooppunten, waar de *clusters van melkwegstelsels* zich bevinden. Deze massieve structuren, die gebonden zijn door de zwaartekracht, bevatten tientallen of honderden individuele sterrenstelsels. In röntgenstraling worden ze gekarakteriseerd door het zogenaamde intra-cluster medium, dat bestaat uit een zeer uitgestrekte gaswolk van 1-2 megaparsec groot, met een temperatuur van  $10^7 - 10^8$  K, een dichtheid van  $10^{-4} - 10^{-2}$  cm $^{-3}$ , en een gemiddelde abundantie van 0.3 keer de abundantie van de zon.



**Figuur 1:** Omslag van dit proefschrift. Een artistieke interpretatie van het O VII ion (links) en het cluster van melkwegstelsels samen met de filamenten van het kosmische web (rechts).

## Dit proefschrift: van atomen naar de kosmos

Hoewel veel theoretisch en ook observationeel bewijs aantoont dat de structuur van ons Universum een kosmisch web is, zijn er veel vragen over zijn eigenschappen op verschillende fysische schalen. Zoals al genoemd in de introductie, richt dit proefschrift zich op twee delen van het kosmische web: clusters van melkwegstelsels en kosmische webfilamenten. De methodologie die door dit hele proefschrift wordt gebruikt, is röntgenspectroscopie, wat hand in hand gaat met het modelleren van het röntgenplasma. Het modelleren zou onmogelijk zijn zonder kennis van processen die op atomair niveau plaatsvinden. Het doel van dit proefschrift is om te laten zien dat op röntgengolflengten de microscopische en macroscopische schalen in het kosmische web onlosmakelijk met elkaar verbonden zijn. Dit is ook het idee achter de omslag van dit proefschrift (Fig. 1).

Dit proefschrift begint met een samenvatting van alle onderwerpen die voorkomen in de wetenschappelijke artikelen van dit proefschrift. In **Hoofdstuk 1** beschrijf ik de grote-schaalstructuur van ons Universum en toon ik enkele van de waarneembare eigenschappen van de clusters van sterrenstelsels (zoals temperatuur-, dichtheids-, druk-, entropie- en metalliciteitsprofielen), evenals de kosmische webfilamenten, met focus op de röntgenstraling van deze objecten. Ik beschrijf kort de kosmologische hydrodynamische simulaties die later worden gebruikt in Hoofdstuk 2. De tweede helft van de introductie beschrijft de basis van de atomaire processen in röntgenstraling, zowel de processen die leiden tot continuüm emissie als de processen die spectraallijnen veroorzaken. Het modelleren van röntgenplasma's is niet mogelijk zonder plasmacodes, die kort worden beschreven in dit hoofdstuk, samen met aannames zoals botsingsionisatie-evenwicht of foto-ionisatie-evenwicht, en de verschillen daartussen. Aan het einde van dit hoofdstuk vat ik de eigenschappen samen die kunnen worden afgeleid uit de röntgenspectra en noem ik enkele van de hoge-resolutie röntgendetectoren (Chandra, XMM-Newton, XRISM en de toekomstige missie Athena).

In **Hoofdstuk 2** demonstreer ik de kracht van de microcalorimeters die gepland zijn aan boord van toekomstige missies zoals de X-ray Integral Field Unit (X-IFU) aan boord van Athena of de voorgestelde Integral Field Unit van de Line Emission Mapper X-ray probe (LEM). Met behulp van de Hydrangea kosmologische hydrodynamische simulaties voorspel ik de verwachte eigenschappen van het intergalactisch gas in en rondom massieve clusters van melkwegstelsels. In deze studie onderzoek ik in totaal 138 projecties uit de simulatieruimtes, waarbij ik 16 richtingen vind met een totale kolomdichtheid  $N_{\text{O VII}} > 10^{14.5} \text{ cm}^{-2}$ . De sterkste absorptielijnen zijn doorgaans verschoven met  $\pm 1000 \text{ km/s}$  ten opzichte van het rustframe van het cluster waar ze het dichtst bij in de buurt zijn. Realistische gesimuleerde waarnemingen met toekomstige microcalorimeters (Athena's X-IFU en LEM's Integral Field

Unit) laten zien dat de detectie van kosmische webfilamenten in O VII en O VIII in absorptie mogelijk zal zijn als de kernen van clusters als achtergrond worden gebruikt. Een O VII detectie met een 5 sigma significantie kan worden bereikt in 10 – 250 ks met Athena voor de meeste van de geselecteerde clusters van melkwegstelsels. De O VIII detectie wordt pas haalbaar met een spectrale resolutie van ongeveer 1 eV, vergelijkbaar met die van LEM.

In **Hoofdstuk 3** wordt aangetoond dat foto-ionisatiemodellen die alleen de kosmische ultraviolet- en röntgenachtergrond meenemen mogelijk niet voldoende zijn om de kolomdichtheden van het gas in kosmische webfilamenten te schatten. Ik laat zien dat fotonen van clusters van melkwegstelsels, afkomstig uit het intra-cluster medium, de ionisatietoestand van het nabijgelegen intergalactische medium veranderen. Dit is in strijd met het typische beeld waarin wordt aangenomen dat het gas in het kosmisch web volledig kan worden beschreven door alleen botsingsionisatie-evenwicht. Ik laat zien dat de ionfracties moeten worden geparаметriseerd met de dichtheid en temperatuur van het foto-geïoniseerde gas, evenals de afstand tussen de ioniserende bron en het foto-geïoniseerde gas. De ionisatiefracties (in het bijzonder van C IV, C V, C VI, N VII, O VI, O VII, O VIII, Ne VIII, Ne IX, en Fe XVII) die uitgerekend zijn met foto-ionisatie door de kosmische achtergrond zijn ofwel een bovengrens of een ondergrens voor de ionisatiefractie berekend als functie van de afstand tot de emissie van de cluster. Met behulp van een eenvoudig model van een kosmisch webfilament voorspel ik hoe de straling van het cluster de kolomdichtheden verandert voor twee verschillende oriëntaties van de gezichtslijn. Voor gezichtslijnen die door de buitengebieden van clusters gaan, kan O VI worden onderdrukt met een factor 4.5, O VII met een factor 2.2, C V met een factor 3, en Ne VIII kan worden versterkt met een factor 2 voor gas met lage dichtheid.

In **Hoofdstuk 4** wordt het nieuwe ‘clus’ model beschreven dat onderdeel is van het SPEX softwarepakket. Het model berekent het spectrum en het radiële profiel voor een sferisch symmetrische benadering van een cluster van melkwegstelsels, een groep van melkwegstelsels, of zelfs een massief elliptisch sterrenstelsel. Met het model onderzoek ik de omvang van systematische effecten, veroorzaakt door projectie-effecten en resonante verstrooiing, op de afgeleide temperaturen en ijzerabundantie. Ik beschouw thermodynamische profielen van nabijgelegen cool-core clusters (A383, A2029, A1795, A262, Perseus) en het massieve elliptische sterrenstelsel NGC 4636, en laat zien dat de ingevoerde emissiemaatverdeling niet uit de gesimuleerde spectra kan worden afgeleid door gebruik te maken van modellen zoals enkelvoudige temperatuur, dubbele temperatuur, of een normaal verdeelde emissiemaat. Bovendien laat ik zien dat voor sommige cool-core clusters de projectie-effecten de gemeten temperaturen aanzienlijk beïnvloeden. Eerdere studies in de literatuur tonen aan dat resonante verstrooiing het afgeleide abundantieprofiel met maximaal 10 – 20% kan beïnvloeden. Dit komt overeen met onze bevindingen voor clusters met thermodynamische profielen die vergelijkbaar zijn met de Perseuscluster, waarvoor ik een 10 – 15% verandering van het abundantieprofiel rapporteer als gevolg van resonante verstrooiing. Voor het massieve elliptische sterrenstelsel NGC 4636 kan echter, wanneer rekening wordt gehouden met het resonante verstrooiingseffect in het centrum, de centrale abundantieafname die is gemeten met XMM-Newton en Chandra worden verklaard. Deze bevindingen kunnen van invloed zijn op kruis-calibratiestudies tussen verschillende instrumenten, evenals op precisie-cosmologie.

In **Hoofdstuk 5** ligt de focus op de updates van de afkoelingscurve in het foto-ionisatiemodel ‘pion’, dat een van de modellen is in de plasma-code SPEX. Ik beschrijf berekeningen van het radiatieve verlies door botsings-excitatie, di-electronische recombinatie, en de impact hiervan op de afkoelingscurve in dit foto-ionisatiemodel in de limiet van optisch dunne en lage-dichtheidsplasma’s. Bovendien bespreek ik de updates van de atomaire gegevens voor neutraal waterstof. Ik vergelijk de bijgewerkte atomaire database en de afkoelingscurve in SPEX met andere plasmacodes (MEKAL, APEC, Cloudy) en atomaire databases (CHIANTI, ADAS). Ik toon de impact van deze updates op de stabiliteitscurve die is gesimuleerd voor de actieve galactische kern NGC 5548, waarbij ik een nieuwe stabiele tak vind. Daarnaast bereken ik de kolomdichtheden van ionen en laat ik zien welke ionen pieken op deze nieuwe stabiele tak. Dergelijke updates van de afkoelingscurve zijn ook belangrijk voor de schatting van de absorptiemaatverdeling die de ionisatiestructuur van winden bij actieve galactische kernen beschrijft.





## English summary

---

### “The big picture”

The vast majority of the mass of a human body is formed from just six elements: oxygen, carbon, hydrogen, nitrogen, calcium, and phosphorus. Five out of these six elements are **metals**, which is a collective term that in astrophysics (unlike in other scientific disciplines) is used for all elements heavier in mass than hydrogen and helium. *But how were these metals created, where do they come from, and how did they reach Earth?*

Nowadays, it is well known that hydrogen and helium (and small traces of lithium and beryllium) are of primordial origin, while the heavier elements are created in the cores of stars at different evolutionary stages (see e.g. Cameron 1957; Burbidge et al. 1957, Mernier 2017). When these stars explode as supernovae, they expel metals synthesised in their cores to the medium around them. By enriching the environment in which the stars are embedded, these metals can get captured on dust grains or even larger astrophysical objects (e.g. asteroids or comets), travel long distances, and potentially create the building blocks of life. For example, the warm-hot intergalactic medium in the cosmic web filaments, the intra-cluster medium of galaxy clusters, and the circum-galactic medium around individual galaxies is full of such metals. By studying the medium of these massive astrophysical objects through spectroscopy, and by studying the impact of different feedback processes on the metal transport on various physical scales, we can get closer to the understanding of the origin and evolution of metals in some of the most massive objects in our Universe.

### Large scale structure of the Universe

Among many theories that describe the evolution of our Universe, the hierarchical structure growth is accepted by many researchers. Measurements of the light from the Cosmic Microwave Background indicate that our Universe evolved from small density fluctuations, which over time grew into larger systems under the influence of gravity. At the current epoch ( $z = 0$ ), our Universe has a filamentary structure which is famously known as the “**Cosmic Web**”. Most of the yet undetected gas in X-rays, which is predicted to have temperatures between  $10^5 - 10^7$  K, and electron densities between  $10^{-6} - 10^{-4} \text{ cm}^{-3}$  is expected to be found with future X-ray spectroscopic missions in the *filaments* of this cosmic web. So far, it has been very challenging to observe this hot, diffuse, and tenuous plasma, though it has not been impossible, as already discussed in section 1.3 of this thesis.

A better understanding of the cosmic web has so far been gained through its nodes, where the *galaxy clusters* reside. These massive gravitationally bound structures have tens or hundreds of individual galaxy members. In X-ray wavelengths, they are characterized by the so called intra-cluster medium, which consists of very extensive (1-2 megaparsecs in radius), hot ( $10^7 - 10^8$  K), and rarefied plasma ( $10^{-4} - 10^{-2} \text{ cm}^{-3}$ ), which has an average abundance of 0.3 times the Solar abundance.

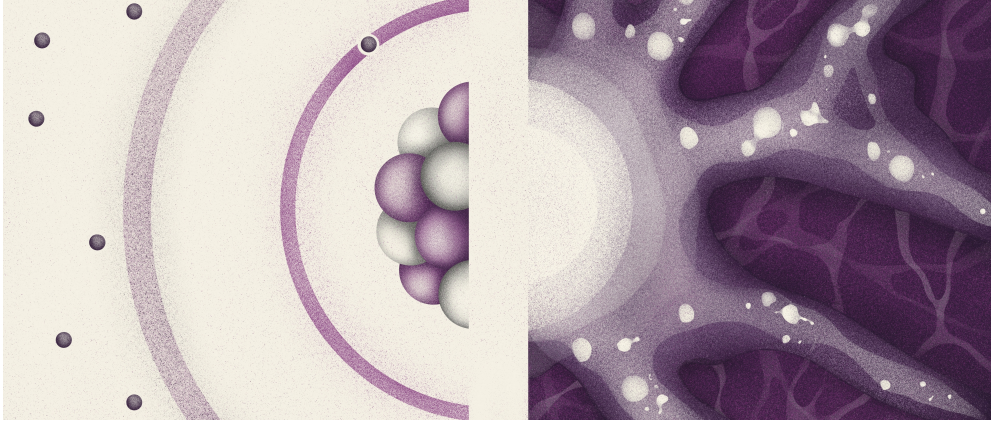


**Figure 1:** Cover of this thesis. An artistic interpretation of the O VII ion (left) and the galaxy cluster together with the cosmic web filaments (right).

## This thesis: from atoms to the cosmos

Even though much theoretical and also observational evidence shows that the cosmic web is the structure of our Universe, there are many questions about its properties on various physical scales. As already mentioned in the introduction, this thesis focuses on two parts of the cosmic web: galaxy clusters and cosmic web filaments. The methodology used throughout this thesis is X-ray spectroscopy, which goes hand in hand with modelling of the X-ray plasma. Such modelling would be impossible without the knowledge of processes happening on the atomic level. The goal of this thesis is to show that in X-ray wavelengths, the microscopic and macroscopic scales in the cosmic web are inseparable. This also serves as an idea behind the cover of this thesis, which is shown in Fig. 1.

This thesis starts with a summary of all topics which appear in the scientific papers of this thesis. In **Chapter 1** I describe the large scale structure of our Universe, and show some of the observable properties of the galaxy clusters (such as temperature, density, pressure, entropy, and metallicity profiles), as well as the cosmic web filaments, with focus on the X-ray wavelengths. I briefly describe the cosmological hydrodynamical simulations, which are later used in Chapter 2. The second half of the introduction describes the basics of the atomic processes in X-rays, either in continuum or in spectral lines. Modelling X-ray plasmas is not possible without plasma codes, which are briefly described in this chapter, together with assumptions such as collisional ionisation equilibrium or photoionisation equilibrium, and the differences between them. Towards the end of this chapter, I summarize the properties that can be derived from the X-ray spectra, and mention some of the high-resolution X-ray detectors (Chandra, XMM-Newton, XRISM or the future mission Athena).

In **Chapter 2** I demonstrate the power of the micro-calorimeters planned to be on board of future missions, such as the X-ray Integral Field Unit on board of Athena or the proposed Integral Field Unit of the Line Emission Mapper X-ray probe. Using the Hydrangea cosmological hydrodynamical simulations, I predict the expected properties of intergalactic gas in and around massive galaxy clusters. In this study, I probe a total of 138 projections from the simulation volumes, finding 16 directions with a total column density  $N_{\text{O VII}} > 10^{14.5} \text{ cm}^{-2}$ . The strongest absorbers are typically shifted by  $\pm 1000 \text{ km/s}$  with respect to the rest frame of the cluster they are nearest to. Realistic mock observations with future micro-calorimeters (Athena's X-ray Integral Field Unit and LEM's Integral Field Unit) show that the detection of cosmic web filaments in O VII and O VIII absorption against galaxy cluster cores will be feasible. An O VII detection with a  $5\sigma$  significance can be achieved in 10–250 ks with Athena for most of the galaxy clusters considered. The O VIII detection becomes feasible only with a spectral resolution of around 1 eV, comparable to that envisioned for Line Emission Mapper.

**Chapter 3** shows that considering photoionisation by just the cosmic ultraviolet and X-ray background might not be sufficient to estimate the column densities of the gas in cosmic web filaments. In this publication, I show that galaxy cluster photons, originating from the intra-cluster medium, alter the ionization state of the nearby warm-hot intergalactic medium, which is in conflict with a “typical” view, in which it is assumed that the cosmic web gas can be fully described by just collisional ionisation equilibrium. I show that the ion fractions need to be parametrized with density and temperature of the photoionised gas, as well as the distance between the ionising source and the photoionised gas. The ionisation fractions (in particular of C IV, C V, C VI, N VII, O VI, O VII, O VIII, Ne VIII, Ne IX, and Fe XVII) obtained by taking into account the photoionisation by the cosmic background are either an upper or lower limit to the ionisation fraction calculated as a function of distance from the emission from the cluster. Using a toy model of a cosmic web filament, I predict how the cluster illumination changes the column densities for two different orientations of the line of sight. For lines of sight passing close to the cluster outskirts, O VI can be suppressed by a factor of up to 4.5, O VII by a factor of 2.2, C V by a factor of 3, and Ne VIII can be boosted by a factor of 2, for low density gas.

**Chapter 4** describes the ‘clus’ model which has been newly implemented in the SPEX software package. Using this model, which calculates the spectrum and radial profile for a spherically symmetric approximation of a galaxy cluster, galaxy group, or even a massive elliptical galaxy, I investigate the magnitude of systematic effects, namely projection and resonant scattering, on the inferred temperatures and iron abundances. I consider thermodynamic profiles of nearby cool-core galaxy clusters (A383, A2029, A1795, A262, Perseus), and the massive elliptical galaxy NGC 4636, and show that the input emission measure distribution can not be recovered by using models like single-temperature, double-temperature, or gaussian differential emission measure. Additionally, I show that for some cool-core clusters, the projection effects significantly affect the measured temperatures. Previous literature studies show that resonant scattering can influence the inferred abundance profile by maximally 10 – 20%. This is in agreement with our findings for galaxy clusters with thermodynamic profiles similar to the Perseus cluster, for which I report 10 – 15% change of the abundance profile due to resonant scattering. However, for the massive elliptical galaxy NGC 4636, taking into account the RS effect in its centre can explain the central abundance drop measured with XMM-Newton and Chandra. These findings might have an impact on cross-calibration studies between different instruments, as well as on precision cosmology.

**Chapter 5** focuses on the updates of the cooling curve in the photoionization model ‘pion’, which is one of the models implemented in the plasma code SPEX. In this chapter, I describe the calculations of the radiative loss from collisional excitation, dielectronic recombination, and its impact on the cooling curve in this photoionization model in the limit of optically thin and low-density plasmas. Moreover, I discuss the updates of the atomic data for neutral hydrogen. I show the comparisons of the updated atomic database and the cooling curve in SPEX to other plasma codes (MEKAL, APEC, Cloudy) and atomic databases (CHIANTI, ADAS). I show the impact of these updates on the stability curve simulated for the active galactic nucleus NGC 5548, where I find a new stable branch. Additionally, I calculate the ionic column densities, and show which ions peak at this new stable branch. Such updates of the cooling curve are important also for the estimation of the absorption measure distribution, which describes the ionisation structure of the active galactic nucleus wind.



## Zhrnutie v slovenčine

---

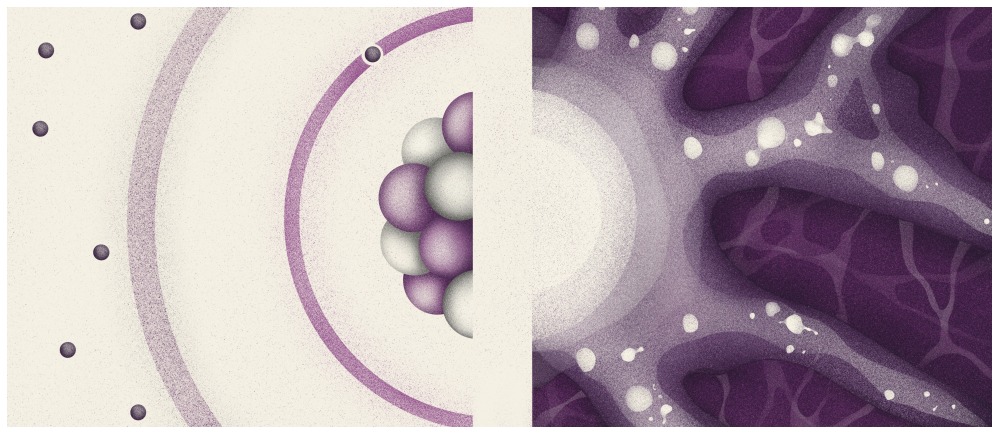
### Prečo študujeme kovy vo vesmíre?

Veľká väčšina hmoty ľudského tela sa skladá iba zo šiestich prvkov: kyslík, uhlík, vodík, dusík, vápnik a fosfor. V astrofyzike, narozdiel od iných vedných disciplín, sa päť z týchto šiestich prvkov nazýva **kovmi**. Kovy sú všeobecný termín pre všetky prvky ťažšie ako vodík a hélium. *Ako tieto kovy vznikli, odkiaľ pochádzajú a ako sa dostali na Zem?*

Dnes je dobre známe, že vodík a hélium (a malé množstvo lítia a berýlia) majú pôvod krátko po Veľkom tresku, zatiaľ čo ťažšie prvky boli a sú syntetizované v jadrách hviezd, ktoré sú v rôznych evolučných štádiách (pozri napríklad Cameron 1957; Burbidge et al. 1957; Mernier 2017). Keď tieto hviezdy vybuchnú ako supernovy, vychrlia kovy syntetizované v ich jadrách do prostredia okolo nich. Obohatením prostredia, v ktorom sa tieto hviezdy nachádzajú, môžu byť kovy zachytené na prachových zrnách alebo dokonca aj na väčších astrofyzikálnych telesách, ako napríklad na asteroidoch alebo kométach. Skrz tieto telesá môžu kovy precestovať dlhé vzdialenosti a potenciálne vytvárať stavebné kamene života, aký ho poznáme na Zemi. Napríklad plazma, ktorá sa nachádza vo filamentoch kozmickej pavučiny (viď text nižšie, v angličtine známe ako *warm-hot intergalactic medium*), plazma vyplňujúca priestor medzi galaxiami v kopách galaxií (v angličtine známe ako *intra-cluster medium*), alebo aj plazma v okolí jednotlivých galaxií (v angličtine známe ako *circum-galactic medium*) je plná týchto kovov. Štúdiom plazmy v týchto veľmi masívnych astrofyzikálnych objektoch pomocou spektroskopie a štúdiom väzieb medzi rôznymi procesmi, ktoré ovplyvňujú transport týchto kovov na rozličných fyzikálnych škálach môžeme lepšie pochopiť pôvod a vývoj kovov, ktoré sa nachádzajú v niektorých z najmasívnejších objektov v našom vesmíre.

### Veľkoškálová štruktúra vesmíru

Medzi mnohými fyzikálnymi teóriami, ktoré opisujú vznik a vývoj nášho vesmíru, je aj teória o takzvanom hierarchickom raste štruktúr vo vesmíre, ktorá je akceptovaná medzi mnohými odborníkmi. Táto teória vychádza z meraní žiarenia kozmického mikrovlnného pozadia a naznačuje, že sa náš vesmír vyvinul z menších štruktúr, ktoré sa časom pod vplyvom gravitácie zhlukovali a zrážali a vytvárali väčšie a hmotnejšie systémy. V súčasnej dobe, v ktorej je kozmologický červený posun rovný nule, má náš vesmír štruktúru, ktorá je známa ako “**kozmickej pavučiny**”. Predpokladá sa, že väčšina zatiaľ neobjaveného kozmického materiálu na röntgenových vlnových dĺžkach by mala byť nájdená práve vo vláknach/filamentoch tejto kozmickej pavučiny a to pomocou budúcich röntgenových spektroskopických misií. Táto plazma by mala mať teplotu medzi  $10^5 - 10^7$  K a hustotu elektrónov medzi  $10^{-6} - 10^{-4}$  cm $^{-3}$ . Doteraz bolo veľmi náročné pozorovať túto horúcu, rozľahlú a veľmi riedku plazmu, aj keď ako bolo poznamenané v sekcii 1.3 tejto dizertačnej práce, nebolo to nemožné. Lepšie pochopenie kozmickej pavučiny je zatiaľ v časti, ktorá má väčšie hustoty plazmy a to v takzvaných uzloch kozmickej pavučiny, kde sa nachádzajú kopy galaxií. Tieto masívne a gravitáciou viazané štruktúry obsahujú desiatky alebo stovky galaxií. Na röntgenových vlnových dĺžkach sú charakteristické plazmou, ktorá vyplňa priestor medzi týmito galaxiami, a ktorá je veľmi rozsiahla (v priemere 6 až 13 miliónov svetelných rokov), horúca ( $10^7 - 10^8$  K) a riedka ( $10^{-4} - 10^{-2}$  cm $^{-3}$ ). Relatívne množstvá medzi jednotlivými



**Obr. 1:** Obálka tejto dizertačnej práce. Umelecká interpretácia iónu  $O\ VII$  (vľavo) a kopy galaxií spolu s filamentami kozmickej pavučiny (vpravo).

chemickými prvkami v tejto plazme sú v porovnaní s našim Slnkom o 0.3-krát nižšie.

## Táto dizertačná práca: od atómov po kozmos

Aj keď množstvo teoretických a aj pozorovacích dôkazov ukazuje na to, že kozmická pavučina je štruktúra nášho vesmíru, stále existuje nespočetne veľa otázok ohľadom jej vlastností na jej rôznych fyzikálnych škálach. Ako to už bolo spomenuté v úvode, táto dizertačná práca sa zameriava na dve časti kozmickej pavučiny: kopy galaxií a vlákna kozmickej pavučiny. Metodológia použitá v tejto práci je röntgenová spektroskopia, ktorá úzko súvisí s modelovaním plazmy. Takéto modelovanie by bolo neuskutočniteľné bez poznania procesov prebiehajúcich na atomárnych škálach. Cieľom tejto dizertačnej práce je ukázať, že na röntgenových vlnových dĺžkach sú mikroskopické a makroskopické škály v kozmickej pavučine neoddeliteľné. S týmto cieľom sa zrodila aj myšlienka pre vzhľad obálky tejto práce, ktorá je znázornená na obrázku 1.

Táto práca začína súhrnom všetkých tém, ktoré sa objavujú vo vedeckých článkoch tejto dizertačnej práce a ktoré boli publikované vo svetovo uznávaných vedeckých časopisoch. V **kapitole 1** opisujem veľkoškálovú štruktúru nášho vesmíru a opisujem niektoré z pozorovateľných vlastností kôp galaxií (ako napríklad ich teplota, hustota, tlak, entropia a radiálny profil ich chemických prvkov a kovov), ako aj vlákna kozmickej pavučiny s dôrazom na röntgenové vlnové dĺžky. Stručne opisujem aj kozmologické hydrodynamické simulácie, ktoré sú neskôr použité v kapitole 2. Druhá časť úvodu popisuje základy procesov na atomárnych škálach na röntgenových vlnových dĺžkach, buď v spojitom kontinuu, alebo v jednotlivých spektrálnych čiarach. Modelovanie röntgenovej plazmy nie je možné bez špeciálnych softvérov, ktoré sú taktiež stručne popísané v tejto kapitole, spolu s predpokladmi ako je platnosť zrážkovej ionizačnej rovnováhy (anglicky *collisional ionisation equilibrium*, *CIE*) alebo platnosť fotoionizačnej rovnováhy (anglicky *photoionisation equilibrium*, *PIE*) a aké sú rozdiely medzi týmito dvoma typmi rovnováhy. V závere tejto kapitoly zhrňujem veličiny, ktoré možno odvodiť z röntgenových spekier a spomínam aj niektoré z detektorov s vysokým spektrálnym rozlíšením ako je napríklad Chandra, XMM-Newton, XRISM alebo budúca plánovaná misia s názvom Athena.

V **kapitole 2** poukazujem na výhody a silné stránky mikro-kalorimetrov, ktorých prítomnosť je plánovaná na palube misie Athena alebo nedávno navrhutej misie Line Emission Mapper (LEM). S využitím kozmologických hydrodynamických simulácií s názvom Hydrangea som popísala očakávané vlastnosti medzigalaktického plynu vnútri a v okolí veľmi hmotných kôp galaxií. V tejto publikácii skúmam celkovo 138 rôznych smerov v objeme týchto simulácií, z ktorých 16 má stĺpcovú hustotu

$N_{\text{O VII}} > 10^{14.5} \text{ cm}^{-2}$ . Miesta s najväčšou hodnotou absorpcie majú zvyčajne rýchlosti o  $\pm 1000 \text{ km/s}$  väčšie alebo menšie vzhľadom ku referenčnej sústave kopy galaxií, ku ktorej sú najbližšie. Realistické simulácie pozorovaní s použitím rozlíšenia plánovaného pre mikro-kalorimetre budúcich misií Athena a LEM ukazujú, že detekcia vlákien kozmickej pavučiny na pozadí kóp galaxií bude možná v absorpcii iónov O VII a O VIII. Pre väčšinu uvažovaných kóp galaxií bude možné dosiahnuť detekciu so signifikanciou 5 sigma v absorpcii iónu O VII za expozičný čas 10–250 ks pre plánovanú misiu Athena. Detekcia v O VIII sa stáva uskutočniteľnou len pri spektroskopickom rozlíšení okolo 1 eV, porovnateľnom s tým, ktoré je plánované pre LEM.

**Kapitola 3** ukazuje, že zohľadnenie fotoionizácie spôsobenej kozmickým ultrafialovým a röntgenovým pozadím nie je dostatočné na odhad stĺpcových hustôt plazmy vo vláknach kozmickej pavučiny. V tejto publikácii ukazujem, že fotóny vyžiarené z kóp galaxií, konkrétne z plazmy medzi jednotlivými galaxiami v tejto kope, menia ionizačný stav plazmy nachádzajúcej sa vo vláknach kozmickej pavučiny. Takáto myšlienka je v konflikte s „typickým“ pohľadom, v ktorom sa predpokladá, že plazma kozmickej pavučiny môže byť úplne popísaná len CIE rovnováhou plus PIE rovnováhou, ktorá zahŕňa „len“ kozmické ultrafialové a röntgenové pozadie. V tejto publikácii ukazujem, že relatívne podiely rôznych iónov vo fotoionizovanej plazme musia byť parametrizované minimálne tromi veličinami: hustotou a teplotou fotoionizovanej plazmy, ale aj vzdialenosťou medzi zdrojom žiarenia a fotoionizovanou plazmou. Relatívne podiely rôznych iónov, najmä C IV, C V, C VI, N VII, O VI, O VII, O VIII, Ne VIII, Ne IX, a Fe XVII, získané zohľadnením fotoionizácie kozmickým pozadím sú buď horným, alebo dolným prahom ionizačnej rovnováhy, ktorá dodatočne zohľadňuje aj fotoionizáciu, kde zdrojom žiarenia sú fotóny z kóp galaxií. Použitím jednoduchých modelov vlákien kozmickej pavučiny predpovedám, ako žiarenie z kopy galaxií mení stĺpcové hustoty plazmy v týchto vláknach pre dve rôzne orientácie pozorovania. Pre pozorovacie priamky prechádzajúce blízko okrajov kopy galaxií, stĺpcové hustoty môžu byť pre O VI potlačené až o faktor 4.5, pre O VII o faktor 2.2, pre C V o faktor 3, a pre Ne VIII môže byť stĺpcová hustota zvýšená až dvojnásobne.

**Kapitola 4** opisuje model „clus“, ktorý bol nedávno implementovaný do softvéru pre spracovanie röntgenových spektier s názvom SPEX. Použitím tohto modelu, ktorý vypočíta spektrum a radiálny profil pre sféricky symetrickú aproximáciu kopy alebo skupiny galaxií, či dokonca masívnej eliptickej galaxie, skúmam veľkosť systémových efektov, a to konkrétne projekcie a rezonančného rozptylu (anglicky *resonance scattering*, RS), na odvodené teploty a abundancie železa. Zohľadňujem pri tom termodynamické profily blízkych kóp galaxií (A383, A2029, A1795, A262, Perseus) ale aj masívnej eliptickej galaxie NGC 4636. V tejto práci ukazujem, že distribúciu emisivity, ktorá bola použitá ako vstup pre simulácie s „clus“ modelom nie je možné použitím modelov ako jednoteplotný, dvojteplotný alebo gaussovský model zreprodukovať. Pre niektoré „chladné“ kopy galaxií majú projekčné efekty významný vplyv na merané teploty. Predchádzajúca literatúra ukazuje, že RS môže ovplyvniť nameraný profil abundancie maximálne o 10–20%. To súhlasí s našimi zisteniami pre kopy galaxií, ktoré majú termodynamické profily podobné kope galaxií nazývanej Perseus, kde sme tiež našli rozdiel s veľkosťou 10–15% oproti pôvodnému profilu. Avšak, pre masívnu eliptickú galaxiu NGC 4636, zohľadnenie efektu RS môže vysvetliť nízku abundanciu kovov v jej centre ako sme to ukázali pomocou meraní s rozlíšením podobnému prístrojom XMM-Newton a Chandra. Tieto zistenia môžu mať dopad na kalibračné štúdie medzi rôznymi prístrojmi, ako aj na niektoré odvetvia kozmológie (napríklad *precision cosmology*).

**Kapitola 5** sa zameriava na zmeny krivky chladnutia plynu, ktoré som spravila vo fotoionizačnom modeli s názvom „pion“, ktorý je jedným z modelov implementovaných v softvéri SPEX. V tejto kapitole popisujem výpočty strát energie, ktoré vznikli z procesu excitácie kolíziami (anglicky *collisional excitation*), dielektronickej rekombinácie a ich vplyv na krivku chladnutia plynu v tomto modeli fotoionizácie v limite opticky tenkých a nízko-hustotných plaziem. Ďalej diskutujem aktualizácie atómovej databázy SPEX pre neutrálny vodík. Porovnávam aktualizácie atómovej databázy a krivky chladnutia plynu v SPEX s inými softvérmi (MEKAL, APEC, Cloudy) a atómovými databázami (CHIANTI, ADAS). Študujem vplyv týchto aktualizácií na krivku stability simulovanú pre aktívne galaktické jadro NGC 5548, kde som našla novú stabilnú vetvu. Taktiež uvádzam iónové stĺpcové hustoty a ktoré ióny sa nachádzajú na tejto novej stabilnej vetve. Takéto aktualizácie kriviek chladnutia plynu sú dôležité aj pre odhad distribúcie absorpčného merania (anglicky *absorption measure distribution*), ktoré opisuje ionizačnú štruktúru vetra aktívnych galaktických jadier.





# List of publications

---

## Refereed publications:

- *The clus model in SPEX: projection and resonant scattering effects on the iron abundance and temperature profiles of galaxy clusters*  
**L. Štofanová**, A. Simionescu, and J. Kaastra,  
submitted to A&A
- *Prospects for detecting the circum- and intergalactic medium in X-ray absorption using the extended intracluster medium as a backlight*  
**L. Štofanová**, A. Simionescu, N. Wijers, J. Schaye, J. Kaastra, Y. Bahé, A. Arámburo-García,  
Monthly Notices of the Royal Astronomical Society, 2024, Volume 527, Issue 3, pp.5776-5791, ADS link<sup>5</sup>
- *Galaxy cluster photons alter the ionization state of the nearby warm-hot intergalactic medium*  
**L. Štofanová**, A. Simionescu, N. Wijers, J. Schaye, J. Kaastra,  
Monthly Notices of the Royal Astronomical Society, 2022, Volume 515, Issue 3, pp.3162-3173, ADS link<sup>6</sup>
- *New radiative loss curve from updates to collisional excitation in the low-density, optically thin plasmas in SPEX*  
**L. Štofanová**, J. Kaastra, M. Mehdipour, J. de Plaa,  
Astronomy & Astrophysics, 2021, Volume 655, id.A2, 17 pp., ADS link<sup>7</sup>
- *A search for peculiar stars in the open cluster Hogg 16*  
S. Cariddi, N. Azatyan, P. Kurfurst, **L. Štofanová**, M. Netopil, E. Paunzen, O. Pintado, Y. Aidelman,  
New Astronomy, 2018, Volume 58, p. 1-9, ADS link<sup>8</sup>

## Other publications:

- *Modelling the bow-shock evolution along the DSO/G2 orbit in the Galactic centre*  
**L. Štofanová**, M. Zajaček, D. Kunneriath, A. Eckart, V. Karas,  
Proceedings of RAGtime 17-19, 2017, ADS link<sup>9</sup>
- *Agriculture and nutrition for a permanent settlement on Mars*  
Space Studies Program of the International Space University, team project report, 2021, available in the ISU Library<sup>10</sup>

---

<sup>5</sup><https://ui.adsabs.harvard.edu/abs/2024MNRAS.527.5776S/abstract>

<sup>6</sup><https://ui.adsabs.harvard.edu/abs/2022MNRAS.515.3162S/abstract>

<sup>7</sup><https://ui.adsabs.harvard.edu/abs/2021A%26A...655A...2S/abstract>

<sup>8</sup><https://ui.adsabs.harvard.edu/abs/2018NewA...58...1C/abstract>

<sup>9</sup><https://ui.adsabs.harvard.edu/abs/2017bhns.work...153S/abstract>

<sup>10</sup>[https://isulibrary.isunet.edu/index.php?lvl=notice\\_display&id=11353](https://isulibrary.isunet.edu/index.php?lvl=notice_display&id=11353)

- *Spacecamp*

**L. Štofanová**, article in SRONieuws, nr. 110 july 2022, internal publication of the Netherlands Institute for Space Research

## Reproduction packages:

- Reproduction package for the publication *Prospects for detecting the circum- and intergalactic medium in X-ray absorption using the extended intracluster medium as a backlight*  
**L. Štofanová**, available on ZENODO<sup>11</sup>
- Reproduction package for the publication *Galaxy cluster photons alter the ionisation state of the nearby warm-hot intergalactic medium*  
**L. Štofanová**, available on ZENODO<sup>12</sup>
- Reproduction package for the publication *New radiative loss curve from updates to collisional excitation in the low-density, optically thin plasmas in SPEX*  
**L. Štofanová**, available on ZENODO<sup>13</sup>

---

<sup>11</sup><https://zenodo.org/records/10031083>

<sup>12</sup><https://zenodo.org/records/6656840>

<sup>13</sup><https://zenodo.org/records/5497662>

# Curriculum Vitae

---

I was born in the city in the middle of Slovakia called Banská Bystrica. I was blessed to be born to wonderful and supportive parents: my mom Lýdia Štofanová (born Mydlová) and my dad Jaroslav Štofan. From the age of seven, all I talked about was how I am going to work for NASA one day. My parents always supported me and encouraged me to pursue my dreams. I am forever grateful to them for believing in me.

I grew up in a small town in Slovakia called Ružomberok, which is very famous for its paper production, and historically was known for its textile industry. My home town has a neighbouring village called Vlkolínec – which is one of eight UNESCO world heritage sites located in Slovakia. I attended the primary school Sládkovičova in the suburb area called Baničné from 2001 to 2005, and in 2005 at the age of ten I got accepted to Gymnázium Š. Moyzesa, an eight year long gymnasium study where I focused on the foreign languages. During this time, my passion for astrophysics was growing, and I started attending some local astronomy competitions, for which I developed my knowledge through self-study, using encyclopedias and online resources.

During my gymnasium years I got an extensive training in modern dancing (hip-hop, scenic dance, and show dance) and competed in many national and regional Slovak competitions with my dancing crew called REFRESH. In 2012, we won the very first year of the slovak national competition called “The school dance”. The highlight of my semi-professional dancing career was the last year of my high-school, when we prepared an hour long show, which we produced and directed ourselves. The show aimed to raise awareness about domestic violence and bullying in schools. It also gave a platform to those who had faced adversity such as overcoming cancer, racism, or losing a loved one.

In the final year of my high-school education, I applied to the faculty of mathematics and physics at the Charles University in Prague, where in 2013 I started my studies of general physics. During my bachelor studies I had a chance to work in the lab, and I was awarded a scholarship for a student project called “*Study of the resistivity changes in conducting polymers*”. I completed my bachelor thesis under the supervision of Vladimír Karas and Michal Zajaček at the Astronomical Institute of the Czech Academy of Sciences. The subject of my bachelor thesis was our Galactic centre, and its nearby dusty and gaseous structures. More specifically, I studied the bow-shock structures that are generated by stars moving supersonically in the ambient medium of the Galactic centre, and how they vary along their orbit. During this period, I had a chance to attend the ESO/OPTICON/IAU summer school on modern instruments, their science case, and practical data reduction, which later led to my very first publication as a co-author. This publication focuses on chemically peculiar stars.

In 2016, I started my master studies at the Charles University in Prague which were focused on astronomy and astrophysics. My master’s thesis supervisor Jiří Svoboda showed me the beauty (and challenges) of X-ray spectroscopy and he is the reason why I later focused on X-ray spectroscopy during my Ph.D. studies. My master thesis, which I completed at the Astronomical Institute of the Czech Academy of Sciences, was focused on relativistic corrections in hard X-ray spectra of accreting black holes. I re-analysed NuSTAR observations of an active galactic nucleus 1H0419-577 and X-ray binary GRS 1915+105, and found that the extremely low coronal temperatures observed in these sources may be explained by the gravitational redshift due to the proximity of the compact corona to the black hole. During this time I also co-authored lecture notes for the subject called “*Fundamentals of Quantum Theory*” (NOFY042), and I volunteered to be a part of the local organizing committee for the EWASS

conference held in Prague in 2017.

In 2018, I started my Ph.D. studies at the Leiden Observatory, while simultaneously being affiliated to SRON – the Netherlands Institute for Space Research. My Ph.D. was supervised by Jelle Kaastra, Joop Schaye, and Aurora Simionescu. It focused mainly on galaxy clusters, cosmic web filaments, and atomic physics. During these years I worked on a plethora of different topics. Using cosmological hydrodynamical simulations I provided predictions for observing cosmic web filaments with planned X-ray mission Athena and the Line Emission Mapper X-ray probe. I also worked on the photoionisation model in the atomic plasma code SPEX as well as the '*clus*' model, which is used for analysing spectra of galaxy clusters, galaxy groups, and massive elliptical galaxies.

The first year of my Ph.D. was full of training opportunities provided by the Leiden Observatory and the Leiden University. I attended a 5-day long research fall school in Dwingeloo organised by NOVA – The Netherlands Research School for Astronomy. During the Leiden Observatory Ph.D. introductory event I participated in academic skills courses for time management, effective communication, and scientific integrity. In the same year I started my journey as a teaching assistant (TA), which lasted for four semesters. I was a TA for courses such as High Energy Astrophysics (2018/2019 and 2020/2021), Observational Cosmology (2019/2020), and Project Management for Scientists (2021/2022). During these years I also benefited from having my personal career coach.

In 2021, I became the third Slovak alumna who graduated from the Space Studies Program (SSP) at the International Space University (ISU), where I specialized in Management and Business in Space. With my team I worked on a project focused on agriculture and nutrition for a permanent settlement on Mars, which became an official publication, and in 2022 it was presented at the International Astronautical Congress in Paris. Together with my colleague I led the final presentation of this team project as a part of the graduation from the SSP program.

My years at the Leiden Observatory and SRON were full of interesting scientific discussions with many research groups. Leiden Observatory and SRON provided me with an indescribable community of inspiring scientists and colleagues. Thanks to their support I got very close to my childhood dream of working at NASA, and visited the Goddard Space Flight Center (GSFC) in Greenbelt, Maryland (see Fig. 2). Not only did I visit NASA during this period, but I also got a chance to give a talk at Massachusetts Institute of Technology. During my Ph.D. years I enjoyed volunteering and public outreach. In the school year 2019/2020, I was the treasurer and the webmaster for the association for Ph.D. students of Leiden University (LEO). During this time, my fellow board members and I helped other Ph.D. organizations like PhDoc and PNN with putting together official guidelines for the responsibilities of the supervisors as well as Ph.D. candidates. In the year 2020/2021 I was a member-at-large. In 2020, I was a member of the local organizing committee for the EAS and NAC conferences held in Leiden. In 2022, I represented SRON and the NOVA School at the ESA Open Days in the 'NL Space tent' in ESTEC, Noordwijk. In this same year, I also volunteered for the Discover ISU Open Days and I was one of the mentors for the SSP22 program. I would like to think I am known for my passion for giving talks, which makes my experience with public outreach activities very pleasant and enjoyable. I have participated in two "major" public appearances so far, one of them was a live interview for the Slovak national television TA3, and the other was my appearance as a guest in a Slovak podcast that highlights career paths of people who come from the same region as I do - Liptov. I hope I gain more experience with public outreach in the near future.

In the last year of my Ph.D. I attended the SKIES program, focused on mentorship and training of Ph.D. candidates in academia but also in the space industry, where I benefited from a 6-months long mentorship. In July 2024, I started my postdoctoral position at the Masaryk University in Brno under the supervision of Norbert Werner. I am beyond excited for this new chapter of my life, especially because my current supervisor and I are aligned in our goal of identifying ways to enhance cooperation between the astrophysics community and the space industry. During this period I will work on the very first Czech space telescope called QUVIK – Quick Ultra-Violet Kilonovae surveyor. Its primary scientific goal is to detect kilonovae at UV wavelengths. Observing their UV brightness evolution is crucial to distinguish between different explosion scenarios.



**Figure 2:** Pictures from my visit to the Goddard Space Flight Center (GSFC) in Greenbelt, Maryland, where I presented my Ph.D. research at the special seminar of the X-ray Astrophysics Laboratory.

